FACULTY OF MECHANICAL ENGINEERING AND SHIP TECHNOLOGY

The author of the PhD dissertation: M.Sc. Eng. Milad Amiri

Scientific discipline: Field of engineering and technical sciences, Mechanical Engineering

DOCTORAL DISSERTATION

Title of PhD dissertation: CO_2 capture through Direct-Contact Condensation in a spray ejector condenser aided by a cyclone or T-junction separators

Title of PhD dissertation (in Polish): Wychwyt CO_2 poprzez kondensację w bezpośrednim kontakcie w chłodnicy strumieniowej wspomaganej przez separatory typu cyklonowego lub T-junction

Supervisor

signature

prof. dr hab. inż. Dariusz Mikielewicz, czł. koresp. PAN

Gdańsk, 2024

STATEMENT

The author of the PhD dissertation: M.Sc. Eng. Milad Amiri

I, the undersigned, agree/~~do not agree*~~ that my PhD dissertation entitled:
CO2 capture through Direct-Contact Condensation in a spray ejector condenser aided by a cyclone or T-junction separators.[11]

Gdańsk, 05.12.2024 ....

signature of the PhD student

Aware of criminal liability for violations of the Act of 4th February 1994 on Copyright and Related Rights (Journal of Laws 2006, No. 90, item 631) and disciplinary actions set out in the Law on Higher Education (Journal of Laws 2012, item 572 with later amendments),[22]as well as civil liability, I declare, that the submitted PhD dissertation is my own work.

I declare, that the submitted PhD dissertation is my own work performed under and in cooperation with the supervision of prof. dr hab. inż. Dariusz Mikielewicz.

This submitted PhD dissertation has never before been the basis of an official procedure associated with the awarding of a PhD degree.

All the information contained in the above thesis which is derived from written and electronic sources is documented in a list of relevant literature in accordance with art. 34 of the Copyright and Related Rights Act.

I confirm that this PhD dissertation is identical to the attached electronic version.

Gdańsk, 05.12.2024 ....

signature of the PhD student

I, the undersigned, agree/~~do not agree*~~ to include an electronic version of the above PhD dissertation in the open, institutional, digital repository of Gdańsk University of Technology, Pomeranian Digital Library, and for it to be submitted to the processes of verification and protection against misappropriation of authorship.

Gdańsk, 05.12.2024 ....

*) delete where appropriate. *signature of the PhD student*

[1] Decree of Rector of Gdansk University of Technology No. 34/2009 of 9th November 2009, TUG archive instruction addendum No. 8.

[2] Act of 27th July 2005, Law on Higher Education: Chapter 7, Criminal responsibility of PhD students, Article 226.

DESCRIPTION OF DOCTORAL DISSERTATION

The Author of the PhD dissertation: M.Sc. Eng. Milad Amiri

Title of PhD dissertation: CO_2 capture through Direct-Contact Condensation in a spray ejector condenser aided by a cyclone or T-junction separators

Title of PhD dissertation in Polish: Wychwyt CO_2 poprzez kondensację w bezpośrednim kontakcie w chłodnicy strumieniowej wspomaganej przez separatory typu cyklonowego lub T-junction

Language of PhD dissertation: English

Supervision: prof. dr hab. inż. Dariusz Mikielewicz

Date of doctoral defense:

Keywords of PhD dissertation in English: Carbon capture, spray ejector condenser, steam ejector condenser, cyclone, T-junction, separation, condensation, two phase flow

Keywords of PhD dissertation in Polish: Złapanie węgla, chłodnica strumieniowa, chłodnica strumieniowo-parowa, cyklon, separator typu T-junction, separacja, kondensacja, przepływ dwufazowy

Summary of PhD dissertation in English: This dissertation explores the vital task of separating and purifying CO_2 in post-combustion sections of gas power plants. It focuses on integrating spray or steam ejector condenser with cyclone or T-junction separators to enhance CO_2 capture through direct-contact condensation (DCC). The study employs experimental, analytical, and numerical techniques to understand DCC mechanisms within SEC and optimize separator performance. Integration of SEC with cyclone separators is investigated, optimizing steam and CO_2 flow rates, droplet breakup, and cyclone cone size to improve CO_2 purification efficiency. Structural modifications and parameter optimization enhance separator performance. The dissertation also explores optimizing cyclone separators with vanes and integrating SEC with T-junction separators. It emphasizes parameter optimization to enhance CO_2 capture effectiveness and investigates innovative techniques like steam ejector condenser with electrohydrodynamic (EHD) actuators. Therefore, the dissertation contributes to advancing CO_2 capture technologies by providing insights into integrating SEC with separators, optimizing operational parameters, and exploring novel techniques to enhance CO_2 purification efficiency in gas power plant post-combustion sections.

Summary of PhD dissertation in Polish: Niniejsza praca doktorska koncentruje się na zagadnieniach separacji dwutlenku węgla zawartego w spalinach w modelu elektrowni gazowej o ujemnej emisji CO2. Praca koncentruje się na integracji chłodnicy strumieniowej (SEC) z bezpośrednią kondensacją (DCC) z separatorami typu cyklon lub T-junction, aby zwiększyć separację. Przedstawione wyniki oparte są na wykorzystaniu badań eksperymentalnych, analitycznych i numerycznych celem lepszego poznania mechanizmów bezpośredniej kondensacji w SEC i optymalizacji wydajności separatorów do dokładnego oczyszczania gazów. Celem poprawy wydajności separacji CO2 badana jest integracja SEC z separatorami cyklonowymi celem optymalizacji relacji przepływu pary do zawartości CO2, uwzględniając rozpad kropel i geometrię stożka cyklonu. Modyfikacje konstrukcyjne i optymalizacja powyższych parametrów zwiększają wydajność separatorów. Praca doktorska bada również optymalizację separatorów cyklonowych poprzez ustawienie kierownic oraz integrację SEC z separatorami typu T-junction. Przedstawia wynik analizy optymalizacji parametrów w celu zwiększenia skuteczności wychwytu CO2. Rozpatrzony został także dodatkowy efekt, który może być zastosowany w chłodnicy strumieniowej a mianowicie wprowadzenie aktuatorów elektrohydrodynamicznych (EHD). W tym świetle praca doktorska przyczynia się do zaawansowania technologii wychwytu CO2, dostarczając informacji dotyczących integracji SEC z separatorami, optymalizację parametrów pracy układu i badanie nowatorskich technik w celu zwiększenia efektywności separacji CO2 po spalaniu w elektrowniach gazowych.

ACKNOWLEDGEMENTS

To Prof. Dariusz Mikielewicz

I wish to convey my profound and heartfelt gratitude to my esteemed supervisor, Prof. Dariusz Mikielewicz, whose unparalleled guidance, steadfast support, and visionary mentorship have been the cornerstone of my academic journey. His intellectual acumen, unwavering encouragement, and insightful feedback have been indispensable in shaping the direction of this research and fostering my growth as a scholar. I am immensely grateful for the trust he has placed in me, and for the exceptional opportunities he has afforded me to advance my work.

To my family,

I am equally indebted to my family for their boundless love, unwavering support, and unrelenting belief in me. Their encouragement has been a continual source of strength and fortitude, providing me with the resilience to persevere through the challenges of this endeavour. To my parents, I offer my deepest appreciation for their patience, understanding, and unwavering faith in my abilities throughout this journey.

To colleagues,

I would also like to extend my sincere appreciation to my colleagues, whose collaboration, camaraderie, and intellectual contributions have enriched this research experience immeasurably. The stimulating discussions, the exchange of ideas, and the collective pursuit of excellence with them have not only enhanced the quality of this work but have also made this scholarly endeavour both enjoyable and profoundly rewarding.

Also,

The research leading to these results has received funding from the Norway Grants 2014–2021 via the National Center for Research and Development. Article has been prepared within the frame of the project: “Negative CO2 emission gas power plant” - NOR/POLNORCCS/NEGATIVE-CO2- PP/0009/2019–00 which is co-financed by programme “Applied research” under the Norwegian Financial Mechanisms 2014–2021 POLNOR CCS 2019 - Development of CO2 capture solutions integrated in power and industry processes. Moreover, I gratefully acknowledge the financial support provided by the Doctoral School Programs Polonium and Francium, as well as the funding from Gdańsk University of Technology, which was instrumental in facilitating the research presented in this thesis.

Contents

MONOTHEMATIC PUBLICATIONS

[A] Dariusz Mikielewicz, **Milad Amiri**, Michał Klugmann, Jarosław Mikielewicz, A novel concept of enhanced direct-contact condensation of vapour-inert gas mixture in a spray ejector condenser. International Journal of Heat and Mass Transfer, 2023. 216: p. 124576. DOI: https://doi.org/10.1016/j.ijheatmasstransfer.2023.124576.
IF: 5.2*; MNISW:200

[B] **Milad Amiri**, Paweł Ziółkowski, Jaroslaw Mikielewicz, Michal Klugmann, Dariusz Mikielewicz, Analysis of cyclone separator solutions depending on spray ejector condenser conditions, Applied Thermal Engineering, 2024. DOI: https://doi.org/10.1016/j.applthermaleng.2024.124235.
IF: 6.4*; MNISW: 140

[C] **Milad Amiri**, Jarosław Mikielewicz, Paweł Ziółkowski, Dariusz Mikielewicz, Optimizing CO2 purification in a Negative CO2 Emission Power Plant, Chemical Engineering & Technology, 2024. DOI: https://doi.org/10.1002/ceat.202300568.
IF: 2.1*; MNISW: 70

[D] **Milad Amiri**, Michal Klugmann, Jaroslaw Mikielewicz, Paweł Ziółkowski, Dariusz Mikielewicz, CO2 capture through direct-contact condensation in a spray ejector condenser and T- junction separator, International Communications in Heat and Mass Transfer, 2024. DOI: https://doi.org/10.1016/j.icheatmasstransfer.2024.107596.
IF: 7* ; MNISW: 140

[E] **Milad Amiri**, Jaroslaw Mikielewicz, Dariusz Mikielewicz, CO2 capture using steam ejector condenser under electro hydrodynamic actuator with non-condensable gas and cyclone separator: A numerical study. Separation and Purification Technology, 2024. **329**: p. 125236. DOI: https://doi.org/10.1016/j.seppur.2023.125236.
IF: 9.2*; MNISW: 140

The Author's contribution to each of the papers mentioned above were as follows:

[A] Methodology, Writing – review & editing, Validation, Formal analysis, Investigation, Data curation;

[B] Conceptualization, Methodology, Data curation, Formal analysis, Investigation, Resources, Software, Validation, Visualization, Writing – original draft, Writing – review & editing.

[C] Conceptualization, Methodology, Data curation, Formal analysis, Investigation, Resources, Software, Validation, Visualization, Writing – original draft, Writing – review & editing.

* The impact factors of the journals have been considered based on the submission date of the article to each respective journal.

[D] Conceptualization, Methodology, Data curation, Formal analysis, Investigation, Resources, Software, Validation, Visualization, Writing – original draft, Writing – review & editing.

[E] Conceptualization, Methodology, Data curation, Formal analysis, Investigation, Project administration, Resources, Software, Validation, Visualization, Writing - original draft, Writing - review & editing.

SUPPLEMENTARY PUBLICATIONS

[F] **Milad Amiri**, Paweł Ziółkowski, Dariusz Mikielewicz, Synergistic effects of a swirl generator and MXene/water nanofluids used in a heat exchanger pipe of a Negative CO2 Emission Gas Power Plant, Numerical Heat Transfer, Part A: Applications, 2024. DOI: https://doi.org/10.1080/10407782.2024.2368277

[G] Paweł Ziółkowski, Paweł Madejski, **Milad Amiri**, Tomasz Kuś, Kamil Stasiak, Navaneethan Subramanian, Halina Pawlak-Kruczek, Janusz Badur, Łukasz Niedźwiecki and Dariusz Mikielewicz, Thermodynamic Analysis of Negative CO2 Emission Power Plant Using Aspen Plus, Aspen Hysys, and Ebsilon Software, Energies, 2021. DOI: https://doi.org/10.3390/en14196304

[H] **Milad Amiri**, Dariusz Mikielewicz, Three Dimensional Numerical investigation of hybrid nanofluids in chain microchannel under electrohydrodynamic actuator, Numerical Heat Transfer, Part A: Applications, 2022. DOI: https://doi.org/10.1080/10407782.2022.2150342

[I] Paweł Madejski, Krzysztof Banasiak, Paweł Ziółkowski, Dariusz Mikielewicz, Jarosław Mikielewicz, Tomasz Kuś, Michał Karch, Piotr Michalak, **Milad Amiri**, Paweł Dąbrowski, Kamil Stasiak, Navaneethan Subramanian, Tomasz Ochrymiuk, Development of a spray-ejector condenser for the use in a negative CO2 emission gas power plant, Energy, 2023. DOI: https://doi.org/10.1016/j.energy.2023.129163

[J] Paweł Ziółkowski, Kamil Stasiak, **Milad Amiri**, Dariusz Mikielewicz, Negative carbon dioxide gas power plant integrated with gasification of sewage sludge, Energy, 2023. DOI: https://doi.org/10.1016/j.energy.2022.125496

[K] Paweł Ziółkowski, Janusz Badur, Halina Pawlak- Kruczek, Kamil Stasiak, **Milad Amiri**, Lukasz Niedzwiecki, Krystian Krochmalny, Jakub Mularski, Paweł Madejski, Dariusz Mikielewicz, Mathematical modelling of gasification process of sewage sludge in reactor of negative CO2 emission power plan, Energy, 2022. DOI: https://doi.org/10.1016/j.energy.2021.122601

[L] **Milad Amiri**, Mohammad bagher Ayani, Pawel Ziolkowski, Dariusz Mikielewicz, Numerical analysis of vacuum drying of a porous body in the integrated domain, Journal of Food Process Engineering, 2022. DOI: https://doi.org/10.1111/jfpe.14006

[M] Safoura Zadhossein, Yousef Abbaspour-Gilandeh, Mohammad Kaveh, Mariusz Szymanek, Esmail Khalife, Olusegun D. Samuel, **Milad Amiri**, Jacek Dziwulski, Exergy and Energy Analyses of Microwave Dryer for Cantaloupe Slice and Prediction of Thermodynamic Parameters Using ANN and ANFIS Algorithms, Energies, 2021. DOI: https://doi.org/10.3390/en14164838

Patent

Układ do bezpośredniej kondensacji mieszaniny pary z gazem inertnym oraz separacji gazu inertnego, zwłaszcza CO2 i sposób kondensacji mieszaniny pary z gazem inertnym oraz separacji gazu inertnego od mieszaniny pary z gazem inertnym, zwłaszcza CO2.

Zgłoszenie oznaczono numerem: P.449542. [WIPO ST 10/C PL449542].

Conference presentations (Presenting Author: Milad Amiri)

[1] Dariusz Mikielewicz, **Milad Amiri**, Jarosław Mikielewicz. Direct-contact condensation from vapour- gas mixture in a spray ejector condenser for negative CO2 power plant. 2nd International Conference on Negative CO2 Emissions, Gothenburg, Sweden. June 14-17 (2022).

[2] **Milad Amiri**, Paweł Ziółkowski, Kamil Stasiak, Dariusz Mikielewicz. Numerical analysis of CO2-water separation in a horizontal double T-junction. 7th International Conference on Contemporary Problems of Thermal Engineering | Hybrid event, Warsaw, Poland. September 20-23 (2022).

[3] **Milad Amiri**, Paweł Ziółkowski, Kamil Stasiak, Dariusz Mikielewicz. Analysis of cyclone separator solutions depending on SEC outlet conditions in nCO2PP. 36th International Conference on Efficiency Cost Optimization Simulation and Environmental Impact of Energy system. Las Palmas, Spain. June 25-30 (2023).

[4] **Milad Amiri**, Paweł Ziółkowski, Kamil Stasiak, Mario Ditaranto, Samuel Wiseman, Dariusz Mikielewicz. Numerical Simulation of Cold Flow and Combustion in a Swirl-Stabilized Combustor. Nordic Flame Days 2023 (NFD 2023), Trondheim, Norway. November (28-30)

Workshops

[5] **Milad Amiri**, Paweł Ziółkowski, Dariusz Mikielewicz. Selected CFD results for CO2 separator - comparison of system with and without spray-ejector condenser. Wdzydzeanum. September 05-10 (2021)

[6] **Milad Amiri**, Jarosław Mikielewicz, Paweł Ziółkowski, Dariusz Mikielewicz. Numerical investigation of decreasing pressure drops by adding conical section to cyclone separators of CO2 from water for innovative power plant nCO2PP. Wierzyca. September 02-04 (2021)

SYMBOLS

$\dot{m}$	$\frac{g}{s}$	fuel mass flow
N	kW	turbine power
p	Bar	pressure
$\dot{Q}_{cc}$	kW	chemical energy rate of combustion
t	ºC	temperature
X	%	mole fraction
Greek Symbols		
η	%	efficiency
Abbrevations		
ASU	-	Air Separation Unit
DCC	-	Direct Contact Condensation
EHD	-	electrohydrodynamic
PFD	-	Process Flow Diagram
SEC	-	Spray Ejector Condenser
WCC	-	Wet Combustion Chamber

I. Introduction

1. Carbon capture and storage (CCS)

Climate change, exacerbated by the accumulation of global warming agents including CO2, presents a critical threat to global environmental safety. Elevated concentrations of CO2 amplify the retention of thermal radiation within the Earth's atmosphere, resulting in global warming and consequential disruptions to weather patterns, sea levels, and ecosystems. Effective mitigation of this crisis necessitates urgent actions to reduce CO2 emissions through sustainable practices and policies. Issues related to carbon capture fall into the category of CCS technologies and are perceived as playing a pivotal role in the endeavour to combat climate change. Carbon capture, often referred to as CCS, is a pivotal technology in the initiative to resist climate change [1-3]. This process entails the interception of CO2 emissions generated by the combustion of fossil fuels or industrial activities, effectively sequestering them to preclude their release into the atmosphere. This technology is essential because CO2 stands as a predominant greenhouse gas, significantly contributing to the phenomena of global warming and climate change [4]. The process of carbon capture typically encloses three fundamental stages: capture, transportation, storage or utilization into another useful product [5-8]. During the capture phase, CO2 is separated from the effluent gases of power generation facilities or industrial installations through the application of diverse methodologies, including absorption, adsorption, or chemical reactions [5-14]. Once captured, the CO2 is pressurized into a supercritical or dense fluid state for efficient transportation via pipelines, ships, or trucks to suitable storage sites. Alternatively, a technology can be applied to produce useful products such as methanol, synthetic fuels such as dimethyl ether (DME), or even synthetic methane [15]. The issue of CO2 management is not the topic of the present work. Storage of captured CO2 is usually done underground in geological formations. These subsurface structures offer reliable and enduring storage solutions where CO2 can be stored for thousands of years without leaking back into the atmosphere. Carbon capture technology is crucial for several reasons [2, 16, 17]:

- Mitigating climate change: Through the sequestration of CO2 emissions from energy generation and industrial processes, carbon capture technology plays a pivotal role in curtailing greenhouse gas emissions, thereby alleviating the adverse effects of global warming and mitigating the progression of climate change.
- Fossil fuel use: Carbon capture enables the continued utilization of fossil fuels such as coal, natural gas, and oil, whilst substantially mitigating their environmental repercussions. This is especially important in regions where fossil fuels remain a significant part of the energy mix.
- Industrial emissions: Many industrial processes produce significant CO2 emissions, including cement production, steel manufacturing, and chemical production. Carbon capture technology can be implemented within these industries to substantially mitigate their carbon emissions footprint.
- Transition to renewable energy: While the ultimate goal is to shift towards sustainable energy alternatives like hydroelectric power, wind, and solar. Carbon capture

technology can help bridge the gap during this transition period by reducing emissions emanating from incumbent fossil fuel-driven power generation facilities.

Despite its benefits, carbon capture technology encounters obstacles, including substantial financial expenditures, energy requirements, and public acceptance [18]. Continued research initiatives are essential to enhance the efficiency and economic viability of carbon capture technologies and to develop policies and regulations that incentivize their deployment [19-23]. There are several methods employed for carbon capture in power generation facilities, incorporating I) pre-combustion [24], II) oxy-combustion [25, 26] and III) post-combustion [21, 27, 28], which will be described in further detail.

1.1 Pre-combustion method

The pre-combustion method in power plants is a carbon capture technique that comprises capturing CO2 emissions before the fossil fuel combustion [29, 30]. In the pre-combustion process, syngas production can be achieved through two primary methodologies: steam reforming and oxidation [31-33]. Steam reforming involves incorporation of steam to primary fuel, resulting in a chemical reaction that produces a mixture of CO and H2. This method is particularly effective for processing natural gas and other hydrocarbon fuels. Alternatively, the incorporation of oxygen into the primary fuel leads to a process known as oxidation, which can be further categorized based on the state of the fuel. For gaseous and liquid fuels, this process is termed “partial oxidation”, while for solid fuels, it is referred to as “gasification”. Despite the differing terminologies, both methods operate on similar principles: the conversion of carbonaceous materials into syngas through high-temperature reactions with an oxidizing agent [34]. Reactions 1 and 2 for steam reforming and oxidation are as follows.

Steam reforming:

$$C_xH_y + xH_2O \leftrightarrow xCO + (x + \frac{y}{2})H_2 \tag{1}$$

Gasification/partial oxidation:

$$C_xH_y + \frac{x}{2}O_2 \leftrightarrow xCO + (\frac{y}{2})H_2 \tag{2}$$

Syngas production is subsequently followed by the water-gas shift (WGS) reaction, wherein carbon monoxide (CO) is transformed into CO2 and H2 through the introduction of steam:

$$CO + H_2O \leftrightarrow CO_2 + H_2 \tag{3}$$

Once the syngas is produced, various separation methods, including pressure swing adsorption (PSA), membrane filtration, or physical solvent absorption, are employed to isolate CO2 from H2. [35]. Table 1 presents an overview of the concepts, advantages, and drawbacks of the aforementioned technologies.

Table. 1 Evaluation of CO_2 separation techniques in pre-combustion processes

Technology	Idea	Advantages	Drawbacks
pressure swing adsorption (PSA)	separates CO_2 from syngas using porous materials that adsorb gases at different rates under varying pressures	- effective separation of CO_2 - can be integrated into existing systems - relatively low operational costs	- high maintenance costs for adsorbent materials - limited by the capacity of adsorbent materials
membrane separation	utilizes selective permeability of membranes to separate CO_2 from hydrogen	- high selectivity and efficiency - continuous operation - compact and scalable technology	- high cost of membrane materials - potential fouling and degradation over time
physical solvent absorption	uses physical solvents like Selexol or Rectisol to absorb CO_2 from syngas	- highly efficient at high CO_2 concentrations - solvents can be regenerated and reused - suitable for large-scale operations	- energy-intensive regeneration process - requires careful handling and disposal of solvents

These techniques exploit variations in physical or chemical properties between CO_2 and H_2 to selectively capture the CO_2 while allowing the hydrogen to pass through. The concept of pre-combustion capture is depicted in Fig.1 [36].

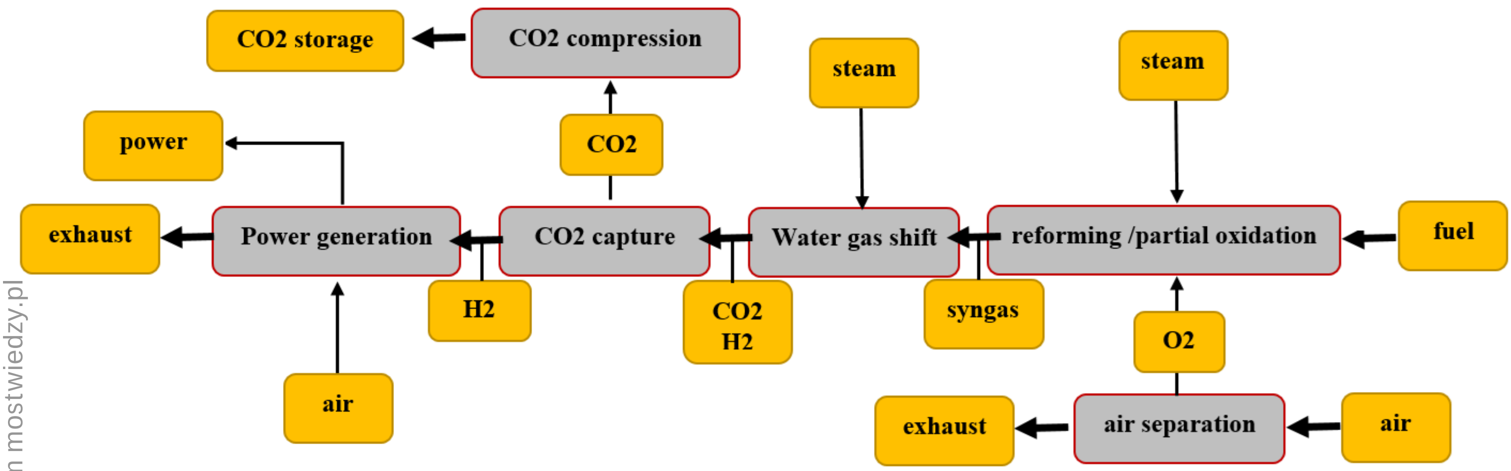

Fig.1 Pre-combustion capture technology in power generation [36]

A principal merit of pre-combustion capture lies in the fact that it produces a concentrated stream of CO_2, streamlining and more energy-efficient to capture compared to post-combustion methods. Additionally, integrating pre-combustion capture with other processes such as hydrogen production can provide additional economic benefits and synergies [37]. Notwithstanding, pre-combustion capture is not without its challenges, which encompass the complexity and cost of gasification or steam reforming processes, as well as the need for additional equipment and infrastructure for CO_2 separation [34, 38]. Ongoing research and development endeavours seek to enhance the efficiency and economic viability of pre-combustion capture technologies while simultaneously addressing the inherent challenges associated with their implementation. Therefore, the pre-combustion method in power plants offers a promising pathway for reducing CO2 emissions and advancing towards a more sustainable energy future.

1.2 Oxy-fuel combustion

This method in power plants reflects a forward-thinking approach to carbon capture and combustion that aims to minimize CO2 emissions while generating energy [25, 39-41]. Unlike traditional combustion processes, where fossil fuels are burned in air, oxy-combustion entails combustion of fuels within an atmosphere composed of pure oxygen and recirculated flue gas, leading to a flue gas stream consisting primarily of CO2 and water vapour. In this method, oxygen is segregated from the air and supplied to combustion chamber, eliminating the presence of nitrogen, which makes up the majority of air. By eliminating nitrogen, the formation of nitrogen oxides (NOx) is also prevented, reducing the emission of these harmful pollutants. Oxygen can be generated through various methods, with the most common being cryogenic air distillation, subsequently preceded by oxygen transport membranes, PSA, electrolysis of water and chemical looping air separation [42]. The concepts of these techniques, along with their privileges and drawbacks, are detailed in Table 2, and the schematic of each technology is shown in Fig. 2.

Table. 2 Comparison of oxygen production technologies: ideas, advantages, and drawbacks [43]

Technology	Idea	Advantages	Drawbacks
cryogenic air distillation	uses low-temperature distillation to separate oxygen from air.	- high purity oxygen - scalable for large capacities - allows recovery of other industrial gases	- very energy-intensive - high initial investment - large physical footprint
pressure swing adsorption (PSA)	utilizes adsorbents to selectively adsorb nitrogen from air under varying pressures.	- lower energy consumption compared to cryogenic distillation - compact size and modular design	- limited by adsorbent capacity - requires high-pressure operation
oxygen transport membranes	relies on selective permeability of membranes to separate oxygen from air.	- energy efficient compared to cryogenic methods - continuous operation - modular and scalable	- limited by membrane lifespan and stability - high capital cost
chemical looping air separation	uses metal oxides to facilitate O2 separation from air without direct contact between air and oxygen.	- potential for lower energy consumption - integrated CO2 capture capabilities	- complexity in handling metal oxide materials - potential for operational challenges
electrolysis of water	electrochemically splits water into oxygen and hydrogen using electricity.	- can utilize renewable electricity sources - produces high purity oxygen and hydrogen	- high energy consumption - expensive electrolyte materials - requires water and electrolyte management

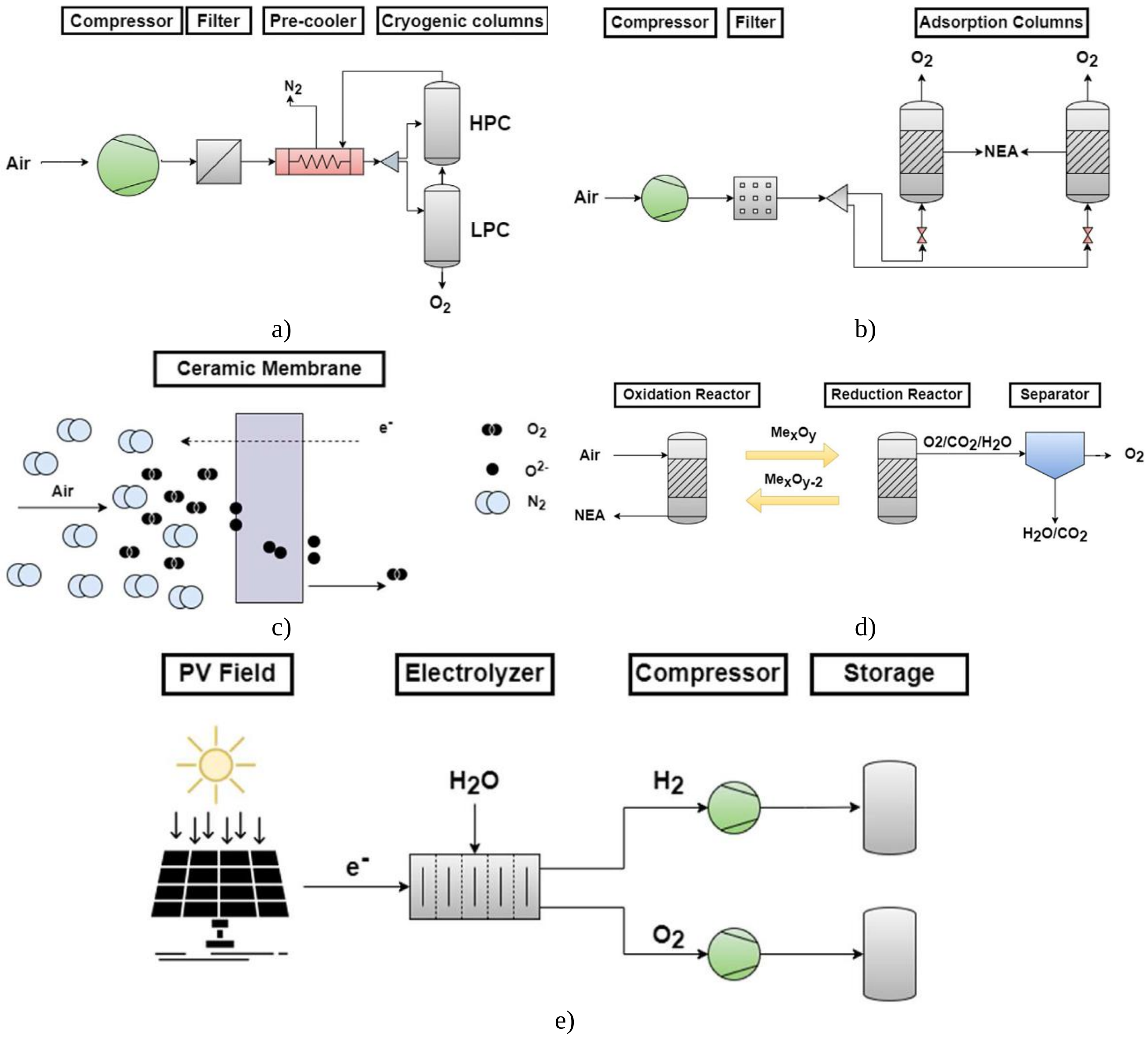

Fig. 2 Diagram of oxygen production technologies including a) cryogenic air separation unit, b) PSA process, c) O2 transport membranes, d) chemical looping air separation and e) electrolysis of water [43]

By doing so, the resulting flue gas contains a more intense concentration of CO2, simplifying the mechanism of CO2 capture. After combustion, flue gas undergoes cooling, facilitating condensation of vapor, thereby leads to a concentrated CO2 stream. This captured CO2 can then be compressed for transportation and storage, typically in geological formations deep underground. One of the foremost benefits of oxy-fuel combustion is its capacity for achieving high CO2 capture rates with reduced operational complexities. By eliminating the need for extensive separation processes to sequester CO2 from exhaust gases, oxy-fuel combustion offers a more streamlined approach to carbon capture. Additionally, oxy-fuel combustion can be integrated with in-service power plant infrastructure, allowing for retrofitting of conventional plants to incorporate carbon capture capabilities. This integration can help minimize the costs and logistical challenges associated with deploying new carbon capture technologies. Moreover, oxy-fuel combustion holds the capacity to generate energy more efficiently compared to traditional combustion methods [44, 45]. The void of nitrogen in the combustion process diminish volume of flue gas produced, leading to higher combustion temperatures and increased thermal efficiency. However, oxy-fuel combustion also presents certain challenges, including the need for oxygen production and the potential for corrosion and material degradation in combustion equipment due to the high CO2 concentrations. Additionally, the energy requirements for oxygen production has potential to alter overall effectiveness of the process [46]. In spite of these obstacles, persistent innovation and advancement initiatives are dedicated to boost oxy-fuel combustion technologies to enhance their efficiency, reduce costs, and address technical barriers [47, 48].

1.3 Post-combustion capture

This technique in power plants is a widely utilized approach for capturing CO2 emissions generated during incineration of fossil fuels [49, 50]. Unlike previous methods, which capture CO2 before or during combustion, this procedure focuses on extracting CO2 from the exhaust gas after combustion has occurred. In the post-combustion process, flue gas containing CO2, along with other gases such as nitrogen, water vapour, and pollutants, is extracted from the combustion chamber and passed through a carbon capture system. This system typically employs absorption, adsorption or membrane techniques (Table.3) to precisely sequester CO2 from the exhaust gas while allowing other gases to pass through [51-55]. One significant benefit of capturing CO2 post-combustion is the potential for its subsequent implementation across different industrial domains. Utilization of captured CO2 in various products offers an opportunity to convert captured CO2 into worthwhile commodities, minimizing overall emissions and creating economic benefits. CO2 may be harnessed through a variety of applications, including the synthesis of chemicals, the generation of fuels, and the fabrication of construction materials. For instance, captured CO2 can be converted into methanol, which can serve as both a fuel and a chemical precursor. It can also be used in the production of urea for fertilizers, as well as in the manufacturing of synthetic fuels and polymers. By integrating CO2 utilization into post-combustion capture processes, it is possible to create a circular carbon economy, transforming a by-product into a valuable resource. while simultaneously addressing climate change challenges.

Table. 3 Evaluation of post-combustion methods

Method	Concept	Advantages	Drawbacks
chemical absorption	CO2 reacts with a liquid solvent (e.g., aqueous amine solution) to form a stable compound.	high capture efficiency, ability to handle large flue gas volumes.	high energy consumption for solvent regeneration, potential solvent degradation over time.
adsorption	flue gas is passed through a solid adsorbent that selectively captures CO2 molecules.	lower energy requirements for regeneration, variety of adsorbent materials available.	limited capacity of adsorbents, potential stability and longevity issues.
membrane separation	CO2 is separated from flue gas using selective membranes that retain certain gases.	compact size, lower operational energy requirements.	membrane fouling, high costs of membrane materials, lower CO2 selectivity compared to other methods.

The technique employed in this thesis, following a post-combustion approach, involves integrating a SEC in combination with a separator. In this procedure, a mixture consisting of CO2, steam, and water has been fed into the SEC., where full condensation occurs. Consequently, at the outlet of the SEC (or at the inlet of the separator), a mixture comprising CO2 (as a non-condensable gas) and water is obtained. This mixture is then directed into the separator (either a cyclone or a T-junction) for the intent of refining the CO2. Figure 3 illustrates concept of the post-combustion section of power plant, which comprises a SEC and a separator.

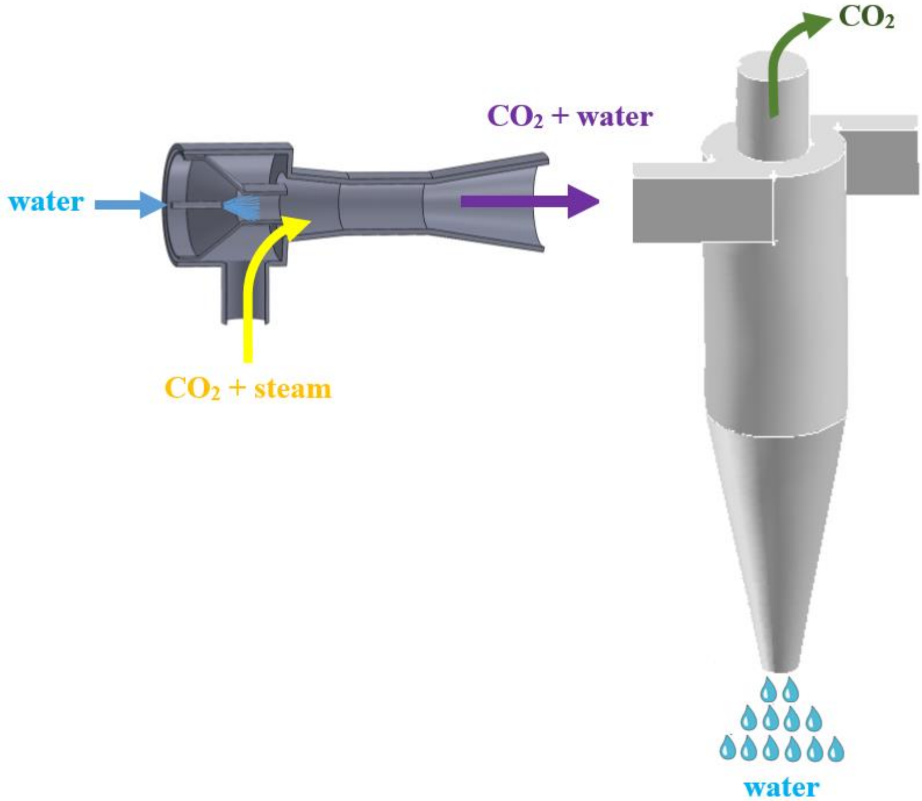

Fig. 3 Post-combustion section of nCO2PP including a SEC and a separator [56]

Post-combustion capture technologies offer several advantages, including the ability to enhance operational power stations without necessitating substantial alterations to their combustion systems. [57, 58]. This makes post-combustion capture a cost-effective mechanism for addressing CO2 emissions in current fossil fuel plants. However, post-combustion capture also faces challenges, such as the energy requirements for capturing and compressing CO2, as well as the cost of implementing and operating carbon capture systems. Additionally, the efficiency of post-combustion capture processes may be significantly influenced by the presence of ancillary gases and impurities within the flue gas stream [59-61]. Despite these challenges, innovations such as the development of more efficient solvents and adsorbents, as well as process optimization techniques, are helping to advance the leading-edge in post-combustion capture. Therefore, post-combustion capture represents a critical strategy for curbing CO2 emissions and mitigating climate change.

In light of these advancements and growing urgency of addressing climate change, development of more efficient and innovative CCS solutions is critical. The necessity for effective CCS technologies has directly influenced the elaboration of the nCO2PP project, which focuses on enhancing efficiency of CO_2 capture. By utilizing advanced methods such as spray ejector condensers and separators, the project aims to curtail CO_2 emissions in industrial activities and contribute to the achievement of negative emissions. This project not only conforms to global climate objectives but also offers a potential pathway for sustainable energy production, emphasizing importance of integrating innovative CCS solutions to combat climate change. This project consists of six work packages, each directing attention to different features of CO_2 emission reduction technologies. The partners involved in the project and their respective responsibilities are as follows: Gdańsk University of Technology – leading the technical feasibility study and conducting thermodynamic analysis of different circulation options. Responsible for tasks related to the design of the SEC, as well as various experimental and analytical activities throughout the project. AGH University of Science and Technology – responsible for collaborating with GUT on thermodynamic analysis and providing expertise in CO_2 capture technologies and sludge valorization. SINTEF – leading research tasks on CO_2 utilization and alternative solutions, such as combining CO_2 with H_2 to produce methanol. They are also responsible for exergetic analyses and various aspects of the project focused on technology optimization. NTNU (Norwegian University of Science and Technology) – leading the evolution of waste heat utilization methods to improve system efficiency and optimizing multi-stage thermal valorization processes. IMP PAN – Leading the design and experimental testing of key components, including the combustion chamber. They are also involved in experimental work and performance verification. WUST (Wrocław University of Science and Technology) – leading several tasks related to the valorization of thermally treated sewage sludge, including the design of a control system for multi-stage thermal valorization processes, and coordinating activities related to the techno-economic analysis of carbon capture technologies. Also, some industrial partners involved in this project include the Institute of Power Systems Automation Ltd. and BROS CONTROL Sp. z o.o. Sp. K. Each of these work packages is interlinked, and the collective efforts of all partners will contribute to advancing carbon capture technologies, concentrating on improving effectualness and achieving negative CO_2 emissions.

My task in the project was to simulate the PFD of the project using Aspen HYSYS, followed by the simulation of the SEC analytically and its validation with experimental results. I conducted experimental tests in collaboration with Dr. Michal Klugmann to obtain the necessary data for validation. Additionally, I simulated the SEC numerically, taking into account the effect of thermophysical properties such as the pressure and temperature of water to address the challenge of using CO_2, and explored an alternative solution involving a steam ejector condenser with electrohydrodynamic (EHD) actuators, validating the results with experimental evidence in the published work. I also simulated and optimized a cyclone separator and an alternative solution, the T-junction separator, validating both with experimental data from the literature. Furthermore, I numerically simulated oxy-fuel combustion with injected water to assess its impact on the system. The forthcoming section will deliver a detailed overview of the nCO2PP project, its structure, and the specific objectives and methodologies of each part.

2. A novel concept of the gas power plant

Figure 4 depicts a trailblazing strategy to electricity generation, forming a part of an extensive research and development project [62]. This power plant comprises pre-combustion, oxy-combustion, and post-combustion sections, each featuring its own unique novelty. One notable novelty in the pre-combustion sector is the conversion of sewage sludge into fuel, employing plasma technology for decomposition of Reactants. This underscores a commitment to waste recycling and reducing environmental impact. By employing oxy-combustion technology, the plant efficiently burns fuel in a novel concept of combustion chamber while minimizing emissions. The innovative use of a wet combustion chamber, utilizing injected water to enable a robust combustion process, regulates temperature and facilitates the separation of water and CO_2. Furthermore, the compact SEC and separator, as a novelty of post-combustion part, enhance CO_2 purification, ensuring only pure CO_2 is seized and pressurized for either storage or commercial use. This advanced power plant cycle represents a significant breakthrough in sustainable energy production. Additionally, the establishment of a carbon capture unit (CCU) permits optional release of a gasifying agent, providing operational flexibility. Thus, this innovative power plant design signifies a promising step towards achieving carbon neutrality in electricity generation.

The SEC and separator are integral components in the process, performing essential functions to ensure the production of pure CO_2. The SEC is responsible for condensing the flue gas and separating it into its constituent components, while the separator further refines the process by separating the CO_2 from other gases and impurities. These components are vital for achieving high-purity CO_2, which is essential for various industrial applications and carbon capture processes.

In this thesis, special prominence is accorded to the post-combustion section of the power plant, which includes both the SEC and separator. This section is of primary interest as it represents a critical stage in the carbon capture process. By focusing on the post-combustion section, the thesis aims to explore the performance, efficiency, and optimization strategies associated with the SEC and separator. Additionally, the thesis may delve into the design considerations, operational challenges, and potential enhancements of these components to improve overall CO_2 capture efficiency and reduce environmental impact. In the following sections, detailed explanations of some of the important devices involved in the process have been provided.

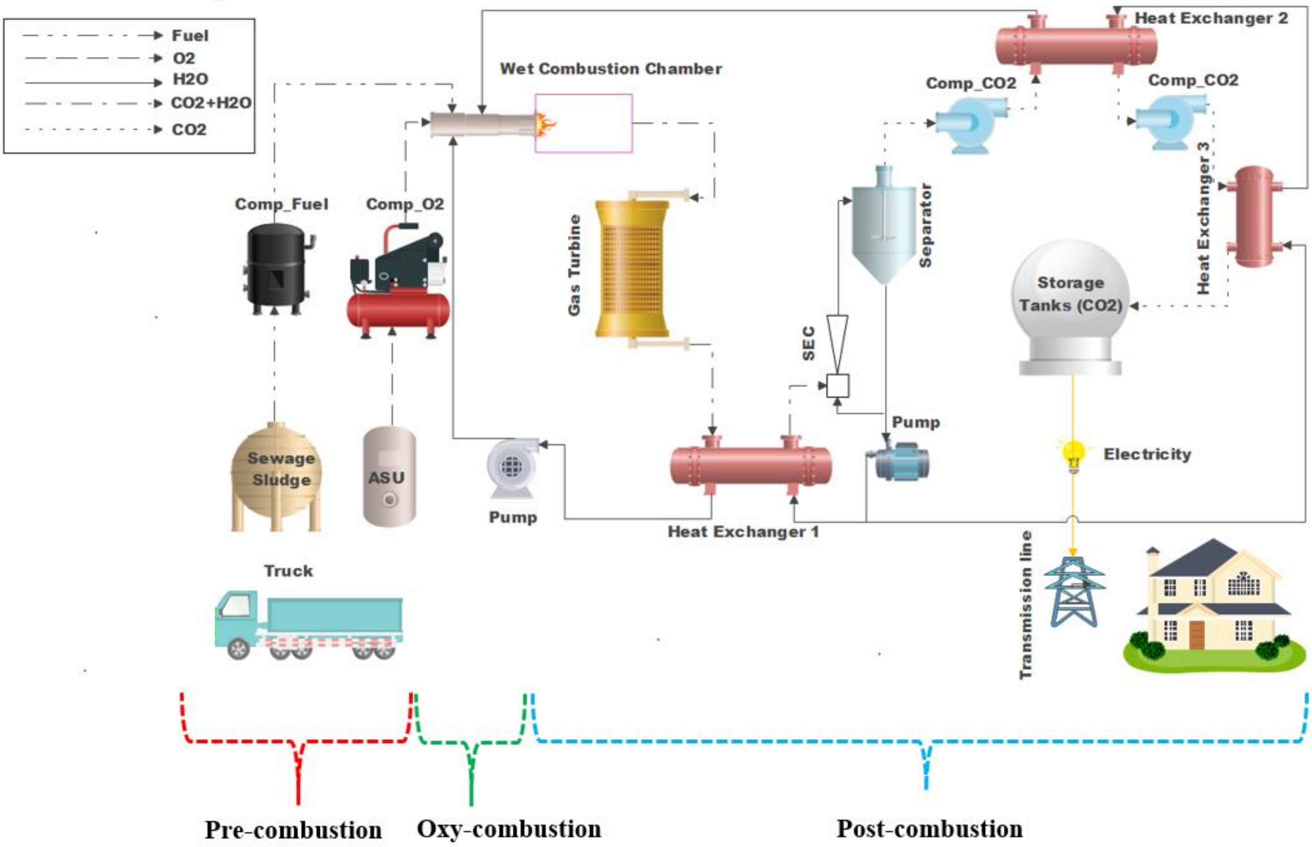

Fig. 4 Flowchart of the advanced gas power plant [63-67]

2.1 Fuel preparation

Fuel preparation is a critical step in the utilization of sewage sludge as a viable fuel source in power plants. Sewage sludge, a residue from wastewater treatment processes, undergoes a series of treatments to remove contaminants and optimize its properties for efficient combustion. This preparatory phase is essential to ensure consistent fuel quality, enhance combustibility, and mitigate potential environmental impacts. Procedure commences with the gathering of sewage sludge from wastewater treatment facilities. This sludge typically contains organic matter, moisture, and various contaminants such as heavy metals, pathogens, and other impurities. To render it suitable for use as fuel, the sludge undergoes several treatment steps [68, 69]:

1. Dewatering: the first step involves removing excess moisture from the sludge. Dewatering processes such as centrifugation, belt pressing, or vacuum filtration are employed to reduce water content and strengthen concentration of solid matter in sludge.
2. Stabilization: sewage sludge often contains organic compounds that can decompose and release odorous gases and volatile organic compounds (VOCs) during storage and handling. Stabilization techniques such as aerobic or anaerobic digestion, composting, or thermal treatment are utilized to reduce the organic content and stabilize the sludge, thereby improving handling characteristics.

3. Contaminant removal: various contaminants present in sewage sludge, including heavy metals, pathogens, and organic pollutants, must be removed or reduced to acceptable levels to ensure compliance with environmental regulations and safeguard human health. Treatment methods such as chemical precipitation, adsorption, filtration, or thermal desorption may be employed to effectively remove contaminants from the sludge.
4. Drying: once stabilized and dewatered, the sludge may undergo drying processes to further reduce moisture content and increase its calorific value. Drying methods such as direct or indirect heat drying, fluidized bed drying, or solar drying may be employed to achieve the desired moisture content. Additionally, briquetting may be utilized to compress the dried sludge into uniform pellets or briquettes, facilitating handling, storage, and combustion.
5. Quality control: throughout the fuel preparation process, rigorous quality control measures are implemented to ensure that the resulting fuel meets specifications for moisture content, calorific value, particle size distribution, and chemical composition. Analytical techniques such as proximate and ultimate analysis, calorimetry, and chemical characterization are utilized to assess fuel quality and performance.

By effectively preparing sewage sludge as fuel through dewatering, stabilization, contaminant removal, drying, and pelletization, power plants can harness its energy potential while minimizing environmental impacts and ensuring compliance with regulatory requirements.

2.2 Air separation unit (ASU)

In the context of power plant operations, the ASU functions as a decisive component in the segregation of atmospheric air into its primary constituents, namely nitrogen (N2), oxygen (O2), and other trace gases [70-74]. This process is essential for facilitating efficient combustion within the power plant, as it ensures a readily available and concentrated oxygen supply for the combustion of fuels. Typically, ASUs employ advanced separation techniques such as cryogenic distillation to achieve the separation of air components [75]. Cryogenic distillation involves cooling the air to extremely low temperatures, causing it to liquefy and enabling the separation of its constituents based on differences in boiling points. Oxygen, with a lower boiling point than nitrogen, vaporizes first and can be collected as a separate stream. Alternatively, ASUs may utilize other separation methods like PSA [76] or membrane separation [77], depending on factors such as plant size, efficiency requirements, and operational constraints. Pressure swing adsorption involves the selective adsorption of gases onto solid adsorbent materials under pressure, allowing for the separation of oxygen from nitrogen. Membrane separation utilizes semi-permeable membranes to selectively permeate oxygen molecules, separating them from the nitrogen and other trace gases. Once separated, the oxygen obtained from the ASU serves as the oxidant for combustion processes within the power plant. Unlike traditional combustion methods that rely on atmospheric air for oxygen supply, utilizing oxygen from the ASU offers several advantages. By providing a concentrated oxygen stream, the ASU enables more efficient and controlled combustion, resulting in enhanced energy production. Additionally, absence of nitrogen in the combustion process helps minimize the formation of nitrogen oxides (NOx), contributing to improved environmental performance. Therefore, the ASU plays a crucial role in power plant operations by providing a reliable and concentrated source of oxygen for combustion processes.

2.3 Wet combustion chamber (WCC)

The wet combustion chamber presents a pioneering approach to fuel combustion, wherein both the fuel and oxygen are introduced into the chamber along with injected water for temperature control [78]. This innovative method revolutionizes traditional combustion processes by leveraging the cooling properties of water to enhance operational efficiency and safety. In the wet combustion chamber, the prepared fuel, often derived from unconventional sources like sewage sludge, is introduced into the chamber alongside oxygen obtained from an ASU. This combination creates an environment conducive to combustion, facilitating the release of energy from the fuel. A key distinguishing feature of the wet combustion chamber is the incorporation of injected water for temperature reduction. Water is introduced into the chamber in controlled amounts to mitigate excessive heat build-up during the combustion process. This water serves as a coolant, absorbing heat energy and effectively moderating the temperature within the chamber. The injection of water into the combustion chamber effectively lowers the temperature, preventing overheating and potential damage to equipment components. By maintaining optimal operating temperatures, the wet combustion chamber ensures operational safety and prolongs the lifespan of critical infrastructure. In addition, the controlled reduction of temperature through injected water promotes efficient combustion of the fuel-O2 mixture. By preventing temperature spikes that could hinder combustion efficiency, the wet combustion chamber optimizes energy extraction from the fuel, resulting in higher thermal efficiency and energy output. Moreover, the use of injected water in the combustion process contributes to environmental sustainability by reducing emissions of harmful pollutants. Lower combustion temperatures help minimize the formation of nitrogen oxides (NOx) and other pollutants, thereby mitigating the environmental impact of power generation operations. Therefore, the wet combustion chamber represents a cutting-edge technology in power plant design, offering efficient and environmentally conscious combustion of fuels. By integrating injected water for temperature control, this innovative approach enhances operational safety, combustion efficiency, and environmental performance, paving the way for sustainable energy generation practices.

2.4 Spray ejector condenser

Condensers are crucial components in thermal power cycles, refrigeration systems, and industrial processes, where they function to convert vapor into liquid by removing heat from the working fluid. Condenser design is critical to the efficiency and performance of any thermodynamic system. Broadly, condensers can be arranged into two dominant types: surface condensers and direct contact condensers, each with distinct operational mechanisms and applications (Fig.5).

Surface condensers are widely deployed in power plants and industries where the working fluid, typically steam, has been condensed by indirect contact with a cooling medium. Vapor and coolant are separated by a solid surface, such as a series of tubes, through which heat is transferred. The condensed vapor is collected in a chamber, while the cooling medium (water or air) flows over or through the tubes. Surface condensers are particularly useful in applications requiring fluid separation, ensuring that the cooling medium and condensed liquid do not mix.

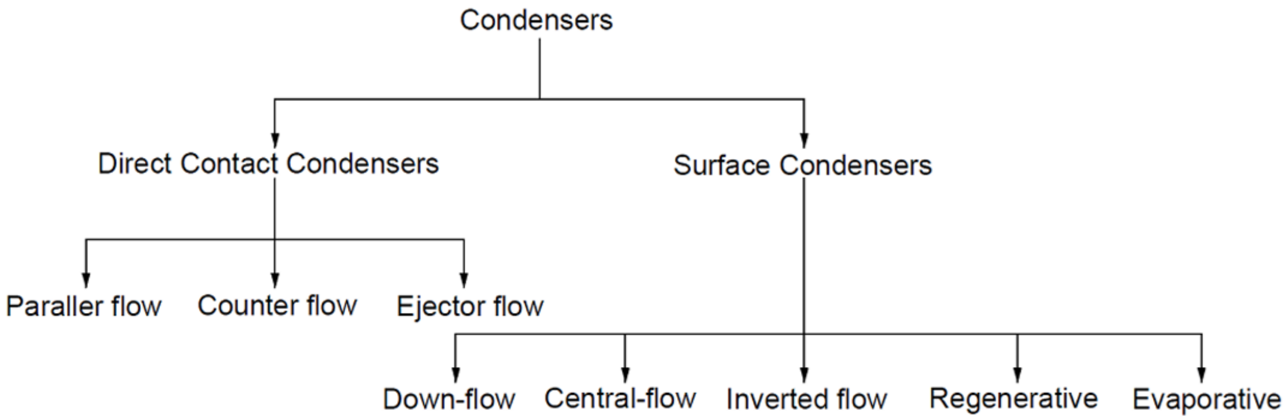

Fig.5 Classification of condensers [79]

Direct-contact condensers enable condensation through the direct interaction between vapor and cooling liquid, promoting swift heat exchange. In these systems, the cooling fluid is injected into the gas phase, rapidly initiating condensation and optimizing thermal performance. Heat transfer occurs from vapor to cooling liquid, aligning condensate temperature with that of the outgoing liquid. However, if the cooling liquid contains impurities, condensate is not viable for repurposing as feed water. These condensers are frequently employed in processes where fluid mixing is permissible, as they deliver enhanced heat transfer rates by eliminating the need for a solid barrier between the vapor and the liquid. As illustrated in Fig. 5, direct contact condensation is categorized into parallel flow, counter flow, and ejector flow types.

The cooling liquid is pumped into a parallel flow jet-type condenser or sprayed directly into the vapor stream. This direct contact allows for rapid heat exchange, enabling the vapor to condense quickly as it transfers its heat to the cooling liquid. The design of parallel flow jet-type condensers often includes features that maximize surface region for vapor-liquid contact such as nozzles or other atomization techniques. These features ensure that the cooling liquid is effectively dispersed within the vapor, enhancing the overall condensation process.

In a counter flow jet-type condenser, the exhaust steam and cooling water enter the condenser from opposing directions, enhancing heat exchange efficiency. Typically, the exhaust steam ascends while the cooling water descends, allowing for a continuous interaction that maximizes condensation. In this design, as illustrated in Fig.7a, the steam enters the condenser chamber at a slightly lower position compared to a parallel flow jet-type condenser, while cooling water has been introduced from top. An air pump is strategically positioned above the condenser to create a vacuum, which aids in drawing the cooling water into the system. The vacuum effectively siphons the cooling water, which then cascades down and is collected by a hollow cone plate. This configuration allows falling water to mix with exhaust steam entering from below, thereby facilitating an efficient heat transfer process.

Another variation of the jet-type condenser is the barometric condenser, as shown in Fig.7b. In this configuration, the condenser shell is elevated to approximately 10.363 meters above the hot well, eliminating the need for an extraction pump. This gravitational setup utilizes the natural pressure differential created by height of water column, enhancing efficiency of the condensation process while simplifying the overall design.

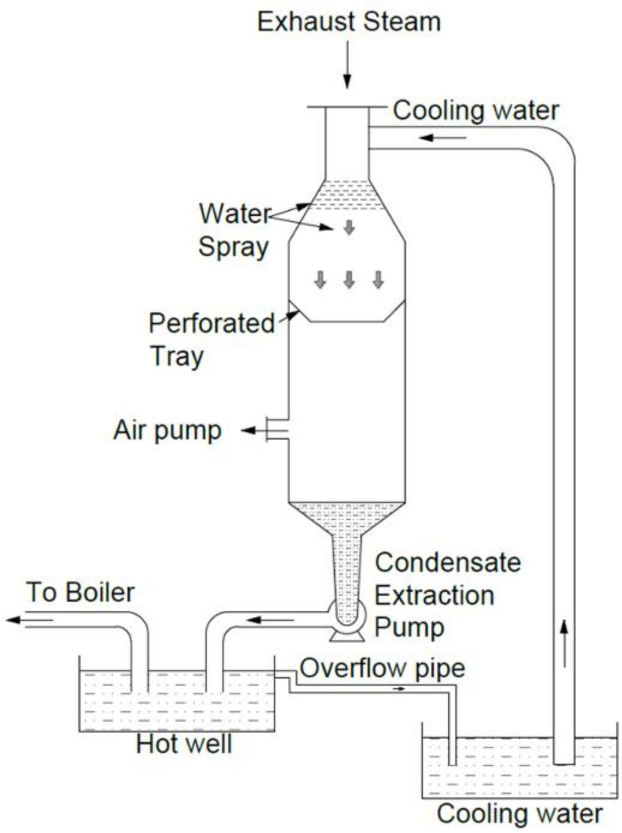

Fig.6 Parallel flow type condenser [79]

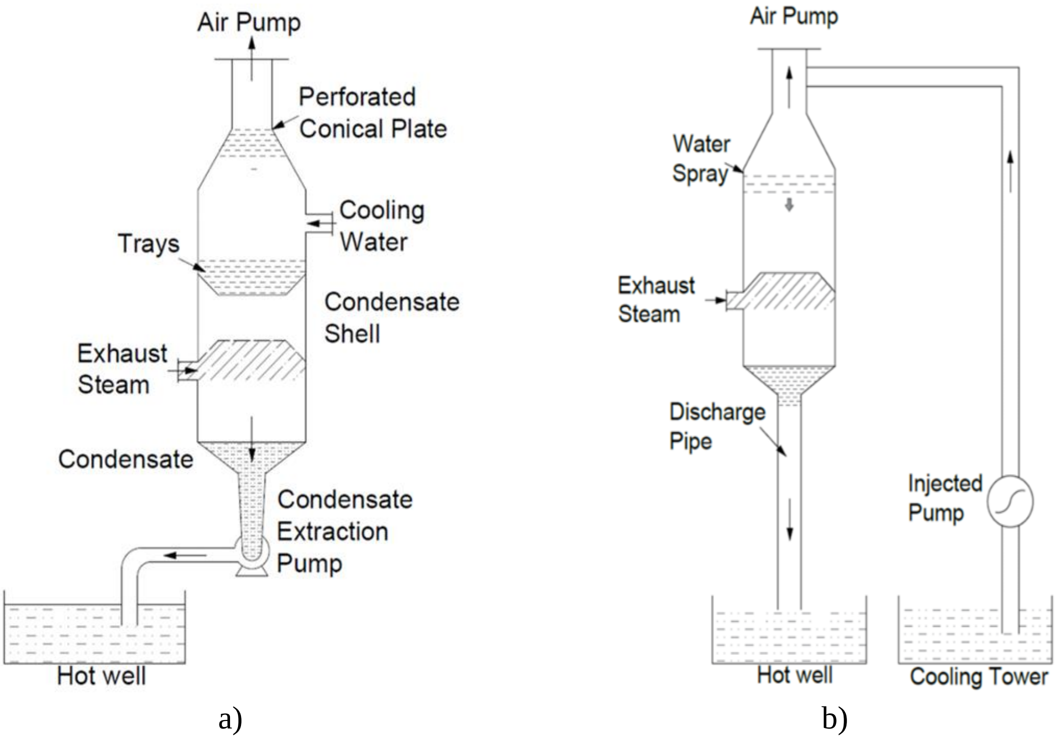

Fig.7 a) Low-level and b) High-level counter-flow jet type condenser [79]

SEC is a crucial component in diverse industrial operations, notably in power stations and chemical facilities where the condensation of vapour is required [65, 66, 79-82]. Its primary function is to efficiently condense vapour into liquid form by utilizing a combination of spray water and steam/non-condensable gas. The SEC operates based on the principle of ejector technology, where steam is used to create a vacuum that draws in the vapour to be condensed. As the vapour enters the SEC, it comes into contact with a fine spray of water, which rapidly cools and condenses it (Fig.8). The condensed vapour then exits the SEC as liquid, while any remaining non-condensable gases are typically vented out. One of the primary strengths of the SEC lies in its aptitude for handling large volumes of vapour while maintaining high efficiency in condensation. Additionally, it offers flexibility in operation, as the condensation process can be adjusted by controlling parameters such as spray water flow rate, motive fluid pressure, and temperature [83, 84]. In power plants, the SEC fulfils an integral role in condensation of steam from the turbine exhaust, converting it back into water for re-use. This helps improve the overall efficiency of the power generation process by maximizing the utilization of steam. Moreover, the SEC is also utilized in various industrial applications where the condensation of vapour is required, such as in chemical processing plants for the recovery of solvents or in refrigeration systems for the liquefaction of refrigerants. Therefore, privileges of SEC can be summarised as follows [85]:

- The SEC can achieve high condensation rates due to its ability to create a large surface area for vapour-to-liquid contact using fine water sprays.
- SECs typically have a compact design, making them suitable for installations where space is limited.
- SECs can handle a wide range of vapour flow rates and operating conditions, making them suitable for diverse industrial applications.
- By utilizing steam to create a vacuum, SECs can effectively lower the pressure inside the condenser, reducing the energy required for vapour condensation.
- SECs are robust and reliable devices with minimal moving parts, leading to reduced maintenance requirements and extended operational lifespans.

And, its drawbacks can be categorised as [79]:

- SECs require a continuous supply of water for spray generation, which can result in high water consumption, especially in large-scale applications.
- While SECs are effective at condensing vapour, they may struggle to remove non-condensable gases efficiently, leading to the accumulation of gases in the condenser and potential performance degradation.
- Despite their robust design, SECs still require periodic maintenance, including cleaning of spray nozzles and inspection of internal components, which can add to operational costs.
- The energy required to generate steam and maintain water supply for the SEC can contribute to operating costs, particularly in applications with high vapour loads.
- SECs may have limitations in terms of operating pressure and temperature ranges, which could restrict their suitability for certain process conditions.

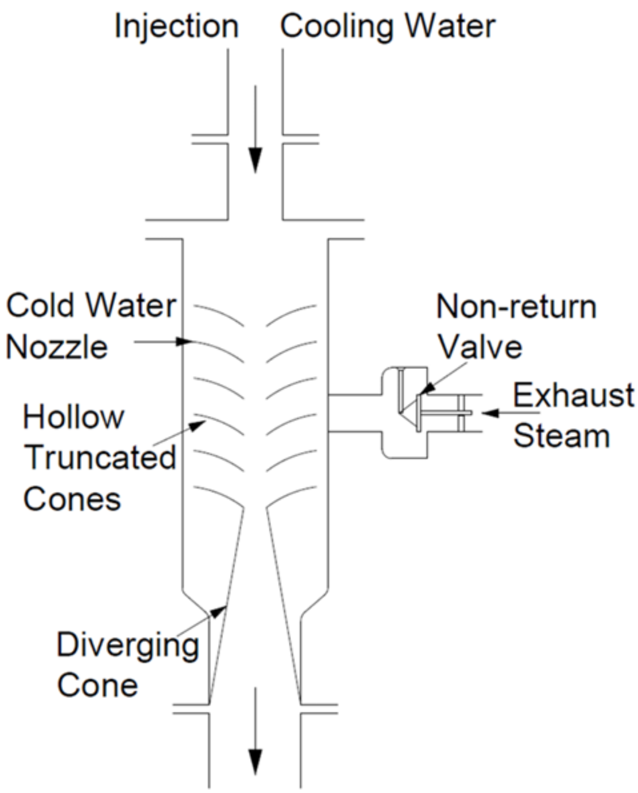

Fig.8 Ejector-flow jet type condenser [79]

2.5 Separator

Within the post-combustion stage of nCO2PP, the carbon capture process involves two main components: SEC and separator. SEC is responsible for fully condensing the flue gas, resulting in the production of CO2 and water at its outlet or the inlet of the separator. The separator functions to distinguish CO2 from water. In this thesis, two types of separators have been employed: cyclone separators and T-junction separators. These separators perform an essential function in the carbon capture procedure by effectively separating different components or phases of the fluid stream based on their respective densities or velocities. Cyclone separators utilize centrifugal force to extract particles or droplets from gas flow [64], while T-junction separators operate based on momentum transfer to separate phases based on their velocities and momentum [86]. Therefore, the combination of SEC and separators in the carbon capture section of the nCO2PP facilitates the efficient capture of CO2, contributing to the plant's negative CO2 emission capabilities. The utilization of cyclone and T-junction separators highlights the comprehensive approach to fluid separation in the thesis, ensuring effective separation of CO2 from water for further processing or storage.

2.5.1 Cyclone separator

In various industries, a cyclone separator is employed to differentiate particles or droplets from gas flows. It operates relying on centrifugal force as the fundamental principle, where swirling motion of the fluid inside the separator causes particles with higher densities to move towards the outer wall, while the cleaner fluid moves towards the center and exits through the top [87-89]. Cyclone separators consist of a cylindrical or conical body with an inlet at the top for the gas stream and an outlet at the bottom for the separated particles or droplets. Upon entering the cyclone separator, the gas stream is compelled to rotate at high speed, creating a vortex. This centrifugal force causes the heavier particles or droplets to move outward and downward, eventually collecting at the bottom of the separator. Cyclone separators find applications in various industries, including oil and gas [90], chemical processing [91], power generation [92], and environmental protection [93]. They are commonly used for dust collection, gas cleaning, and particle separation in processes such as pneumatic conveying, gas-solid separation, and air pollution control.

Cyclone separators based on their inlet come in various classes, each designed to suit targeted purposes and operating conditions. Some common types of cyclone separators include:

- Tangential-Flow Cyclones [94]: In tangential-flow cyclones, the gas stream enters the cyclone chamber tangentially, causing it to rotate in a spiral motion upward. This design allows for efficient segregation of particulates from gas stream due to centrifugal force generated. tangential-flow cyclones are often used in applications where high efficiency in particle removal is required (Fig.9a).

- Axial-Flow Cyclones [95]: Unlike tangential-flow cyclones, axial-flow cyclones have a straight-through design, with the gas stream entering axially at one end and exiting at the other end. This design is advantageous in applications where space constraints are present or where the gas stream needs to be directed in a specific direction. Axial-flow cyclones are commonly used in ventilation systems and HVAC applications (Fig.9b).

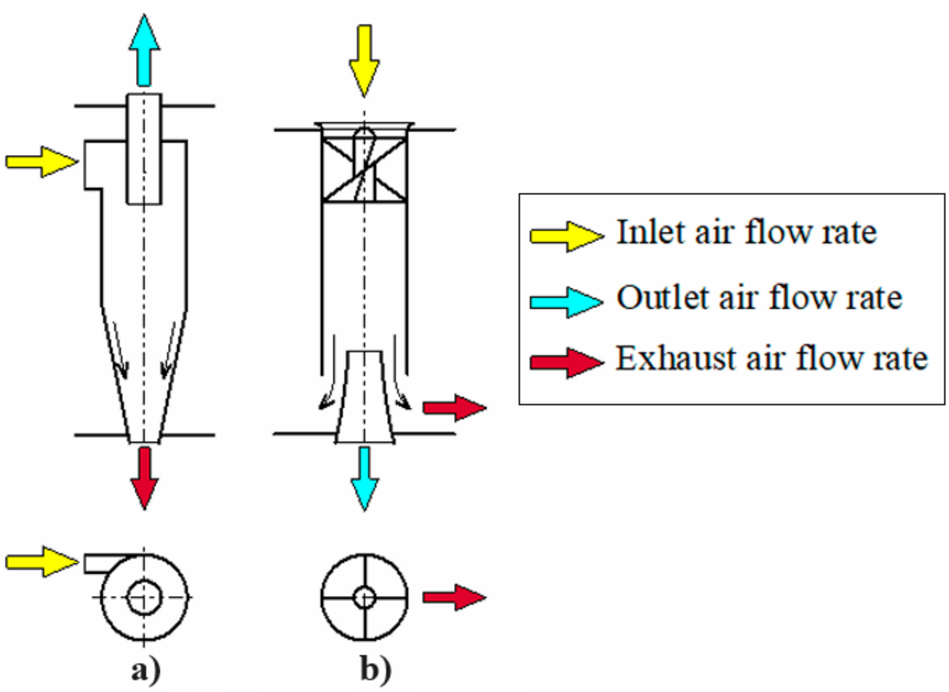

Fig. 9 Types of cyclones (a) tangential, (b) axial flow cyclones [95]

In addition, Multi-Cyclones and High-Efficiency Cyclones can be considered based on their efficiency (Fig. 10). Multi-cyclones consist of multiple individual cyclone chambers arranged in parallel or series configurations within a single housing. This design increases the overall surface area available for particle separation, leading to higher efficiency and capacity compared to single cyclone separators. Multi-cyclones are often used in large-scale industrial applications where high flow rates and particle loadings are present. Also, high-efficiency cyclones are designed with enhanced geometry and internal components to achieve higher separation efficiencies while minimizing pressure drop. These cyclones often feature specialized inlet designs, vortex finders, and outlet configurations to optimize particle separation. High-efficiency cyclones are suitable for applications requiring stringent emission regulations or where energy conservation is a priority.

a)

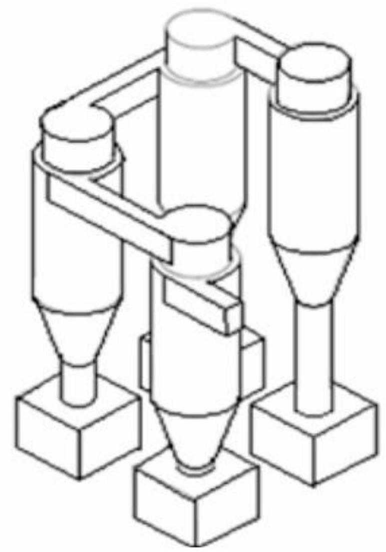

b)

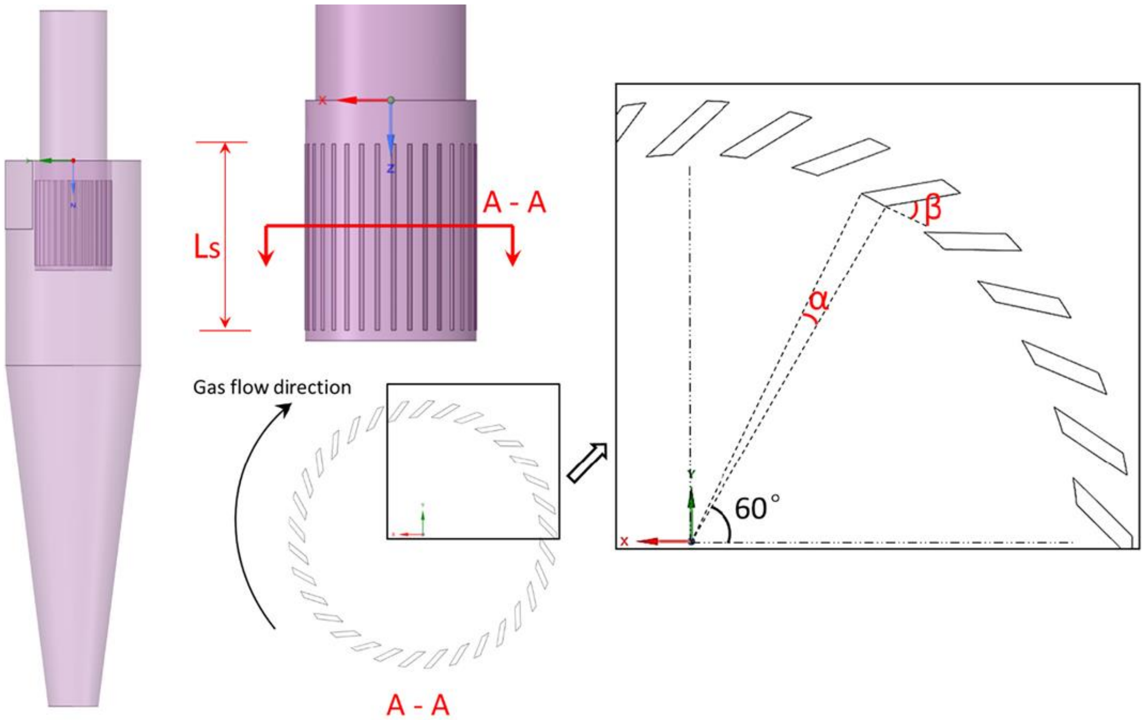

Fig. 10 a) Multi-Cyclones [96] and b) High-efficiency cyclones using a novel vortex finder [97]

Therefore, the choice of cyclone separator type is shaped by considerations such as the intended purpose requirements, operating conditions, particle characteristics, and space limitations. Each type of cyclone separator offers distinct advantages and is selected based on its suitability for the given application. In this thesis, a tangential cyclone separator is utilized as part of the carbon capture process. This type of cyclone separator is characterized by its tangential inlet, which directs the gas stream into the separator chamber in a swirling motion. The separator typically consists of several key components, including the cylinder section, conical section, and vortex finder. The tangential inlet is a crucial feature of the cyclone separator, as it induces a swirling motion in the gas stream as it enters the separator chamber. The centrifugal forces resulting from the swirling motion pushing particles or droplets toward the separator's outer edge. After entering the separator chamber, the gas stream moves through the cylinder section, where further separation of particles occurs. The cylindrical shape of this section allows for the smooth flow of the gas stream and helps to maintain the swirling motion initiated at the inlet. As gas stream progresses via cyclone, it enters the conical section, where the diameter gradually decreases towards the apex. This tapering geometry helps to increase the velocity of gas and enhances centrifugal forces exerted on the particulates, leading to improved separation efficiency. The vortex finder is a cylindrical or conical structure situated at center of cyclone, extending from top of cylinder zone to top of conical portion. Its primary function is to capture the clean gas exiting the separator and direct it towards the outlet. Additionally, the vortex finder helps to stabilize the swirling motion of the gas stream and prevents re-entrainment of separated particles.

In this study, a mixture of CO2 and water enters the tangential cyclone separator, which offers several advantages for separating CO2 from water in the carbon capture process [98-100]:

- ❖ Tangential inlet of cyclone induces a rotating motion within gas stream, creating centrifugal forces that promote efficient separation of CO2 from water droplets. This swirling motion helps to maximize the contact between the CO2 and water, facilitating effective separation.

- ❖ Tangential cyclone separators have a relatively compact design, making them suitable for installation in confined spaces or retrofitting into existing process units. This compactness allows for flexibility in system integration and minimizes the footprint of the carbon capture equipment.

- ❖ Tangential cyclone separators are capable of handling large volumes of gas and water streams, making them suitable for industrial-scale carbon capture applications. Their robust design and high throughput capacity ensure continuous operation and optimal performance in demanding operating conditions.

- ❖ Compared to other separation technologies, tangential cyclone separators have fewer moving parts and minimal maintenance requirements.

- ❖ Tangential cyclone separators can be easily adapted to accommodate variations in gas composition, flow rates, and operating conditions. This versatility allows for efficient separation of CO_2 from water in a wide range of industrial applications, including power plants, refineries, and chemical processing facilities.

- By effectively separating CO_2 from water, tangential cyclone separators aid in lowering greenhouse gas emissions and lessening environmental consequences This aligns with sustainability goals and regulatory requirements aimed at minimizing carbon footprint and promoting cleaner energy production.

While tangential cyclone separators offer various advantages for separating CO_2 from water in the carbon capture process, they also have some disadvantages [101, 102]:

- Tangential cyclone separators are most effective for separating particles within a certain size range. Particles that are too small may not experience sufficient centrifugal force for effective separation, while larger particles may be prone to re-entrainment. This limitation can impact the overall separation efficiency, especially in applications with a wide range of particle sizes.

- Variations in parameters like gas flow rate, pressure, and temperature may affect the swirling motion of gas stream and distribution of particulates within separator, leading to fluctuations in separation efficiency.

- In some cases, tangential cyclone separators may experience particle re-entrainment, where separated particulates are conveyed back into gas stream and carried out of separator. This phenomenon can occur due to factors such as turbulence, improper design, or high gas velocities, resulting in reduced separation efficiency and potential contamination of the clean gas outlet.

- Tangential cyclone separators require energy to maintain the swirling motion of the gas stream and achieve effective separation. This energy consumption can contribute to operating costs, especially in applications with high gas flow rates or where continuous operation is required.

- While tangential cyclone separators are suitable for many industrial applications, they may have limitations in scalability for large-scale carbon capture projects. As the size of the separator increases, challenges such as pressure drop, residence time, and equipment complexity may become more significant, potentially impacting overall system performance and cost-effectiveness.

- Tangential cyclone separators require periodic maintenance to ensure optimal performance and reliability. This may include cleaning of internal components, inspection for wear or damage, and adjustment of operating parameters. Maintenance activities can result in downtime and associated costs, affecting the overall efficiency of the carbon capture system.

Therefore, while tangential cyclone separators offer gains regarding effectiveness and simplicity, their disadvantages must be carefully considered and addressed to optimize their performance in CO2-water separation applications.

2.5.2 T-junction separator

It is another way to perform separation process and is a crucial component used for the separation of gases, and in our case CO2 in particular from water in carbon capture processes. In this separator design, the incoming gas and liquid streams are directed into a T-shaped junction, where they are subjected to a sudden change in direction. This change in flow direction induces a separation of the CO2 gas from the water, based on their differing densities and flow characteristics [103, 104]. Operation of T-junction relies on principle of phase separation through gravitational forces and fluid dynamics. As gas and liquid streams enter T-junction, heavier water phase is inclined to settle at the base of the junction, whereas the CO2 phase rises to the upper region. This separation process is facilitated by the differences in density and momentum between the two phases. Numerous configurations of T-junctions are utilized for separation of CO2 and water, each with its unique design and operational principles. Here are two main different types of T-junction separators commonly employed for this purpose:

1. Horizontal Separator: In a horizontal T-junction separator (Fig. 11), the fluid streams enter the T-junction horizontally. Turbulence is generated by the collision between the incoming streams, aiding in mixing and enhancing phase separation. Horizontal separators are versatile and can be integrated into systems with specific flow orientations or space constraints.

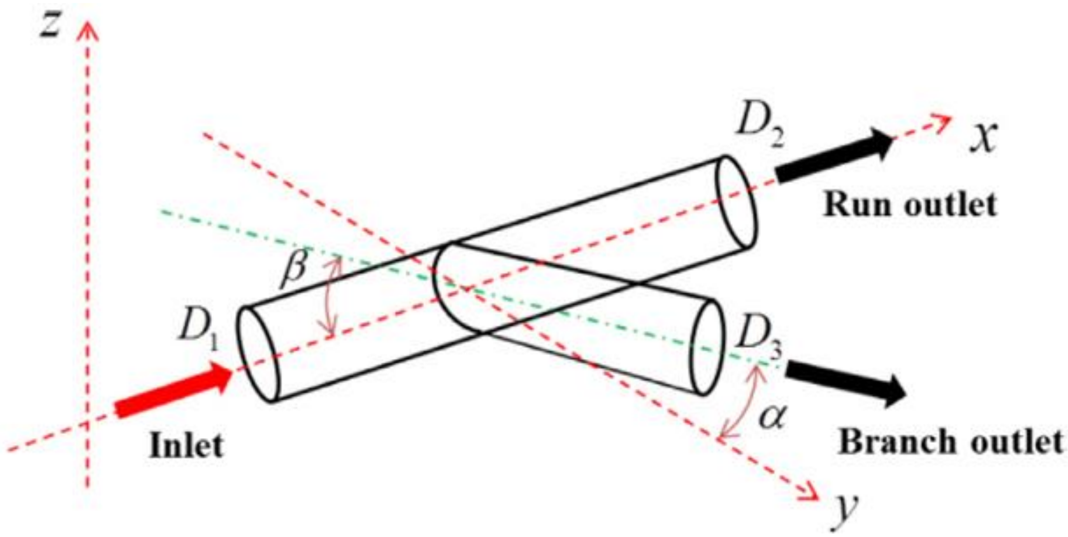

Fig. 11 Horizontal T-junction separator [105]

2. Vertical Impact T-Junction Separator: Vertical impact T-junction separators (Fig. 12) involve the introduction of fluid streams in a vertical direction. Gravity-driven separation occurs, with the heavier phase (water) settling at bottom and lighter one (CO2) rising to top. These separators are effective in large-scale industrial processes where gravity assists in phase separation.

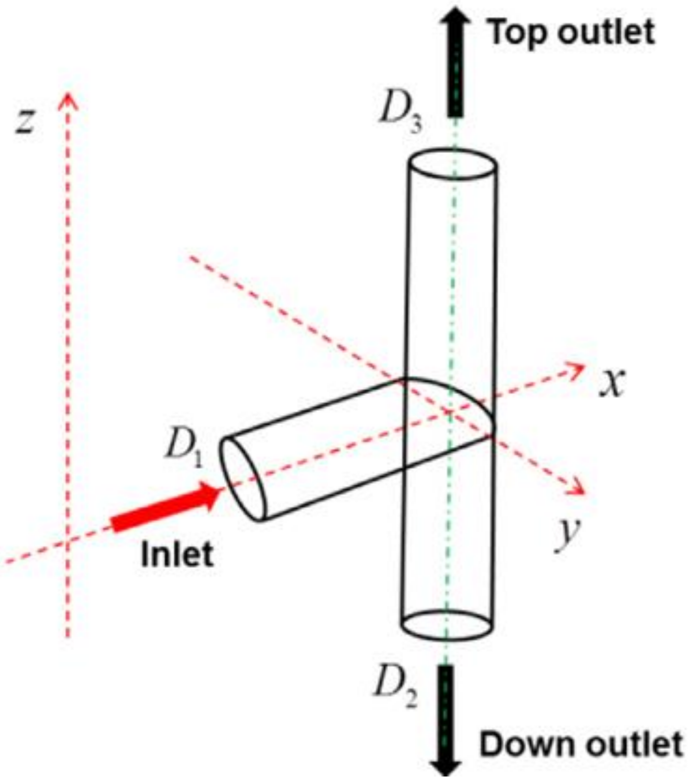

Fig. 12 Vertical impact T-junction separator [105]

Each type of T-junction offers specific advantages and is selected based on factors such as separation efficiency, throughput requirements, and space constraints. The selection of a separator is determined by the specific requirements of the application and the desired outcome of the separation process.

T-junction separators offer several advantages for the separation of water and CO2 in various industrial processes [106]:

- T-junction separators have a straightforward design, making them easy to implement in different systems and processes. Their simplicity allows for cost-effective manufacturing and installation.

- T-junction separators can handle a wide range of flow rates and fluid compositions, making them suitable for diverse applications across different industries. They can be adapted to various operating conditions and environments.

- T-junction separators effectively separate water and CO2 based on their density or velocity differences. The design of the separator promotes phase separation, ensuring the desired components are efficiently extracted from the mixture.

- T-junction separators are often compact in size, making them ideal for use in space-constrained environments or within existing infrastructure. Their small footprint allows for easy integration into different systems without significant modifications.

- Due to their simple design and robust construction, T-junction separators typically require minimal maintenance. This reduces downtime and operational costs associated with regular servicing and repairs.

- T-junction separators can be scaled up or down to accommodate varying processing capacities, from laboratory-scale experiments to large-scale industrial operations. This scalability makes them aptly tailored to a multitude of implementations.

- In some configurations, T-junction separators operate without the need for additional energy input, relying on gravity or fluid dynamics for phase separation.

- When properly designed and optimized, T-junction separators can achieve high separation efficiencies, ensuring the purity of the separated components. This is crucial for applications requiring precise separation and product quality control.

While T-junction separators offer several advantages for the separation of water and CO2, they also have some limitations and disadvantages [107]:

- T-junction separators may struggle to achieve high separation efficiencies, especially when dealing with complex mixtures or fine particulate matter. This can result in incomplete separation and contamination of the separated components.

- The performance of T-junction separators can be sensitive to variations in flow rates, fluid properties, and operating conditions. Changes in these parameters may affect the efficiency of phase separation, leading to inconsistent results.

- T-junction separators are susceptible to fouling, especially when dealing with fluids containing suspended solids or contaminants. Fouling can occur on the internal surfaces of the separator, reducing separation efficiency and requiring frequent cleaning or maintenance.

- ❖ While T-junction separators are scalable to some extent, they may not be suitable for extremely large-scale operations or high-throughput applications. Scaling up the separator can introduce challenges related to fluid dynamics, pressure drop, and equipment size.

- ❖ Designing an efficient T-junction separator requires careful optimization of geometry, fluid dynamics, and operating parameters. Achieving optimal performance may involve iterative testing and modelling, which can be time-consuming and resource-intensive.

- ❖ In certain configurations, T-junction separators may be prone to channelling, where fluid streams preferentially flow along specific paths, bypassing the separation mechanism. This can result in uneven distribution of separated components and reduced efficiency.

- ❖ While T-junction separators are generally compact, they may still require significant space for installation and operation. In applications with limited space availability, accommodating the separator and associated equipment can be challenging.
- ❖ Depending on the design and operating conditions, T-junction separators may consume energy for fluid pumping or agitation, leading to operational costs and environmental impacts associated with energy usage.

Therefore, while T-junction separators offer advantages such as simplicity and versatility, their limitations must be carefully considered when selecting a separation solution for water-CO2 separation applications. Mitigating these disadvantages may require advanced design strategies, operational controls, and maintenance practices.

3. Development of crucial operational parameters in nCO2PP concept

The core focus of this thesis revolves around the post-combustion CO2 capture process (SEC+separator) within the nCO2PP. Prior to delving into this, a comprehensive evaluation of the entire process flow diagram (PFD) is indispensable to establish boundary conditions required for simulating SEC and separator. The initial step in exploring the feasibility of a gas power plant involves conducting a feasibility study of the process flow diagram (PFD), which is simulated using Aspen HYSYS software. HYSYS is a formidable resource for simulating widely used in the industry for modelling and analysing various chemical processes. During the feasibility study, the PFD is developed to represent the proposed operation of the power plant, including all relevant components and process units. This includes the integration of technologies such as compressor of fuel and O2, oxy-combustion, gas turbines, heat exchanger, separator other advanced systems aimed at achieving negative CO_2 emissions. The simulation in Aspen HYSYS allows us to evaluate functionality and efficiency of the proposed system across a range of operating parameters and scenarios. It helps in analysing key parameters such as energy consumption, CO_2 capture efficiency, and overall plant economics. By simulating the PFD using Aspen HYSYS, engineers can identify potential challenges, optimize the design, and assess the feasibility of implementing the negative CO_2 emission concept. This step is crucial at the inception of the project. In the feasibility study for the nCO2PP, two types of fuels are utilized: methane and a mixture of gases denoted as mixture1. The components of mixture1 are illustrated in Fig. 13. This mixture is composed of various gases, each contributing to the overall composition and properties of the fuel. By investigating the feasibility of using both methane and mixture1 as fuels, we can assess performance and efficiency of the power plant under different fuel compositions. This analysis is essential for understanding the potential impacts on process dynamics, emissions, and overall feasibility of the proposed power plant concept.

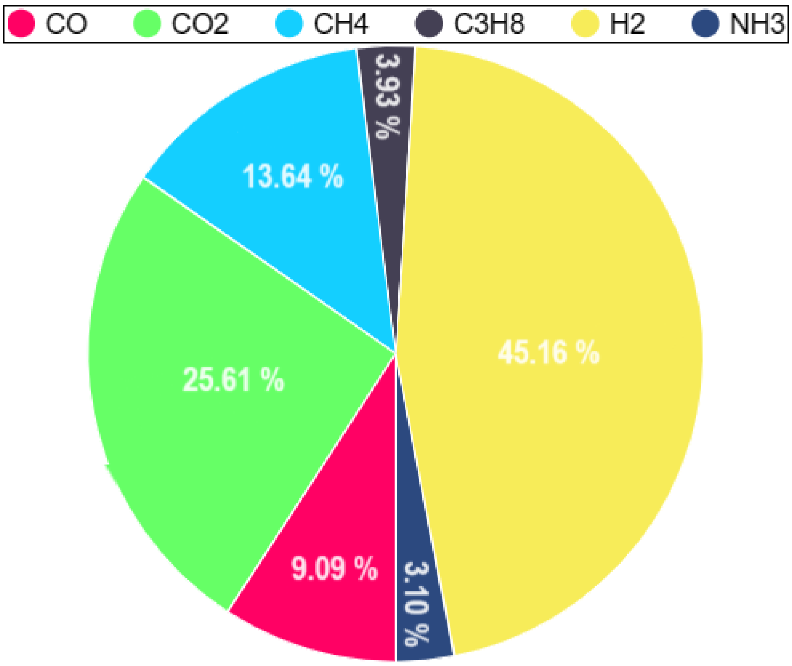

Fig. 13 Fuel (mixture1) compositions for the analysed cycle in volume fraction [108]

The process flow diagram (PFD) of the nCO2PP is divided into two distinct parts known as PFD0 and PFD1. PFD0 specifically focuses on the oxy-combustion stage of the nCO2PP, while PFD1 encompasses the entire process flow of the nCO2PP. In PFD0 as depicted in Fig.14, the emphasis is on the initial stages of energy generation process, including compression of fuel and O_2, the subsequent wet combustion chamber reactions, gas turbines and heat exchanger.

On the other hand, PFD1 (Fig.15) provides an overview of entire nCO2PP, incorporating all stages and components involved in the power generation process. This includes not only the oxy-combustion step but also the post-combustion processes such as spray ejector condenser as well as separator.

By dividing the PFD into PFD0 and PFD1, we can effectively analyse and optimize each stage of the power generation process independently while also considering the overall performance and efficiency of the entire nCO2PP. This division allows for a more detailed and systematic approach to design, operation, and evaluation of the power plant, consequently giving rise to improved performance and reduced environmental impact.

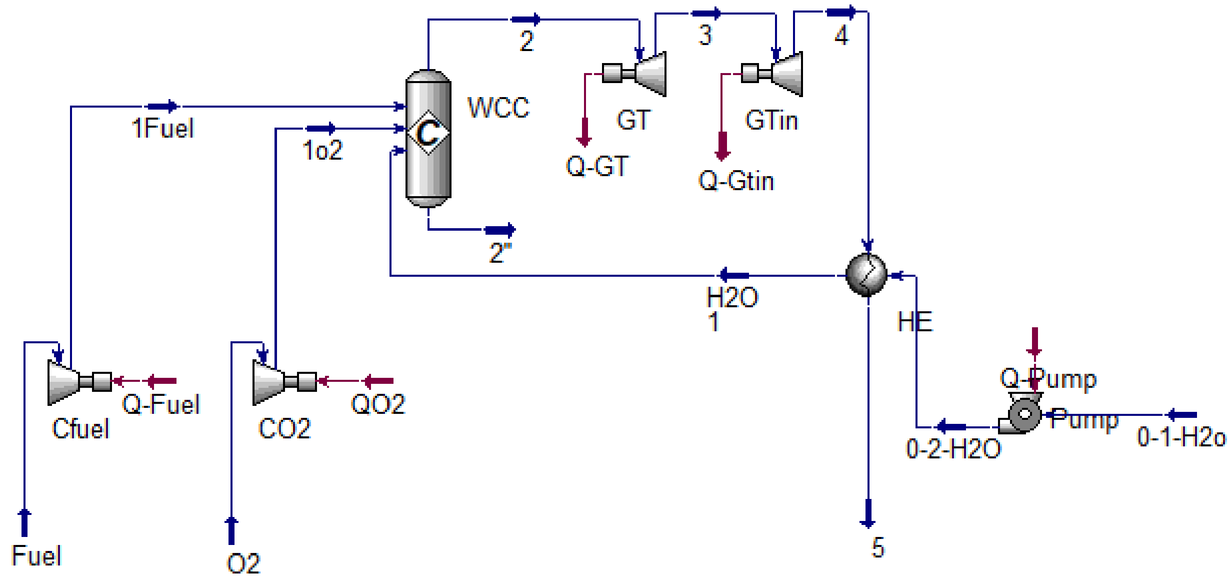

Fig. 14 PFD0 of a gas mixture cycle (in Aspen HYSYS)

Tables 4 and 5 illustrate the cycle nodal points of PFD0 for mixture1 and methane, respectively. Table 6 represents the summarised results of PFD0 for both mixture1 and methane fuels. In this stage of the process, it is observed similar outlet temperatures of 1100°C within the wet combustion chamber (WCC) for both Mixture1 and methane. However, upon the introduction of water into the system, a notable attenuate in temperature of WCC products is observed. To maintain desired temperature of 1100°C, distinct quantities of water are required: 66.48 $\frac{g}{s}$ for methane and 58.8 $\frac{g}{s}$ for Mixture1. Upon analysis of turbine power outputs, methane exhibits slightly superior values for turbine power N_{GT} (92.93 kW compared to 88.73 kW) and N_{GT-bap} (68.49 kW compared to 65.64 kW), as well as for combined turbine gross power (161.42 kW compared to 154.37 kW). This disparity in performance can be attributed to methane's elevated calorific value when contrasted with that of Mixture1. Despite methane's superior turbine power outputs, Mixture1 demonstrates a marginally higher net efficiency of the system, reaching 44% compared to methane's 43.32%. This discrepancy implies that Mixture1 displays a slightly more efficient conversion of fuel to useful work, notwithstanding methane's higher chemical energy rate of combustion, recorded at 336.23 kW compared to Mixture1's 307.42 kW. To further elucidate these findings, a comprehensive examination of the intrinsic properties and combustion characteristics of both fuel types is warranted. Mixture1 derived from sources like biomass or coal gasification, exhibits distinct combustion kinetics relative to methane, a simple hydrocarbon. The compositional variance and molecular structure of each fuel profoundly influence combustion efficiency and heat release rates within the oxy-combustion framework.

Additionally, exploring the impact of operational factors including pressure, temperature, and oxygen concentration on the performance of both fuel types can offer valuable insights into optimizing the system for improved efficiency and power generation. Furthermore, a holistic assessment of the environmental ramifications and emissions associated with each fuel type is imperative in evaluating the overall sustainability and applicability of oxy-combustion technology across diverse domains. Moreover, further inquiry into potential technological advancements or modifications to system design aimed at augmenting the performance and efficiency of both fuel types would be beneficial. This avenue of investigation may encompass research into advanced turbine configurations, innovative combustion methodologies, or integration with CCS technologies to to curtail greenhouse gas emissions effectively.

Table.7 shows the summarised results for Mixture1 and Methane of PFD1. The fuel mass flow analysis reveals substantial disparities between Mixture1 and methane, with Mixture1 demonstrating a markedly higher flow rate (16.68 $\frac{g}{s}$) compared to methane (6.23 $\frac{g}{s}$) to attain similar temperatures within the WCC. This discrepancy underscores a higher consumption rate for Mixture1 in achieving the requisite temperature, a phenomenon attributable to disparities in fuel composition and energy content. Mixture1 encompasses a diverse array of hydrocarbons and gases derived from gasification processes, necessitating a greater mass of fuel for combustion relative to the comparatively simpler hydrocarbon methane. Regarding water mass flow in the exhaust, methane manifests a higher rate (82.90 $\frac{g}{s}$) compared to Mixture1 (76.50 $\frac{g}{s}$). This variance potentially reflects differences in combustion characteristics between the two fuels and the efficacy of heat exchange processes within the system. The elevated water mass flow in methane's exhaust implies a more thorough combustion process, likely resulting in enhanced heat transfer efficiency and lower exhaust temperatures relative to Mixture1. Remarkably, only Mixture1 reports Nitrogen Oxide (NO) mass flow in the exhaust, indicating disparities in nitrogen oxide emissions between the two fuel types, a salient environmental consideration. The absence of NO mass flow data for methane may suggest either substantially lower emissions or a paucity of monitoring pertaining to this specific pollutant, underscoring the necessity for comprehensive understanding and mitigation of NO emissions for environmental compliance and air quality management. Analysis of SEC Pump power consumption scenarios underscores the influence of operational conditions on system energy requirements, with methane exhibiting lower power consumption across both optimistic and non-optimistic scenarios relative to Mixture1. These variances may stem from differential pressure and temperature requisites inherent in the combustion processes of each fuel, alongside disparities in pump system efficiency. In terms of net efficiencies under optimistic SEC scenarios, methane evidences superior performance, boasting net efficiencies of 41.58% compared to Mixture1's 39.91%. This disparity suggests a more efficient conversion of fuel to useful work under optimistic conditions for methane, with factors such as combustion completeness, heat transfer efficiency, and overall system performance under varying operational conditions contributing to the observed differences. Gross efficiency for Mixture1 and methane is reported at 55.18% and 52.10%, respectively, reflecting the overall energy conversion efficacy of the system for each fuel type.

Table. 4 Cycle nodal points for mixture1 (syngas) as a fuel in Aspen HYSYS

Parameter	Unit	Value										
Node designation	-	0^{Fuel}	1^{Fuel}	0^{O2}	1^{O2}	$0^{1\text{-}H2O}$	$0^{2\text{-}H2O}$	1^{H2O}	2	3	4	5
Mass flow ($\dot{m}$)	g/s	18.0	18.0	23.2	23.2	58.8	58.8	58.8	100	100	100	100
O_2 fraction (X_{O_2})	mol%	-	-	100	100	-	-	-	0.00	0.00	0.00	0.00
CO_2 fraction (X_{CO_2})	mol%	-	-	-	-	-	-	-	11.75	11.75	11.75	11.75
H_2O fraction (X_{H_2O})	mol%	-	-	-	-	100	100	100	87.63	87.63	87.63	87.63
NO fraction (X_{NO})	mol%	-	-	-	-	-	-	-	0.62	0.62	0.62	0.62
Temperature (t)	ºC	15	255.6	15	314.8	15	25.11	125.11	1100	672.5	324.7	178.6
Pressure (p)	bar	1	10.5	1	10.5	1	300	300	10	1	0.078	0.078

Table. 5 Cycle nodal points for methane as a fuel in Aspen HYSYS

Parameter	Unit	Value										
Node designation	-	0^{Fuel}	1^{Fuel}	0^{O2}	1^{O2}	$0^{1\text{-}H2O}$	$0^{2\text{-}H2O}$	1^{H2O}	2	3	4	5
Mass flow ($\dot{m}$)	g/s	6.72	6.72	26.80	26.80	66.48	66.48	66.48	100	100	100	100
O_2 fraction (X_{O_2})	mol%	-	-	100	100	-	-	-	0.00	0.00	0.00	0.00
CO_2 fraction (X_{CO_2})	mol%	-	-	-	-	-	-	-	8.47	8.47	8.47	8.47
H_2O fraction (X_{H_2O})	mol%	-	-	-	-	100	100	100	91.53	91.53	91.53	91.53
Temperature (t)	ºC	15	225.39	15	314.8	15	25.11	125.11	1100	667.3	318.4	158.6
Pressure (p)	bar	1	10.5	1	10.5	1	300	300	10	1	0.078	0.078

Table. 6 Effect of different fuels (simulated by Aspen HYSYS) [63]

Parameter	Symbole	Unit	Mixture1 (syngas)	methane
Temperature at the WCC outlet	t	ºC	1100	1100
Fuel mass flow	$\dot{m}_{1-fuel}$	g/s	18.00	6.72
Oxygen mass flow	$\dot{m}_{1-O2}$	g/s	23.2	26.8
Water mass flow	$\dot{m}_{1-H2O}$	g/s	58.8	66.48
Exhaust temperature after HE	t_5	ºC	178.60	161.10
Turbine power GT	N_{GT}	kW	88.73	92.93
Turbine power GT^{bap}	N_{GT-bap}	kW	65.64	68.49
Combined turbines gross power	N_t	kW	154.37	161.42
Power for own needs	N_{cp}	kW	19.12	15.75
Chemical energy rate of combustion	$\dot{Q}_{cc}$	kW	307.42	336.23
Net efficiency	η_{net}	%	44.00	43.32
Gross efficiency	η_g	%	50.21	48.01

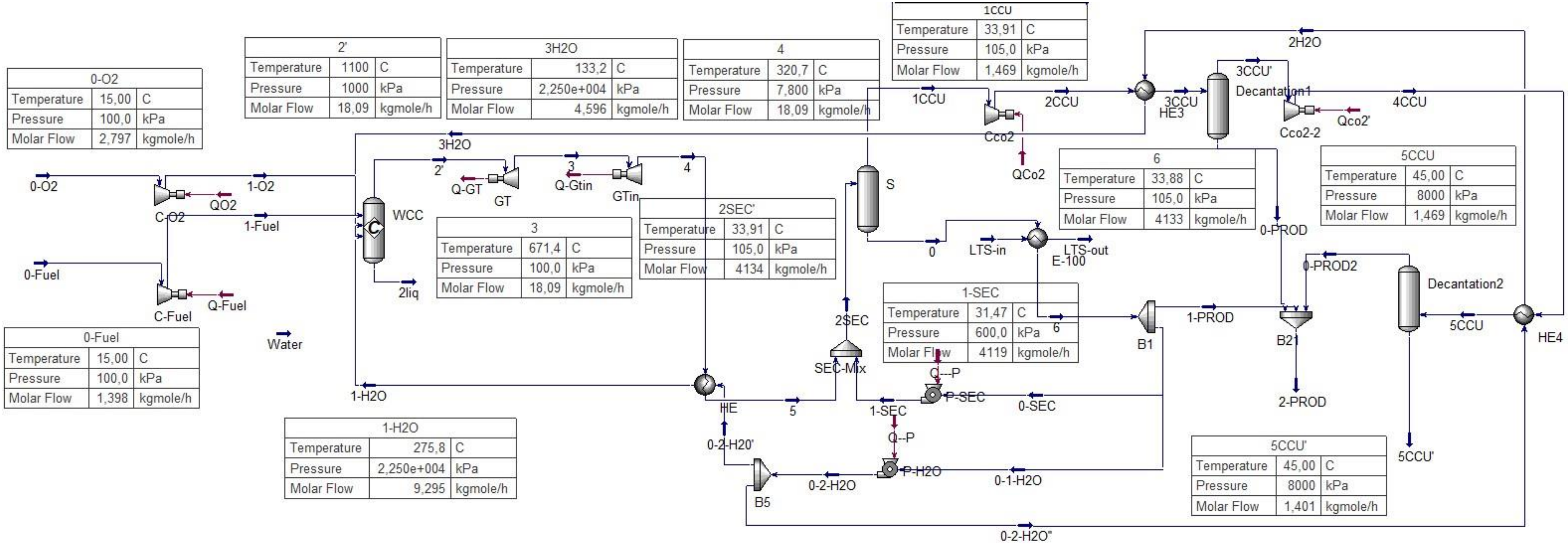

Fig. 15 Process flow diagram of a gas mixture cycle PFD1 (in Aspen HYSYS) [108]

Table. 7 Results for Mixture1 and Methane of PFD1 [63]

Parameter	Symbol	Unit	Aspen HYSYS	
Fuel type	–	-	Mixture 1	Methane
Fuel mass flow	$\dot{m}_{1-fuel}$	g/s	16.68	6.23
Oxygen mass flow	$\dot{m}_{1-O2}$	g/s	21.21	24.86
Water mass flow	$\dot{m}_{1-H2O}$	g/s	62.11	68.91
CO_2 mass flow in exhaust	$\dot{m}_{2-CO2}$	g/s	22.68	17.10
NO mass flow in exhaust	$\dot{m}_{2-NO}$	g/s	0.82	-
Water mass flow in exhaust	$\dot{m}_{2-H2O}$	g/s	76.50	82.90
Water production	$\dot{m}_{p-H2O}$	g/s	14.38	14.00
Exhaust temperature (before regenerative HE1, after GT^{bap})	t_4	ºC	321.4	317.1
Exhaust temperature (after regenerative HE1, x=0.9999)	t_5	ºC	38.95	39.73
Turbine power GT	N_{GT}	kW	91.05	95.38
Turbine power GT^{bap}	N_{GT-bap}	kW	66.14	69.04
Combined turbines gross power	N_t	kW	157.19	164.42
Optimistic SEC Pump power consumption (x=0 in mixing part of SEC)	$N_{P-SEC,o}$	kW	17.79	12.89
Not optimistic SEC Pump power consumption (x=0.25 in mixing part of SEC)	$N_{P-SEC,n}$	kW	54.93	53.18
Power for own needs with optimistic SEC	$N_{cp,o}$	kW	43.59	32.62
Power for own needs with not-optimistic SEC	$N_{cp,no}$	kW	80.63	72.91
Chemical energy rate of combustion	$\dot{Q}_{CC}$	kW	284.88	311.72
Net efficiency with optimistic SEC	$\eta_{net,o}$	%	39.91	41.58
Net efficiency with not optimistic SEC	$\eta_{net,no}$	%	26.87	28.66
Gross efficiency	η_g	%	55.18	52.10

4. Aim and scope of the study

This dissertation aims to tackle the critical challenge of CO2 purification within post-combustion section of gas power plants. The majority of analysis were performed on the example of nCO2PP concept described earlier. The focal point revolves around pioneering methodologies that integrate spray or steam ejector condensers with separators like cyclones or T-junctions. Employing a multifaceted approach, the research amalgamates experimental, analytical, and numerical techniques to delve deep into CO2 capture via direct-contact condensation (DCC) within SEC, enhanced by various separators.

The chief aim of the investigation is to gain a comprehensive understanding of intricate physical mechanisms governing DCC within the spray ejector condenser. This involves development of experimental setups and analytical framework to delve into DCC mechanisms, taking into account heat and mass transfer mechanisms. Furthermore, the interaction of SEC with cyclone separator will be explored to shed light on the operational dynamics and optimize CO2 purification.

Another pivotal aspect is the exploration of strategies aimed at bolstering the efficiency of separators, particularly cyclones, through structural modifications and optimization of operational parameters. This entails a detailed analysis of single, dual and quadruple inlet as well as cone size of cyclones and assessment of the impact of thermophysical parameters on SEC performance.

The dissertation delves into the optimization of cyclone separator by integrating vanes to Augment separation efficiency whilst alleviating pressure drop. This phase involves a combination of numerical simulations, experimental validations, and assessment of parameters such as volume fraction and droplet breakup within the SEC. These efforts are geared towards refining CO2 purification processes and overcoming operational challenges.

Moreover, the inclusion of T-junction separators expands the scope of the research to explore diverse methods for enhancing CO2 purification efficiency. The investigation into T-junction separators involves a detailed analysis of their operational dynamics and their interaction with the spray or steam ejector condensers. Specifically, the research aims to understand how thermophysical factors such as temperature and pressure of water influence condensation efficiency within the SEC when coupled with T-junction separators. By examining the interplay between these parameters, the dissertation seeks to identify optimal conditions for achieving superior CO2 capture efficacy whereas minimal energy expenditure. Additionally, the research explores alternative techniques for CO2 capture, including the utilization of steam ejector condensers with electrohydrodynamic (EHD) actuator. Overcoming challenges associated with CO2 presence in the steam phase is paramount, along with optimizing cyclone separators to achieve remarkable separation efficiencies. Through these endeavours, the dissertation seeks to push the boundaries of CO2 capture technologies.

To put it in a nutshell, the aim and scope of the study are as follows:

- Focusing extensively on understanding the physical dynamics of DCC within SEC through the development of experimental, analytical, and numerical models.

- Developing experimental setups and analytical models to investigate heat and mass transfer mechanisms in DCC.
- Examining how thermophysical factors, such as water temperature and pressure, affect condensation efficiency within the SEC, with the intention of minimizing the ramifications of non-condensable gases (CO_2) on heat transfer rates.
- Exploring advanced CO_2 capture techniques, including steam ejector condensers with electrohydrodynamic (EHD) actuators, to optimize condensation efficiency.
- Optimizing cyclone separators by incorporating vanes to improve separation efficiency while reducing pressure drops. Analyzing multi-inlet configurations for cyclones and optimizing cyclone cone dimensions to maximize CO_2 purification efficiency.
- Investigating the potential of T-junction separators as an alternative to cyclones, aiming to achieve optimal separation efficiencies.

II. PAPER [A] - A Novel Concept of Enhanced Direct-Contact Condensation of Vapour-Inert Gas Mixture in a Spray Ejector Condenser

1. Concept of the paper

The paper postulates the development of an analytical model to elucidate the mechanism of direct contact condensation (DCC) within a newly proposed spray ejector condenser (SEC) framework, particularly accompanied with CO2. This model is constructed on foundational principles encompassing continuity, momentum, and energy equations that dictate the behaviour of the CO2-steam mixture. It takes into account both concentration and heat transfer effects related to DCC. Moreover, the size of atomized droplets in a SEC significantly influences the condensation effect within the system. As the droplet size increases, there is a notable amplification of the condensation effect. Larger droplets possess a greater surface area-to-volume ratio, which enhances their capability to absorb latent heat from the surrounding steam-CO2 mixture. Consequently, larger droplets facilitate more efficient condensation by efficiently transferring heat to the droplets, leading to their rapid cooling and subsequent phase transition into liquid form. This phenomenon underscores the importance of controlling and optimizing the size of atomized droplets in the SEC to maximize condensation efficiency and overall system performance. In addition, optimizing the initial velocities of both the steam-CO2 mixture and the droplets is crucial for maximizing heat transfer rates and enhancing the performance of the spray ejector condenser.

This study utilized MATLAB to solve for the temperature gradient of both droplets and the gas mixture, with subsequent comparison to experimental data. The investigation aimed to evaluate the influence of various parameters on system performance throughout its operational duration. Key parameters under scrutiny encompassed the initial velocity of the steam-droplet mixture and the characteristics associated with droplet diameter and breakup.

2. Analytical model

The analytical framework outlined in this paper delves into the intricate physical and mathematical depiction of a SEC utilized within nCO2PP. This ejector serves the purpose of effectively condensing steam from a mixture of vapour and inert gas, thereby augmenting the overall functionality and efficiency of the power plant.

Comprising various essential components and phases, the model elucidates the following:

In the Pre-Mixing Chamber, delineated as a converging-single-nozzle setup, condensation phenomena manifest within the mixing zone. Mathematical formulations are derived to ascertain the pressure and mass flow rate of the steam-inert gas blend at different points within the ejector. Within the Mixing Section, the interplay between the primary liquid flow and the secondary vapour-gas flow is expounded upon. Equations are formulated to prognosticate the fragmentation of liquid droplets, the dynamics of liquid droplet flow, and the vapour condensation onto subcooled droplets. The ramifications of droplet breakup are addressed through equations predicting the characteristics and distribution of primary and secondary droplets resulting from the liquid jet disintegration. Liquid droplet flow is described through equations governing the motion of liquid droplets owing to condensation and aerodynamic influences. Vapour condensing on a subcooled droplet flow is governed by equations accounting for vapour condensation on liquid droplets, incorporating considerations of mass transfer and partial pressure. Thermal equilibrium of the droplet stream is achieved through energy balance equations determining the temperature of the liquid droplet stream as it interacts with the vapour-gas mixture. Mass and thermal equilibrium for the gas-steam mixture are established through equations delineating the mass and energy equilibrium for the steam-gas blend, facilitating the determination of temperature gradients and heat transfer rates. The following are the equations for the temperature gradient in the droplet and the gas mixture:

$$\frac{dT_d}{dx} = -\left(\frac{T_d}{\dot{m}_d} + \frac{h_{lv}}{c_{pl}\dot{m}_d}\right)\frac{d\dot{m}}{dx} + \frac{\pi d_d^2 \frac{n}{l} h_{mg}(T_m - T_d)}{c_{pl}\dot{m}_d} \tag{1}$$

$$\frac{dT_m}{dx} = -\frac{T_m}{\dot{m}_m}\frac{d\dot{m}}{dx} - \frac{h_m \pi d_d^2 n}{(L - L_j)\,\dot{m}_m c_{pm}}(T_m - T_d) \tag{2}$$

Reduction in pressure within the mixing chamber is quantified by calculating the pressure decrease across the mixing chamber, accounting for factors such as friction and momentum. Therefore, the analytical framework offers a holistic comprehension of the physical processes unfolding within the ejector, enabling the prognosis of critical performance parameters such as pressure, temperature, mass flow rates, and heat transfer rates. This exhaustive scrutiny is imperative for refining the design and operation of the ejector within the CO2 emission gas power plant, thereby elevating its efficiency and efficacy.

3. Experimental model

The experimental setup focuses on investigating DCC processes within the throat section of a SEC. The test section comprises a tube with an 80 mm diameter, allowing for visual observation. The motive fluid, delivered via a nozzle with a diameter of 1 mm, consists of water with varying inlet pressures and temperatures, essential for initiating droplet formation and jet breakup. The throat's length is 600 mm, facilitating the DCC process. A mixture of water vapour and CO2 is introduced into the mixing length through the mixing chamber. The wet vapour, obtained from a generator, undergoes regulation to control vapour and CO2 feed rates. The resulting steam-gas mixture encounters droplets in the throat, initiating the DCC process. Experimental parameters, including flow rates and pressures, are accurately measured using specialized equipment, ensuring precise control and data collection. Experimental temperature distributions of the steam mixture are compared with model predictions, revealing insights into the DCC efficiency. Increasing steam flow rates lead to higher inlet and outlet temperatures, while the presence of CO2 reduces temperature levels due to its impact on heat transfer. These findings underscore the importance of steam-CO2 flow rates in optimizing DCC efficiency. Therefore, the experimental setup provides valuable insights into the intricate dynamics of DCC processes and their sensitivity to operating parameters, enabling a robust comparison with the analytical model. The consistency observed between experimental results and the analytical model (Fig.16) validates the reliability of the proposed approach, confirming its applicability for accurately predicting the performance of DCC systems under various conditions.

a)

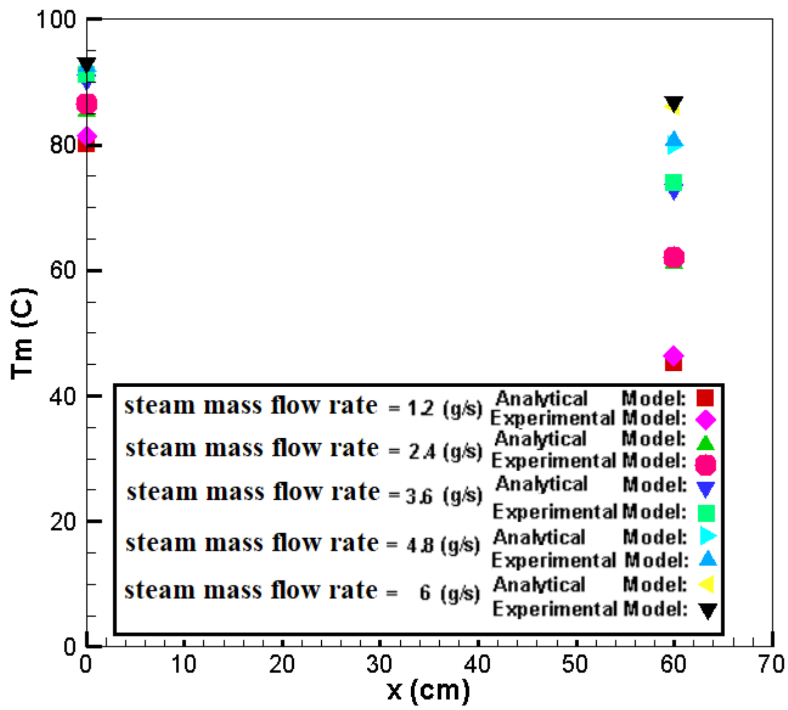

b)

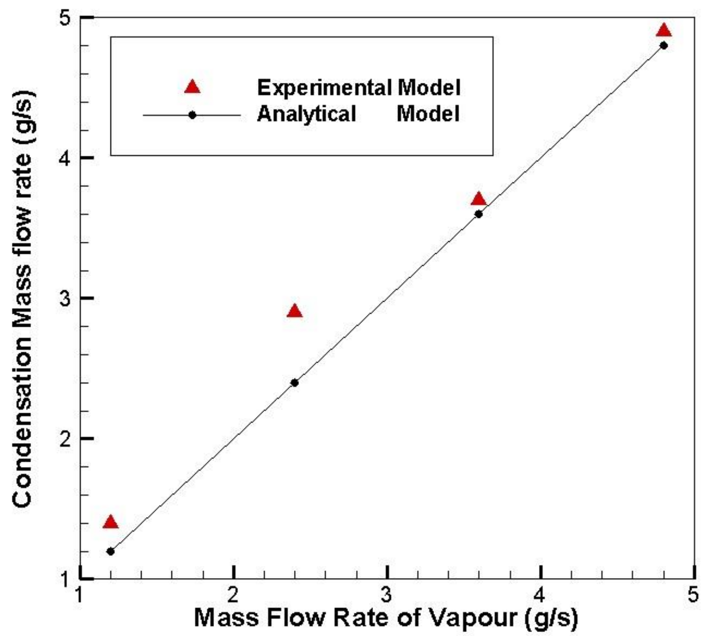

Fig.16 Comparison between analytical predictions and experimental data for a liquid jet mass flow rate of 29 $\frac{g}{s}$ for, a) the mixture temperature and b) condensation mass flow rate, at CO_2 flow rate of 2.6 $\frac{m^3}{h}$ [65]

4. Conclusions

The study presents a thorough investigation into DCC on a stream of subcooled droplets, combining analytical modelling and experimental analysis. Unique to previous research, the study explores the complex dynamics of DCC in the presence of inert gases, incorporating considerations of heat and mass transfer mechanisms. The findings underscore the intricate relationship between droplet characteristics and condensation efficiency. It suggests that factors such as droplet size, velocity, and initial conditions play crucial roles in determining how effectively condensation occurs. By understanding and optimizing these droplet characteristics, it becomes possible to enhance the efficiency and effectiveness of the condensation process, thereby improving the overall performance of the system. Calculations demonstrate that inert gases diminish condensation effectiveness by impacting mass transfer, with the analytical model consistently aligning with experimental results. The DCC model demonstrates that lower steam-CO2 flow rates induce a more substantial temperature drop within the mixing section, whereas higher steam flow rates yield a reduction in temperature, albeit with a diminished effect in the presence of CO2. Notably, increasing the steam mixture flow from 1.2 $\frac{g}{s}$ to 3.6 $\frac{g}{s}$ leads to a reduction in steam temperature from 25°C to 14°C at a CO2 flow rate of 6.8 $\frac{m^3}{h}$. In contrast, in the absence of CO2, the temperature drops more drastically, from 56°C to 25°C within the same steam flow range, emphasizing the pronounced influence of CO2 on DCC efficiency. Thermal analysis uncovers notable trends: droplet temperature along the throat increases while steam mixture temperature decreases, influenced by DCC dynamics and the presence of CO2. Additionally, larger droplet diameters lower the droplet temperature but increase the steam mixture temperature, indicating that smaller droplets improve DCC efficiency by providing more heat transfer surface area. For droplets with diameters of 1 and 1.5 mm, the peak temperature occurs at 8 cm and 12 cm, respectively (with a total throat length of 20 cm), followed by a slight decrease. For 2 mm droplets, the temperature increases up to 16 cm and then stabilizes. Overall, larger droplet diameters lead to lower droplet temperatures and higher steam mixture temperatures. Further investigation into droplet size distribution and the evaluation of droplet formation post-jet breakup are recommended avenues for advancing understanding of DCC mechanisms.

III. PAPER [B] – Analysis of cyclone separator solutions depending on spray ejector condenser conditions

1. Concept of the paper

The investigation conducted in this paper primarily focuses on understanding the operational dynamics of the SEC, both experimentally and analytically. Additionally, the study explores the impact of various factors, such as CO2 volumetric flow rate and droplet break-up, on the separation efficacy of the cyclone separator. Furthermore, the influence of cone size on cyclone performance is explored through numerical simulation. Firstly, the cone size of the cyclone separator is a critical parameter that significantly influences its performance. Through numerical simulations, the study investigates how variations in cone size impact the efficiency of CO2 purification. Different cone sizes alter the internal flow dynamics of the cyclone, affecting the separation efficiency and pressure drop across the separator. By systematically varying the cone size, the research aims to identify the optimal configuration that maximizes separation efficiency while minimizing energy consumption. Secondly, the CO2 volumetric flow rate plays a pivotal role in the purification process within the cyclone separator. The study explores how changes in CO2 flow rates affect the separation efficiency and pressure drop across the separator. Higher CO2 flow rates lead to increased pressure drop within the cyclone, impacting its performance and energy consumption. By analysing the relationship between CO2 volumetric flow rate and separation efficiency, the research aims to optimize operating conditions for efficient CO2 purification. Lastly, the phenomenon of droplet break-up of water droplets within the cyclone separator is investigated to understand its impact on CO2 purification. Droplet break-up influences the size distribution and behaviour of water droplets within the separator, affecting the overall efficiency of CO2 separation. The study examines how droplet break-up phenomena vary with different operational parameters and how they can be controlled to enhance separation efficiency. By comprehensively studying these factors, the paper aims to provide valuable insights into optimizing the performance of cyclone separators for CO2 purification.

2. Experimental and analytical model of SEC

As the mixture of gas-steam flows into the throat, it encounters a finely dispersed spray of droplets, initiating the DCC process. This interaction involves atomization of droplets, heat transfer leading to steam condensation, and turbulent mixing facilitating efficient mass and heat transfer. The throat region facilitates vigorous heat and mass transfer processes, which are essential for the initiation of the DCC process. After entering the throat, the fluid jet experiences a breakup phenomenon dependent on the inlet water pressure. Weber formulated an equation to determine the size of secondary droplets.

$$\frac{d_d}{Dj} = 1.436\left(1 + 3\frac{We^{0.5}}{Re}\right)^{1/6} \tag{3}$$

$$We = \frac{\rho_l u_l^2 D_j}{\sigma_l} \tag{4}$$

$$Re = \frac{\rho_l u_l D_j}{\mu_l} \tag{5}$$

In this context, Dj refers to the nozzle diameter, while u_l, μ_l, σ_l and ρ_l denote the velocity of the water, dynamic viscosity, surface tension and density respectively. The surplus CO2 and any vapour that has not undergone condensation are released through an outlet, controlled to maintain system efficiency.

The Analytical Analysis of the SEC focuses on design considerations, emphasizing critical components such as the pre-mixing region, nozzle, and mixing sector. The analysis omits the diffuser component, presuming complete condensation within the mixing sector. The operational stages of the system are outlined, along with suggestions for alternative approaches, such as the utilization of a cyclone separator in lieu of a diffuser. Equations derived from conservation principles governing momentum, mass, and energy are utilized to understand fluid dynamics within the SEC. Model verification involves comparing analytical and experimental results to validate the precision and reliability of the model. Acceptable concordance between theoretical predictions and experimental observations is observed under varying conditions, confirming the model's accuracy.

3. Numerical model of cyclone

The section on numerical modelling of the cyclone separator delves into the intricate process of replicating the fluid dynamics within the separator using computational methods. This approach offers a cost-effective and efficient means of understanding the complex flow phenomena involved in cyclone separation. Numerical modelling begins with the creation of a detailed geometry of the cyclone, including its various components such as the conical and cylindrical sections, as well as inlet and outlet ports. This geometry is subsequently meshed to divide the computational domain into smaller elements, facilitating accurate numerical simulations. Meshing involves refining the mesh in critical regions to accurately capture flow features while minimizing computational costs. Once the geometry is meshed, computational fluid dynamics (CFD) simulations are performed using software like ANSYS Fluent 2021R1. These simulations employ mathematical models to solve the governing equations of fluid flow within the cyclone separator. The mixture model, are utilized to simulate two-phase flow, considering interactions between phases like CO2 and water.

The equation representing mass conservation for the mixture is given as follows:

$$\frac{\partial(\rho_m)}{\partial t} + \frac{\partial(\rho_m u_m)}{\partial x_i} = 0 \tag{6}$$

The equation governing the momentum of the mixture can be expressed as:

$$\frac{\partial(\rho_m u_{mi})}{\partial t} + \frac{\partial(\rho_m u_{mi} u_{mj})}{\partial x_i} = \frac{\partial P}{\partial x_i} + \frac{\partial}{\partial x_j}\mu_m\left(\frac{\partial u_{mi}}{\partial x_j} + \frac{\partial u_{mj}}{\partial x_j}\right) + \rho g_i + \frac{\partial}{\partial x_i}\left(\sum_{q=1}^{n} \alpha_q \rho_q u_{dr,qi} u_{dr,qj}\right) \quad (7)$$

In this context, u_m represents the velocity averaged by mass, while ρ_m refers to the density of the mixture, and μ_m indicates the viscosity of the mixture.

$$u_m = \frac{\sum_{q=1}^{n} \alpha_q \rho_q u_q}{\rho_m}, \ \rho_m = \sum_{q=1}^{n} \alpha_q \rho_q, \ \mu_m = \sum_{q=1}^{n} \alpha_q \mu_q \quad (8)$$

The variable $u_{dr,q}$ represents the drift velocity of the secondary phase, which is calculated using the equation: $u_{dr,q} = u_q - u_m$.

Boundary conditions are specified to define the behaviour of fluid at inlet and outlet ports, as well as along the walls of the separator. The simulation methodology adopts a transient approach to capture time-varying flow phenomena, with convergence criteria set to ensure accuracy. During simulation, the software iteratively solves the governing equations, predicting flow characteristics such as velocity profiles and pressure distributions. The SIMPLE algorithm is commonly used to couple pressure and velocity, while schemes like PRESTO and QUICK are employed for accurate discretization of equations. Grid independence tests are conducted to determine the minimum grid resolution needed for accurate simulations. This involves comparing results obtained with different grid configurations to ensure consistency and reliability of the numerical solution. Finally, model validation is performed by comparing simulation results with experimental data. This ensures that the numerical model accurately captures the flow dynamics observed in real-world cyclone separators, validating its capability to predict performance under various operating conditions. Therefore, numerical modelling of cyclone separators offers a comprehensive approach to understanding and optimizing their performance, providing valuable insights into the design and operation of these crucial components in industrial processes.

4. Conclusions

The results of this paper delves into the performance and behaviour of cyclone separators in carbon capture processes. In cyclone, maintaining a uniform particle distribution considers crucial for optimal separation efficiency. Irregular particle distribution can cause to instability in the CO2 core, affecting separation performance. Different inlet configurations, such as single and dual inlet cyclones, are explored to address this issue, with dual inlet cyclones showing improved stability. The length of the cone (ranging from 0.2 to 0.5 m) and the cylindrical sections of cyclone separators influence their separation efficiency, which varies from 77.30% to 80.98%. Additionally, these dimensions affect CO2 recovery and pressure drop, which increases from 6.08 Pa to 10.91 Pa. Adjusting these dimensions allow for optimization of performance while managing energy consumption and operational costs. Longer residence times within the cyclone facilitate a more efficient CO2 separation from water droplets. Furthermore, the mass flow rate of CO2 affects separation efficiency and pressure drop within the system. Higher CO2 flow rates lead to increased separation efficiency but also result in higher pressure drop, necessitating a balance between efficiency and energy consumption. The discussion also delves into the dynamics of droplet formation within a SEC and its impact on separation efficiency. The investigation into droplet breakup has led to a significant increase in separation efficiency, rising from 50.98% to 100% for droplet sizes varying between 1 and 20 μm. Understanding surface wave dynamics and jet characteristics is crucial for optimizing SEC performance and improving CO2 capture effectiveness. Therefore, the findings highlight the importance of various parameters, such as cone size, CO2 mass flow rate, and droplet characteristics, in enhancing the performance of cyclone separators and SEC for carbon capture applications.

IV. PAPER [C] – Optimizing CO2 purification in a Negative CO2 Emission Power Plant

1. Concept of the paper

This paper aims to investigate the optimization of CO2 purification through the integration of a SEC and a cyclone. A thorough analysis is conducted, using a numerical method to simulate the cyclone separator's performance under different SEC outlet conditions. From a methodological perspective, the simulation is carried out using Fluent software, which accounts for three-dimensional, transient, and turbulent dynamics. The model utilizes the mixture model and Reynolds Stress Model (RSM) to accurately simulate the turbulent two-phase flow. Structural elements are of paramount importance in this study, emphasizing the assessment of single and dual inlet cyclone separators to optimize CO2 purification efficiency. The investigation further addresses the role of crucial parameters, such as liquid volume fraction (LVF) and droplet size, in enhancing the separation efficiency. By varying these parameters, the study identifies optimal conditions for maximizing CO2 capture effectiveness while minimizing energy consumption. Additionally, the analysis investigates the effects of structural alterations, notably the introduction of vanes, on both the separation efficiency and the pressure drop in the system.

2. Numerical Modelling of Cyclone Separator

Numerous factors influence the efficiency of cyclone separators, necessitating precise modelling to optimize performance while minimizing pressure drop. Cyclone separators are categorized based on their structural configurations, with tangential inlet cyclones being particularly common due to their reliability and simplicity. Utilizing Computational Fluid Dynamics (CFD), the study employs the Fluent software to simulate fluid flow within the cyclone separator. The Euler-Euler approach, specifically mixture model, is chosen to handle multiphase nature of flow. The Reynolds-averaged Navier-Stokes (RANS) equations, continuity equation, and momentum equations form the basis for describing the fluid flow within the cyclone separator. Additional terms, including stress diffusion, shear production, pressure-strain, and dissipation, are incorporated to accurately model turbulence. Among turbulence models, the Reynolds Stress Model (RSM) is preferred for cyclone flow due to its ability to capture anisotropic turbulence phenomena. Unlike other models, such as the k–ε model or algebraic stress model (ASM), the RSM model comprehensively accounts for swirling, rotation, and rapid strain rate changes inherent in cyclone separators.

Within the RSM, the transport equation is defined with a time step of 0.001 seconds, as outlined in [64].

$$\frac{\partial}{\partial t}\left(\rho\overline{u_i'u_j'}\right)+\frac{\partial}{\partial x_k}\left(\rho u_k\overline{u_i'u_j'}\right)=D_{ij}+P_{ij}+\Pi_{ij}+\varepsilon_{ij}+S \tag{9}$$

The equation features two elements on the left-hand side: the first reflects the temporal rate of change in stress, while the second represents the convective transport term. On the right-hand side, five distinct terms are articulated, each encapsulating specific phenomena

The stress diffusion term:

$$D_{ij} = -\frac{\partial}{\partial x_k}\left[\rho\overline{u_i'u_j'u_k'} + \overline{(P'u_j')}\delta_{ik} + \overline{(P'u_i')}\delta_{jk} - \mu(\frac{\partial}{\partial x_k}\overline{u_i'u_j'})\right] \tag{10}$$

The shear production term:

$$P_{ij} = -\rho\left[\overline{u_i'u_k'}\frac{\partial u_j}{\partial x_k} + \overline{u_j'u_k'}\frac{\partial u_i}{\partial x_k}\right] \tag{11}$$

The pressure-strain term:

$$\Pi_{ij} = \overline{p(\frac{\partial u_i'}{\partial x_j} + \frac{\partial u_j'}{\partial x_i})} \tag{12}$$

The dissipation term:

$$\varepsilon_{ij} = -2\mu\overline{\frac{\partial u_i'}{\partial x_k}\frac{\partial u_j'}{\partial x_k}} \tag{13}$$

and S is the source term.

The numerical simulation setup in ANSYS Fluent involves selecting appropriate boundary conditions, including velocity inlet, pressure outlet, and no-slip wall. The simulation employs algorithms such as SIMPLE for pressure-velocity coupling and PRESTO for handling high-speed swirling flows. To ensure accuracy, grid independence analysis is conducted, varying mesh configurations to validate results across different grid sizes. Additionally, model validation compares simulated data with experimental findings to assess predictive capability, confirming the reliability of the numerical model in predicting separation efficiency and other performance metrics. Therefore, the numerical modelling section provides a comprehensive methodology for simulating fluid flow within the cyclone separator, ensuring accuracy in predicting performance metrics essential for optimizing cyclone efficiency.

3. Summary and conclusions

The effectiveness of particle separation in diverse industrial settings is largely determined by the design and operation of cyclone separators, with the inlet configuration being a key factor influencing performance. This study investigates the effect of single and dual inlets on cyclone separator efficiency. Our objective here is to assess how these inlet configurations affect particle separation efficiency. To achieve this, we conducted computational flow visualization to analyze the internal flow structure of cyclones. Two types of cyclones, with single and dual inlets, were created to elucidate the flow mechanism. The comparison between single and dual inlet cyclones revealed a notable advantage for the dual inlet configuration in terms of separation efficiency.

Across various flow rates, the dual inlet cyclone consistently exhibited superior performance compared to its single inlet counterpart. Specifically, the dual inlet cyclone demonstrated higher separation efficiency when treating the CO2–water feed, indicating its effectiveness in achieving enhanced particle separation. Several factors contribute to these compelling findings. Firstly, the design of the dual inlet cyclone enables improved control and distribution of the incoming gas mixture, facilitating more effective separation. The enhanced uniformity in flow distribution within the cyclone is a key factor driving the observed increase in separation efficiency. The investigation into the influence of single and dual inlets on cyclone separator efficiency revealed significant disparities in performance. The dual inlet configuration demonstrated superior efficiency, particularly evident at higher flow rates, due to its ability to effectively separate CO2-rich and water-rich cores. As results showed, the processing of the CO2-water mixture at a flow rate of 2.8 $\frac{kg}{s}$ demonstrated enhanced performance in the dual-inlet cyclone, achieving a separation efficiency of 90.7%, which surpasses the 85.6% efficiency observed in the single-inlet cyclone. This underscores the critical role of inlet configuration in optimizing separator performance. In addition, an analysis of the outlet conditions of the Spray Ejector Condenser (SEC), specifically focusing on liquid volume fraction and water droplet diameter, revealed their substantial impact on separator performance. Lower liquid volume fractions and larger water droplet diameters were found to enhance separation efficiency significantly. Optimal operating conditions, particularly a liquid volume fraction of 10%, yielded a remarkable separation efficiency of 90.7%. The diameter of liquid droplets emerged as a crucial parameter influencing separator efficiency. Variations in droplet diameter underscored the importance of parameter tuning for achieving desired performance outcomes. Notably, the study identified optimal operating conditions, with a liquid volume fraction of 10% and larger water droplet diameters yielding superior separation efficiency. Moreover, the incorporation of vanes within the cyclone separator was found to be a pivotal factor in enhancing performance. Vanes led to a notable reduction in pressure drop by 16.8%, consequently lowering energy requirements and operational costs. Simultaneously, they boosted separation efficiency by 9.2% at a liquid volume fraction of 10%, ensuring efficient capture of CO2. Therefore, this study offers valuable insights into the optimization of CO2-water separators, particularly in the context of nCO2PP. The findings underscore the significance of inlet configuration of cyclone, outlet conditions of SEC, and vane integration in enhancing separator performance. These insights are crucial for industries aiming to improve gas-liquid separation processes, reduce energy consumption, and promote sustainable CO2 capture practices. Overall, this research contributes to addressing environmental challenges and advancing the development of cleaner energy solutions.

V. PAPER [D] – CO2 capture through direct-contact condensation in a spray ejector condenser and T- junction separator

1. Concept of the paper

The fundamental premise of this paper centers on the development of an innovative system tailored for condensation of steam and CO2 purification within gas power plants, with the overarching goal of mitigating CO2 emissions. Integral components of this system include a SEC and a separator, with a primary emphasis placed on optimizing heat transfer efficiency within the SEC and refining phase separation process in the T-junction separator. Employing a blend of experimental and numerical methodologies, the study underscores the detrimental impact of CO2 on resistance to diffusion and convective heat transfer within the steam and subcooled water phases. In response, the investigation systematically evaluates influence of key metrics such as temperature and pressure of the injected water, alongside the steam mass flow rates to ameliorate these effects and bolster heat transfer efficacy within the system.

2. Modelling

2.1 Numerical model of SEC

The numerical modelling of the SEC in this study involves a computational investigation of the DCC process within an ejector setup. The layout of the ejector includes a centrally positioned water nozzle enveloped by a region containing steam and CO2. This arrangement enables direct contact between the motive fluid ejected via a 1 mm nozzle and the steam/CO2 mixture, leading to condensation. The SEC simulation employs a Eulerian-Eulerian multiphase model, where water and mixture of CO2 and steam constitutes the continuous and dispersed phases. Turbulent dynamics within the ejector are characterized using the standard k - ε model [109].

$$\frac{\partial}{\partial t}(r_\alpha \rho_\alpha k_\alpha) + \nabla(r_\alpha \rho_\alpha \boldsymbol{U}_\alpha k_\alpha) = \nabla\left(r_\alpha\left(\mu_\alpha + \frac{\mu_{t\alpha}}{\sigma_k}\right)\nabla k_\alpha\right) + r_\alpha(P_\alpha - \rho_\alpha \varepsilon_\alpha) \tag{14}$$

$$\frac{\partial}{\partial t}(r_\alpha \rho_\alpha \varepsilon_\alpha) + \nabla(r_\alpha \rho_\alpha \boldsymbol{U}_\alpha \varepsilon_\alpha) = \nabla\left(\mu_\alpha + \frac{\mu_{t\alpha}}{\sigma_\varepsilon}\right)\nabla \varepsilon_\alpha + r_\alpha \frac{\varepsilon_\alpha}{k_\alpha}(C_{\varepsilon 1} P_\alpha - C_{\varepsilon 2} \rho_\alpha \varepsilon_\alpha) \tag{15}$$

Interfacial surface density between water and steam is computed to understand the heat transfer surface area [109].

$$A_{sw} = \frac{6\gamma_\beta}{d_\beta} \tag{16}$$

d_β represents the mean bubble diameter in dispersed phase, whilst γ_β refers to the gas volume fraction present in liquid phase.

Momentum transfer between the gas and liquid phases has been analysed via drag force ($\mathbf{M}_{D\alpha}$) and turbulent dispersion force mechanisms ($\mathbf{M}_{TD\alpha}$).

$$\mathbf{M}_{D\alpha} = -\mathbf{M}_{D\beta} = \frac{3}{4}\frac{C_D}{D_\beta} r_\beta \rho_\alpha \left|\mathbf{U}_\beta - \mathbf{U}_\alpha\right| (\mathbf{U}_\beta - \mathbf{U}_\alpha) \tag{17}$$

$$\mathbf{M}_{TD\alpha} = -\mathbf{M}_{TD\beta} = -C_{TD}\rho_\alpha \kappa_\alpha \nabla_{r_\alpha} \tag{18}$$

κ_α denotes the turbulent kinetic energy, an essential factor in evaluating turbulent flow behavior. On the other hand, C_{TD} stands for the coefficient controlling the turbulent dispersion force, which is uniformly set to 0.3 for this analysis, ensuring a consistent reference for computational modeling and assessments.

Heat and mass transfer between the phases are examined to address challenges posed by the presence of CO2, such as the reduction of convective heat transfer. Computational modelling involves setting boundary conditions for mass flow rates at the inlet, defining wall conditions, and using drag force and turbulent dispersion models to simulate interphase momentum transfer.

2.2 Experimental model of Spray Ejector Condenser

The experimental setup described in this paper mirrors the one detailed in Section III. The objective is to ensure The precision and dependability of the computational model by comparing its results with experimental data. Initially, the simulation is conducted without considering the presence of CO2. This enables an ability to make a direct comparison between the numerical results and experimental measurements under controlled conditions. The setup for the experiment takes into account critical parameters such as water mass flow rate, water temperature, water pressure, and steam temperature. The comparison typically focuses on key performance metrics of the system, such as outlet temperatures of the condenser, under various operating conditions, such as different steam mass flow rates. The satisfactory agreement between the simulated and experimental outcomes demonstrate the accuracy of the computational model in capturing the system's behaviour accurately in the absence of CO2. Subsequently, the computational model is extended to incorporate the presence of CO2, reflecting real-world scenarios where CO2 is involved in the process. The model's performance is then assessed by comparing its predictions with experimental data collected under similar conditions but with the inclusion of CO2. This comparison helps evaluate how well the computational model accounts for the effects of CO2 on the system's behaviour. Again, key performance parameters, such as inlet temperatures of the condenser, are compared across different volumetric flow rates of CO2. The significant consistency between the experimental and simulated results in this scenario indicates the model's ability to accurately predict the system's response to the presence of CO2. Finally, both numerical and experimental condensation mass flow rates are examined under varying steam mass flow rates. This comprehensive comparison further reinforces the confidence in the computational model's predictive capabilities, as it demonstrates consistent alignment between numerical predictions and experimental observations across different operating conditions.

2.3 T-junction separator

The T-junction separator serves a pivotal function in the integrated system with the SEC by facilitating the separation of CO2 and water after fully condensation of steam within the SEC. Once the steam undergoes full condensation, the resulting mixture comprises CO2 and water, which are then directed to the inlet of the T-junction separator. In this setup, the T-junction separator acts as a pivotal component for phase separation, ensuring that the CO2 and water are effectively separated into distinct streams. This separation is essential for several reasons. Firstly, it allows for the efficient removal of CO2 from the system, which is vital for reducing emissions and improving the environmental sustainability of the process. Additionally, separating the water from the CO2 enables the recycled water to be reused within the system, minimizing water wastage and optimizing resource utilization. The T-junction separator achieves this separation through its design and operating principles, leveraging the difference in physical properties between CO2 and water. By utilizing the inherent characteristics of the T-junction geometry and employing appropriate boundary conditions, the separator effectively segregates the two phases, directing them into their respective outlets. The study explores the T-junction, investigating both horizontal and vertical configurations. Validation of T-junction separator's efficiency against experimental data and the horizontal counterpart's pressure drop against empirical findings forms the core of this comprehensive approach. Ensuring precise fluid flow in numerical simulations is paramount, thus precisely implementing boundary conditions from corresponding experiments was imperative. This step aimed to validate the simulation via Ansys Fluent 2021 R1, instilling confidence in the validity of the results. Although the main focus is on the vertical T-junction, the inclusion of the horizontal variant aims to verify the modeling approach, mirroring dimensions from prior research. Equations governing continuity, momentum, and turbulence, along with boundary conditions such as velocity inlets and outflows, ensure realistic replication of practical situations. Utilizing the standard k-ε turbulence model enables effective capture of turbulent flow dynamics.

3. Summary and conclusions

Addressing the diminishing convective heat transfer and escalating diffusion resistance in carbon capture systems requires a multifaceted approach, drawing upon insights derived from the research elucidated in the provided discourse. Firstly, optimizing the mass flow rate of incoming steam (2.2-4.6 $\frac{g}{s}$) stands as a paramount strategy. Modulating this parameter can intricately influence the dynamics of the water plume within the SEC, thereby augmenting condensation efficiency. Through analysis of water volume fraction contours, valuable insights into mixing dynamics and condensation efficiency can be gleaned, thereby facilitating the maximization of carbon capture efficacy. It is imperative to ensure the presence of fully condensed water, as it serves as a linchpin for effective heat transfer processes. Secondly, management of CO2 and steam influence on SEC temperatures is essential. Vigilant monitoring and control of both inlet and outlet temperatures are indispensable for evaluating the system's thermal efficiency. Lower outlet temperatures signify proficient extraction of thermal energy from incoming streams, consequently fostering efficient condensation and heightened energy efficiency. Such control mechanisms are instrumental in upholding optimal conditions for heat transfer and condensation processes. Furthermore, fine-tuning water temperature (20-40 °C) emerges as a pivotal endeavour. The temperature of the coolant water significantly modulates heat transfer efficiency within the SEC. Lower temperatures of the coolant water bolster heat transfer efficiency, thereby engendering improved condensation efficacy and commensurately lower outlet temperatures. By optimizing water temperature settings in accordance with investigative findings, a judicious balance can be struck, minimizing energy consumption while maximizing condensation efficiency. Likewise, optimizing water pressure (12-16 bar) warrants meticulous attention. Water pressure exerts a direct influence on heat transfer characteristics within the SEC, with elevated pressures facilitating greater temperature differentials between inlet and outlet streams. The optimization of pressure conditions thus assumes paramount significance in fostering efficient heat exchange processes and bolstering SEC performance. Such optimization attempts are instrumental in ensuring efficient carbon capture by maintaining ideal temperature gradients, as the effectiveness of SEC can be significantly enhanced by optimal combination of cooler water temperatures (20°C) and higher pressures (16 bar), which improve condensation effectiveness. Lastly, enhancing the functionality of T-junction separators represents a vital avenue for advancing fluid separation efficiency. These separators offer compact and cost-effective solutions for fluid partitioning. An understanding of their operational dynamics and subsequent optimization thereof is crucial for realizing efficient fluid separation. The impact of factors like inlet mass flow rates on separation efficiency highlights the essential of fine-tuning operational parameters to achieve optimal fluid partitioning. In concert with the aforementioned strategies, an integrated approach that controls metrics like steam mass flow rates, CO2 flow rates, water temperature, and pressure holds the promise of realizing efficient condensation and separation processes. This integrated methodology, when judiciously applied, serves to elevate the overall effectiveness and carbon capture efficiency of system, thereby effectuating effective mitigation of CO2 emissions.

VI. PAPER [E] – CO2 capture using steam ejector condenser under electro hydrodynamic actuator with non-condensable gas and cyclone separator: A numerical study

1. Concept of the paper

This paper encompasses the application of a steam ejector condenser for the simultaneous tasks of steam condensation and CO2 separation within nCO2PP. This SEC facilitates the DCC of steam with CO2, utilizing a water jet, followed by the separation process to obtain pure CO2. However, presence of CO2 can impede efficiency of heat transfer owing to a decline in convective heat flux and increased diffusion resistance. To mitigate this issue, the investigation incorporates EHD to augment heat transfer mechanisms within the system. Furthermore, the investigation delves into the comparative efficacy of various inlet structure on the overall performance of CO2 purification.

Initially, the impact of steam flow rate at the inlet and back pressure on steam volume fraction is analysed to define their effects on the system. Subsequently, the influence of CO2 on hydraulic-thermal factors is investigated using EHD techniques in the system. Once the model is obtained, efficiency of the separator is evaluated considering multiple inlets. The study aims to estimate how different inlet configurations affect the separator's efficiency. Through CFD analysis, the flow fields and separation efficiencies of each inlet configuration are compared, providing insights into the optimal design for efficient CO2 capture.

2. Numerical model

2.1 Steam ejector condenser

The study utilizes a Eulerian-Eulerian multiphase model, a common approach for handling complex flow phenomena, to accurately represent the dispersion of phases within the system. To account for turbulent behaviour in the flow field, standard k - ε model has been adopted.

Determining interfacial area density is critical for accurately predicting steam condensation rates, a pivotal parameter in SEC simulations. This density, essentially representing the contact area between the two phases, profoundly impacts the heat transfer process. To calculate it, the simulation considers the existence of extremely small bubbles of gas, dispersed within the mixture. These bubbles, assumed to interact with steam and water phases, contribute to overall interfacial area, enabling a more precise estimation of condensation rates. This approach ensures that the simulation captures the intricate interplay between the different phases, facilitating a comprehensive understanding of the system operation. In addition, interphase momentum transfer is a crucial aspect of the simulation, as it directly influences the dynamics of the gas-liquid flow within the system. This momentum transfer between the liquid and gas phases has been primarily governed by two key forces including turbulent dispersion force and drag force. The drag force arises because of an interaction between the gas and liquid phases as they move through the condenser. It represents the resistance experienced by each phase due to the motion of the other, effectively slowing down the movement of the phases. This force is instrumental in determining the overall flow pattern and distribution of velocities. On the other hand, the turbulent dispersion force accounts for the dispersion of momentum caused by turbulent fluctuations in the flow. Turbulence engages a significant role in mixing and redistributing momentum within the fluid, leading to enhanced transport phenomena. By accounting for this turbulent dispersion, the simulation can accurately capture the complex flow dynamics and momentum exchange occurring within the system.

Moreover, interphase heat and mass transfer are vital to the performance of system, especially considering the presence of CO2 within the system. To accurately model the complex heat and mass transfer phenomena occurring among phases, a two-resistance model is implemented. This model accounts for the dual resistances encountered in heat transfer process: one on gas side and another on liquid side. The presence of CO2 gas on the gas side forms a barrier to diffusion, reducing the direct interaction between steam and subcooled water. This diffusion resistance reduces convective heat transfer among the phases, leading to decreased thermal efficiency. Regarding the liquid component, water promotes increased steam condensation, whereas the presence of CO2 gas counteracts this enhancement. The two-resistance model considers both enhancement and inhibition factors, providing a comprehensive framework for analysing thermal performance in the system. Additionally, the model incorporates convective and diffusive heat transfer mechanisms to accurately capture heat transfer processes among phases. Convective heat transfer accounts for bulk movement of fluid and heat exchange at the phase interface, while diffusive heat transfer accounts for heat transfer through molecular diffusion in the fluid.

The presence of CO2 gas within a system can significantly impact heat transfer efficiency due to its effects on convective heat transfer and diffusion resistance. Firstly, CO2 can hinder convective heat transfer by reducing the effectiveness of fluid movement and mixing within the system. Convective heat transfer relies on the bulk movement of fluid to transport heat from one location to another. However, presence of CO2 can disrupt this process by altering the flow patterns and inhibiting fluid motion. As a result, the efficiency of convective heat transfer is reduced, leading to decreased thermal performance. Secondly, CO2 increases the diffusion resistance within the system, further impeding heat transfer processes. Diffusion resistance refers to the hindrance encountered by heat as it diffuses through a medium. When CO2 is present, it creates an additional barrier for heat to overcome, making it more difficult for thermal energy to be transferred between different regions of the system. This increased diffusion resistance leads to slower heat transfer rates and reduced thermal efficiency.

However, to mitigate these challenges, innovative electrohydrodynamic (EHD) techniques are applied. EHD enhancement techniques entail the implementation of an electric field to induce additional fluid motion, thereby improving convective heat flux and addressing adverse effectiveness of CO2 on heat flux efficiency. Incorporating EHD techniques in model is a crucial feature of this study. The modelling for the electric field involves formulating governing equations for electric potential, electric field strength, and electric current density. These equations are crucial for accurately capturing the electrohydrodynamic effects induced by the applied electric field.

The electric force density has been composed of three integral components.

$$\overrightarrow{F_e} = \rho_c\vec{E} - \frac{1}{2}\vec{E}^2\nabla\varepsilon_s + \frac{1}{2}\nabla\left[\vec{E}^2\rho\left(\frac{\partial\varepsilon_s}{\partial\rho}\right)\right] \tag{19}$$

In this context, ρ_c denotes the charge density $(\frac{C}{m^3})$, and $\vec{E}$ symbolizes the electric field strength $(\frac{V}{m})$. ε_s represents the dielectric permittivity $(\frac{F}{m})$.

The Poisson equation is formulated as:

$$\nabla^2 V = -\frac{\rho_c}{\varepsilon_s} \tag{20}$$

V stands for the electric potential (V).

The corresponding expression for the electric field has been given as:

$$\vec{E} = -\nabla V \tag{21}$$

The equation governing current continuity may be described:

$$\nabla.\vec{j} = 0 \tag{22}$$

j denotes the electric current density $(\frac{A}{m^2})$, defined by the following equation:

$$\vec{j} = \rho(\rho_c\beta\vec{E} + \rho_c\vec{u} + D_e\nabla\rho_c) \tag{23}$$

Here, β refers to the ion mobility $(\frac{m^2}{V.s})$, and $\vec{u}$ represents the velocity vector $(\frac{m}{s})$. Additionally, D_e signifies the ion diffusion coefficient $(\frac{m^2}{s})$.

By incorporating EHD techniques, the study aims to enhance heat transfer efficiency and mitigate negative consequenceof CO2 gas on thermal performance. To implement and simulate the EHD effects, the study relies on the FLUENT software platform. FLUENT offers advanced features such as User-Defined Functions (UDF), User-Defined Memory (UDM), and User-Defined Scalar (UDS), which allow for the customization and integration of custom equations into the simulation model. These features enable the accurate representation of EHD phenomena and facilitate the evaluation of heat transfer enhancement techniques within the SEC.

2.2 Cyclone separator

This research utilizes the mixture model, a streamlined adaptation of the Euler-Euler framework, chosen for its effectiveness in handling flows with high dispersed phase volume fractions exceeding 10%. The mixture model accommodates distinct velocities for the fluid phases and their mutual interaction, enabling the exchange of mass, momentum, and energy between them. Furthermore, the RANS equations are applied to resolve the dynamics of both the continuous and dispersed phases. Numerous studies have explored the efficiency of cyclones using diverse numerical approaches, such as the RSM, the RNG k-ε model, and the ASM. RSM model accounts for factors like streamline curvature and swirling, is considered the perfectly appropriate for modelling cyclone flow due to its ability to capture anisotropic turbulence characteristics accurately.

3. Conclusions

The findings from the numerical analysis offer valuable insights into optimizing the integration of SEC and cyclone separator for CO2 purification in nCO2PP. They reveal that adjusting steam inlet mass flow rates can significantly impact steam condensation efficiency, with lower rates expediting condensation but excessively high rates leading to steam plume expansion. Additionally, precise management of backpressure plays a crucial role in regulating condensation effectiveness. Elevated backpressure hinders condensation, while lower backpressure enhances condensation rates. Maintaining backpressure confined to a particular range, from 96 to 106 kPa is crucial for optimizing both static pressure distribution and condensation efficiency. EHD techniques and increased mass flux proficiently attenuates thermal resistance, thereby augmenting the heat transfer coefficient during the condensation. Also, with a steam mass flux of $51(\frac{kg}{m^2.s})$, the condensation heat transfer coefficients were recorded as 0.98, 1.029, 1.08, and 1.134 $(\frac{MW}{m^2.K})$ corresponding to electrode voltages of 0, 20, 25, and 30 kV, respectively. Furthermore, cyclones with multiple inlets, particularly those with four inlets, demonstrate remarkable separation efficiencies, reaching up to 99.9%, compared to 95.1% for single inlets and 97.9% for dual inlets. This suggests that adopting cyclones with multiple inlets could enhance the overall system's effectiveness in practical scenarios.

Overall, these findings underscore the potential for optimizing SEC-cyclone separator integration to achieve more efficient and effective carbon capture processes in power plants.

VII.SUMMARRY AND CONCLUSIONS

The research conducted in this study aimed to overcome the obstacle of separation and purifying of CO2 in the post-combustion section of gas power plants. The purification process involves utilizing a spray or steam ejector condenser in conjunction with a separator, such as a cyclone or T-junction, to remove impurities from the CO2 stream. Throughout this study, various aspects of CO2 capture via DCC in an SEC aided by different separators have been explored.

To address the challenge of investigating the physical processes of direct contact condensation (DCC) within the spray ejector condenser, an experimental facility and analytical model were developed. The experimental facility allowed for a detailed examination of DCC mechanisms, particularly focusing on the influence of CO2 and steam mass flow rates on heat transfer phenomena. Notably, the analytical model offered a novel approach by incorporating considerations for both heat and mass transfer mechanisms, a feature not commonly found in similar treatments. The experimental verification of the model demonstrated adequate consistency with the collected data, affirming its reliability in predicting condensation efficiency. The analytical model accounted for continuity, momentum, and energy equations for the mixture and considered DCC mechanisms. The results emphasized the significance of atomized droplet size and fluid flow parameters such as velocity of droplet and mixture of steam and CO2 in the condensation process.

The core objective of this thesis was to explore innovative methodologies for CO2 capture in gas power plants, focusing on the integration of an ejector condenser and a separator. This combination aimed to achieve efficient steam condensation and CO2 purification, crucial for minimizing CO2 emissions. The next phase of the investigations encompassed both experimental and analytical approaches, providing valuable insights into the operational dynamics of the SEC and its interaction with the cyclone separator. This phase of the study emphasized the significance of understanding the impact of SEC conditions on cyclone efficiency. Specifically, fluctuations in CO2 volumetric flow rate and droplet breakup in the SEC were examined to evaluate their influence on separation efficacy. Also, the effect of cyclone cone size on results was investigated through numerical simulations. It was observed that lowering the steam and CO2 flow rates led to enhanced temperature difference and heat transfer rate. Additionally, augmenting cyclone cone size enhanced separation efficiency while increasing pressure drop, indicating a trade-off between energy consumption and CO2 refinement. Moreover, investigation into droplet breakup within the SEC demonstrated its role in enhancing separation efficiency, highlighting the importance of droplet size in optimizing CO2 capture effectiveness. So, the integration of experimental and analytical modelling alongside numerical simulation proved instrumental in developing a comprehensive methodology to enrich efficiency of CO2 purification. By addressing variables such as steam mass flow rate, CO2 volumetric flow rate, cyclone cone size, and droplet breakup, this approach aims to guarantee the production of high-purity CO2 in the post-combustion sector of gas power plants.

After investigating the SEC and cyclone, the focus shifts towards optimizing the structural and operational parameters that impact separator efficiency. This involves analysing the performance of single and dual inlet cyclones and assessing influence of SEC outlet conditions on separator efficiency. Additionally, one of the challenges associated with cyclone separators is the surge in pressure drop, which can be addressed by addition of vanes. The results underscored the superior performance of dual-inlet cyclone in contrast to single-inlet, underscoring the significance of inlet configuration in optimizing separator efficiency. Furthermore, factors like water droplet diameter and LVF exert significant influence on separator performance, with lower liquid volume fractions and larger water droplet diameters enhancing separation efficiency. Also, the incorporation of vanes within cyclone leads to a notable reduction in pressure drop and a simultaneous enhancement in separation capability. This highlighted the potential for structural modifications to enhance separator performance and overcome operational challenges.

Another viable option for use as a separator is the T-junction separator. Moreover, one of the challenges associated with the SEC is deterioration in convective heat transfer and an elevation in diffusion resistance attributable to the presence of CO2. Consequently, subsequent phase of the research focused on examining the influence of various thermophysical characteristics of the injected water, notably temperature (20 to 40 ℃) and pressure (12 to 16 bar), in conjunction with steam mass flow rates (2.2 to 4.6 $\frac{g}{s}$), to optimize and augment heat transfer rates within the SEC. The findings indicated that reduced water temperature, coupled with augmented water pressures, markedly facilitated the optimization of condensation efficiency, underscoring the significance of parameter optimization. Furthermore, gaining insights into the decrease in separation efficiency of T-junction with higher inlet mass flow rates proved invaluable for optimizing separation systems across diverse industrial applications.

Another feasible alternative for ejector condensation is the steam ejector condenser. However, as previously noted, CO2 in the steam phase presents challenges, such as attenuated convective heat transfer and amplified diffusion resistance. To overcome these obstacles, an EHD was utilized to enhance heat transfer within the system. Furthermore, the study investigates the impact of different inlet configurations. Results demonstrated that increasing steam mass flux and voltage of the EHD actuator improves condensation heat transfer coefficient. Additionally, cyclone separators with multiple inlets exhibit notable advantages in separation efficiency, with a cyclone featuring four inlets achieving an impressive 99.9% separation efficiency. Moreover, precise management of backpressure proves essential for effectively regulating condensation efficiency within the SEC.

Further research

Building upon the findings of previous research on spray or steam ejector condenser and separators such as cyclones or T-junctions, further investigations could delve into optimizing their operational parameters for enhanced CO2 purification efficiency. For instance, exploring novel designs or materials for ejector condensers to mitigate the impact of non-condensable gases, such as CO2, on heat transfer could be a promising avenue. Additionally, studying advanced control strategies for regulating the inlet conditions of ejector condensers and separators could lead to more precise and efficient CO2 capture processes.

Moreover, future research could focus on developing innovative separator technologies that offer higher separation efficiencies while minimizing energy consumption and operational costs. This could involve exploring alternative separation mechanisms or geometries for cyclones or T-junctions to improve their performance in capturing CO2 from the steam-water mixture. Additionally, investigating the integration of advanced materials or coatings to enhance the separation efficiency of these separators, particularly in scenarios with high CO2 concentrations, could be beneficial. Furthermore, studying the synergistic effects of combining different types of separators, such as cyclones and T-junctions, within a single CO2 capture system could provide valuable insights into optimizing the overall purification process. Overall, future research endeavours should aim to advance the state-of-the-art in CO2 capture technologies by addressing the challenges and limitations associated with spray or steam ejector condensers and separators.

VIII. BIBLIOGRAPHY

1. Roy, P., A.K. Mohanty, and M. Misra, *Prospects of carbon capture, utilization and storage for mitigating climate change.* Environmental Science: Advances, 2023. **2**(3): p. 409-423.
2. Bahman, N., et al., *Review of carbon capture and storage technologies in selected industries: potentials and challenges.* Reviews in Environmental Science and Bio/Technology, 2023. **22**(2): p. 451-470.
3. Shu, D.Y., et al., *The role of carbon capture and storage to achieve net-zero energy systems: Trade-offs between economics and the environment.* Renewable and Sustainable Energy Reviews, 2023. **178**: p. 113246.
4. Ramirez-Corredores, M.M., M.R. Goldwasser, and E. Falabella de Sousa Aguiar, *Carbon dioxide and climate change*, in *Decarbonization as a Route Towards Sustainable Circularity*. 2023, Springer. p. 1-14.
5. Maniarasu, R., S.K. Rathore, and S. Murugan, *A review on materials and processes for carbon dioxide separation and capture.* Energy & Environment, 2023. **34**(1): p. 3-57.
6. Larki, I., et al., *Mitigation approaches and techniques for combustion power plants flue gas emissions: A comprehensive review.* Science of The Total Environment, 2023: p. 166108.
7. Gautam, A. and M.K. Mondal, *Review of recent trends and various techniques for CO2 capture: Special emphasis on biphasic amine solvents.* Fuel, 2023. **334**: p. 126616.
8. Wang, P., et al., *Advances in life cycle assessment of chemical absorption-based carbon capture technologies.* Separation and Purification Technology, 2024: p. 127252.
9. Das, D., T. Agarwal, and A.K. Biswal, *A review on different methods of CO2 capture, separation and utilization.* Brazilian Journal of Chemical Engineering, 2023: p. 1-19.
10. Goren, A.Y., D. Erdemir, and I. Dincer, *Comprehensive review and assessment of carbon capturing methods and technologies: An environmental research.* Environmental Research, 2024. **240**: p. 117503.
11. Astuti, A.R., et al., *Advances in Carbon Control Technologies for Flue Gas Cleaning.* Separation & Purification Reviews, 2024: p. 1-30.
12. Nedoma, M., M. Netušil, and J. Hrdlička, *Integration of adsorption based post-combustion carbon dioxide capture for a natural gas-fired combined heat and power plant.* Fuel, 2023. **354**: p. 129346.
13. Yu, X., et al., *Trends in research and development for CO2 capture and sequestration.* ACS omega, 2023. **8**(13): p. 11643-11664.
14. Allangawi, A., et al., *Carbon capture materials in post-combustion: adsorption and absorption-based processes.* C, 2023. **9**(1): p. 17.
15. Anwar, M., et al., *CO2 utilization: Turning greenhouse gas into fuels and valuable products.* Journal of environmental management, 2020. **260**: p. 110059.
16. Liu, E., X. Lu, and D. Wang, *A systematic review of carbon capture, utilization and storage: status, progress and challenges.* Energies, 2023. **16**(6): p. 2865.
17. Olabi, A., et al., *Membrane-based carbon capture: Recent progress, challenges, and their role in achieving the sustainable development goals.* Chemosphere, 2023. **320**: p. 137996.
18. Ketabchi, M.R., et al., *Latest advances and challenges in carbon capture using bio-based sorbents: A state-of-the-art review.* Carbon Capture Science & Technology, 2023. **6**: p. 100087.

19. Kim, Y., et al., *Novel cryogenic carbon dioxide capture and storage process using LNG cold energy in a natural gas combined cycle power plant.* Chemical Engineering Journal, 2023. **456**: p. 140980.
20. Zhu, M., et al., *Dynamic modeling and comprehensive analysis of direct air-cooling coal-fired power plant integrated with carbon capture for reliable, economic and flexible operation.* Energy, 2023. **263**: p. 125490.
21. Su, D., et al., *Thermal integration of waste to energy plants with Post-combustion CO2 capture.* Fuel, 2023. **332**: p. 126004.
22. Ziółkowski, P., et al., *Negative carbon dioxide gas power plant integrated with gasification of sewage sludge.* Energy, 2023. **262**: p. 125496.
23. Lim, J., et al., *Novel process design for waste energy recovery of LNG power plants for CO2 capture and storage.* Energy Conversion and Management, 2023. **277**: p. 116587.
24. Meng, L., et al., *Modeling of pre-combustion carbon capture with CO2-selective polymer membranes.* International Journal of Greenhouse Gas Control, 2023. **123**: p. 103830.
25. Hu, F., et al., *Comparative study on process simulation and performance analysis in two pressurized oxy-fuel combustion power plants for carbon capture.* Energy Conversion and Management, 2024. **303**: p. 118178.
26. Okeke, I.J., T. Ghantous, and T.A. Adams, *Design strategies for oxy-combustion power plant captured CO2 purification.* Chemical Product and Process Modeling, 2023. **18**(1): p. 135-154.
27. Ibigbami, O.A., O.D. Onilearo, and R.O. Akinyeye, *Post-combustion capture and other Carbon Capture and Sequestration (CCS) technologies: A review.* Environmental Quality Management, 2024.
28. Subramanian, N. and P. Madejski, *Analysis of CO2 capture process from flue-gases in combined cycle gas turbine power plant using post-combustion capture technology.* Energy, 2023. **282**: p. 128311.
29. Ni, Z., et al., *Synchronous design of membrane material and process for pre-combustion CO2 capture: A superstructure method integrating membrane type selection.* Membranes, 2023. **13**(3): p. 318.
30. Jinlu, Y., et al., *Characteristics of a pre-combustion plasma jet igniter.* Chinese Journal of Aeronautics, 2024.
31. Smith, K.H., et al., *Performance of hydrophobic physical solvents for pre-combustion CO2 capture at a pilot scale coal gasification facility.* International Journal of Greenhouse Gas Control, 2023. **124**: p. 103863.
32. Cormos, C.-C., *Green hydrogen production from decarbonized biomass gasification: An integrated techno-economic and environmental analysis.* Energy, 2023. **270**: p. 126926.
33. Liang, W., et al., *Investigation of a novel near-zero emission poly-generation system based on biomass gasification and SOFC: A thermodynamic and exergoeconomic evaluation.* Energy, 2023. **282**: p. 128822.
34. Wu, Z., et al., *CO2 Capture from Biomass Gasification Current Technologies, Challenges and Future Prospects.* Academic Journal of Science and Technology, 2023. **7**(1): p. 206-212.
35. Wang, J., et al., *Integrated vacuum pressure swing adsorption and Rectisol process for CO2 capture from underground coal gasification syngas.* Chinese Journal of Chemical Engineering, 2023. **57**: p. 265-279.

36. Jansen, D., et al., *Pre-combustion CO2 capture.* International Journal of Greenhouse Gas Control, 2015. **40**: p. 167-187.
37. Alalaiwat, D. and E. Khan, *Current status and future scenarios of carbon capture from power plants emission: a review.* Reviews in Environmental Science and Bio/Technology, 2023. **22**(3): p. 799-822.
38. Singh, N., et al., *Carbon capture, sequestration, and usage for clean and green environment: challenges and opportunities.* International Journal of Sustainable Engineering, 2023. **16**(1): p. 248-268.
39. Zhou, Z., et al., *Thermodynamic and environmental analyses of a hydrogen-enriched natural gas oxy-fuel combustion power plant.* International Journal of Hydrogen Energy, 2024. **64**: p. 247-260.
40. Tan, L., et al., *Numerical investigation of biomass and liquefied natural gas driven oxy-fuel combustion power system.* Renewable Energy, 2023. **208**: p. 94-104.
41. Cai, L., et al., *Investigation on the integration of supercritical CO2 cycle with natural gas oxy-fuel combustion power plant.* Chemical Engineering Research and Design, 2024.
42. Kaszuba, M., P. Ziółkowski, and D. Mikielewicz, *Performance of cryogenic oxygen production unit with exhaust gas bleed for sewage sludge gasification and different oxygen purities.* Archives of Thermodynamics, 2023. **44**: p. 63-81.
43. García-Luna, S., et al., *Oxygen production routes assessment for oxy-fuel combustion.* Energy, 2022. **254**: p. 124303.
44. Luján, J.M., et al., *Design of a carbon capture system for oxy-fuel combustion in compression ignition engines with exhaust water recirculation.* Energy Conversion and Management, 2023. **284**: p. 116979.
45. Fu, Y., et al., *Thermodynamic and economic performance comparison of biomass gasification oxy-fuel combustion power plant in different gasifying atmospheres using advanced exergy and exergoeconomic approach.* Renewable Energy, 2024: p. 120290.
46. Guo, J., et al., *Review on research and development of oxy-coal burner for carbon capture.* Science China Technological Sciences, 2024: p. 1-26.
47. Kong, R., et al., *Energy efficiency analysis and optimization of a pressurized oxy-fuel circulating fluidized bed combustion system.* Energy, 2024. **286**: p. 129613.
48. Fu, R., et al., *An Optimized Methane Reaction Model for Oxyfuel Combustion.* Energy & Fuels, 2023. **37**(15): p. 11284-11297.
49. Hosseinifard, F., et al., *Optimizing post-combustion carbon capture: A comprehensive 3E analyses of energy, exergy, and exergoeconomic aspects with solar integration.* Sustainable Energy Technologies and Assessments, 2024. **62**: p. 103626.
50. Wu, X., et al., *Solvent-based post-combustion CO2 capture for power plants: A critical review and perspective on dynamic modelling, system identification, process control and flexible operation.* Applied Energy, 2020. **257**: p. 113941.
51. Oexmann, J., et al., *Post-combustion CO2 capture: chemical absorption processes in coal-fired steam power plants.* Greenhouse Gases: Science and Technology, 2012. **2**(2): p. 80-98.
52. Lawal, A., et al., *Dynamic modelling and analysis of post-combustion CO2 chemical absorption process for coal-fired power plants.* Fuel, 2010. **89**(10): p. 2791-2801.
53. Zhao, H., et al., *Carbon-based adsorbents for post-combustion capture: a review.* Greenhouse Gases: Science and Technology, 2018. **8**(1): p. 11-36.

54. Jiang, L., et al., *Post-combustion CO2 capture from a natural gas combined cycle power plant using activated carbon adsorption.* Applied Energy, 2019. **245**: p. 1-15.
55. Hedin, N., et al., *Adsorbents for the post-combustion capture of CO2 using rapid temperature swing or vacuum swing adsorption.* Applied Energy, 2013. **104**: p. 418-433.
56. Amiri, M., et al., *Analysis of cyclone separator solutions depending on spray ejector condenser conditions.* Applied Thermal Engineering, 2024. **257**: p. 124235.
57. Goto, K., K. Yogo, and T. Higashii, *A review of efficiency penalty in a coal-fired power plant with post-combustion CO2 capture.* Applied Energy, 2013. **111**: p. 710-720.
58. Merkel, T.C., et al., *Power plant post-combustion carbon dioxide capture: An opportunity for membranes.* Journal of membrane science, 2010. **359**(1-2): p. 126-139.
59. Chao, C., et al., *Post-combustion carbon capture.* Renewable and Sustainable Energy Reviews, 2021. **138**: p. 110490.
60. Liang, Z., et al., *Review on current advances, future challenges and consideration issues for post-combustion CO2 capture using amine-based absorbents.* Chinese journal of chemical engineering, 2016. **24**(2): p. 278-288.
61. Drage, T.C., et al., *Materials challenges for the development of solid sorbents for post-combustion carbon capture.* Journal of Materials Chemistry, 2012. **22**(7): p. 2815-2823.
62. Negative, C., *Emission Gas Power Plant*. 2020.
63. Ziółkowski, P., et al., *Thermodynamic analysis of negative CO2 emission power plant using Aspen Plus, Aspen Hysys, and Ebsilon software.* Energies, 2021. **14**(19): p. 6304.
64. Amiri, M., J. Mikielewicz, and D. Mikielewicz, *CO2 capture using steam ejector condenser under electro hydrodynamic actuator with non-condensable gas and cyclone separator: A numerical study.* Separation and Purification Technology, 2024. **329**: p. 125236.
65. Mikielewicz, D., et al., *A novel concept of enhanced direct-contact condensation of vapour-inert gas mixture in a spray ejector condenser.* International Journal of Heat and Mass Transfer, 2023. **216**: p. 124576.
66. Madejski, P., et al., *Development of a spray-ejector condenser for the use in a negative CO2 emission gas power plant.* Energy, 2023. **283**: p. 129163.
67. Ziółkowski, P., et al., *Mathematical modelling of gasification process of sewage sludge in reactor of negative CO2 emission power plant.* Energy, 2022. **244**: p. 122601.
68. Pennline, H.W., et al., *Progress in carbon dioxide capture and separation research for gasification-based power generation point sources.* Fuel Processing Technology, 2008. **89**(9): p. 897-907.
69. Zhao, P., et al., *Clean solid biofuel production from high moisture content waste biomass employing hydrothermal treatment.* Applied energy, 2014. **131**: p. 345-367.
70. Gürsoy, E., et al., *Performance improvement of air separation unit for an iron-steel industry using enhanced exergy analysis.* Journal of Thermal Analysis and Calorimetry, 2024: p. 1-18.
71. Prosser, N. and M. Shah. *Air separation units for oxy-coal power plants*. in *2nd Oxyfuel Combustion Conference*. 2011.
72. Han, L., et al., *Integration optimisation of elevated pressure air separation unit with gas turbine in an IGCC power plant.* Applied thermal engineering, 2017. **110**: p. 1525-1532.
73. Janusz-Szymańska, K. and A. Dryjańska, *Possibilities for improving the thermodynamic and economic characteristics of an oxy-type power plant with a cryogenic air separation unit.* Energy, 2015. **85**: p. 45-61.

74. Jones, D., et al., *Optimal design and integration of an air separation unit (ASU) for an integrated gasification combined cycle (IGCC) power plant with CO2 capture.* Fuel processing technology, 2011. **92**(9): p. 1685-1695.
75. Ong, C.W., et al., *Decarbonizing the energy supply chain: Ammonia as an energy carrier for renewable power systems.* Fuel, 2024. **360**: p. 130627.
76. Kamin, Z., M.H. Bahrun, and A. Bono. *A short review on pressure swing adsorption (PSA) technology for nitrogen generation from air*. in *AIP Conference Proceedings*. 2022. AIP Publishing.
77. Wu, D., et al., *Membrane separation process modeling for CO2 partial removal in prepurification of air separation units.* Chemical Engineering Communications, 2019. **206**(12): p. 1676-1688.
78. Froissart, M. and T. Ochrymiuk, *Novel wet combustion chamber concept CFD studies with triple water inlet.* Energy, 2023. **278**: p. 127854.
79. Madejski, P., et al., *Direct contact condensers: a comprehensive review of experimental and numerical investigations on direct-contact condensation.* Energies, 2022. **15**(24): p. 9312.
80. Kuś, T. and P. Madejski, *Analysis of the Multiphase Flow With Condensation in the Two-Phase Ejector Condenser Using Computational Fluid Dynamics Modeling.* Journal of Energy Resources Technology, 2024. **146**(3).
81. Madejski, P., et al., *Conceptual Design of Experimental Test Rig for Research on Thermo-Flow Processes During Direct Contact Condensation in the Two-Phase Spray-Ejector Condenser.* Journal of Energy Resources Technology, 2024. **146**(3).
82. Madejski, P., et al., *Monitoring of Thermal and Flow Processes in the Two-Phase Spray-Ejector Condenser for Thermal Power Plant Applications.* Energies, 2022. **15**(19): p. 7151.
83. Kitrattana, B., et al., *Comparison of traditional and CRMC ejector performance used in a steam ejector refrigeration.* Energy Procedia, 2017. **138**: p. 476-481.
84. Little, A.B. and S. Garimella, *A review of ejector technology for refrigeration applications.* International Journal of Air-Conditioning and Refrigeration, 2011. **19**(01): p. 1-15.
85. Yadav, S.K., K.M. Pandey, and R. Gupta, *Recent advances on principles of working of ejectors: A review.* Materials Today: Proceedings, 2021. **45**: p. 6298-6305.
86. Memon, Z.Q., et al., *Experimental investigation of two-phase separation in T-Junction with combined diameter ratio.* Journal of Natural Gas Science and Engineering, 2020. **73**: p. 103048.
87. El-Emam, M.A., L. Zhou, and E. Yasser, *Numerical Investigation of Cyclone Separators: Physical Mechanisms and Theoretical Algorithms.* ChemBioEng Reviews, 2024.
88. Feng, M., et al., *Numerical study on performance optimization and flow mechanism of a new cyclone separator.* Green Chemical Engineering, 2024.
89. Kouba, G. and O. Shoham. *A review of gas-liquid cylindrical cyclone (glcc) technology*. in *Production Separation Systems International Conference, Aberdeen, England, April*. 1996. Citeseer.
90. Fu, Z., et al., *Impact of Built-in Helical Fins on the Performance of Oil-Gas Cyclone Separators.* Chemical Engineering & Technology, 2024. **47**(3): p. 520-530.
91. Wang, L., et al., *A study on the characteristics and geometric optimization of a cyclone filter.* Separation and Purification Technology, 2024: p. 127313.

92. Dai, R., S. Fu, and H. Yuan, *Study on the wall film behavior and droplet catching performance of a micro cyclone in hydrogen fuel cells.* International Journal of Hydrogen Energy, 2024. **61**: p. 125-136.
93. Rivera-García, M., et al., *Cyclone Separator for Air Particulate Matter Personal Monitoring: A Patent Review.* Atmosphere, 2023. **14**(4): p. 624.
94. Haig, C., et al., *An empirical investigation into the influence of pressure drop on particle behaviour in small scale reverse-flow cyclones.* Powder technology, 2015. **275**: p. 172-181.
95. Dziubak, T. and L. Bąkała, *Computational and experimental analysis of axial flow cyclone used for intake air filtration in internal combustion engines.* Energies, 2021. **14**(8): p. 2285.
96. Venkatesh, S., et al., *Performance investigation of the combined series and parallel arrangement cyclone separator using experimental and CFD approach.* Powder technology, 2020. **361**: p. 1070-1080.
97. Guo, M., et al., *Multi-objective optimization of a novel vortex finder for performance improvement of cyclone separator.* Powder Technology, 2022. **410**: p. 117856.
98. Guo, M., et al., *An overview of novel geometrical modifications and optimizations of gas-particle cyclone separators.* Separation and Purification Technology, 2023: p. 125136.
99. Malahayati, N., et al., *Comparative performance analysis between conventional and square cyclones for solid Particle-Gas Separation: A review.* Materials Today: Proceedings, 2022. **63**: p. S318-S325.
100. Vermande Paganel, T., et al., *CFD Simulation of an Industrial Dust Cyclone Separator: A Comparison with Empirical Models: The Influence of the Inlet Velocity and the Particle Size on Performance Factors in Situation of High Concentration of Particles.* Journal of Engineering, 2024. **2024**.
101. Knowlton, T., *Cyclone separators.* Handbook of fluidization and fluid-particle systems. New York: Marcel Dekker, 2003.
102. Mazyan, W., A. Ahmadi, and M. Hoorfar, *A comparison between cyclone separator efficiency enhancement using ferrous powder and additional tangential chamber.* 2018.
103. Margaris, D.P., *T-junction separation modelling in gas–liquid two-phase flow.* Chemical Engineering and Processing: Process Intensification, 2007. **46**(2): p. 150-158.
104. Ejaz, F., W. Pao, and H.M. Ali, *Two Phase Separation in the T-junction*. 2024: Springer.
105. Su, W., et al., *Experimental study on phase separation of refrigerant at horizontal T-junction.* International Journal of Multiphase Flow, 2018. **105**: p. 217-233.
106. Yang, B., et al., *State-of-art of impacting T-junction: Phase separation, constituent separation and applications.* International Journal of Heat and Mass Transfer, 2020. **148**: p. 119067.
107. Yang, B., et al., *State-of-art of branching T-junction: Experiments, modeling, developing prospects and applications.* Experimental Thermal and Fluid Science, 2019. **109**: p. 109895.
108. Amiri, M., et al., *Optimizing CO2 Purification in a Negative CO2 Emission Power Plant.* Chemical Engineering & Technology, 2024. **47**(9): p. e202300568.
109. Amiri, M., et al., *CO2 capture through direct-contact condensation in a spray ejector condenser and T-junction separator.* International Communications in Heat and Mass Transfer, 2024. **156**: p. 107596.

ABSTRACT

This thesis delves into the imperative task of purifying CO2 in the post-combustion sections of gas power plants, focusing on innovative methodologies centred around the integration of spray or steam ejector condenser with separators such as cyclone or T-junction. The research adopts a diverse approach, integrating experimental, analytical, and numerical techniques to comprehensively explore CO2 capture through direct-contact condensation (DCC) within SEC, supported by different separators.

A substantial segment of the study is devoted to understanding the physical processes of DCC within SEC through the development of experimental facilities and analytical models. The experimental setup enables an examination of DCC mechanisms, while the analytical model incorporates considerations for heat and mass transfer mechanisms, offering a unique perspective on condensation efficiency. Additionally, the thesis investigates the operational dynamics of SEC and their interaction with cyclone separators, shedding light on factors such as steam and CO2 flow rates and droplet breakup to optimize CO2 purification.

The investigation extends to explore novel strategies to enhance separator efficiency, encompassing the analysis of single and dual inlet cyclones and the examination of thermophysical parameters affecting SEC performance. Moreover, the study explores the potential of utilizing electrohydrodynamic (EHD) actuators to overcome challenges associated with CO2 presence in the steam phase, alongside optimizing inlet configurations for cyclone separators. The findings underscore the importance of parameter optimization and structural modifications in achieving high-purity CO2 production while addressing operational challenges within gas power plant post-combustion sections.

The first phase of the study focuses on developing experimental facilities and analytical models to understand the physical processes of DCC within SEC. The experimental setup allows for a detailed examination of DCC mechanisms, particularly effect of CO2 and steam mass flow rates on condensation efficiency. Simultaneously, analytical model incorporates considerations for heat and mass transfer mechanisms, providing insights into condensation dynamics. The achievement of this phase lies in validation of analytical model through satisfactory agreement with experimental results, affirming its reliability in predicting condensation efficiency.

Building upon the understanding of SEC operation, the research extends to investigate the integration of SEC with cyclone separators. This phase explores factors such as steam and CO2 flow rates, droplet breakup, and cyclone cone size to optimize CO2 purification efficiency. Observations highlight potential of structural modifications in enhancing separator performance, thus contributing to the overall efficiency of CO2 capture systems.

Another significant aspect of the study involves optimizing cyclone separators by integrating vanes. Through numerical simulations and experimental validations, the research evaluates the impact of vane addition on separation efficiency and pressure drop. Results underscore effectiveness of structural modifications and operation conditions of SEC like volume fraction and

breakup of droplet in improving separator performance, paving the way for more efficient CO2 purification processes.

Further advancements in CO2 capture technologies are explored through the integration of SEC with T-junction separator. During this stage, the study examines how thermophysical factors like temperature and pressure of water influence condensation efficiency within the SEC, aiming to alleviate the consequences of CO2 on heat transfer rates. Findings emphasize the importance of parameter optimization in enhancing CO2 capture effectiveness, providing crucial perspectives for subsequent investigations industrial applications.

The final phase of the study explores innovative techniques for CO2 capture, focusing on the utilization of steam ejector condenser with electrohydrodynamic (EHD) actuators. This approach aims to overcome challenges associated with CO2 presence in the steam phase, enhancing condensation efficiency within SEC. Additionally, the investigation delves into the optimization of cyclone separators, highlighting the advantages of multi-inlet configurations in achieving high separation efficiencies.

STRESZCZENIE

Niniejsza praca pogłębia zagadnienie separacji dwutlenku węgla po spalaniu w elektrowniach gazowych, w których końcowy bilans emisji CO2 jest ujemny, koncentrując się na innowacyjnych metodach integracji eżektorów z separatorami typu cyklon lub T-junction. Badania przyjmują wieloaspektowe podejście, łącząc techniki eksperymentalne, analityczne i numeryczne w celu wszechstronnego zbadania separacji CO2 poprzez bezpośrednią kondensację (DCC) w eżektorze dwufazowym (SEC), wspieranego przez kilka typów separatorów.

Znacząca część badań jest poświęcona zrozumieniu procesów fizycznych DCC w SEC poprzez budowę instalacji doświadczalnej i opracowanie modeli analitycznych. Układ eksperymentalny umożliwia badanie mechanizmów DCC, a model analityczny uwzględnia mechanizmy wymiany ciepła i masy, oferując możliwość oceny efektywności kondensacji bezpośredniej. Ponadto, badania analizują dynamikę pracy SEC oraz ich interakcję z separatorami cyklonowymi, podkreślając wpływ takich parametrów jak przepływ pary i CO2 oraz rozpad kropli w SEC, w celu optymalizacji separacji CO2.

Przedstawione badania obejmują także próby poprawy wydajności separatorów pary i cieczy poprzez analizę cyklonów z pojedynczym i podwójnym wlotem oraz badanie wpływu parametrów termofizycznych na efektywność SEC. W przeprowadzonych analizach zbadano także dodatkowo potencjał zastosowania aktuatorów elektrohydrodynamicznych (EHD) w celu intensyfikacji procesów separacji CO2 z mieszaniny parowo-gazowej, a także optymalizacji liczby i konfiguracji wlotów dla separatorów cyklonowych. Wyniki podkreślają znaczenie optymalizacji tych parametrów i modyfikacji strukturalnych w osiągnięciu produkcji czystego CO2.

Pierwsza faza badań w pracy skupia się na opracowaniu instalacji doświadczalnej i opracowaniu modeli analitycznych celem głębszego poznania procesów fizycznych DCC w SEC. Układ eksperymentalny umożliwia szczegółowe badanie mechanizmów DCC, zwłaszcza wpływu strumieni przepływów CO2 i pary na efektywność kondensacji. Jednocześnie model analityczny uwzględnia mechanizmy wymiany ciepła i masy, dostarczając wglądu w dynamikę kondensacji. Osiągnięciem tej części pracy jest walidacja modelu analitycznego poprzez satysfakcjonującą zgodność z danymi eksperymentalnymi, co potwierdza jego niezawodność w przewidywaniu wydajności kondensacji.

Bazując na zrozumieniu działania bezpośredniej kondensacji w SEC, badania rozszerzono na analizę integracji SEC z separatorami cyklonowymi celem dalszej puryfikacji CO2. Ta faza prac rozpatruje przepływy masy pary i CO2, rozpad kropli oraz wymiary geometryczne stożka cyklonu na zoptymalizowanie wydajności dalszej separacji CO2. Uzyskane wyniki podkreślają potencjał modyfikacji strukturalnych i optymalizacji parametrów w poprawie wydajności separatorów, przyczyniając się tym samym do ogólnego wzrostu efektywności systemów separacji CO2.

Kolejny istotny aspekt badań dotyczy optymalizacji separatorów cyklonowych poprzez wprowadzenie do cyklonów kierownic. Poprzez symulacje numeryczne i walidacje eksperymentalne badania oceniono wpływ dodania kierownic na wydajność separacji i spadek ciśnienia w instalacji. Wyniki podkreślają skuteczność modyfikacji strukturalnych i warunków

pracy SEC, takich jak udział objętościowy fazy gazowej i rozpad kropel, w poprawie wydajności separatora, otwierając tym samym drogę do bardziej wydajnych procesów separacji CO2.

Przeprowadzono także inne analizy możliwości separacji CO2 z mieszaniny parowo-gazowej poprzez integrację SEC z separatorem typu T-junction. Analizowano wpływ czynników termofizycznych, takich jak temperatura i ciśnienie wody, mających wpływ na efektywność kondensacji w SEC oraz dodatkowym elemencie separującym niekondensujący się gaz (CO2) poprzez współczynniki wymiany ciepła. Wyniki podkreślają znaczenie optymalizacji parametrów w poprawie skuteczności separacji CO2, dostarczając cennych wskazówek dla przyszłych badań i zastosowań przemysłowych.

Ostatnia faza przeprowadzonych prac koncentruje się na nowatorskich technikach separacji CO2, skupiając się na wykorzystaniu eżektorów parowych z aktuatorami elektrohydrodynamicznymi (EHD). Podejście to ma na celu pokonanie wyzwań związanych z usuwaniem CO2 z fazy parowej, poprawiając w wyniku efektywność kondensacji bezpośredniej w SEC. Badania dodatkowo zagłębiają się w optymalizację separatorów cyklonowych, podkreślając zalety wielowlotowych konfiguracji w osiągnięciu wysokich efektywności separacyjnych.

APPENDICES

International Journal of Heat and Mass Transfer 216 (2023) 124576

Contents lists available at ScienceDirect

International Journal of Heat and Mass Transfer

journal homepage: www.elsevier.com/locate/ijhmt

A novel concept of enhanced direct-contact condensation of vapour- inert gas mixture in a spray ejector condenser

Dariusz Mikielewicz [a,*], Milad Amiri [a], Michał Klugmann [a], Jarosław Mikielewicz [b]

[a] Faculty of Mechanical Engineering and Ship Technology, Institute of Energy, Gdańsk University of Technology, Gdańsk 80-233, Poland
[b] Institute of Fluid-Flow Machinery, Gdansk 80-231, Poland

ARTICLE INFO

Keywords:
Spray ejector condenser
Direct-contact condensation
Jet breakup

ABSTRACT

An analytical model of direct steam condensation (DCC) in the novel idea of spray ejector condenser (SEC) in the presence of inert gas has been developed. It is based on continuity, momentum and energy equations for the steam-carbon dioxide mixture and direct contact condensation mechanisms due to heat transfer and concentration. Crucial in the process of DCC is atomisation of the motive fluid in the ejector. The effect of atomised droplet size is exhibiting a significant amplification influence with increasing size of the droplet. Motive fluid is driving the secondary fluid-mixture of steam and inert gas in the Venturi nozzle and is cold enough to cause direct condensation. The intensity of heat transfer process from steam to water when the phases are in direct contact is much higher than the heat transfer intensity in surface heat exchangers. The analytical model pertains to a subcritical flow of a mixture of steam and gas in SEC. The model exhibits satisfactory agreement with experimental data. The model of DCC predicts higher values of temperature drop between inlet and outlet from the mixing section for the case of smaller steam-CO_2 flow rates. Increasing the flow rate of steam mixture from 1.2 g/s to 3.6 g/s results in a reduction of steam mixture temperature from 25 °C to 14 °C respectively, at CO_2 flow rate of 6.8 m^3/h. Condensation without presence of CO_2 in the same range of steam flow rate, i.e. from 1.2 g/s to 3.6 g/s results in reduction of steam mixture temperature from 56 °C to 25 °C respectively, confirming in such way the effect of CO_2 presence on the efficiency of DCC. Such model allow for discussion of parameters affecting process of condensation in SEC and ability of application such condenser in power plants.

1. Introduction

Direct-contact condensation (DCC) plays a pivotal role for both engineering and natural sciences that has been exploited in many fields [1–5]. DCC is when a gas/vapour stream comes into direct contact with a subcooled liquid, Mazed et al. [6]. Such process is associated with much higher heat transfer coefficients than in conventional heat exchange processes [7]. DCC of vapour with inert gas on a spray of subcooled liquid exists in a number of technical applications such as for example in the nuclear industry (e.g. depressurization under normal operating conditions, (see e.g. Celata et al. [8]), safety analyses) and in the chemical industry (e.g. mixing-type heat exchanger, degasser, sea water desalting). Another application is when the supersonic steam jet flows combines with cold water in the mixing nozzle in the emergency cooling system of nuclear reactor, causing DCC. The condensing-injector is envisaged as a potential heat exchanger or energy-efficient pump due to its higher heat exchange coefficient, low-grade thermal energy utilization and ability to pressurize without rotating components [9]. Novel applications of SEC pursuit by Authors are considered in gas power cycles for condensing steam in exhaust gases [4,5,10]. As a result, the inert gas with a high purity can be separated from the steam-carbon dioxide mixture. The phenomenon of direct-condensation heat transfer is primarily characterized by the transport of heat and mass through a moving vapour-liquid interface. Accurate predictions of the properties of DCC, particularly the heat and mass transfer phenomena near the vapour-liquid interface, are crucial for upgrades and designs. Literature survey shows that this problem is not sufficiently understood and described [11–16]. This is particularly the case for DCC at sub-atmospheric pressure, see Lo Frano et al. [17]. Condensation of vapour on a spray of drops is an even more complicated process. Drop size distribution, drop velocity, and condensation on droplets should be all investigated in detail in order to characterize it. A jet coming out of the nozzle dissipates and breaks up into various-sized drops. Condensation of vapour on the drops occurs when saturated vapour comes into contact with subcooled drops (their temperature is lower than the

* Corresponding author.
E-mail address: dariusz.mikielewicz@pg.edu.p (D. Mikielewicz).

https://doi.org/10.1016/j.ijheatmasstransfer.2023.124576
Received 7 April 2023; Received in revised form 19 July 2023; Accepted 4 August 2023
Available online 19 August 2023

Nomenclature

a	thermal diffusivity, m^2/s,
c_p	specific heat, J/(kg K)
C	constant
g	gravitational acceleration, m/s^2
h_m	mass transfer coefficient,
$h_{m,g}$	convection heat transfer coefficient, W/m^2K
K_t	loss coefficient
Le	Lewis number
l_m	distance between the centres of neighbouring droplets
m	mass flow rate, kg/s
$\dot{m}_v$	mass flow rate of condensation of vapour on the droplet surface, kg/s
N	total number of droplet
n_x	number of droplets being within distance x
p	pressure, N/m^2
q	heat flux, W/m^2
R	individual gas constant, kJ/kgK
Re	Reynolds number
Sh	Sherwood number
t	time, s
T	temperature, °C
T_d	Temperature of droplet, °C
T_m	Temperature of mixture of steam, °C
We	Weber number
u	velocity in the x-direction, m/s
x	coordinate along the flow measured from throat outlet
x_0	thermal entry (development length, m)
z	ratio of droplet velocity to mixture velocity

Greek Symbols

α	local heat transfer coefficient, $W/(m^2 K)$
δ	liquid film thickness, m
μ	dynamic viscosity, kg/(m s)
ν	kinematic viscosity, m^2/s
ρ	density, kg/m^3
σ	surface tension, N/m
τ	shear stress, N/m^2
ω	mass fraction
κ	the ratio of specific heat at constant pressure to specific heat at constant volume

Subscripts

c	condensation
l	liquid,
0	initial parameter (at the slit outlet)
v	vapour
t	turbulent
x	axial component
w	wall

Superscript

+	dimensionless value

Acronyms

DCC	direct contact condensation
SEC	spray ejector condenser

saturation temperature of the vapour at the given pressure). Instead of the drop size distribution that occurs in the spray, Brown [18] applied mean diameters (arithmetic mean diameter for the trajectory of drops and Sauter mean diameter for the heat transfer rate) in his analysis of the process. Heat transfer coefficients up to 27,200 W m^{-2} K^{-1} have been achieved in his experimental research of steam condensation on a spray of subcooled water drops (dia. 125–520 μm), suggesting the high efficiency of this type of condensation, providing a further incentive to the present study. A one parameter drop size distribution function and the volume mean diameter were utilized in the analysis of Isachenko et al. [19]. Comparing the experimental and theoretical results, they have found that the obtained rate of the process is larger than that theoretically expected [20]. Madejski et al. [21] concluded that their review of the numerical investigation shows that various types of direct contact condensation modelling approaches are still developing because of the immense diversity and complexity of the phenomenon.

In this paper, an analytical approach of DCC in a SEC in the presence of inert gas (CO_2) has been postulated to study the phenomenon. The model is based on consideration of the twofold influence on the process, namely due to the convective heat transfer of the mixture of steam and CO_2 and the mass flow due to difference in concentration of vapour on interface of droplets. Such analytical model allows to analyse the influence of various parameters on the DCC process, which subsequently develops knowledge on better design procedures of SEC. Moreover, effect of breakup of jets on droplets is investigated and best estimate for droplet diameter has been obtained. Also, impact of initial velocity of droplet and mixture of steam and inert gas on temperature of droplet and mixture of gases as well as the effect of diameter of droplet and

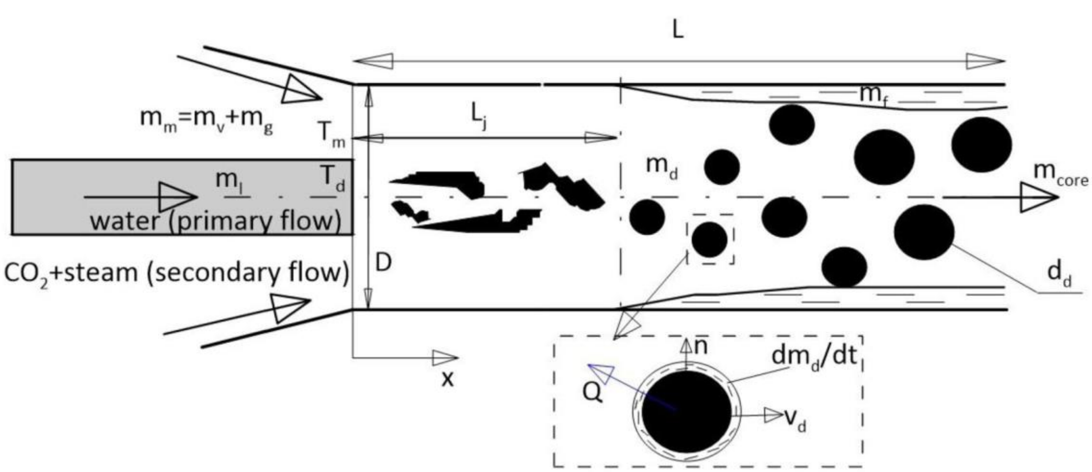

Fig. 1. Schematic of mixing chamber with multi- nozzles.

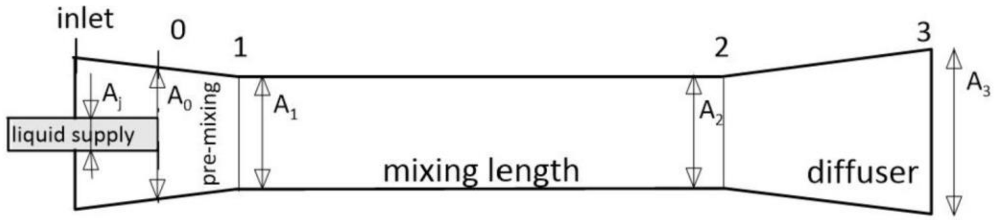

Fig. 2. General outlay of the ejector.

geometry of throat has been examined. SEC is a combination of an ejector providing pressure lift and a condenser allowing for steam-gas mixture condensation. The flow of steam-gas mixture is of subsonic character. Such condensers are rarely used in power plants in spite of the fact that they have many advantages as they can be smaller, cheaper, and have a simpler construction than the surface, shell and tube condensers. When a supercritical flow of such a mixture of steam and gas and cooling water is considered, a shock wave is formed, rendering condensation of the steam under conditions of thermodynamic non-equilibrium. Such condensation can arise without the cooling water. This kind of modelling with CFD is pretty common in literature [22,23], but is not a topic of the present study.

The purpose of this paper is to develop analytical model of SEC for the case when a subcritical flow is formed from a mixture of steam and gas and cooling water. Such a model allows for a wide discussion of parameters affecting process of condensation in SEC and ability of application such condenser in power plants, which in a perspective can be competitive to existing power plant condensers, especially in the view of the fact that separation of the carbon dioxide can be an added value to the condensation process.

2. Physical ejector model and its mathematical description

The theoretical analysis in the paper concerns the issue of DCC of vapour with inert gas within ejector creating a subcooled water spray. The physical situation considered is shown in Fig. 1.

In order to maximize the device efficiency a proper ejector design and analysis is required. The ejector, being the crucial component of a considered thermodynamic cycle, which in our case is a negative CO_2 emission gas power plant [4,5,10], determines the overall performance and efficiency of the condensing steam from mixture of vapour-inert gas system. For the ejector design, the study should focuses on the ejector nozzle, pre-mixing chamber, mixing section and the diffuser part. However the latter element of the device is not a subject of analysis here due to the fact that it is assumed that the complete condensation takes place in the mixing section and the diffuser acts only on the pure carbon dioxide flow to transfer it to subsequent sections of the system.

2.1. *Pre-mixing chamber*

The considered spray ejector condenser is basically a converging-single nozzle with the condensation in mixing section inside combined with diffuser. Fig. 2 demonstrates the division of the ejector into elementary control volumes from the inlet up to the exit. Alternatively a cyclone separator of droplets can be implemented instead of the diffuser.

It is assumed that the inlet properties of the fluids, which are supplied at a state denoted as "inlet" in Fig. 2, are all known. At that location the liquid jets have a subscript "*l*" whereas the mixture of vapour and non-condensable is denoted as "*g*". In order to determine the properties at state "0" the procedure of reduction of inlet parameters due to change of flow geometry and friction is required. Before premixing section (state 0), the liquid jet inside the nozzle and a mixture of gases (around the nozzle) are flowing as single phase fluids. It ought to be borne in mind that the mixture of gases flowing with the velocity higher than 0.3 Ma number should be treated as a flow of compressible fluid. In the paper non-compressible fluids are considered. Presented model is devoted to the case when in the mixing length there is a subcritical flow of the mixture of steam and inert gas with cold liquid droplets. Their velocities are below Mach number less than 0.3. Such parameters are also common in traditional condensers as the heat transfer occurs at moderate velocities of vapour not exceeding 40 m/s.

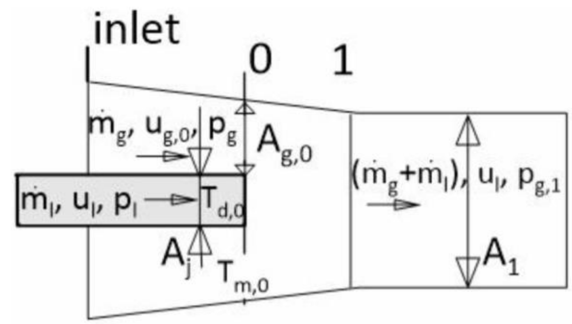

Fig. 3. Terms present in the analysis of the state "0″ and "1".

Of our subsequent interest is determination of the pressure and mass flow rate of the steam-inert gas mixture at state "1″. That location is the starting point of steam condensation process. For this purpose, the conservation equations of mass, momentum and energy have been applied in the analysis. In the view of solving the arising equations some thermodynamic relations such as Clausius-Clapeyron equation, ideal gas equation etc. are applied.

In order to calculate, for a particular ejector design, the suction mass, m_g and the pressure at the beginning of the mixing zone, it is necessary to know the equations resulting from the flow in the inlet zone resulting from mass, energy and momentum conservation equations for gas mixture. The continuity equation between locations denoted by indices "inlet" and "0″ from Fig. 3 yields:

$$\dot{m}_g = u_{gin}\rho_g A_{gin} = u_{g0}\rho_g\left(A_0 - A_j\right) \tag{1}$$

Bernoulli equation for real gases (with losses) can replace the momentum equation in the course of evaluation of the state "0″, which is different with respect to state at "inlet" due to the fact that there is geometry of the flow change. The equation yields:

$$p_{g,in} + \frac{1}{2}\cdot\rho_{g,0}u_{g,in}^2 = p_{g,0} + \frac{1}{2}\cdot\rho_{g,0}u_{g,0}^2 + \Delta p_{loss,1} \tag{2}$$

The pressure drop due to losses can be evaluated from the classical expression for the pressure losses [24]:

$$\Delta p_{loss,1} = K_m\frac{\rho_{g,0}\ u_{g,0}^2}{2} \tag{3}$$

There are no information about evaluation of K_m in literature. For the sake of present calculations it has been assumed as K_m=0.0015. As will be seen later the results of calculation agree well with the experiment.

Suction pressure $p_{g,1}$ of mixed gases caused by liquid jet can be determined from the balance of momentum between pre mixing section and entrance to the mixing section, that means between states 0 and 1. Precise values of mass flow rates of steam-carbon dioxide mixture and motive fluid mass flow rate together with respective temperatures are required to determine the pressure at the beginning of condensation process, namely location 1. Transition from location 0 to location 1 can be determined from the momentum balance equation of the mixture:

$$p_{g,0}A_{g,0} + \dot{m}_g u_{g,0} + p_l A_j + \dot{m}_l u_l = p_{g,1}A_1 + (\dot{m}_g + \dot{m}_l)u_l \tag{4}$$

Eq. (4) represents forces due to acting pressures on suitable areas of cross sections and momentum due to mass flow rate crossing boundary of considered control volume. The model is 1D and for simplicity the frictional losses are neglected. Such approach is common in literature for relatively small distances.

Determination of pressure in locations 0 and 1 can be accomplished when we assume values of inlet velocity of motive liquid and steam-gas mixture, i.e. u_l and u_g. Then the respective mass flow rates can be determined. Due to mixing after location 1 the total mass flow rate has velocity u_l stemming from (4).

$$\dot{m}_g = u_g \rho_g (A_0 - A_j) \tag{5}$$

In the subsequent analysis it is assumed that $\dot{m}_{g,0} = \dot{m}_{g,1} = \dot{m}_g$. We assume also that the liquid velocity will not change over that distance, u_l value is assumed for the entire flow. Following re-arrangements, the pressure after pre-mixing is obtained:

$$p_{g,1} = p_{g,0}a + p_l b - \frac{\dot{m}_g (u_l - u_g)}{A_1} \tag{6}$$

In (6) two terms related to surface area ratios are introduced, namely $a = \frac{A_{g0}}{A_1}$ and $b = \frac{A_j}{A_1}$.

From the Eqs. (1)–(3) we can determine:

$$p_{gin} - p_{g0} = \frac{1}{2}\rho_g u_{g0}^2 (1 + K_m) - \frac{1}{2}\rho_g u_{gin}^2 \tag{7}$$

Substituting the relation for mass flow of gas mixture into (7) we obtain the expression:

$$p_{gin} - p_{g0} = \frac{1}{2}\frac{\dot{m}_g^2}{\rho_g A_0}\left(1 + K_m - \frac{A_0}{A_{in}}\right) \tag{8}$$

Hence the mass flow rate of steam-inert gas mixture reads:

$$\dot{m}_g = A_0 \sqrt{\frac{2(p_{gin} - p_{g,0})\rho_g A_0}{1 + K_m - \frac{A_0}{A_{in}}}} \tag{9}$$

The pressure at location 1 can be determined from the expression (6).

At the location 0, we determined the mass flow rate of the mixture which subsequently will take place in the condensation process and the pressure at location 1, described by Eq. (6).

Conditions leading to state 2 can be found by a marching procedure outlined in the next section. In order to determine the properties at state 2 after an increment distance dx, the conservation equations and thermodynamic relations are applied. The aforementioned equations are applied successively for every given distance until the exit of the nozzle is reached.

2.2. Mixing section

2.2.1. Determination of state 2

The cylindrically-shaped region of the ejector with a constant-area is the mixing section. It is where the primary and secondary fluids start to interact. Then a fully mixed flow travels towards the inlet of the diffuser. Having a trial value of mass stream of vapour gas, we can determine molar concentration of vapour in the mixing chamber. This allows finding a partial pressure of vapour and gas. Partial pressure of vapour permits to evaluate temperature of saturation from which varies from location 1 to location 2. The above initial value allows to proceed calculations forward to subsequent values of coordinate x.

In order to get the values in state 2 conservation equations for mass, energy and momentum were applied together for the adiabatic process. The details of the terms taking place in the analysis have been provided in Fig. 4.

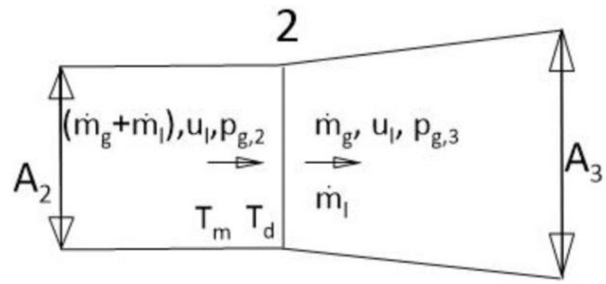

Fig. 4. Terms taking place in the analysis of state "2″.

A cold liquid stream creating the jet has the inlet mass flowrate m_l, temperature, $T_{l,0}$, velocity, $u_{l,0}$, and flows along the ejector driving a vapour-gas stream having the mass flow rate $m_{m,0}$, velocity $v_{g,0}$ and temperature $T_g > T_{sat}$ – where the saturation temperature on interface depends on gas concentration in the gas-vapour mixture. Coordinates are chosen in such a way that the y axis is directed from the interface outward the liquid spray, and its origin is always located on the inlet cross section of the entrance of sub cooled liquid, whereas the x axis origin is located at the inlet cross section. The following assumptions and simplifications are made in the analysis:

1. Parameters at the inlet (state denoted in Fig. 2 as "inlet") to SEC are known, i.e. sub-cooled motive liquid mass flow rate is $m_{l,0}$, its temperature $T_{l,0}$, and velocity $u = u_{l,0}$. Initial mass flow rate of steam and inert gas mixture $m_{g,0}$ is also known. Mixture temperature at inlet is $T_{m,0}$ and pressure p_g;
2. Breakdown of liquid jets into droplets occurs after some distance from the injection of liquid to mixing chamber. At the beginning of calculations this distance is assumed zero;
3. Diameter of droplets after breakdown is d_d;
4. Both phases are flowing under steady-state conditions. The amount of droplets in the mixing throat is constant for a given flow rate of liquid;
5. Physical properties of the liquid droplets and vapour-gas mixture are constant;
6. Thermal diffusivity of liquid layer a is constant. The distribution of temperature in liquid spray and gas mixture due to vapour condensation on interface is described by mass and energy conservation equations.

2.2.2. Effect of breakup of droplets

Firstly, it is assumed that there will be an extra length of jet prior to the liquid breakup into droplets, followed by the breakup. The liquid jet breaks into droplets under the influence of waves formed on the surface of the jet, due to instability. These waves cause a loss of stability and the formation of primary droplets. The size of these droplets results from the volume of the wave on jet and depends on jet diameter and length of waves. Developed droplets feature a minimum surface energy, Jain et al. [25]. For certain outflow conditions of a liquid jet, there is an optimum wavelength whose length is greater than the jet circumference, at which the wave amplitude increases and the liquid jet bursts. The droplets so formed during primary atomization further undergo secondary breakup resulting in much smaller droplets. Weber developed a relation for the size of secondary droplets [26]:

$$\frac{d_d}{D_j} = 1.436\left(1 + 3\frac{We^{0.5}}{Re}\right)^{1/6} \tag{10}$$

where: $We = \frac{\rho_l u_l^2 D_j}{\sigma_l}$ – Weber number, $Re = \frac{\rho_l u_l D_j}{\mu_l}$ - Reynolds number, D_j – nozzle diameter.

The criterion for the beginning of primary droplets breakup is $We > We_{cr}$. Following Jain et al. [25] the value $We_{cr} = 12$ has been assumed.

The distance from the nozzle exit to the location where the breakdown of the jet into primary droplets is observed is named the breakup length, L_j. For turbulent liquid jets it can be calculated is [27]:

$$\frac{L_j}{D_j} = 5.0We^{0.5} \tag{11}$$

Secondary droplet breakup occurs under the influence of aerodynamic forces with account of viscous forces. Primary droplets are deformed and broken up by aerodynamic drag forces and surface tension forces. The maximum secondary droplets size can be determined from the definition of Weber number relationship with We_{cr}=12.

$$D_{max} = \frac{\sigma We_{cr}}{\rho_g (u_l - u_g)^2} \tag{12}$$

The average droplet size can be assumed as [28]:

$$D_m \approx \frac{D_{max}}{2} \tag{13}$$

A more accurate value could be calculated from the droplet size distribution spectrum [29]. The mean drop diameter, d_m, can be approximately predicted using Nukijama-Tanazawa equation:

$$d_m = \frac{1.83\theta\sigma}{(V_g - V_l)\rho_l} \tag{14}$$

The most probable droplet diameter is equal to half of the mean diameter $d_{mp} = d_m/2$ which can be found from the size distribution:

$$P(d_d) = 4\frac{d_d}{d_m^2}e^{-2\left(\frac{d_d}{d_m}\right)^2} \tag{15}$$

In the present work we would like to show the underlying physics of the DCC model so Eq. (13) was used in calculations.

2.2.3. Liquid droplet flow

Let us now consider the averaged mass and force balance equations for the liquid drops. Stream of drops leaving the supplying water nozzles has the mass flow rate the same as the stream of liquid on inlet channel, so the mass of droplets is the same as the mass of liquid within the length of mixing chamber:

$$\dot{m}_d = \frac{\pi\, d_d^3 \rho_l}{6} n = \dot{m}_{l0} = \frac{\pi\, D^2}{4}\ (L - L_j)\ \rho_l \tag{16}$$

Where: n - total number of droplets in one jet exchanging mass and heat in mixing chamber, L – length of the mixing section.

$n = \frac{3}{2}\left(\frac{D}{d_d}\right)^2 \frac{(L-L_j)}{d_d}$ denotes total number of droplets in mixing zone

n_x - number of droplets in one jet being within distance x.

$$n_x = \frac{x}{(L - L_j)} \times n$$

The motion of the liquid due to condensation of droplets in the x-direction is described by the force balance of inertia and drag forces in line with the equation:

$$\frac{d(m_d u_d)}{dt} = \dot{m}_d \frac{d(u_d(x))}{dx} u_d(x) + \frac{d(m_d)}{dt} u_d = -\frac{1}{2}\rho_m C_D (u_d - \overline{u}_m)^2 \frac{\pi\, \overline{d_d^2}}{4} \tag{17}$$

where: $\frac{dm_d}{dt} = \dot{m}_v$ denotes the mass flow rate of droplets with condensation of vapour on the droplet surface, which will be determined in the later.

Rearranging (17) we get:

$$\frac{du_d}{dx} + \frac{1}{8}\frac{\rho_m C_D (u_d - \overline{u}_m)^{2\frac{\pi\, \overline{d_d^2}}{4}}}{m_d u_d} + \frac{\dot{m}_v}{m_d} = 0 \tag{18}$$

Following separation of variables in (18) and integrating the resulting relation we obtain the expression for the function linking the ratio of velocities, $z = \frac{u_d}{u_m}$, in function of the distance x:

$$\int \frac{z\, dz}{z^2 - 2\left(1 - \frac{4\dot{m}_v}{\rho_m \pi C_D u_m\, \overline{d_d^2}}\right) z + 1} = -\frac{1}{8}\frac{\rho_m C_D \pi\, \overline{d_d^2}}{m_d} x + C \tag{19}$$

In general, the integral on the left hand side of (18) can be presented in a closed form:

for $(b^2 - 4) > 0$

$$\int \frac{z\, dz}{z^2 + bz + 1} = \frac{1}{2}ln(z^2 + bz + 1) - \frac{1}{2}\frac{b}{\sqrt{b^2 - 4}} ln\left(\frac{2z + b - \sqrt{b^2 - 4}}{2z + b + \sqrt{b^2 - 4}}\right) \tag{20}$$

for $4 - b^2 > 0$

$$\int \frac{z\, dz}{z^2 - bz + 1} = -\frac{b}{\sqrt{4 - b^2}} arc\ tg\left(\frac{2z + b}{\sqrt{4 - b^2}}\right) \tag{21}$$

where: $b = -2\left(1 - \frac{4\dot{m}_v}{\rho_m C_D \pi\, \overline{d_d^2}}\right)$.

Exact solution of Eqs. (20) and (21) can be sought with the following boundary conditions:

$$\text{for } x = 0\ u_d = u_{0d} \text{ and } z = 1 \tag{22}$$

The solution can be obtained in the form:

$$x(z) = \frac{(A(z) - A(1))}{e} \tag{23}$$

where $e = 3\frac{\rho_m}{4\rho_l}d_d$, $\rho_m = \frac{1}{\frac{x}{\rho_v} + \frac{1-x}{\rho_{in}}}$ and $\rho_v = \frac{p_s}{\frac{R_u}{M_s}T_{m0}}$.

We can formulate a simple approximate relation, corresponding motion of droplet in stagnant environment, which can be serving as a first iteration of the problem in numerical procedure allowing to solve (18) as:

$$u_d = u_{d0} exp\left(-\frac{3\rho_m C_D}{4 d_d \rho_l} x\right) \tag{24}$$

2.2.4. Condensation of vapour on subcooled droplet stream

Mass balance on the droplet's interface gives the relation:

$$\frac{dm_d}{dt} = \rho_v w_v \pi d_d^2 \tag{26}$$

Where: $\dot{m}_v = \rho_v w_v$ - mass flux of condensing vapour, which will be analysed later.

The mass flux of condensing vapour can be determined taking advantage of the Fick's Law:

$$\rho_v w_v = -D_v \frac{d\rho_v}{dn} \tag{27}$$

Introducing Eq. (27) to (26) returns the expression for the rate of change of droplets in function of mass fractions in the vicinity of the droplet and freestream concentration:

$$\frac{dm_d}{dt} = -\rho_v D_v \frac{d\omega}{dn}\pi d_d^2 = -\rho_v D_v \frac{\omega_d - \omega_\infty}{d_d}\pi d_d^2 \tag{28}$$

Where: $\omega = \rho_v/\rho_m$ yields the mass fraction, whereas $\omega_d - \omega_\infty$ is a difference in concentrations between the vicinity of the droplet and the freestream concentration, which lead to the differences in partial pressures between these locations, and subsequently promoting the condensation process.

After rearranging (28) and introducing the definition of Sherwood number Sh the following form of the rate of mass droplets is obtained:

$$\frac{dm_d}{dt} = \pi\rho_v \frac{d_d^2}{l_m} D_v(\omega_\infty - \omega_d)Sh = S \tag{29}$$

Where l_m represents the distance between the centres of neighbouring droplets, $l_m = \frac{d_d}{2}\left(\frac{D_1}{D_l}\right)^2$.

Following the introduction of the chain rule of differentiation, i.e. $\frac{d}{dt} = \left(\frac{d}{dx}\right)\left(\frac{dx}{dt}\right) = \left(\frac{d}{dx}\right)u_d(x)$, the change of the mass of droplets along the distance of the mixing chamber is obtained:

$$\frac{dm_d}{dx} = \frac{\pi\rho_v d_d D_v(\omega_\infty - \omega_d)}{u_d(x)} Sh = \frac{S}{u_d(x)} \tag{30}$$

Where S is defined by Eq. (29).

In our subsequent calculations we will also utilise the following relations for the longitudinal rate of mass of droplets:

$$\frac{d\dot{m}_d}{dx} = \frac{d\left(\frac{dm_d}{dt}\right)}{dx} = \frac{dS}{dx} \tag{31}$$

Where the definition of the Sherwood number Sh denotes the dimensionless concentration gradient at the droplet surface:

$$Sh = h_m \frac{d_d}{D_v} \tag{32}$$

The Sherwood number can be expressed from established empirical correlations. In the present study the Ranz-Marshall correlation has been used, which takes into account the difference in velocity between the droplet and the surrounding gas, when information about the Reynolds number and the Schmidt number are known [25]:

$$Sh = 2 + 0.6Re^{0.5}Sc^{0.33} \tag{33}$$

Where the droplet Reynolds number yields:

$$Re = \frac{d_d(u_d - u_m)}{v_l} \tag{34}$$

And the Schmidt number reads:

$$Sc = \frac{\nu}{D_v} \tag{35}$$

In (32) h_m denotes the mass transfer coefficient, which can be approximately evaluated through the Lewis number definition, $Le = \frac{a}{D_v}$, in relation to the convection heat transfer coefficient $h_{m,g}$:

$$h_m = \frac{h_{m,g}}{\rho_{v,g} c_{p,vg}} \tag{36}$$

Bearing in mind that the mass flow rate of vapour and gas is known we can determine the molar concentration of vapour and inert gas at the arbitrary throat location in function of the flow rate of mixture of gases. Concentration of inert gas yields:

$$n(x) = \frac{\frac{\dot{m}_v(x)}{M_v}}{\frac{\dot{m}_v(x)}{M_v} + \frac{\dot{m}_g}{M_g}} \tag{37}$$

Where the amount of droplets condensing from the flow can be evaluated from the mass continuity:

$$\dot{m}_v(x) = \dot{m}_{v0} - n_x \int_0^x \frac{d\dot{m}_d}{dx} dx = \dot{m}_{v0} - n_x S\, x = \dot{m}_{v0} - nS\, \frac{x}{(L - L_j)} \tag{38}$$

This allows to find the partial pressure of water vapour and inert gas:

$$p_v(x) = \frac{\frac{\dot{m}_v(x)}{M_v}}{\frac{\dot{m}_v(x)}{M_v} + \frac{\dot{m}_g}{M_g}} p = n(x)\, p \tag{39}$$

Where, p denotes the total pressure. Partial pressure of gas fraction results from the Dalton's Law:

$$p_g = p - p_v \tag{40}$$

The mass fraction difference in concentrations between the vicinity of the droplet and the freestream concentration $\omega_d - \omega_\infty$, can be calculated using the equation of state for ideal gas:

$$p_v = \rho_v R_v T_m \tag{41}$$

When a non-condensable gas is present in the condensation space, both heat and mass transfer must be analysed. There exists a boundary layer in which the partial pressure of the condensable vapour p_v decreases from the constant concentration in the free stream to the value p_{sat}, where the vapour is condensing to a liquid. The condensing liquid must diffuse through this boundary layer to the liquid-vapour interface. The partial pressure of the non-condensable gas p_g on the other hand increases from the pressure in the core p_{an} to the value p_{sat} at the liquid -vapour interface. At any point in space and time the summation of the partial pressures of this mixture must equal the total pressure, $p=p_v+p_g$ (Dalton's Law).

Decreasing partial pressure of vapour in the end approaches the pressure at the interface and its corresponding saturation temperature $T_{sat}(p_v)$.

The pressure of condensing vapour above the liquid droplet can be determined from Clausius -Clapeyron equation:

$$\frac{dp_v}{dT_d} = \frac{h_{lv}}{(v_v - v_l)T_d} \tag{42}$$

Assuming that specific volume of vapour is significantly greater than that of liquid, $v_{v>>}v_l$ and taking advantage of the equation of state we get:

$$\frac{dp_v}{dT_d} = \frac{h_{lv}p_v}{R_v T_d^2} \tag{43}$$

Integrating (43) we obtain the distribution of vapour pressure:

$$p_v = C\, exp\left(-\frac{h_{lv}}{R_v\, T_d}\right) \tag{44}$$

where C is a constant dependant on the fluid, h_{lv} – latent heat of condensation dependant on the fluid.

In effect the total mass flow rate of droplets is:

$$\dot{m}_l(x) = \dot{m}_{l0} + n_x \int_0^x \frac{d(\dot{m}_d(x))}{dx} dx \tag{45}$$

Taking advantage of (28) and (31) we can find approximate values of liquid mass flow rate:

$$\dot{m}_l(x) = \dot{m}_{l0} + n_x\, S = \dot{m}_{l0} + \frac{x\, n}{(L - L_j)}\, S \tag{46}$$

The length required for a particular stream of droplets to completely condensate from the mixture of gases can be determined approximately from the mass balance equation, assuming that steam occupies the total volume of the mixing chamber:

$$l_{end} = \frac{4nS}{\pi D^2 \rho_v} \tag{47}$$

2.2.5. Heat balance of droplet stream

The energy balance can be used to determine temperature of a stream of droplets. That means that on one side the change of enthalpy of a stream of droplets and heat obtained due to condensation are forming the rate of heat transferred to the mixture of vapour and non-condensable gas:

$$\frac{d}{dx}(c_{pl}\dot{m}_d T_d) + \frac{h_{lv}}{dx} d\dot{m} = \frac{d\dot{Q}}{dx} \tag{48}$$

That rate of heat is subsequently transferred by convection to the interface of the droplet surface:

$$\frac{d\dot{Q}}{dx} = \pi d_d^2 \frac{n}{(L-L_j)} h_{mg}(T_m - T_d) \tag{49}$$

where h_{mg} is a convective heat transfer coefficient, whereas $\frac{d\dot{m}_d}{dx}$ is described by (28).

Introducing (29) and (49) to (48) and rearranging the longitudinal droplet temperature gradient is obtained:

$$\frac{dT_d}{dx} = -\left(\frac{T_d}{\dot{m}_d} + \frac{h_{lv}}{c_{pl}\dot{m}_d}\right)\frac{d\dot{m}}{dx} + \frac{\pi d_d^2 \frac{n}{(L-L_j)} h_{mg}(T_m - T_d)}{c_{pl}\dot{m}_d} \tag{50}$$

Eq. (50) is a first order ordinary linear differential equation with variable coefficients.

To find the solution for temperature T_d the knowledge of temperature of flowing vapour-gas mixture T_m is required. For this purpose, balance of energy for the mixture of vapour will be developed.

2.2.6. Balance of mass and heat for vapour-gas mixture

Balance of mass for the mixture of vapour and gas rate yields:

$$\dot{m}_m(x) = \dot{m}_{m0} - \int_0^l \frac{d(\dot{m}_d(x))}{dx} dx \tag{51}$$

Incorporating into the Eq. (51) the Eq. (31) the following expression is obtained:

$$\dot{m}_m(x) = \dot{m}_{m0} - n_x \int_0^x \frac{d(\dot{m}_d(x))}{dx} dx = \dot{m}_{m0} - \frac{x\ n}{(L-L_j)} S \tag{52}$$

Mass flow rate of mixture vapour-gas allows calculating velocity distribution of mixture, assuming the cross section area of the flow is not changing:

$$u_m(x) = u_{m0} \frac{\dot{m}_m(x)}{\dot{m}_{m0}} \tag{53}$$

Temperature of flowing vapour-gas mixture can be determined from the balance of heat for the mixture of vapour-gas flow:

$$-c_{pm} d(\dot{m}_m T_m) = d\dot{Q} = \frac{h_m \pi d_d^2 n}{(L-L_j)}(T_m - T_d)dx \tag{54}$$

or in the form when the left hand side of Eq. (54) is expanded:

$$-c_{pm}(\dot{m}_m dT_m + d\dot{m}_m T_m) = \frac{h_m \pi d_d^2 n}{(L-L_j)}(T_m - T_d)dx \tag{55}$$

Eq. (54) describes the mechanism of condensation of the steam-gas mixture. Left hand side describes the heat removed from the mixture, whereas the right hand side the transfer of that heat to the droplets.

Eq. (55) can be rearranged to provide the equation for temperature gradient for the mixture of gases:

$$\frac{dT_m}{dx} = -\frac{T_m}{\dot{m}_m}\frac{d\dot{m}}{dx} - \frac{h_m \pi d_d^2 n}{(L-L_j)\ \dot{m}_m c_{pm}}(T_m - T_d) \tag{56}$$

As can be seen we obtained a first order ordinary linear differential equation with variable coefficients.

Eqs. (50) and (56) can be solved numerically. To find approximate solution we subtract eq. (50) from (56) obtaining:

$$\frac{d(T_m - T_d)}{dx} + \frac{h_m \pi d_d^2 n}{(L-L_j)}\left(\frac{1}{\dot{m}_m c_{pm}} + \frac{1}{\dot{m}_l c_{pl}}\right) = \left(\frac{T_d}{\dot{m}_m} - \frac{T_m}{\dot{m}_d} + \frac{h_{lv}}{\dot{m}_m c_{pm}}\right)\frac{d\dot{m}}{dx} \tag{57}$$

In line with Eq. (30) $\frac{d\dot{m}}{dx} = \frac{nS}{(L-L_j)}$. Assuming that coefficients in Eq. (57) are not changing too much and are approximately constant we can find the solution for the difference of temperatures $(T_m - T_d)$ assuming the following initial conditions:

$$\text{For} x = 0 \rightarrow T_m = T_{m0} \text{and} T_d = T_{d0} \tag{58}$$

The solution to Eq. (57) yields:

$$(T_m - T_d) = \frac{B\ n\ S}{(L-L_j)\ f}(1 - exp(fx)) + (T_{m0} - T_{d0})exp(-f) \tag{59}$$

where:

$$B = \left(\frac{T_d}{\dot{m}_m} - \frac{T_m}{\dot{m}_d} + \frac{h_{lv}}{\dot{m}_m c_{pm}}\right),\quad f = \frac{h_m \pi d_d^2 n}{(L-L_j)}\left(\frac{1}{\dot{m}_m c_{pm}} + \frac{1}{\dot{m}_l c_{pl}}\right).$$

Having the above difference of streams temperatures, we can determine temperature of the vapour- inert gas mixture as well as that of the cold water on which vapour is condensing.

Introducing (56) to (59) we obtain the temperature gradient of vapour-inert gas mixture:

$$\frac{dT_m}{dx} = -\frac{h_m \pi d_d^2 n(T_m - T_d)}{(L-L_j)\ \dot{m}_m c_{pm}} - \frac{T_m}{\dot{m}_m}\frac{d\dot{m}}{dx} = \frac{K(T_m - T_d)}{\dot{m}_m c_{pm}} - \frac{T_m}{\dot{m}_m}\frac{nS}{(L-L_j)} \tag{60}$$

Where $K = -\frac{h_m \pi d_d^2 n}{(L-L_j)\ \dot{m}_m c_{pm}}$

Integrating eq. (60) with initial conditions, for $x = 0$ $T_m = T_{m0}$ the temperature of the mixture is obtained:

$$T_m = -\frac{T_m}{\dot{m}_m}\frac{nS}{(L-L_j)} - \frac{h_m \pi d_d^2 n}{(L-L_j)\ \dot{m}_m c_{pm}}\left[\frac{-(T_m - T_d)}{f}exp(fx) + \frac{B\ n\ S}{(L-L_j)\ f}\left(x + \frac{exp(-fx)}{f}\right)\right] + C_1 \tag{61}$$

Where:

$$C_1 = T_{m0} + \frac{h_m \pi d_d^2 n}{(L-L_j)\ \dot{m}_m c_{pm}}\left[\frac{-(T_m - T_d)}{f} + \frac{B\ n\ S}{(L-L_j)\ f}\right] \tag{62}$$

Having determined temperature T_m and temperature difference between streams we can find temperature of droplets surface T_d as:

$$T_d = -(T_m - T_d) + T_m \tag{63}$$

Eqs. (59) and (61) have terms containing expression S responsible for process of condensation.

To see the effect of condensation, for comparison $S = 0$ can be assumed in Eqs. (59) and (61), which means the lack of condensation on droplets. In such case we can also get approximate equations describing the problem and by applying a similar procedure we determine the difference of streams of temperatures and then temperatures of the streams themselves.

Heat obtained from the mixture of vapour and inert gas yields:

$$d\dot{Q} = -c_{pm}\dot{m}_m dT_m = \frac{h_m \pi d_d^2 n}{(L-L_j)}(T_m - T_d)dx \tag{64}$$

Heat transferred to the droplet surface:

$$d\dot{Q} = -c_{pd}\dot{m}_d dT_d = \frac{h_m \pi d_d^2 n}{(L-L_j)}(T_m - T_d)dx \tag{65}$$

Determining the difference between the two of them we obtain:

$$d(T_m - T_d) = -\left(\frac{1}{\dot{m}_m c_{pm}} + \frac{1}{\dot{m}_m c_{pm}}\right)\frac{h_m \pi d_d^2 n}{(L-L_j)}(T_m - T_d)dx \tag{66}$$

Solution of (66) yields:

$$T_m - T_d = (T_{m0} - T_{d0})exp(-fx) \tag{67}$$

Where: $f = -\left(\frac{1}{\dot{m}_m c_{pm}} + \frac{1}{\dot{m}_l c_{pl}}\right) \frac{h_m \pi d_d^2 n}{(L - L_j)}$.

From (67) we can determine temperature of the mixture of gases and water flow:

$$dT_m = -\frac{h_m \pi d_d^2 n}{(L - L_j)\ \dot{m}_m c_{pm}} (T_{m0} - T_{d0}) exp(-fx) dx \tag{68}$$

Integration of eq. (68) leads to determination of the mixture of gases and droplet temperatures, respectively:

$$T_m = T_{m0} - \frac{h_m \pi d_d^2 n}{(L - L_j)\ \dot{m}_m c_{pm}} (1 - exp(-fx)) \tag{69}$$

$$T_d = T_m - (T_{m0} - T_{d0}) exp(-fx) \tag{70}$$

The process of condensation stops when temperature of the drops will reach temperature of saturation.

2.2.7. Pressure drop in mixing chamber

The pressure drop of the Venturi throat is the sum of friction and momentum terms [29]:

$$\Delta p = \frac{2 \cdot G^2}{\rho_v \cdot d} \cdot I_z + G^2 \cdot \left(\frac{\frac{x_1^2}{\rho_v}}{\varphi_1} - \frac{\frac{(1-x_1)^2}{\rho_l}}{1 - \varphi_1} \right) \Bigg|_{z=z1} - G^2 \cdot \left(\frac{\frac{x_0^2}{\rho_v}}{\varphi_0} - \frac{\frac{(1-x_0)^2}{\rho_l}}{1 - \varphi_0} \right) \Bigg|_{z=z0} \tag{71}$$

Where:

$$I_z = \int_{z=z_0}^{z=z_1} f_v \cdot x^2 \cdot \phi_v^2 dz \tag{72}$$

$$\phi_v^2 = \left(1 + C \cdot X + X^2\right) \tag{73}$$

X is the Lockhart-Martinelli parameter, defined as follows:

$$X = \frac{-2 \cdot f_l \cdot G^2 \cdot (1 - x)^2}{\rho_l \cdot d} \tag{74}$$

$$f_v = B \cdot Re_v^{-n} \tag{75}$$

$$f_l = B \cdot Re_l^{-n} \tag{76}$$

Where $B = 0.079$ and $n = 0.25$ or $B = 16$ and $n = 1$ for the turbulent and laminar flow, respectively. The value of the constant C differs depending on the flow regime associated with the vapour flow alone through the Venturi throat. In the research studies presented in the current paper only two flow regimes have been considered, namely turbulent (vapour)-turbulent (liquid) and turbulent (vapour)-viscous (liquid) two-phase flow. Accordingly, the value of the parameter C used in the calculus was 20 or 12, respectively. Following Butterworth, the general form of the void fraction correlations is introduced through the following equation [29]:

$$\varphi = \left[1 + B_B \cdot \left(\frac{1 - x}{x}\right)^{n_1} \cdot \left(\frac{\rho_v}{\rho_l}\right)^{n_2} \cdot \left(\frac{\mu_l}{\mu_v}\right)^{n_3}\right] \tag{77}$$

and φ_1 and φ_0 were computed using formula (77). In the current research studies there were set the following values of the parameters $B_B = 1$, $n_1 = 1$, $n_2 = 1$, $n_3 = 0$, corresponding to the homogenous two-phase flow regime [29]. The analytical two-phase fluid flow pressure drop was calculated using formula which is commonly known and available in the literature. In the pressure drop calculus all needed parameters such as the friction factor for vapour coming alone in the tube, the quality, the two-phase multiplier and the void fraction come from the analytical model results. The pressure drop was calculated in two ways. In the first one there were used the two-phase fluid flow parameters for the total flow in the Venturi. In the second one there were used parameters of the core of the flow. The total pressure drop and the pressure drop in the flow core should be equal. Calculating the pressure drop based on the core flow parameters requires the knowledge about the flow morphology in the core which results directly from the analytical model results presented in the paper. The core pressure drop was calculated with use of the following equation [29]:

Table 1
Calculated and input parameters.

Calculated Parameters	Input data	Value
	u_{d0}	20–100 (m/s)
u_d	ρ_m	$\frac{1}{\frac{x}{\rho_{steam}} + \frac{1-x}{\rho_{\_inert\ gas}}} \left(\frac{kg}{m^3}\right)$
	d_d	1–20 (mm)
	u_{m0}	0–45 (m/s)
	$\dot{m}_m$	$\dot{m}_{m0} - \frac{x\,n}{(L - L_j)} S \left(\frac{kg}{s}\right)$
	$\dot{m}_{m0}$	$m_{steam} + m_{inert\ gas} \left(\frac{kg}{s}\right)$
	m_{steam}	$r_{steam} \times m_g \times \frac{M_{steam}}{M_{mix}}$
u_m	$m_{inert\ gas}$	$r_{inert\ gas} \times m_g \times \frac{M_{inert\ gas}}{M_{mix}}$
	m_g	$(A_0 - A_j) \times \rho_g \times u_{m0} \left(\frac{kg}{s}\right)$
	M_{steam}	$18 \left(\frac{kg}{kmol}\right)$
	$M_{inert\ gas}$	$44 \left(\frac{kg}{kmol}\right)$
	r_{steam}	0.9
	$r_{inert\ gas}$	0.1
	ρ_v	$\frac{p_s\, M_s}{R_u T_{m0}} \left(\frac{kg}{m^3}\right)$
	l_m	$\frac{d_d}{2}\left(\frac{D_1}{D_l}\right)^2$
S	D_v	$1.5 \times 10^{-3} \left(\frac{m^2}{s}\right)$
	ω_∞	1.573
	ω_d	0.062
Sh	υ_l	$31.6 \times 10^{-6} \left(\frac{m^2}{s}\right)$
	$\dot{m}_d$	$\dot{m}_{d0} + \frac{x\,n}{(L - L_j)} S$
	h_{lv}	$2460.6 \left(\frac{kJ}{kg}\right)$
T_d	C_{pl}	$4.190 \left(\frac{kJ}{kg.K}\right)$
	n	Eq.16
	l	0.2 (m)
	h_m	$580.5 \times 10^{-6} \left(\frac{m}{s}\right)$ (Eq.36)
T_m	C_{pm}	$r_{steam} \cdot C_{pl} + r_{inert\ gas} \cdot C_{p_{inert} gas} \left(\frac{kJ}{kg.K}\right)$
	$C_{p_{inert}\ gas}$	$0.971 \left(\frac{kJ}{kg.K}\right)$

$$\Delta p = \frac{2 \cdot G_{core}^2}{\rho_v \cdot d} \cdot I_z + G_{core}^2 \cdot \left(\frac{\frac{x_1^2}{\rho_v}}{\varphi_{c,1}} - \frac{\frac{(1-x_1)^2}{\rho_l}}{1 - \varphi_{c,1}} \right) \Bigg|_{z=z1} - G_{core}^2 \cdot \left(\frac{\frac{x_0^2}{\rho_v}}{\varphi_{c,0}} - \frac{\frac{(1-x_0)^2}{\rho_l}}{1 - \varphi_{c,0}} \right) \Bigg|_{z=z0} \tag{78}$$

$$\varphi_c = \frac{-\frac{\rho_l}{\rho_v} \cdot \frac{u_l}{u_v}}{1 - \frac{\rho_l}{\rho_v} \cdot \frac{u_l}{u_v} - \frac{1}{x}} \tag{79}$$

Above equation was derived for the purpose of the core void fraction estimation. After substituting the needed parameters mentioned just above, the core pressure drop can be estimated. If the two-phase flow is fully mixed pressure drop in core flow is the same as total pressure flow in throat.

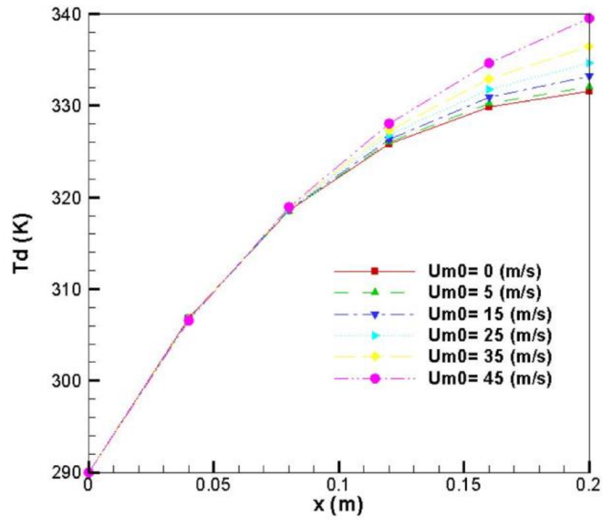

Fig. 5. Distribution of droplet temperature for different initial velocity of steam-gas mixture at Ud_0=50 m/s and diameter of droplet 1 mm.

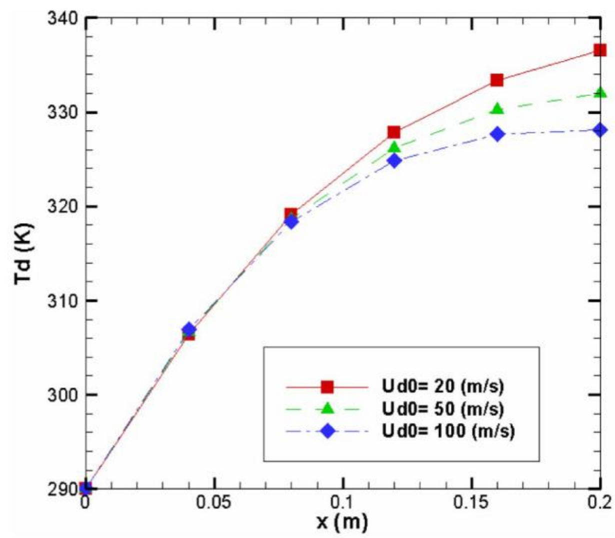

Fig. 7. Distribution of temperature of droplet for different initial velocity of droplet at Um_0=20 m/s and diameter of droplet 1 mm.

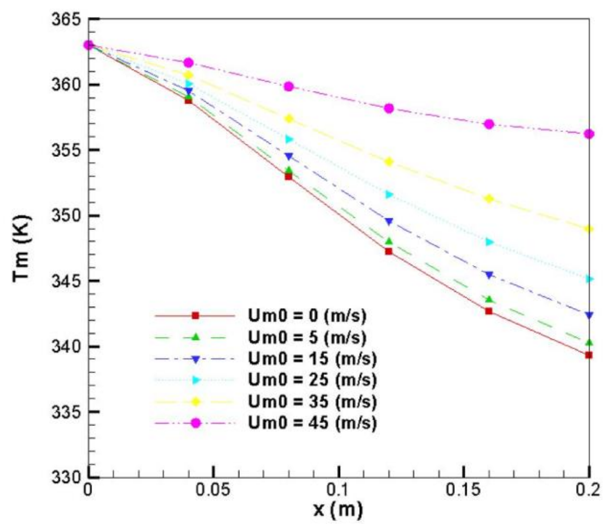

Fig. 6. Distribution of steam-gas mixture temperature for different initial mixture velocity at Ud_0=50 m/s and diameter of droplet 1 mm.

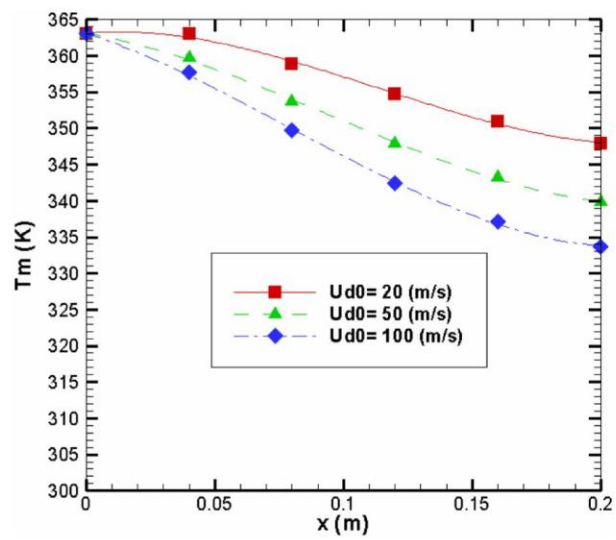

Fig. 8. Distribution of temperature of mixture of steam for different initial velocity of droplet at Um_0=20 m/s and diameter of droplet 1 mm.

3. Results and discussion

In this section, the effects of initial velocity of mixture of steam and droplets, diameter and breakup of droplets and throat diameter have been investigated with respect to the length of the process. For calculation ofu_d, S, $\dot{m}_m(x)$ and$u_m(x)$, Eqs. (24), (29), (52) and (53) have been used, respectively. Calculations have been using the MATLAB code. The MATLAB code applies an iterative solution approach in which the value of x is assumed and the T_d *and* $T_m$values are to be determined. Location x for calculation of T_d and T_m is a location along the mixing section, i.e. the location where droplets are formed after the distance L_j from the nozzle outlet. Since the solution method exploits an iterative process all other parameters will be given as inputs (Table 1) and the dependence of parameters on T_d and T_m is evaluated. The parametric study has been accomplished by varying the dependant parameters (u_d, u_m, and n), whilst keeping other as constants. The convergence of the solution has been acquired by keeping the error tolerance as 1×10^{-6}. As mentioned earlier, the length required for a particular stream of droplets to completely evaporate can be determined as $z_{end} = \dot{m}_{v0}\frac{(L-L_j)}{n\ S}$, where z_{end} is the length of condensation zone and if $z_{end} > L$, it means that $L = 0.2$ (m) is appropriate assumption. So,

$$\dot{m}_{v0} = r_{steam}.\dot{m}_{m0} \tag{80}$$

Taking the data for case study from Table 1, the value of z_{end} is greater than L, so in this study $L = 0.2$ m has been considered.

3.1. Effect of initial velocity of mixture of steam

Temperature of droplet and mixture of steam are depicted in Figs. 5 and 6, respectively. It can be seen vividly that temperature of droplet along the length of throat is faced with a rising trend, whereas temperature of mixture of steam is experiencing a decreasing trend. In addition, having studied the data from Figs 5 and 6 it can be considered that temperature of droplet at the length of throat ($x = 0.2$ m) for u_{m0} = 0, 5, 15, 25, 35 and 45 m/s is 331.55, 332.08, 333.25, 334.66, 336.50 and 339.54 K, respectively, whilst temperature of mixture of steam for mentioned u_{m0} is 339.31, 340.24, 342.40, 345.15, 348.99 and 356.21 K, respectively. So, increasing the value of u_{m0} not only results in increasing the droplets temperature, but also leads to rise in temperature of mixture of steam at the length of throat. Moreover, the lowest value for temperature of droplet and mixture of steam is when the drop is

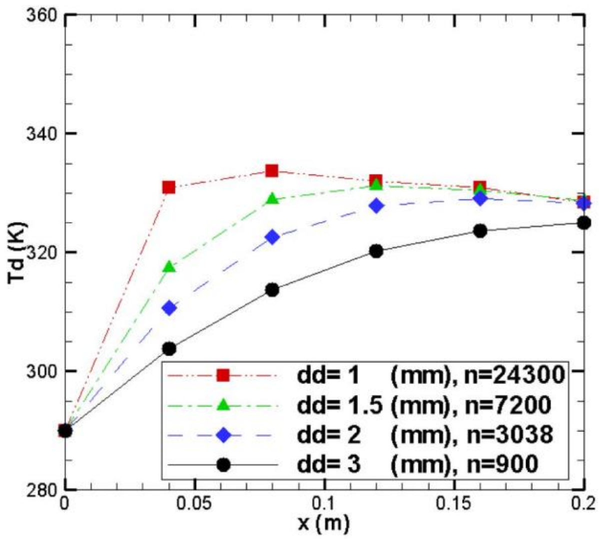

Fig. 9. Distribution of temperature of droplet for different diameter of droplet at Ud_0=50 m/s and Um_0=20 m/s and diameter of throat D_0 = 9 mm.

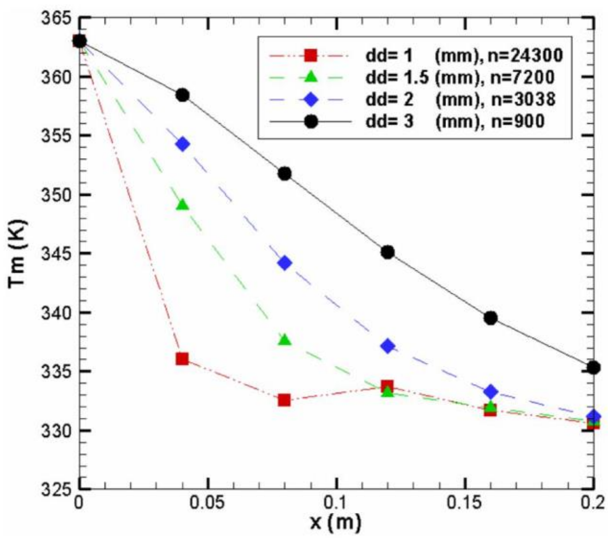

Fig. 10. Distribution of temperature of mixture of steam for different diameter of droplet at Ud_0=50 m/s and Um_0=20 m/s and diameter of throat D_0 = 9 mm.

moving in stagnant environment ($u_m(x) = 0$). In such case, there is a lack of motion of the steam-gas mixture, and the droplets feature the inertia resulting from their initial velocity from the nozzle.

3.2. Effect of initial velocity of droplet

Figs. 7 and 8 indicate the temperature of droplet and mixture of steam along the length of throat for wide range of initial velocity of droplet (20–100 m/s), respectively. Results show that temperature of droplet faces a rising trend for Ud_0 = 20, 50 and 100. In addition, increasing the value of initial velocity of droplet from 20 to 100 (m/s) causes decline the temperature of droplet at the length of throat ($x = 0.2$ m), so that its value for 20, 50 and 100 m/s is 336.56, 331.9848 and 328.11 K, respectively. On the other hand, the temperature of mixture of steam has been faced with a falling trend for mentioned initial velocity of droplet. Moreover, increasing the initial velocity of droplet from 20 to 100 m/s result in decline the temperature of mixture of steam, so that it decreases by 4% between 20 and 100 m/s at the full length of throat ($x = 0.2$ m).

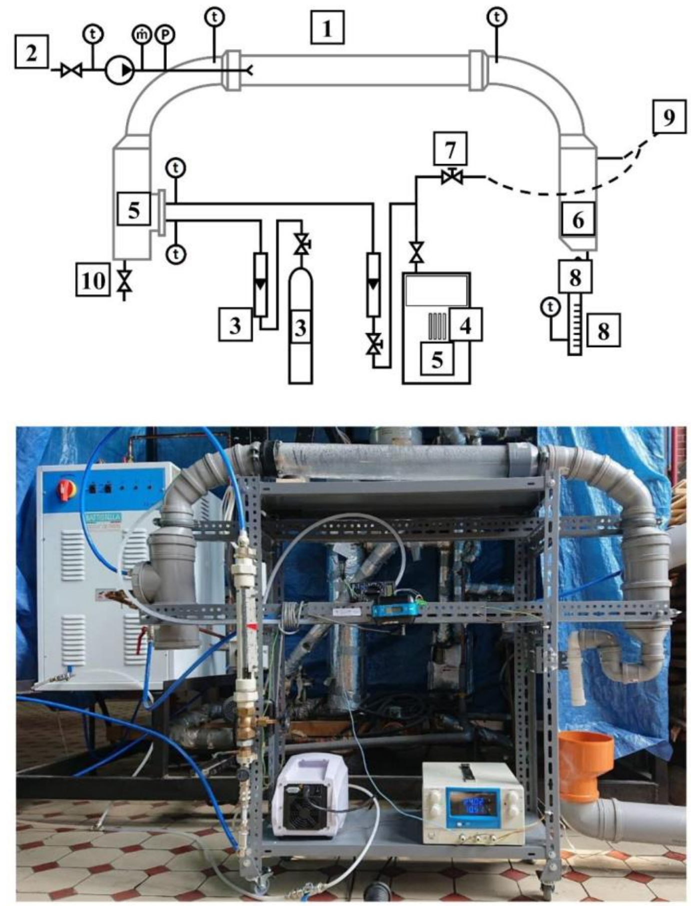

Fig. 11. Schematic diagram of the experimental facility: 1 – measuring section, 2 – motive water input, pump and nozzle, 3 – compressed carbon dioxide, 4 – vapour generator, 5 – mixing chamber, 6 – separation chamber, 7 – vapour by-pass, 8 – water and condensate outlet and titration, 9 – carbon dioxide and vapour outlet to atmosphere.

3.3. Effect of diameter of droplet

According to Eq. (17), there is a direct relation between the number of droplet and its diameter under the constant geometry of the throat. Distribution of temperature of droplet and mixture of steam at different diameter of droplets have been represented in Figs. 9 and 10, respectively. Initial velocity of droplet and mixture is 50 m/s and 20 m/s, respectively, and diameter of throat (D_1) is equal to 8 mm.

Results demonstrate that although temperature of droplet except for 1, 1.5 and 2 mm of diameter has a surging trend along length, temperature of mixture of steam is faced with a decreasing trend. For 1 and 1.5 mm of diameter of droplet, maximum value of temperature of droplet takes place at 8 and 12 cm of length, respectively, and then exhibits a slight reduction. For 2 mm, it boosts up to 16 cm of length and then remains approximately constant. In addition, increasing the diameter of droplet leads to decrease the temperature of droplet and rise the temperature of mixture of steam. As it can be seen, distribution of temperature of mixture of steam for 1 mm, apart from a brief rise again from 8 to 12 cm, gradually declined from 12 to 20 cm of length of throat.

4. Experimental facility

The process of direct contact condensation is taking place in the main part of SEC that is in the throat. In the developed facility the physical processes in the throat only are investigated experimentally by authors of the present paper, as the processes in converging and diverging parts of Venturi nozzle are pretty well known in literature for single or two –phase flow [30]. The test section of the spray ejector throat is made in

Table 2
Measurement accuracies in the SEC experiment.

No.	Measurement device	Accuracy of measurements
1.	nozzle inlet - Atrato AT740 ultrasonic flow metre, measuring range of 83 g/s	± 1% of the range
2.	titration at location (8) – Fig. 11	Menzotube - ± 0.125 g/s Balance weight - ± 0.5 g/s
3.	Trafag NAH pressure gauge (range of 25 bar, class 0.15)	± 0.038 bar
4.	Temperature of steam, CO_2, inlet and outlet sections - T-type thermocouples	± 0.3 K
5.	Nozzle feed water temperature - class A resistance thermometer	± 0.1 K
6.	condensate temperature - liquid thermometer	± 0.1 K

the form of a transparent tube of 80 mm internal diameter. A schematic diagram of the facility together with a photograph is presented in Fig. 11. A motive fluid is supplied through the 1 mm nozzle. The nozzle is fed with motive water at average inlet temperature of 8 °C and pressure ranging from 5.68 to 10.17 bar at the nozzle inlet that corresponds to mass flow rates of water ranging from 17.56 to 22.90 g/s. The value of inlet pressure equal to 5.68 bar has been noticed as a minimum value at which the spray of drops is formed and the jet breakup takes place. The length of the throat is 600 mm.

A mixture of water vapour and carbon dioxide is fed into the mixing length through the mixing chamber and an inlet manifold. The wet vapour is received from the Battistella Saturno MAX/S generator at the pressure close to atmospheric and temperature of about 100 °C. The maximum vapour feed used for experiment is 6 g/s and its regulation takes place with the use of precision valve and a by-pass. Maximum carbon dioxide feed is 6.7 m^3/h. The mixing chamber with a volume of 2.4×10^{-3} m^3 ensures mixing, temperature equalization and removal of the excess water condensate.

The steam-gas mixture is fed to the throat where it meets spray of drops and the process of direct contact condensation occurs. The process of jet breakup is not taking place right away, but after some distance (depending on the inlet pressure of motive water). Then the products of the process go to the separation chamber, 6, with a volume of 1.9×10^{-3} m^3 through the outlet manifold. The vapour – all or partially, depends on experimental conditions – goes out from the siphoned outlet on the bottom of mixing chamber and is collected for titration or weighing. The subtraction of the known amount of water from the nozzle from the total volume gives information about the amount of condensed vapour during the process. Carbon dioxide with possible excess, non-condensed vapour is released into the atmosphere through the outlet located on the upper part of the separation chamber, 9.

The water feeds the nozzle under municipal water supply pressure (3 bar), raised by the Lead Fluid model CT3001S gear pump. This device ensures a pulse-free flow and, under measurement conditions, stabilization of the flow with an accuracy of ±5 ml/min. A flow rate measurement is made using Atrato AT740 mass flowmeter and is independently verified by a titration at the beginning and the end of each measurements series.

The measurement series consists in going through the full vapour input range for a fixed spray of drops feed and, optionally, a fixed carbon dioxide flow rate or in going through the full carbon dioxide input range at a fixed rate of vapour and spray of drops. The vapour and carbon dioxide flow rates are measured using appropriately calibrated Krohne glass rotameters. Water pressure measurement at the nozzle inlet is performed with the Trafag NAH type 8253.80.2317 transducer. The measurements are carried out using T-type thermocouples with an accuracy of ±0.3 K. Location of the thermocouples is presented in Fig. 11.

The measurement accuracies are presented in Table 2.

The experimental distributions of temperature of mixture of steam

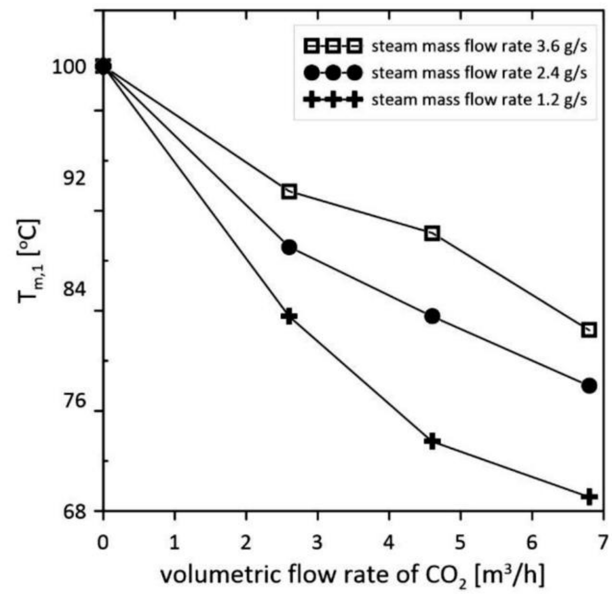

Fig. 12. Distribution of inlet steam temperature at liquid jet mass flow rate = 29 (g/s).

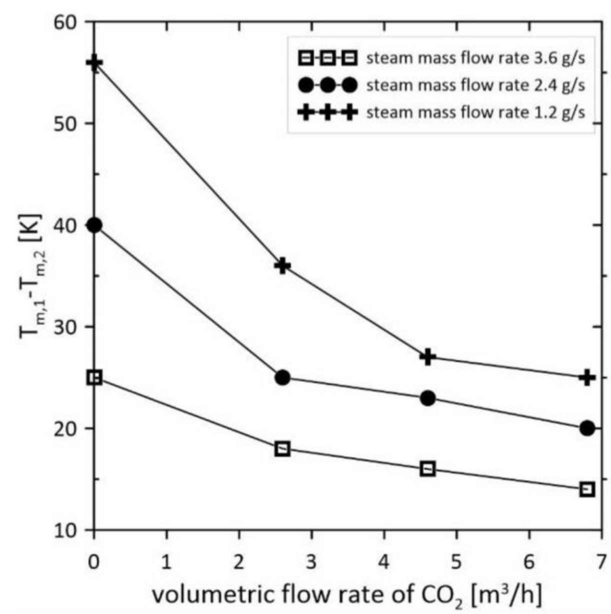

Fig. 13. Distribution of temperature difference at liquid jet mass flow rate = 29 (g/s).

were compared with predictions resulting from the model described earlier. Figs. 12 and 13 show the distribution of temperature at the inlet and the temperature difference between the inlet and outlet of mixing length, respectively, for different mass flow rates of steam (1.2, 2.4 and 3.6 g/s) for a constant mass flow rate of the motive liquid jet set to 29 (g/s). It is apparent that increasing mass flow rate of steam leads to increased levels of temperature at the inlet and outlet of the mixing length, whilst at the constant mass flow rate of steam, increase of the flow rate of CO_2 causes both inlet and outlet temperature of the mixing length to decrease. This is apparent as carbon dioxide as an inert gas strongly impairs the heat transfer. The distributions of temperature along mixing length for different mass flow rate of steam (1.2, 2.4 and 3.6 g/s) when flow rate of CO_2 is 0, 2.6, 4.6 and 6.7 (m^3/h) at liquid jet flow rate = 29(g/s) have been illustrated in Fig. 14. Fig. 13 has been constructed in such a way that presentation of the results is in the form of the temperature difference obtainable at different steam mass flow

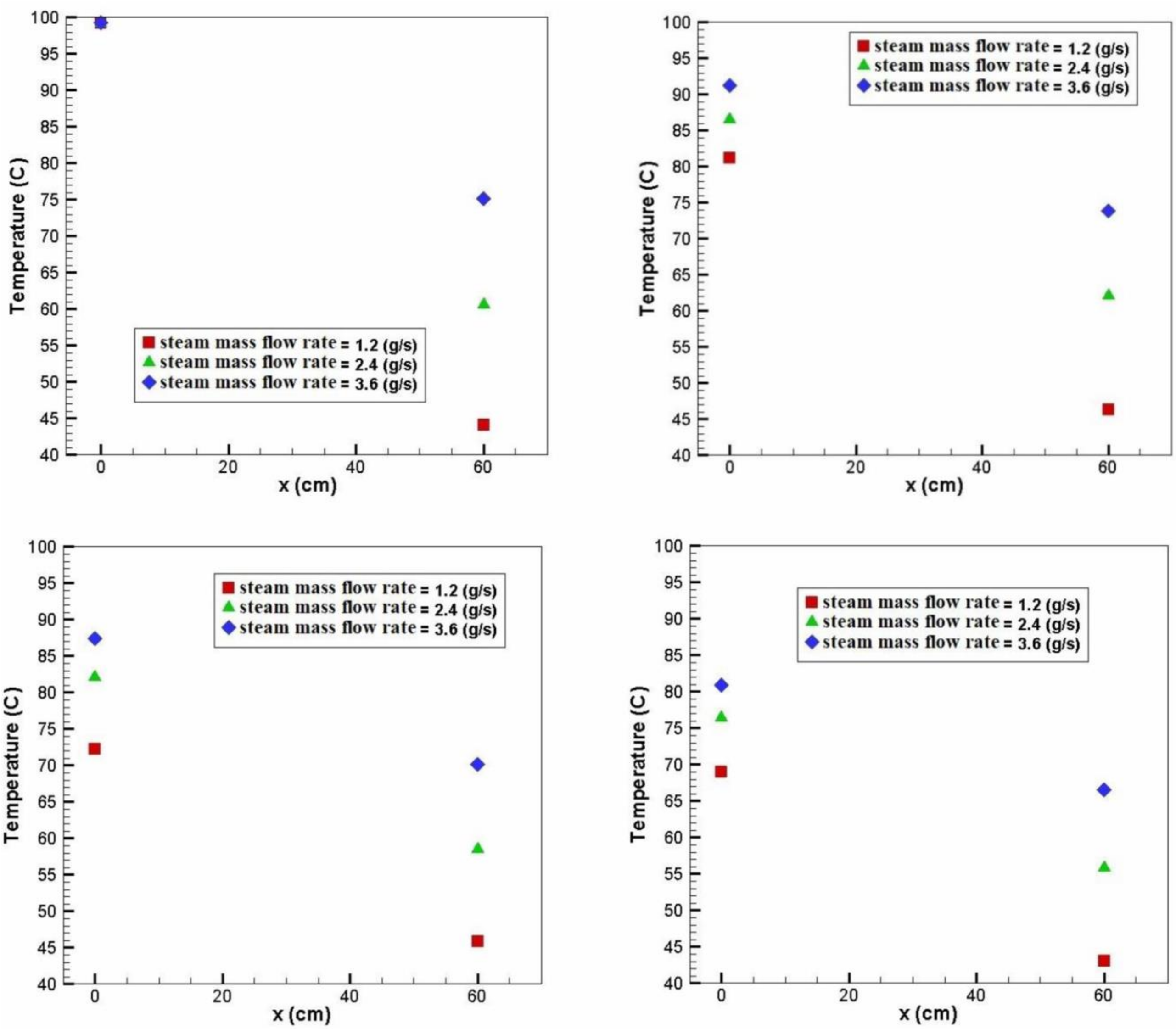

Fig. 14. Distribution of temperature along mixing length for flow rate of CO_2 (m^3/h): a) 0, b) 2.6, c) 4.6 and d) 6.7 (m^3/h) at liquid jet flow rate = 29 (g/s).

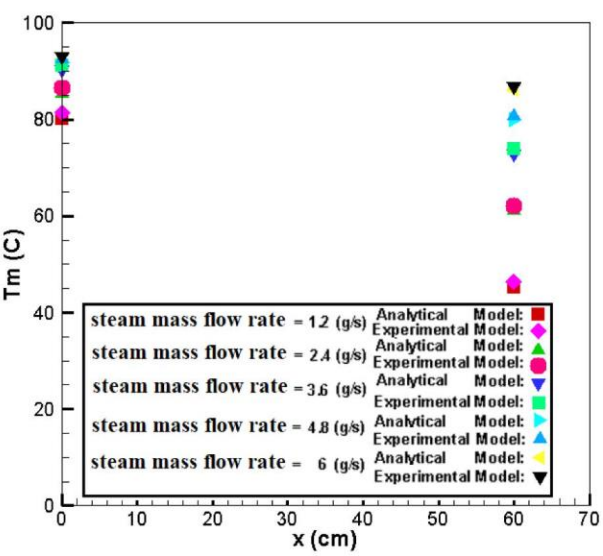

Fig. 15. Distribution of temperature of mixture at liquid jet mass flow rate = 29 (g/s).

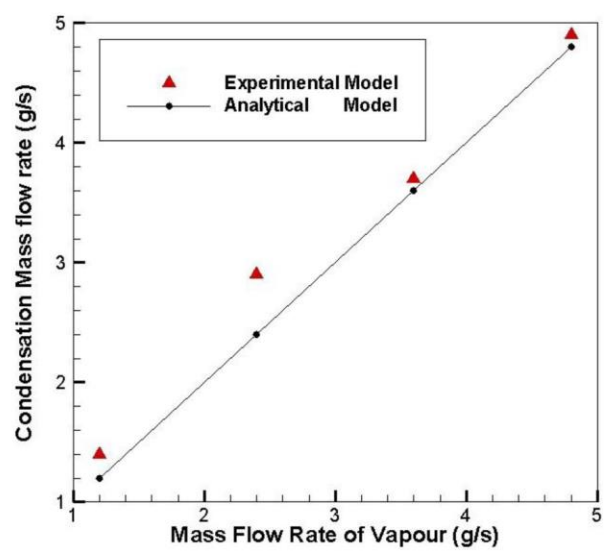

Fig. 16. Condensation mass flow rate at CO_2 flow rate = 2.6 (m^3/h) and liquid jet flow rate = 29 (g/s).

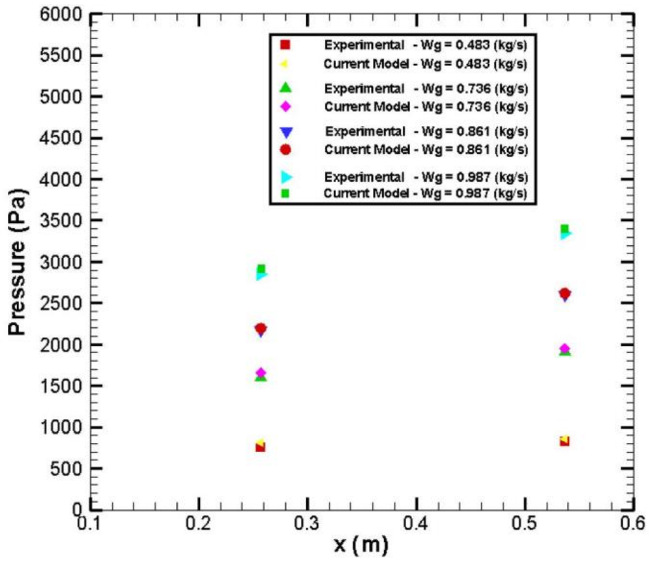

Fig. 17. Validation of pressure distribution along the Venturi scrubber [31].

rates and different amounts of supplied carbon dioxide. The model of DCC predicts higher values of temperature drop between inlet and outlet from the mixing section for the case of smaller steam-CO_2 flow rates. Increasing the flow rate of steam mixture from 1.2 g/s to 3.6 g/s results in a reduction of steam mixture temperature from 25 °C to 14 °C respectively, at CO_2 flow rate of 6.8 m^3/h. Condensation without presence of CO_2 in the same range of steam flow rate, i.e. from 1.2 g/s to 3.6 g/s results in reduction of steam mixture temperature from 56 °C to 25 °C respectively, confirming in such way the effect of CO_2 presence on the efficiency of DCC. Fig. 14 is just another way of presenting the findings in Fig. 13.

5. Model validation

5.1. Throat model validation

For validation purposes of the present model, different mass flow rate of steam was set as: 2.4, 3.6, 4.8 and 6 (g/s), respectively. The results of comparisons of distributions of temperature of mixture of steam and condensation mass flow rate have been presented in Fig. 15. As it can be seen in Fig. 15a good agreement was achieved between the experimental results data. In Fig. 16 is presented the rate of acquired condensate from the flow in function of mass flow rate of supplied vapour. As can be noticed, at the 4.8 g/s of mass flow rate of vapour, there is a complete condensation.

5.2. Pressure distribution validation in the throat

The analytical pressure data calculations were compared with predictions resulting from the experimental models described by Silva [31]. In the experimental Venturi scrubber facility the throat was of a diameter of 125 mm and a total length of 1.27 m. The throat gas velocity was within the range between 34 and 70 m/s and the liquid flow rate was set between 0.013 and 0.075 (kg/s). For validation of the present model, the liquid flow rate of 0.038 kg/s was considered and gas flow rate was set as: 0.483, 0.736, 0.861 and 0.987 (kg/s), respectively. The results of comparisons of pressure at inlet from to the test section as well as at the outlet has been presented in Fig. 17. As it can be seen a good agreement was achieved between the experimental results data taken from the studies by Silva [31]. That consistency is showing up for all values of velocities considered. Unfortunately, there were no temperature values found for the relevant comparisons.

6. Conclusions

In the paper a comprehensive simple analytical model and experimental study of direct contact condensation on a jet of subcooled droplets is presented. The direct condensation process is complex in the presence of inert gases in vapour. In the process of DCC heat and mass transfer mechanisms have been considered, which is not common in similar treatments. This mass transfer due to presence of inert gases renders the process of condensation less effective. Accomplished calculations confirm that. The satisfactory agreement of presented novel modelling with experimental results were obtained. The model of DCC predicts higher values of temperature drop between inlet and outlet from the mixing section for the case of smaller steam-CO_2 flow rates. Increasing the flow rate of steam mixture from 1.2 g/s to 3.6 g/s results in a reduction of steam mixture temperature from 25 °C to 14 °C respectively, at CO_2 flow rate of 6.8 m^3/h. Condensation without presence of CO_2 in the same range of steam flow rate, i.e. from 1.2 g/s to 3.6 g/s results in reduction of steam mixture temperature from 56 °C to 25 °C respectively, confirming in such way the effect of CO_2 presence on the efficiency of DCC.

Through the thermal analysis of studied case, the following results were found:

- Temperature of droplet along the length of throat is experiencing a rising trend, whereas the temperature of mixture of steam is featuring a decreasing trend. That is due to the DCC mechanism in the flow. With a larger presence of carbon dioxide the process of reduction of mixture temperature is smaller.
- Larger diameters of droplets lead to decrease of the temperature of droplet and rise of the temperature of mixture of steam. The larger the number of droplets at the same mass flow rate (smaller size of droplets) the better the effectiveness of DCC due to increased heat transfer surface.
- Droplet size distribution was correlated with considering extra zone prior to the liquid breakup.
- Studies into evaluation of a number of droplets as a result of jet breakup are necessary.

CRediT authorship contribution statement

Dariusz Mikielewicz: Conceptualization, Methodology, Data curation, Writing – original draft, Writing – review & editing, Supervision. **Milad Amiri:** Methodology, Validation, Formal analysis, Investigation, Data curation. **Michał Klugmann:** Methodology, Validation, Formal analysis, Investigation. **Jarosław Mikielewicz:** Conceptualization, Writing – original draft, Writing – review & editing.

Declaration of Competing Interest

The authors declare that they have no known competing financial interests or personal relationships that could have appeared to influence the work reported in this paper.

Data availability

Data will be made available on request.

Acknowledgments

The research leading to these results has received funding from the Norway Grants 2014–2021 via the National Centre for Research and Development. Article has been prepared within the frame of the project: “Negative CO2 emission gas power plant”—NOR/POLNORCCS/NEGATIVECO2-PP/0009/2019–00 which is co-financed by programme “Applied research” under the Norwegian Financial Mechanisms

2014–2021 POLNOR CCS 2019—Development of CO2 capture solutions integrated in power and industry processes.

References

[1] Y.S. Kim, J.W. Park, C.H. Song, Investigation of the stem-water direct contact condensation heat transfer coefficients using interfacial transport models, Int Commun Heat Mass Transf 31 (3) (2004) 397–408.
[2] A. Shah, I.R. Chughtai, M.H. Inayat, Experimental and numerical investigation of the effect of mixing section length on direct-contact condensation in steam jet pump, Int J Heat Mass Transf 72 (2014) 430–439.
[3] Q. Xu, L. Guo, Direct contact condensation of steam jet in crossflow of water in a vertical pipe. Experimental investigation on condensation regime diagram and jet penetration length, Int J Heat Mass Transf 94 (2016) 528–538.
[4] P. Ziółkowski, P. Madejski, M. Amiri, T. Kuś, K. Stasiak, N. Subramanian, H. Pawlak-Kruczek, j. Badur, L. Niedzwiecki, D. Mikielewicz, Thermodynamic analysis of negative CO2 emission power plant using Aspen Plus, Aspen Hysys, and Ebsilon software, Energies 14 (19) (2021) 6304.
[5] P. Ziółkowski, J. Badur, H. Pawlak- Kruczek, K. Stasiak, M. Amiri, L. Niedzwiecki, K. Krochmalny, J. Mularski, P. Madejski, D. Mikielewicz, Mathematical modelling of gasification process of sewage sludge in reactor of negative CO2 emission power plant, Energy 244 (2022), 122601.
[6] F. Kreith, R. Boehm, Direct-contact Heat Transfer, Springer Science & Business Media, 2013.
[7] D. Mazed, R. Lo Frano, D. Aquaro, D. Del Serra, I. Sekachev, M. Olcese, Experimental investigation of steam condensation in water tank at subatmospheric pressure, Nucl Eng Des 335 (2018) 241–254.
[8] G.P. Celata, M. Cumo, F. D'Annibale, G.E. Farello, Direct contact condensation of steam on droplets, Int J Multiph Flow 17 (1991) 191–211.
[9] Z. Ying, L. YuLong, Nonequilibrium molecular dynamics simulations of mass transfer on transient direct-contact condensation, Int J Heat Mass Transf 184 (2022), 122255.
[10] P. Ziółkowski, K. Stasiak, M. Amiri, D. Mikielewicz, Negative carbon dioxide gas power plant integrated with gasification of sewage sludge, Energy (2022), 125496.
[11] X. Gamisans, M. Sarrà, F.,.J. Lafuente, B., .J.. Azzopardi, The hydrodynamics of ejector-Venturi scrubbers and their modelling by an annular flow/boundary layer model, Chem Eng Sci 57 (14) (2002) 2707–2718.
[12] I. Lee, Local condensation rates in horizontal cocurrent steam-water flow, in: Proceedings of the 18th National Heat Transfer Conference, 1970.
[13] M. Akira, H. Fiji, S. Takamoto, Prediction of heat transfer by direct contact condensation at a steam-subcooled water interface, Int J Heat Mass Transf 35 (1) (1992) 101–109.
[14] E. Ihnatowicz, M. Trela, J. Mikielewicz, *Investigation of the thermal development length during direct condensation of vapour on liquid layer.* Arch, Thermodyn 14 (1–4) (1993) 147–164.
[15] Z. Aidoun, K. Ameur, M. Falsafioon, M. Badache, C*urrent advances in ejector modeling, experimentation and applications for refrigeration and heat pumps. Part 1: single-phase ejectors*, Inventions 4 (1) (2019) 15.
[16] R. Neve, The performance and modeling of liquid jet gas pumps, Int J Heat Fluid Flow 9 (2) (1988) 156–164.
[17] R. Lo Frano, D. Mazed, M. Olcese, D. Aquaro, D. Del Serra, I. Sekachev, G. Giambartolomei, Investigation of vibrations caused by the steam condensation at subatmospheric condition in VVPSS, Fusion Eng Des 136 (2018) 1433–1437.
[18] G. Brown, Heat Transmission By Condensation of Steam On a Spray of Water Drops, University of London (Imperial College of Science and Technology, 1948.
[19] V. Isachenko, V. Kushnyrev, Condensation heat transfer in dispersed liquid spray, in: Proceedings of the International Heat Transfer Conference Digital Library, Begel House Inc, 1974.
[20] A. Lekic, J. Ford, Direct contact condensation of vapour on a spray of subcooled liquid droplets, Int J Heat Mass Transf 23 (11) (1980) 1531–1537.
[21] P. Madejski, T. Kuś, P. Michalak, M. Karch, N. Subramanian, Direct contact condensers: a comprehensive review of experimental and numerical investigations on direct-contact condensation, Energies 15 (24) (2022) 9312.
[22] A. Shah, I.R. Chughtai, M.H. Inayat, Numerical simulation of direct-contact condensation from a supersonic steam jet in subcooled water, Chin. J. Chem. Eng. 18 (4) (2010) 577–587.
[23] R. Koirala, K. Inthavong, A. Date, Numerical study of flow and direct contact condensation of entrained vapor in water jet educator, Exp Computl Multiph Flow 4 (3) (2022) 291–303.
[24] Grosshans H., Evaporation of droplets, Project Report 2012 MVK160 Heat and Mass Transfer, Lund, Sweden.
[25] M. Jain, R. Prakash, S.G. Tomar, R.V. Ravikrishna, Secondary breakup of a drop at moderate Weber numbers, Proc Royal Soc A Math, Physi Eng Sci 471 (2177) (2015), 20140930.
[26] C. Bai, K. Liu, T. Zhao, J. Liu, Study on spray characteristics and breakup mechanism of an scr injector, Appl Sci 12 (18) (2022) 9387.
[27] F. Suñol, González-Cinca, *Liquid jet breakup and subsequent droplet dynamics under normal gravity and in microgravity conditions*, Phys Fluids 27 (7) (2015), 077102.
[28] V.P. Carey, Liquid-vapor Phase-Change phenomena: an Introduction to the Thermophysics of Vaporization and Condensation Processes in Heat Transfer Equipment, CRC Press, 2020.
[29] F.W. Schmidt, R.E. Henderson, C.H. Wolgemuth, Introduction to Thermal sciences: Thermodynamics, Fluid mechanics, Heat transfer, John Wiley a& Sons, 1984.
[30] E.N. Ganic, W.M. Rohsenow, Dispersed Flow Heat Transfer, Int. J. Heat and Mass Transfer 20 (1977) 855–866. Vol.
[31] Silva, A., Numerical and experimental study of venturi scrubbers. PhD Thesis, University of Minho, 2008.

Appendix 2. Article [B]

Applied Thermal Engineering 257 (2024) 124235

Contents lists available at ScienceDirect

Applied Thermal Engineering

journal homepage: www.elsevier.com/locate/apthermeng

Research Paper

Analysis of cyclone separator solutions depending on spray ejector condenser conditions

Milad Amiri [a,*], Paweł Ziółkowski [a], Jarosław Mikielewicz [b], Michał Klugmann [a], Dariusz Mikielewicz [a]

[a] Faculty of Mechanical Engineering and Ship Technology, Gdańsk University of Technology, ul. Gabriela Narutowicza 11/12, 80-233 Gdańsk, Poland
[b] Polish Academy of Science, Institute of Fluid-Flow Machinery, ul, Fiszera 14, 80-231 Gdańsk, Poland

ARTICLE INFO

Keywords:
Direct-contact condensation
Cyclone separator
Spray ejector condenser
CO_2 capture

ABSTRACT

The core design strategy for minimizing CO_2 emissions in gas power plant entails combining a spray ejector condenser (SEC) and separator to accomplish steam condensation and CO_2 purification. This innovative process involves direct-contact condensation of steam with CO_2, facilitated by interaction with a subcooled water spray, along with a cyclone separator mechanism intended for generating pure CO_2. The investigation of the SEC section, both experimentally and analytically, provides crucial insights into its operational dynamics. Given the susceptibility of cyclone efficiency to fluctuations in SEC conditions, this research endeavors to examine the impacts of CO_2 volumetric flow rate and droplet break-up within the SEC on the separation efficacy of the cyclone separator. Additionally, the impact of cone size on the performance of the cyclone has been investigated. Here, a three-dimensional, transient, and turbulent cyclone separator is numerically simulated using Ansys Fluent 2021 R1. The Reynolds Stress Model is employed to simulate turbulent flow, while a mixture model is utilized to replicate swirl two-phase flow within the separators. The findings revealed that reductions in steam and CO_2 flow rates were associated with a decrease in outlet temperature but an increase in SEC inlet temperature, leading to a rise in temperature difference and heat transfer rate. Furthermore, an augmentation in cyclone cone size (from 0.2 to 0.5 m) resulted in enhanced separation efficiency (from 77.30 % to 80.98 %) alongside an elevation in pressure drop (from 6.08 Pa to 10.91 Pa), suggesting a compromise between CO_2 purification and energy consumption. Additionally, elevated CO_2 flow rates induced a rise in pressure drop and separation efficiency, ultimately achieving maximum efficiency at a rate of 24 $\frac{g}{s}$. Moreover, the exploration into droplet breakup manifesting in a boost in separation efficiency from 50.98 % to 100 % across droplet diameters ranging from 1 to 20 μm.

1. Introduction

Implementing CO_2 capture technologies in industrial processes is essential for mitigating global climate change by reducing the emission of greenhouse gases [1–3]. Carbon Capture Utilization and Storage (CCUS) technology encompasses a range of industrial engineering processes aimed at extracting CO_2 from industrial emission sources [4]. This extracted CO_2 is then transported to a designated location where it can either be used for various purposes or securely stored to mitigate CO_2 emissions. CCUS technology involves multiple stages consist of CO_2 capture, sequestration, transportation and utilization [5]. Carbon capture technology plays a crucial role in mitigating CO_2 emissions without compromising the utilization of fossil fuels. This technology has garnered considerable global interest and is increasingly recognized as a vital approach to minimizing greenhouse gas emissions. By capturing CO_2 from industrial processes and power plants, carbon capture technology has the potential to lower the overall expense of emission abatement efforts and enhance the flexibility of achieving greenhouse gas emission targets [6]. Capturing CO_2 stands as the initial and pivotal stage within CCUS, serving as a crucial component in conserving energy, mitigating emissions, and managing the greenhouse impacts. Because of variations in pressure, composition, and operational needs of emission sources, capture methods associated with it differ, categorized into pre-combustion, post-combustion, and oxy-fuel combustion enhancement methods [7]. Pre-combustion capture involves extracting CO_2 prior to the fuel's mixture with air for complete combustion, commonly applied in integrated gasification combined cycle (IGCC) power generation

* Corresponding author.
E-mail address: milad.amiri@pg.edu.pl (M. Amiri).

https://doi.org/10.1016/j.applthermaleng.2024.124235
Received 10 April 2024; Received in revised form 2 July 2024; Accepted 22 August 2024
Available online 24 August 2024
1359-4311/

Nomenclature

C_p	specific heat capacity ($\frac{J}{kg.K}$)
D_h	hydraulic diameter (m)
Dj	diameter of jet (m)
D_{ij}	stress diffusion term ($\frac{kg}{m.s^2}$)
D_0	diameter of mixing length (m)
d_d	diameter of droplet (m)
h_m	mass transfer coefficient
$h_{m.g}$	convection heat transfer coefficient, ($\frac{W}{K.m^2}$)
$l\dot{m}_g$	mixing length (m)suction mass ($\frac{kg}{s}$)
n	total number of droplet
P	static Pressure (pa)
$P_{ij}p_{g,1}$	shear production term ($\frac{N}{m^3}$)suction pressure (pa)
Re	Reynolds Number
Re_m	Two-phase Reynolds Number
S	source term
T	temperature (K)
$\overrightarrow{u}$	velocity vector ($\frac{m}{s}$)
$u_{dr,q}$	drift velocity for secondary ($\frac{m}{s}$)
We	Weber number

Greek Symbols

ρ_l	liquid density ($\frac{kg}{m^3}$)
ρ	density ($\frac{kg}{m^3}$)
ρ_m	mixture density ($\frac{kg}{m^3}$)
μ_m	mixture viscosity $\left(\frac{kg}{m.s}\right)$
Π_{ij}	pressure-strain term ($\frac{kg}{m.s^2}$)
μ_l	dynamic viscosity $\left(\frac{kg}{m.s}\right)$
ε_{ij}	dissipation term ($\frac{kg}{m.s^3}$)
η	separation efficiency (%)
σ_l	surface tension ($\frac{N}{m}$)
$\Delta p_{loss,1}$	pressure drop (pa)

subscript

l	liquid
g	steam and CO_2
d	droplet

Acronyms

DCC	direct contact condensation
nCO_2PP	negative CO_2 emissions power plant
SEC	spray ejector condenser

setups [8]. Utilizing oxygen-rich combustion method, carbon capture in combustion entails replacing the combustion air within current power station boiler systems with high-purity oxygen [9–11]. Post-combustion decarburization method involves capturing and isolating CO_2 from the exhaust gases produced during industrial activities, particularly from the combustion of fossil fuels, followed by compression and purification. This method is predominantly applied in facilities such as petrochemical plants, coal-fired power plants and synthetic fuel facilities, where substantial CO_2 emissions occur. This study explores a post-combustion carbon capture approach that incorporates a spray ejector condenser (SEC) and cyclone separator. This approach signifies a groundbreaking advancement over conventional post-combustion methods through its integration of a SEC and cyclone separator, which synergistically augment thermal transfer efficacy, optimize condensation mechanisms, and enable the attainment of superior purity in CO2 separation.

Fig. 1 depicts an innovative gas power plant with negative CO_2 emissions (nCO_2PP) [12–15]. The nCO_2PP concept revolves around utilizing sewage sludge, which undergoes conversion into syngas before being combusted in a wet combustion chamber (WCC). An ASU separates oxygen from air and the separated oxygen is then used in the gasification process in order to produce a syngas mixture consisting of H_2 and CO. The produced syngas is then passed through the water gas shift reactor (WGSR) to produce carbon dioxide (CO_2) and hydrogen (H_2) from the carbon monoxide (CO) of the syngas and the added water. The produced carbon dioxide (CO_2) can then be captured and the produced hydrogen (H_2) can be fed to the power generation device as the

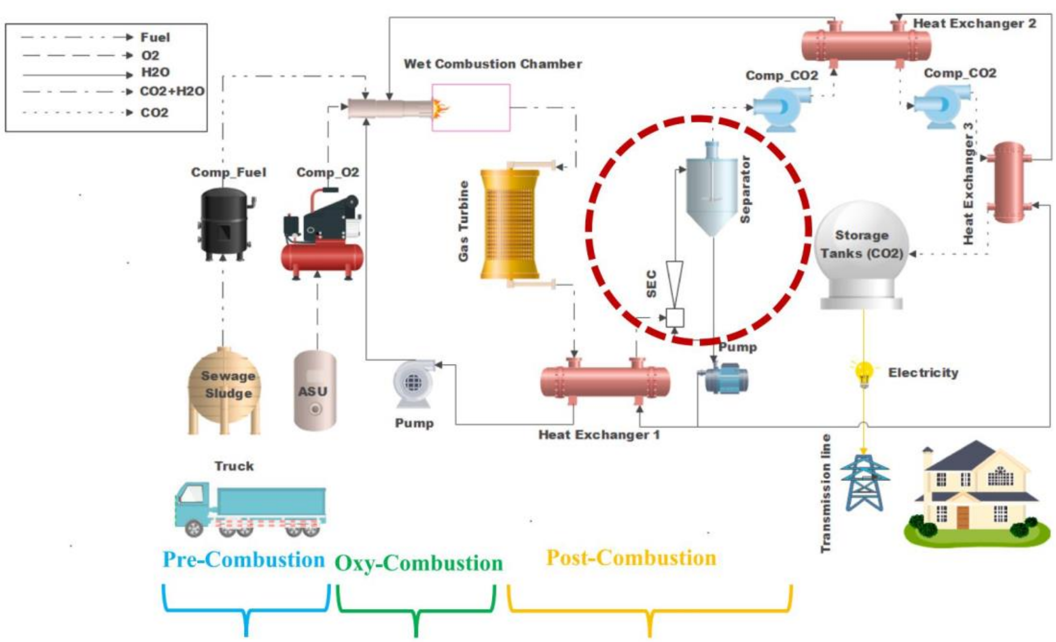

Fig. 1. Flowchart of the Gas Power Plant with Negative CO_2 Emission [12,13].

working fuel. The high concentrations of carbon dioxide (CO_2) in the produced mixture ($CO_2 + H_2$) leaving the WGSR facilitates the capture process of CO_2 when compared with the process of CO_2 capture from normal exhaust flue gas (mixture of NO_x, SO_x, O_2, N_2, and unburned hydrocarbons) out of a conventional combustor. There are different mechanisms for CO_2 separation from the gas mixture leaving the WGSR including absorption, adsorption, cryogenic separation, and membrane separation. Therefore, fuel is generated through a thermochemical process in the gasifier (R) using dry sewage sludge in the presence of a gasifying agent [13,14]. This agent can be optionally released after gas turbine (GT) from a carbon capture unit (CCU) at ambient pressure. The agent's properties, including CO_2 and steam content, temperature, and pressure, can be adjusted. Notably, syngas is classified as a renewable fuel, leading to a net reduction in CO_2 emissions from the power plant. Within the post-combustion unit of the nCO_2PP, exhaust gases from heat exchanger 1, along with water, are directed into a SEC. Upon complete steam condensation in the SEC, both water and CO_2 are directed to the cyclone separator for CO_2 purification.

The initial stage of the carbon capture method utilized in this study involves the operation of the SEC, which facilitates direct contact condensation (DCC) to transform water vapor from exhaust gases into liquid. Through the injection of a cooling liquid via spraying into the gas zone, the condensation process is accelerated, thereby significantly increasing the surface area available for contact between the vapor and the liquid. This process enhances heat transfer efficiency by facilitating rapid heat exchange between the hot gas and the cool liquid droplets. As the small liquid droplets come into direct contact with the hot gas, they absorb heat energy, causing the gas to cool and promoting the condensation of water vapor. This accelerated condensation not only reduces the residence time required for complete condensation but also improves the overall performance of condensers in efficiently removing water vapor from the gas stream. Furthermore, the rate of heat transfer and condensation efficiency are notably influenced by the presence of additional gases [16]. Amiri et al [15] examined how the implementation of an electrohydrodynamic actuator (EHD) in a steam ejector condenser enhances convective transfer for DCC by mitigating resistance. They also examined how different properties of injected water, such as temperature (20–40 °C) and pressure (12–16 bar), as well as varying steam mass flow rates (2.2–4.6 $\frac{g}{s}$), could enhance heat transfer rates in the SEC [17]. This was aimed at overcoming reduced convective heat transfer and increased diffusion resistance between subcooled water and steam phases induced by CO_2. Mikielewicz et al [18] explored an innovative approach to enhance DCC of a vapor-inert gas mixture within a SEC. Their research delved into the breakup of droplets and heat and mass transfer mechanism. Findings indicated that an increased quantity of droplets at identical mass flow rates led to improved DCC effectiveness because of the increased surface of heat transfer. Kus and Madejski [19] examined the impact of different gas inlet velocities and the existence of CO_2 on the performance of the SEC, numerically. Their study revealed that the boiling/condensation model forecasts an increase in condensation effectiveness and a decrease in suction pressure compared to the Spalding/evaporation model. Also, Madejski et al. [20] conducted a numerical investigation into the advancement of SEC. Their findings revealed that both the average droplet diameter and the method of supplying motive water substantially influence the intensity of condensation.

In this study, the cyclone separator serves as the second component of the carbon capture process being examined. Gas-liquid cyclone separators are utilized across various industries for the efficient separation of gas and liquid phases. Common applications include the oil and gas industry, petrochemical plants, chemical processing, environmental protection, pharmaceuticals, biotechnology, and the food and beverage industry. They play a crucial role in processes such as phase separation, purification, pollution control, and product clarification, contributing to process efficiency, product quality, and environmental compliance [21,22]. Gas-liquid cyclone separators come in several types, each tailored to specific applications and operational needs. One notable type is the Stairmand cyclone [23], distinguished by its unique design features aimed at optimizing separation efficiency. A cyclone separator's efficiency is contingent upon a multitude of factors, comprising both its structural configuration and operational parameters such as gas velocity, particle dimensions and characteristics of phases [24]. Amiri et al. [25] studied the impact of implementing vanes in a cyclone separator, achieving a significant 16.8 % decrease in pressure drop and improving separation efficiency by 9.2 %. Yoshida et al. [26], conducted an investigation utilizing various types of apex cones positioned at the dust box inlet. They observed that the impact of the apex cone angle on collection efficiency diminishes under high inlet velocities. Furthermore, studies have probed the efficiency implications of elongating a cyclone with a vertical tube [27,28]. Studies have documented the effect of an opposing cone situated at the base of a cyclone separator on its operational efficiency [29,30]. Brar et al. [31] and Prasanna et al. [32] investigated the impact of cone and cylinder length on both pressure drop and separation efficiency. Osama Hamdy et al. [33] conducted a numerical investigation on the conventional cyclone, systematically altering the length and angle of the cone. The research findings indicated that variations in the angle and length of the cone significantly affect both the internal flow dynamics and separation efficiency.

This paper presents the design of a SEC, both experimentally and analytically, as well as a cyclone separator simulated numerically using Ansys Fluent 2021 R1, to achieve the intended high-purity CO_2 stream for the Negative CO_2 Emission Gas Power Plant (nCO_2 PP) [34]. Initially, experimental and analytical models of SEC are developed to enhance the efficiency of the CO_2 capture unit by investigation of effect of volumetric flow rate of CO_2 and steam mass flow rate on inlet and outlet temperature of SEC, respectively. Subsequently, condensation mass flow rate at different steam mass flow rate is investigated. After obtaining fully condensation of steam on SEC, cyclone separator is modelled to simulate CO_2 −water. To enhance purification of CO_2, effects of cone size, mass flow rate of CO_2 and break-up of droplets are conducted.

2. Exploring spray ejector Condenser: Experimental and analytical perspectives

2.1. Experimental feasibility study of SEC

The core of the SEC, particularly its throat, is where the DCC process eventuate. This section entirely concentrates on investigating the physical occurrences in this throat area, considering the thorough recording of procedures in the converging and diverging segments of the Venturi nozzle for various flow conditions [35]. Characteristics of throat are listed in Table.1.

The thermophysical characteristics of water injected by the nozzle are detailed in Table 2. The recorded minimum inlet pressure, standing at 5.68 bar, represents the critical threshold necessary to trigger both the formation of drop spray and the subsequent breakup of the jet within the system.

The introduction of the steam and CO_2 blend takes place through an inlet manifold, followed by their admixture within the mixing chamber located within the designated mixing length of the system (Fig.2). Table 3 presents a comprehensive overview of the measuring instruments employed in the experimental tests, detailing their respective models and the levels of accuracy they offer.

Table 1
Dimensions of throat.

parameter	unit	value
Internal diameter of throat	mm	80
Nozzle diameter	mm	1
Length of throat	mm	600

Table 2
Thermophysical parameters and flow rates of water.

parameter	unit	value
average inlet temperature	°C	8
pressures	bar	5.68—10.17
mass flow rates	$\frac{g}{s}$	17.56—22.90

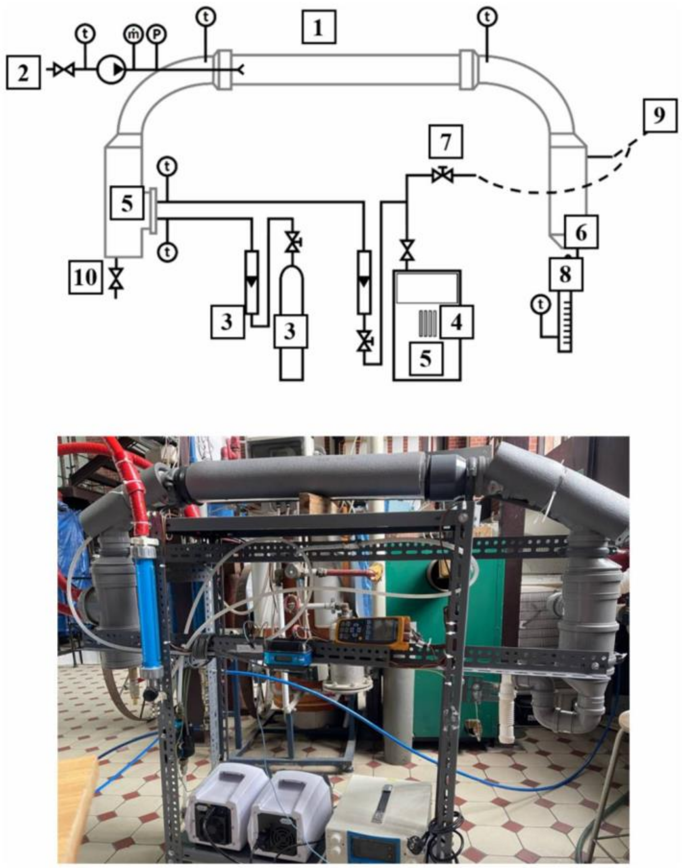

Fig. 2. Illustrative layout of the experimental setup: 1 – measurement segment, 2 – motive water supply, nozzle and pump, 3 – pressurized carbon dioxide, 4 – steam generator, 5 – blending chamber, 6 – separation unit, 7 – steam bypass, 8 – water discharge and condensation for titration, 9 – CO_2 and steam release into the atmosphere.

Table 3
Measuring instrument and their models.

Measuring instrument	Sourced	Model	Accuracy
Generator	Steam	Battistella Saturno MAX/S	–
Gear pump	water	Lead Fluid model CT3001S	±5 ml/min
Inlet of nozzle	water	Atrato AT740	±1%
Pressure gauge	CO_2 −steam	Trafag NAH type 8253.80.2317	±0.038 bar
Temperature gauge	CO_2 −steam	type T thermocouples	±0.3 K
Flow rates	CO_2 −steam	Krohne glass rotameters	–

Steam, controlled to nearly atmospheric pressure and around 100 °C, can be supplied at a maximum rate of 6 $\frac{g}{s}$, while the CO_2 can be delivered at a maximum rate of 8.7 $\frac{m^3}{h}$. The boundary conditions for steam and CO2 are detailed in Tables 4 and 5, respectively.

As the gas-steam mixture flows into the throat, it encounters a spray of droplets. This interaction between the gas-steam mixture and the droplets is crucial, as it initiates the DCC. During this interaction, several physical phenomena occur. Firstly, the high-velocity gas-steam mixture collides with the droplets, causing them to break apart into smaller droplets due to the momentum transfer. This process, known as atomization, increases the surface area of the droplets exposed to the gas-steam mixture. Secondly, the collision between the gas-steam mixture and the droplets causes rapid heat transfer. The high-temperature gas-steam transfers heat to the cooler droplets, causing the steam to condense into liquid water. This release of latent heat of vaporization further increases the temperature of the droplets, promoting further vaporization of the liquid water. Thirdly, the turbulent mixing between the gas-steam mixture and the droplets ensures efficient mass and heat transfer. Turbulent flow enhances the contact between the gas-steam mixture and the droplets, facilitating rapid condensation and vaporization processes. Overall, the interaction between the gas-steam mixture and the spray of droplets in the throat region promotes intense heat and mass transfer processes, leading to the initiation of the DCC process in mixing chamber (2400 cm^3). After entering the throat, the jet of fluid experiences a breakup phenomenon at a certain distance from the throat inlet. This breakup occurrence is dependent on the inlet pressure of the water. To understand the amount of condensed vapor produced during the process, a method involves subtracting the known quantity of water from the total volume at the nozzle. In the system, there exists an outlet located at the upper portion of the separation chamber (chamber 9). This outlet serves a specific purpose: it allows for the controlled release of any surplus CO_2 and any vapor that has not undergone condensation back into the atmosphere.

Table 4
Thermophysical parameters and flow rates of steam.

parameter	unit	value
temperature	°C	100
pressures	bar	1
mass flow rates	$\frac{g}{s}$	1.2–4.8

Table 5
Thermophysical parameters and flow rates of CO_2.

parameter	unit	value
temperature	°C	25
pressures	bar	1
mass flow rates	$\frac{m^3}{h}$	2.4–8.7

2.2. Analytical analysis of SEC

This section presents a discussion on the design considerations pertaining to a spray ejector, with specific emphasis on critical components including the pre-mixing region, nozzle and mixing sector. However, it notably omits the analysis of the diffuser component, positing the presumption that complete condensation is achieved within the mixing sector. The diffuser's primary function lies in facilitating the transfer of CO_2 to subsequent segments of the system. The described SEC fundamentally adopts a converging nozzle configuration, wherein condensation predominantly occurs within the mixing section. Furthermore, the segmentation of the ejector, extending from the inlet to the exit, is visually depicted in Fig. 3. This illustration elucidates the distinct operational phases of the ejector, delineating the flow dynamics of gases and liquids throughout the system. Additionally, it proposes an alternative strategy whereby a cyclone separator could be employed in lieu of the diffuser, suggesting avenues for potential variation in the condensation process. It is elucidated the assumption regarding the inlet characteristics of fluids introduced into a given system, delineated by the designation "inlet" within the schematic representation provided in

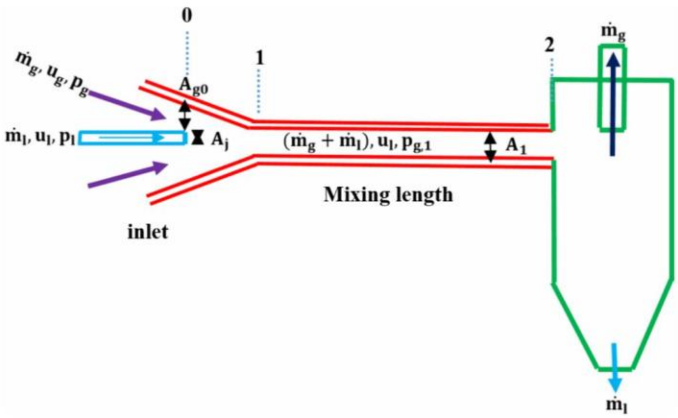

Fig. 3. Details of SEC.

Fig. 3. Within this context, the attributes of these fluid mediums are perceived to be comprehensively understood at this specific juncture. Notably, the liquid constituents within the fluid stream are designated with the subscript "l," whilst amalgamated form comprising steam and non-condensable constituents has been allocated as "g." Moreover, the narrative underscores the imperative of an established protocol for discerning the attributes corresponding to the state denoted as "0." This procedural undertaking entails the systematic reduction of inlet parameters attributed to the transformative effects induced by alterations in flow geometry and the exertion of frictional forces. To expound further, as the fluid medium traverses through the structural confines of the system, traversing varied flow regimes, the initial characteristics exhibited at the inlet undergo progressive modifications. Such modifications are intrinsically influenced by manifold factors including alterations in geometric configuration and the manifestation of frictional interactions.

The focal point on determining the mass flow rate and pressure of the steam- CO_2 mixture at point "1," representing initial phase of the steam condensation procedure. This pursuit is facilitated through the utilization of conservation equations governing momentum, mass and energy. In the context of a designated ejector design, the comprehension of parameters such as suction mass ($\dot{m}_g$) and pressure at the commencement of the mixing chamber necessitates a profound understanding of the equations derived from the conservation principles that regulate flow dynamics within the inlet zone. These equations emerge from the application of mass, momentum and energy principles to the mixture under consideration. Furthermore, the narrative underscores the pivotal significance of ensuring continuity amidst points labeled "inlet" and "0″." This imperative for continuity encompasses the seamless propagation of properties and flow attributes from the inlet region to state "0," thereby fostering an exhaustive comprehension of the intricate fluid dynamics and behavioral manifestations inherent within the system.

$$\dot{m}_g = u_{gin}\rho_g A_{gin} = u_{g0}\rho_g (A_0 - A_l) \tag{1}$$

From Bernoulli equation:

$$p_{g,in} + \frac{1}{2}\bullet\rho_{g,0}u_{g,in}^2 = p_{g,0} + \frac{1}{2}\bullet\rho_{g,0}u_{g,0}^2 + \Delta p_{loss,1} \tag{2}$$

Ascertaining the suction pressure (pg,1) arising from the interplay of a liquid jet with gases has been delineated. Suction pressure through the alignment of momentum considerations between distinct states within the system, specifically the pre-mixing sector denoted as "state 0″ and the ingress point to the mixing section referred to as "state 1."

$$p_{g,0}A_{g,0} + \dot{m}_g u_{g,0} + p_l A_l + \dot{m}_l u_l = p_{g,1}A_1 + \left(\dot{m}_g + \dot{m}_l\right)u_l \tag{3}$$

A procedural framework aimed at determining parameters at state 2 within the system has been elucidated. This endeavor entails the simultaneous application of conservation equations pertaining to mass, momentum and energy, contextualized within an adiabatic process setting. Furthermore, in scenarios where CO_2 coexists within the condensation environment, the analysis necessitates a comprehensive examination incorporating both heat and mass transfer phenomena. This analytical endeavor draws upon the utilization of equations and methodologies previously expounded upon in the authors' antecedent analytical inquiries [18]. These inquiries encompassed diverse facets, including the condensation process of vapour upon a subcooled droplet stream, the attainment of heat equilibrium within the droplet stream, and the reconciliation of mass and heat balances within the vapour-gas mixture.

2.2.1. *Thermal equilibrium of droplet flow*

This section proposes the application of an energy balance methodology to specify the temperature of a droplet stream. This approach entails analyzing the alteration in enthalpy of the droplet stream and the thermal energy acquired during the condensation process. These factors collectively influence the rate of heat transfer to the vapour- CO_2 mixture. Fundamentally, the energy balance equation facilitates the quantification of thermal energy exchange within the system, incorporating considerations of heat release during condensation and consequent temperature variations within the droplet stream.

$$\frac{d}{dx}\left(c_{pl}\dot{m}_d T_d\right) + \frac{h_{lv}}{dx}d\dot{m} = \frac{d\dot{Q}}{dx} \tag{4}$$

The heat transfer rate is then conveyed through convection to the boundary of the droplet surface.

$$\frac{d\dot{Q}}{dx} = \pi d_d^2 \frac{n}{l} h_{mg}(T_m - T_d) \tag{5}$$

Here, h_{mg} represents the coefficient for convective heat transfer.

Droplet temperature gradient:

$$\frac{dT_d}{dx} = -\left(\frac{T_d}{\dot{m}_d} + \frac{h_{lv}}{c_{pl}\dot{m}_d}\right)\frac{d\dot{m}}{dx} + \frac{\pi d_d^2 \frac{n}{l} h_{mg}(T_m - T_d)}{c_{pl}\dot{m}_d} \tag{6}$$

2.2.2. *Equilibrium of mass and thermal energy for steam-CO_2 mixture*

The mass equilibrium equation for the gas-vapour mixture results in:

$$\dot{m}_m(x) = \dot{m}_{m0} - \int_0^l \frac{d\dot{m}_d(x)}{dx}dx \tag{7}$$

The mass flow rate of the gas-vapour mixture enables the calculation of the velocity profile of the mixture, under the assumption of constant flow area.

$$u_m(x) = u_{m0}\frac{\dot{m}_m(x)}{\dot{m}_{m0}} \tag{8}$$

The temperature of the streaming gas-vapour mixture may be ascertained using the heat equilibrium equation for the gas-vapour flow, expressed as:

$$-c_{pm}d\left(\dot{m}_m T_m\right) = d\dot{Q} = \frac{h_m \pi d_d^2 n}{l}(T_m - T_d)dx \tag{9}$$

or

$$-c_{pm}\left(\dot{m}_m dT_m + d\dot{m}_m T_m\right) = \frac{h_m \pi d_d^2 n}{l}(T_m - T_d)dx \tag{10}$$

And the temperature gradient for the mixture of gases:

$$\frac{dT_m}{dx} = -\frac{T_m}{\dot{m}_m}\frac{d\dot{m}}{dx} - \frac{h_m \pi d_d^2 n}{l\dot{m}_m c_{pm}}(T_m - T_d) \tag{11}$$

Used boundary condition have been presented in Table.6.

The details of the equations and their discretization elaborated in our previous study [18].

2.3. Model verification

This section outlines a procedure aimed at validating the precision and dependability of a model through the comparison of analytical and experimental outcomes. Initially, this comparison was conducted between analytical results generated without considering the presence of CO_2 and experimental data obtained within our laboratory setting (Fig. 4a). The experimental setup encompassed specific parameters, including a water mass flow rate ($\dot{m}_{water}$) of $29\left(\frac{g}{s}\right)$, water temperature ($T_{water}$) set at 18°C, water pressure (P_{water}) maintained at $14.7bar$, and a steam temperature (T_{steam}) of 100°C. The investigation primarily focused on assessing the outlet temperature of the SEC under varying steam mass flow rates, which revealed an acceptable concordance between the theoretical predictions and experimental observations. The percent deviations between analytical and experimental results for the outlet temperature of SEC were found to be 2.38 %, 1.61 %, 1.62 %, and 0.87 % for steam mass flow rates of 1.2, 2.4, 3.6, and 4.8 $\left(\frac{g}{s}\right)$, respectively. In sequence, an analysis was conducted to evaluate the model's reliability in the presence of CO_2. Experimental data pertaining to the inlet temperature of the SEC across different volumetric flow rates of CO_2 were juxtaposed against the theoretical model's predictions. This comparison highlighted a notable consistency between the experimental results and the distribution derived from the theoretical model, as evidenced by Fig. 4b. The percent deviations between the analytical and experimental results were all below 1 %. Additionally, both analytical and experimental condensation mass flow rates were scrutinized under various steam mass flow rates, as depicted in Fig. 5. Remarkably, a commendable alignment between the theoretical outcomes and experimental observations was evident. The discrepancies between analytical and experimental results in condensation mass flow rates were 3.7 %, 6.5 %, 2.3 %, and 1.1 % for steam mass flow rates of 1.2, 2.4, 3.6, and 4.8 $\left(\frac{g}{s}\right)$, respectively.

3. Cyclone separator

3.1. Modeling

The capability of cyclone separators is subject to a variety of factors, necessitating precise calibration of component dimensions to achieve maximum separation effectiveness while mitigating pressure drop. Cyclone separators are typically classified into two primary categories according to their structural designs: those with tangential inlets and those with axial inlets. Cyclone separators with tangential inlets are extensively employed across diverse industries due to their established reliability and relatively straightforward design, generally consisting of

Table 6
Boundary conditions.

parameter	unit	value
u_{m0}	$\frac{m}{s}$	0–45
m_g	$\frac{kg}{s}$	$(A_0 - A_j) \times \rho_g \times u_{m0}$
h_{lv}	$\frac{KJ}{kg}$	2460.6
C_{pl}	$\frac{KJ}{kg.K}$	4.190

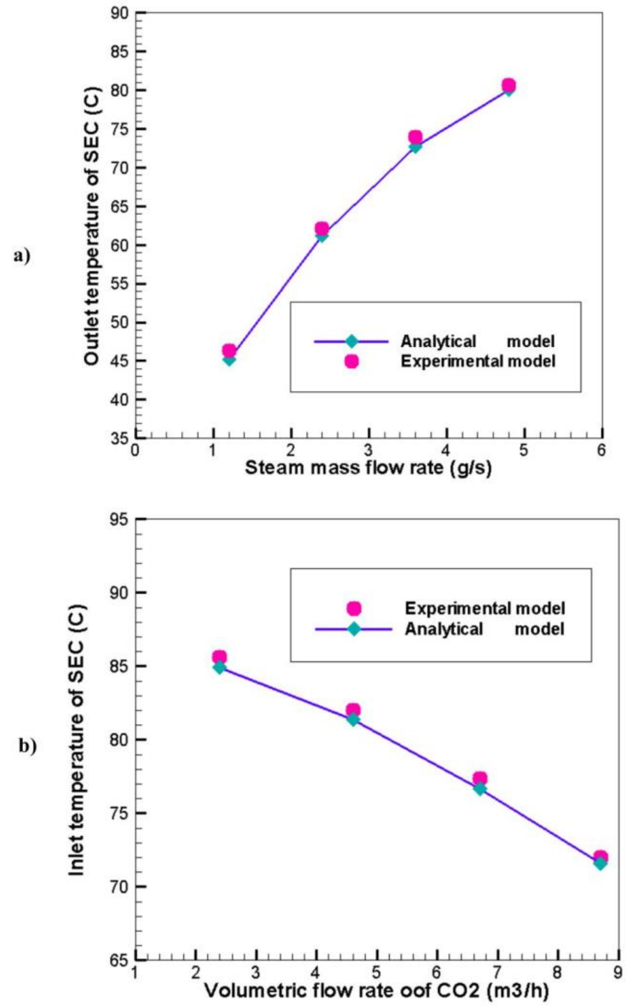

Fig. 4. Validation of SEC for $\dot{m}_{water} = 29\left(\frac{g}{s}\right)$, $T_{water} = 18^{\circ}$C, $P_{water} = 14.7bar$, $T_{steam} = 100^{\circ}$C a) without CO_2 and b) with CO_2 at..$\dot{m}_{steam} = 2.4\left(\frac{g}{s}\right)$

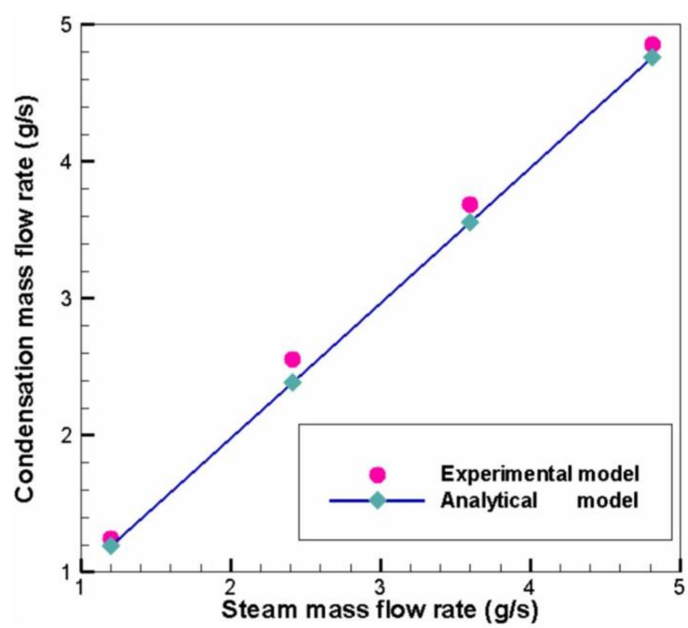

Fig. 5. Condensation mass flow rate at $\dot{m}_{water} = 29\left(\frac{g}{s}\right)$ and volumetric flow rate of $CO_2 = 2.6..\left(\frac{m^3}{h}\right)$

conical and cylindrical parts. As depicted in Fig. 6, a three-dimensional representation of a cyclone separator with a tangential inlet showcases its design layout. After fully condensation of steam along SEC, mixture of water- CO_2 is introduced into the separator with significant tangential velocity, inducing swift swirling motion in the annular gap between the cylinder and exhaust pipe. The resulting centrifugal force propels water droplets within the mixture are hurled to the wall, and then fall down along the wall because of the combined impacts of momentum and gravitational forces. Afterward, they are discharged through the underflow outlet. Concurrently, the purified CO_2 ascends through the central region of the separator and is discharged through the exhaust pipe.

3.2. Governing equations

Computational Fluid Dynamics (CFD) offers several advantages in fluid dynamics research and engineering applications [36,37]. It allows for the simulation of fluid flow in complex geometries and diverse conditions, aiding in the optimization of designs across industries [38]. CFD provides detailed insights into fluid flow characteristics, such as velocity profiles and pressure distributions, enhancing understanding of fluid behavior. Compared to experimental testing, CFD is cost-effective and allows for rapid exploration of design parameters and operating conditions [39]. Numerical modeling plays a crucial role in CFD by enabling the simulation of fluid flow phenomena with high accuracy and efficiency. In CFD, numerical models are employed to address the governing equations of fluid flow, like the Navier-Stokes equations, within a computational domain. These models discretize the domain into a grid or mesh and solve the equations iteratively to predict the behavior of the fluid. Fluent is a leading software package widely used for CFD simulations, offering advanced capabilities for modeling complex fluid flow phenomena, including two-phase flow. Two common approaches for simulating two-phase flow in Fluent are the Euler-Lagrange and Euler-Euler methods. The Euler-Lagrange approach is utilized to model dispersed phase particles, bubbles, or droplets within a continuous fluid phase. In this method, the dispersed phase is tracked individually using Lagrangian particle tracking techniques, while the continuous phase is characterized by solving governing equations of fluid flow. Fluent implements the Euler-Lagrange approach for simulating scenarios where the dispersed phase comprises a small volume fraction (under 10–12 %) of the total flow. On the other hand, the Euler-Euler method regards both phases as continuous entities that interpenetrate, where each phase occupies distinct volumes within the computational domain. This method involves solving separate sets of equations for each phase, including mass and momentum conservation equations, while considering interactions between the phases. Fluent offers various Euler-Euler multiphase models, such as the Eulerian, Volume of Fluid (VOF) and mixture models, each suitable for different types of two-phase flow scenarios [40]. This investigation delves into the application of the mixture model, also known as an algebraic slip method. This model serves as a simplified alternative to the Euler-Euler model and is tailored for simulating flows characterized by a significant presence of dispersed phases (>10 %), including particles, droplets and bubbles, where interparticle collisions exert considerable influence. Unlike the Eulerian approach, which treats the phases as distinct continua, the mixture model accommodates varying velocities among fluid phases and permits their intermingling. The transfer of mass, momentum, and energy between phases is enabled by this feature, rendering it well-suited for capturing the intricate interactions inherent in multiphase flows. Furthermore, successful applications of the mixture model have been observed in CFD modelling, particularly in the study of turbulent swirl multi-phase flow through liquid–gas cyclone separators.

The continuity equation for the mixture can be formulated as follows:

$$\frac{\partial(\rho_m)}{\partial t}+\frac{\partial(\rho_m u_m)}{\partial x_i}=0 \tag{12}$$

Mixture momentum:

$$\frac{\partial(\rho_m u_{mi})}{\partial t}+\frac{\partial(\rho_m u_{mi} u_{mj})}{\partial x_i}=\frac{\partial P}{\partial x_i}+\frac{\partial}{\partial x_j}\mu_m\left(\frac{\partial u_{mi}}{\partial x_j}+\frac{\partial u_{mj}}{\partial x_j}\right)+\rho g_i + \frac{\partial}{\partial x_i}\left(\sum_{q=1}^{n}\alpha_q\rho_q u_{dr,qi}u_{dr,qj}\right) \tag{13}$$

Here, u_m signifies mass-averaged velocity, ρ_m stands for the mixture density and μ_m denotes mixture viscosity.

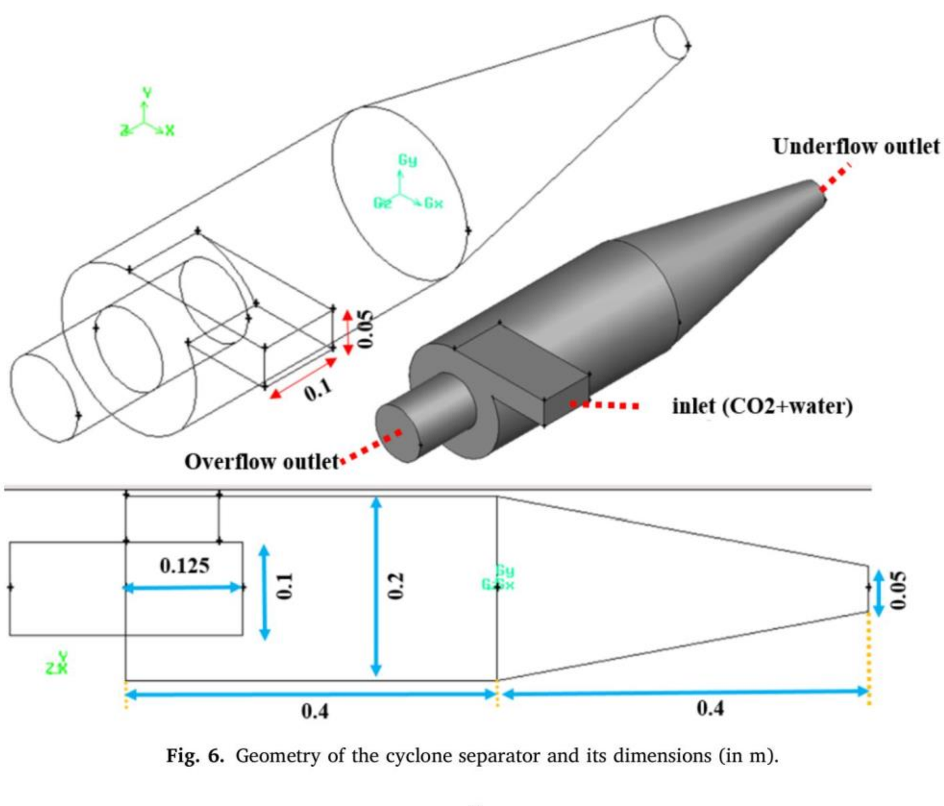

Fig. 6. Geometry of the cyclone separator and its dimensions (in m).

$$u_m = \frac{\sum_{q=1}^{n} \alpha_q \rho_q u_q}{\rho_m}, \rho_m = \sum_{q=1}^{n} \alpha_q \rho_q, \mu_m = \sum_{q=1}^{n} \alpha_q \mu_q \tag{14}$$

The term $u_{dr,q}$ refers to the drift velocity associated with the secondary phase, determined by the relation: $u_{dr,q} = u_q - u_m$.

Many scholars have conducted research on the separation efficiency of cyclone separators through various means, including numerical modelling, theoretical examination and experimental investigations. Three main approaches are used to investigate the flow field through cyclone separators numerically: Reynolds stress model (RSM) [41], RNG $k-\varepsilon$ numerical model [42] and algebraic stress model (ASM) [43]. RSM is considered the most applicable model for cyclone flow. It addresses various flow characteristics such as streamline curvature, swirling, rotation, and rapid strain rate changes by solving transport equations for each component of Reynolds stress. This approach allows for the accurate capture of the anisotropic turbulence character of cyclone separators. However, it is worth noting that the RSM model requires more computational resources compared to other models due to its detailed calculations [44]. On the other hand, the RNG model, which assumes isotropic turbulence, may not be suitable for cyclone flow characterized by anisotropic turbulence. This limitation makes it less appropriate for accurately capturing the complex flow behavior within cyclone separators. Similarly, the algebraic stress model (ASM) has its constraints. While it may be adequate for certain flow scenarios, it may not accurately predict features such as the recirculation zone and Rankine vortex in strong swirling flow conditions typically encountered in cyclone separators. Furthermore, in comparison to large eddy simulation (LES), RSM is regarded as the most favorable choice for modeling turbulence within cyclones, striking a balance between prediction precision and computational cost [45].

In the RSM with a time step of 0.001 s, the transport equation is formulated as follows.

$$\frac{\partial}{\partial t}\left(\rho \overline{u_i' u_j'}\right) + \frac{\partial}{\partial x_k}\left(\rho u_k \overline{u_i' u_j'}\right) = D_{ij} + P_{ij} + \Pi_{ij} + \varepsilon_{ij} + S \tag{15}$$

Describing the terms in the equation, left side comprises the local time derivative of stress and the convective transport term, represented by the first two terms. On the right side, there are five terms that elucidated as:

$$\text{The stress diffusion term}: D_{ij} = -\frac{\partial}{\partial x_k}\left[\rho \overline{u_i' u_j' u_k'} + \overline{(P' u_j')}\delta_{ik} + \overline{(P' u_i')}\delta_{jk} - \mu\left(\frac{\partial}{\partial x_k}\overline{u_i' u_j'}\right)\right] \tag{16}$$

$$\text{The shear production term}: P_{ij} = -\rho\left[\overline{u_i' u_k'}\frac{\partial u_j}{\partial x_k} + \overline{u_j' u_k'}\frac{\partial u_i}{\partial x_k}\right] \tag{17}$$

$$\text{The pressure}-\text{strain term}: \Pi_{ij} = \overline{p\left(\frac{\partial u_i'}{\partial x_j} + \frac{\partial u_j'}{\partial x_i}\right)} \tag{18}$$

$$\text{The dissipation term}: \varepsilon_{ij} = -2\mu\overline{\frac{\partial u_i'}{\partial x_k}\frac{\partial u_j'}{\partial x_k}} \tag{19}$$

and S is the source term.

3.3. Computational modeling and boundary conditions

The simulation methodology employed to accurately replicate the multiphase flow of CO_2 and water through a cyclone separator using ANSYS Fluent 2021 R1. This methodology was deemed crucial because of the expected substantial interaction between water and CO_2 phases in the swirling conditions through the cyclone. The modelling adopted a transient method, with a convergence criterion set to achieve an accuracy of 10^{-6} to ensure the reliability of the results. In order to achieve a compromise between precision in simulation and computational expenses, 0.001(s) of time step was opted for, and surface tension effects were incorporated into the model. The simulation utilized the SIMPLE algorithm to effectively couple pressure and velocity in the continuity and momentum equations. Furthermore, the PRESTO scheme was chosen for its adeptness flows in curved areas and in handling high-speed swirling steams. To discretize the momentum, volume fraction, and kinetic energy equations, the QUICK method was employed owing to its capability to yield more precise results for rotational swirling flows in comparison to first- and second-order schemes, which might introduce higher errors [46]. Detailed boundary conditions employed in the simulation are delineated in Table 7. This comprehensive simulation methodology ensures a robust representation of the intricate multiphase flow dynamics within the cyclone separator, thereby facilitating an in-depth analysis of its performance and behavior across a spectrum of operating conditions.

3.4. Assessment of computational model

The study focused on computing the separation efficiency, a fundamental parameter in cyclone separator performance assessment [15]:

$$\eta = \left(\frac{\dot{m}_{liquidatinlet} - \dot{m}_{liquidatgasoutlet}}{\dot{m}_{liquidatinlet}}\right) \times 100 \tag{20}$$

where $\dot{m}$ refers to the mass flow rate.

Evaluating pressure drop as a means to assess the system's performance enhancement is considered. Pressure drop, delineated as the variance between inlet and CO_2 outlet pressures, emerges as a pivotal parameter for gauging system efficiency. The calculation involves determining pressure drop (ΔP) by subtracting the inlet pressure (P_{in}) from the CO_2 outlet pressure (P_{out}), as denoted by equation (21).

$$\Delta P = P_{in} - P_{out} \tag{21}$$

The two-phase Reynolds number is expressed as follows [21]:

$$Re_m = \frac{D_h V_m \rho_m}{\mu_m} \tag{22}$$

where D_h represents the hydraulic diameter of the inlet, ρ_m denotes the mixture density and μ_m stands for the mixture viscosity.

3.4.1. Mesh independence

Grid independence is a critical concept in numerical modeling, particularly in CFD. It ensures that simulation results are not

Table 7
Boundary conditions.

Boundary	Types
Inlet	Velocity inlet
Outlets	Pressure Outlet
Wall	No Slip wall

significantly affected by changes in the grid or mesh used to discretize the computational domain. This is essential for obtaining reliable and accurate results that accurately represent the underlying physics of the simulated problem. The importance of grid independence stems from the direct influence of grid resolution on the accuracy of the numerical solution. Coarse grids may lead to the underestimation or over-simplification of flow characteristics, while overly fine grids can result in excessive computational costs without substantial improvements in accuracy. Therefore, it is crucial to determine the minimum grid resolution needed to adequately capture the relevant flow phenomena. The assessment of grid independence typically involves conducting simulations with varying grid resolutions and comparing the results to identify the point at which further grid refinement does not significantly alter the solution. Once grid independence is achieved, confidence in the reliability of the numerical model increases. Grid independence offers several advantages, including enhanced accuracy, efficient allocation of computational resources, improved validation of numerical models, and increased robustness of the model across different resolutions and computational domains. In Gambit 2.4.6, the geometry of the cyclone separator was created, representing its intricate structure and components. This involved accurately defining the various geometrical features such as the cylindrical and conical sections, inlet and outlet ports. Subsequently, the created geometry was meshed in Gambit to discretize the computational domain into smaller elements suitable for numerical simulation (Fig 7). Meshing involves dividing the geometry into smaller elements, such as lines, faces, and volumes, to enable the numerical solution of governing equations. In Gambit, meshing operations were performed to refine the mesh in areas of interest, such as near walls, sharp corners, or regions with complex flow patterns, to ensure accurate representation of the flow physics. Mesh refinement was achieved by adjusting the density of mesh lines, increasing the number of mesh faces, and refining the mesh volume. This process aimed to achieve a finer mesh resolution in critical regions of the geometry, where flow gradients or boundary layer effects are significant, while maintaining a coarser mesh in less critical areas to minimize computational costs. To generate a mesh suitable for CFD simulations, Tet/Hybrid elements and the TGrid type were employed in Gambit. Tetrahedral and hybrid elements are well-suited for complex geometries and flow domains with irregular shapes or intricate internal structures, such as the cyclone separator. These elements offer flexibility in capturing flow features accurately and efficiently, particularly in regions with high curvature or geometric complexity. The TGrid type, a feature in Gambit, allowed for the generation of structured or unstructured grids based. This capability enabled the creation of cells that conform well to the geometry of the cyclone separator, ensuring that the mesh accurately represents the flow domain and facilitates efficient numerical simulations [47,48]. To validate the independence of results from the grid size, we examined mesh-independent solutions for the cyclone separator by employing various grid configurations. The graph in Fig. 8 displays the variations in separation efficiency and tangential velocity for different node counts. Notably, the results obtained with 250,042 and 500,172 grids exhibit disparities compared to the other grids (751,052 and 1,056,010). While the outcomes for 751,052 and 1,056,010 nodes are approximately similar, we opted for the 751,052 nodes to reduce computational costs.

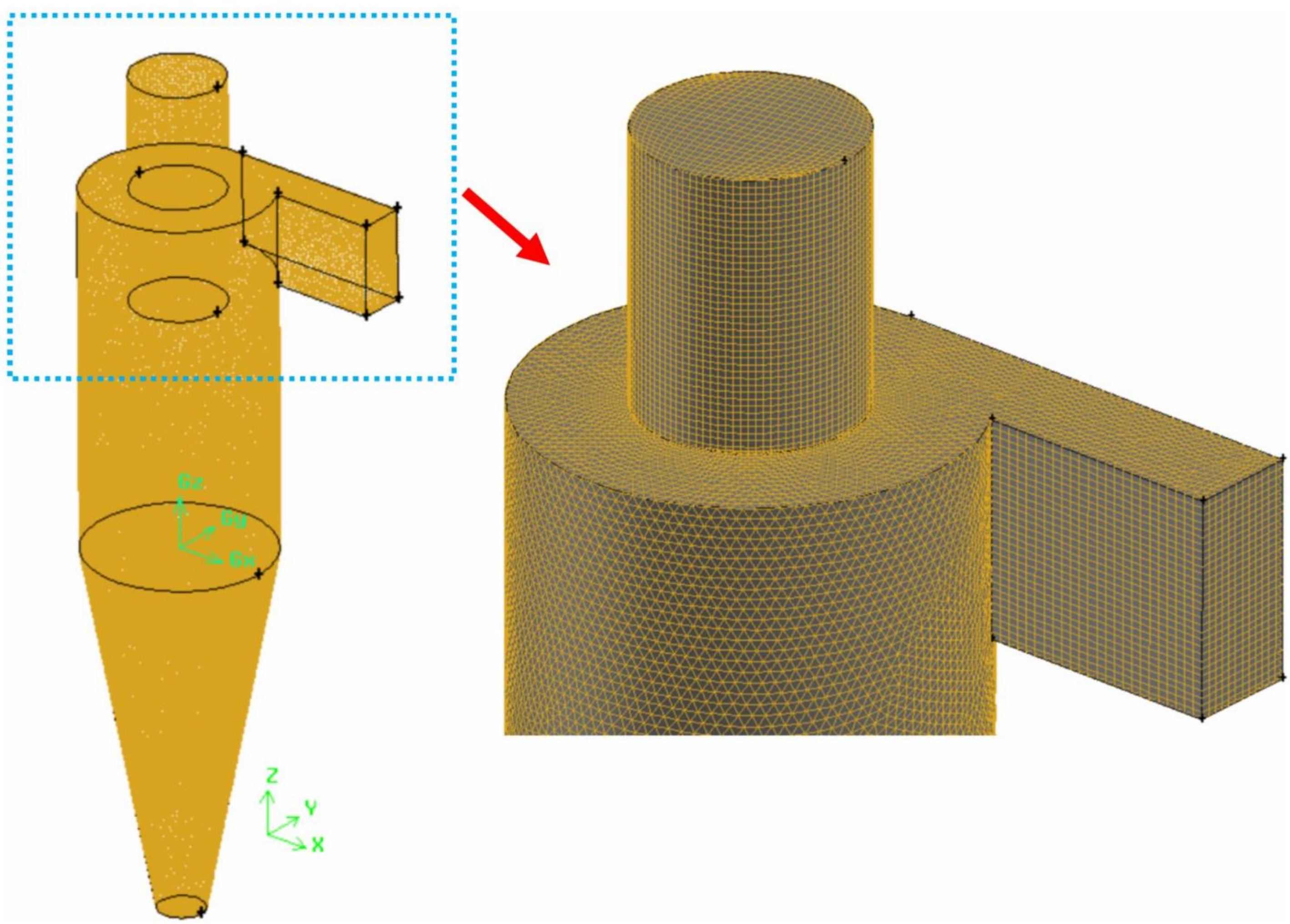

Fig. 7. Mesh of cyclone separator.

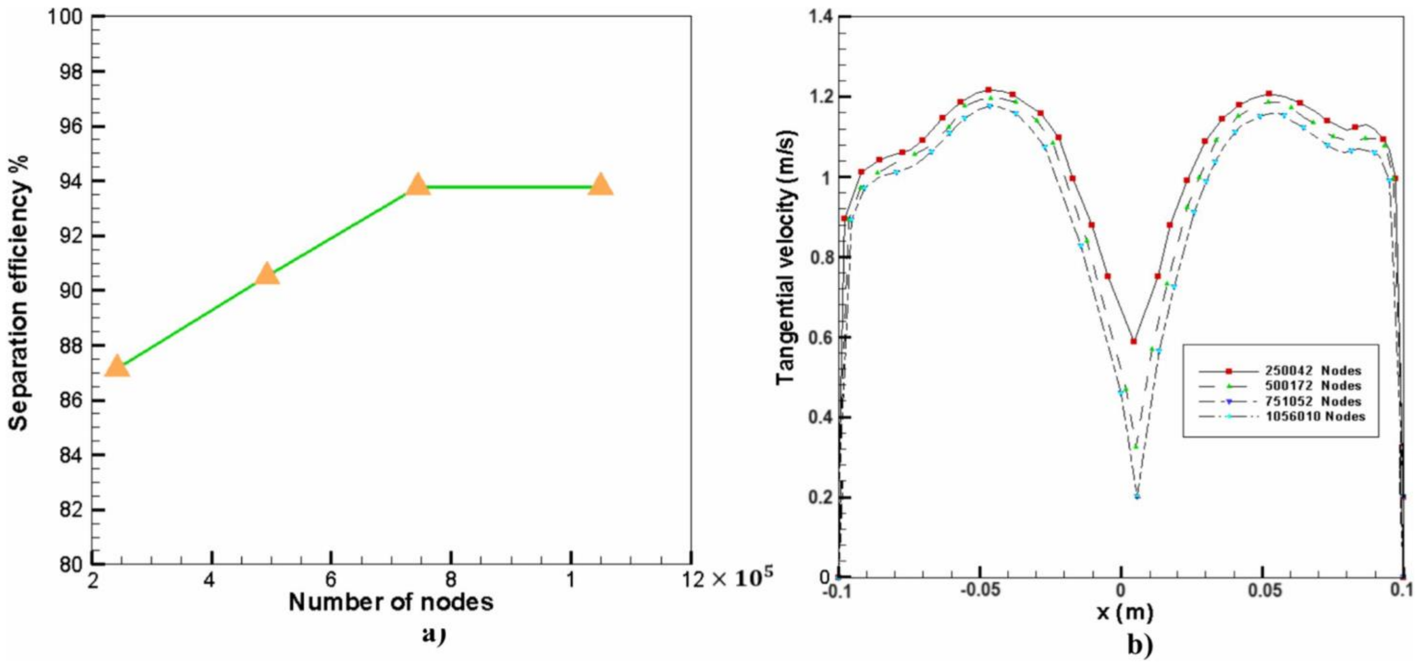

Fig. 8. Mesh independence for a) Separation efficiency at $\dot{m}_{CO2} = 18\frac{g}{s}$ and $\dot{m}_{liquidatinlet} = 100\frac{g}{s}$ and b) Tangential velocity.

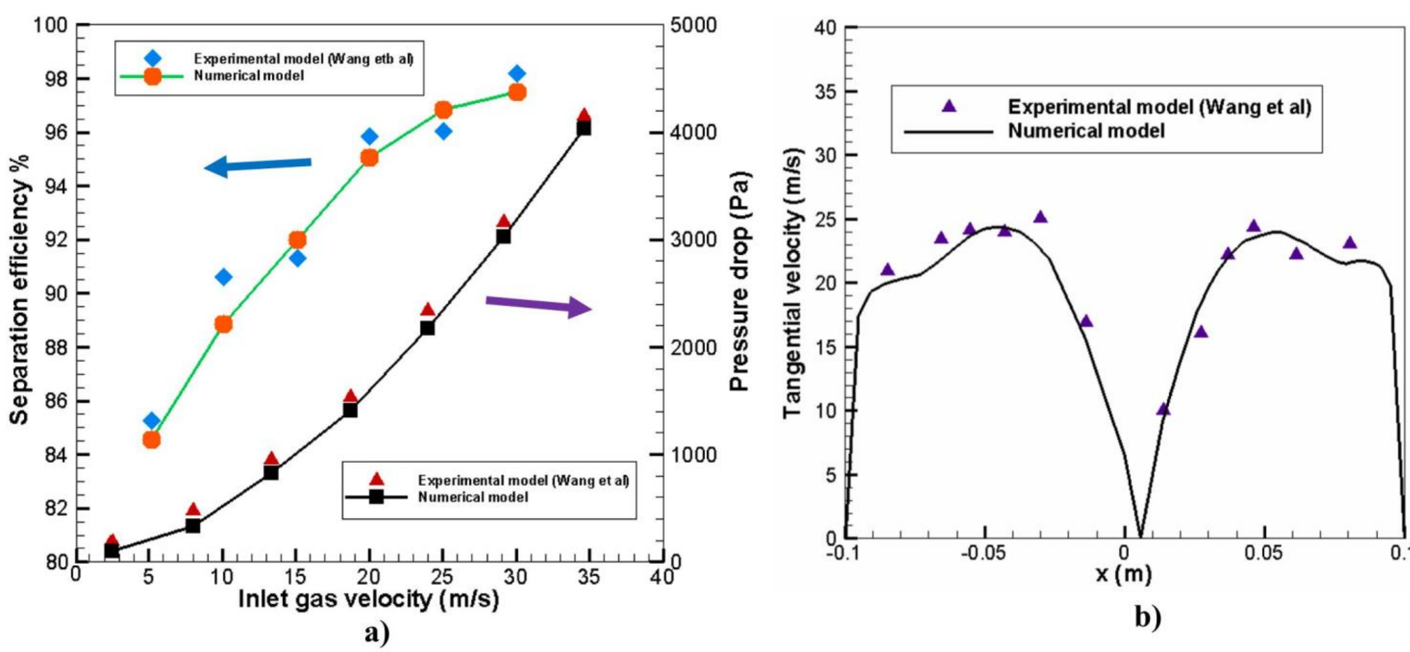

Fig. 9. Comparison of a) pressure drop and separation efficiency and b) tangential velocity between experimental data (Wang et al) and numerical modelling.

3.4.2. Model validation

Estimated deviations in pressure drop, separation efficiency, and tangential velocity, as delineated in Fig. 9, are compared with the experimental observations documented by Wang et al [49]. In the experimental study conducted by Wang et al., a controlled introduction of air was initiated into the inlet of cyclone, and its rate of flow was examined utilizing a flowmeter. Both constituents, exhibited a uniform velocity of 20 m/s throughout the experimental test. The discharge conduit of the cyclone remained open to the atmosphere, while gas pressure at apex of vortex finder was rigorously regulated to maintain a constant pressure of 1 atmosphere. Furthermore, the proportion of second phase was set at 10 %. To ascertain pressure and velocity distributions within the gas field, Wang et al. employed five-hole probe, which was constructed with an adaptable frame housing five pressure transducers. These transducers facilitated the generation of voltage, subsequently amplified post-placement through gas flow field. Enhanced voltage was collected utilizing a data collection apparatus, which was furnished with and interfaced with a personal computer and microprocessor. The comparison delineated in Fig. 9 accentuates a robust concordance between the experimental data acquired by Wang et al. and the numerical findings procured in the present study. This congruence between experimental and numerical outcomes confers validation and instills confidence in the precision of the numerical simulation, signifying that the model adeptly encapsulates the intricate flow dynamics and behavioral nuances within the cyclone separator. Such alignment between empirical and numerical results augments the reliability of the numerical model and underscores its efficacy for subsequent analyses and refinements aimed at optimizing the performance of cyclone separators.

4. Results and discussion

4.1. Effect of cone size

In cyclone separators, ensuring a uniform distribution of particles is imperative to optimize the separation efficiency of particles from the gas stream. The uniformity in particle distribution guarantees that all particles experience comparable centrifugal forces, thereby maintaining consistent separation performance across the cyclone. Conversely, an irregular distribution of particles can induce instability in the CO_2 core within the gas stream, a phenomenon known as wavering CO_2 core, resulting from uneven particle dispersion. Such instability can lead to fluctuations within the CO_2 core, compromising separation efficiency and potentially diminishing the purity of the extracted CO_2. Therefore, the maintenance of uniform particle distribution stands as a fundamental aspect in preserving stable and effective separation processes, thereby mitigating wavering phenomena in the CO_2 core and enhancing the purity of the isolated CO_2. Several factors, including cyclone geometry, significantly influence particle distribution and should be optimized to attain optimal separation performance. As a strategic approach to address this concern, the utilization of single and dual inlet cyclone separators has been considered (Fig. 10), driven by previous studies suggesting an enhanced efficiency with an increased number of inlets [15]. In single inlet cyclones, the presence of a wavering flow pattern presents obstacles to efficient separation. This wavering flow results in droplets positioned close to boundary where the flow reverses to be transported upward in conjunction with CO_2, thereby diminishing the effectiveness of separation. On the other hand, dual inlet cyclones exhibit a stable and unwavering flow structure. Therefore, cyclones with dual inlets has been considered for further investigation of the results.

The length of the cone and cylinder sections plays a critical role in determining the separation efficiency of cyclone separators utilized in gas–solid or gas–liquid separation processes. Modifying the dimensions of these sections allows for the optimization of the cyclone's performance to achieve maximum CO_2 recovery while minimizing the carry-over of water droplets at the gas outlet. By comprehending how alterations in cone size and cylinder section impact separation efficiency, engineers can design cyclones that effectively segregate CO_2 from water droplets. Additionally, appropriately sizing the cone and cylinder section is imperative for managing pressure drop across the cyclone separator. In scenarios involving a mixture of water and CO_2, excessive pressure drop can lead to heightened energy consumption and operational expenses. Investigating the influence of cone size and cylinder section on pressure drop empowers engineers to engineer cyclones that strike a delicate balance between separation efficiency and pressure drop, thereby optimizing the overall performance of the system. Furthermore, the duration for which particles remain within the cyclone is influenced by both cone and cylinder sections. Prolonged residence times facilitate more thorough separation of CO_2 from water droplets. Through an examination of the effects of cone size and cylinder section dimensions on particle dynamics, researchers can design cyclones that guarantee adequate particle residence time for complete CO_2 recovery, thereby enhancing separation efficiency. Moreover, meticulously designed cyclone separators ensure the uniform distribution of particles throughout the separation process. Variations in cone size can impact particle distribution and flow patterns within the cyclone. A thorough investigation of these parameters facilitates the design of cyclones that promote uniform particle distribution, mitigating issues such as channeling or bypassing of particles and enhancing overall separation efficiency. Therefore, comprehending the impact of cone size is vital for scaling up cyclone separators for industrial applications. By selecting the appropriate dimensions, engineers can develop cyclones that seamlessly integrate into larger carbon capture systems. Investigating these parameters facilitates the development of cyclones that fulfill the scalability and performance requirements of industrial carbon capture processes. Fig. 11 depicts the geometry and mesh of the cyclone separator with varying cone sizes, ranging from 0.2 m to 0.5 m, while maintaining a constant length of cyclone.

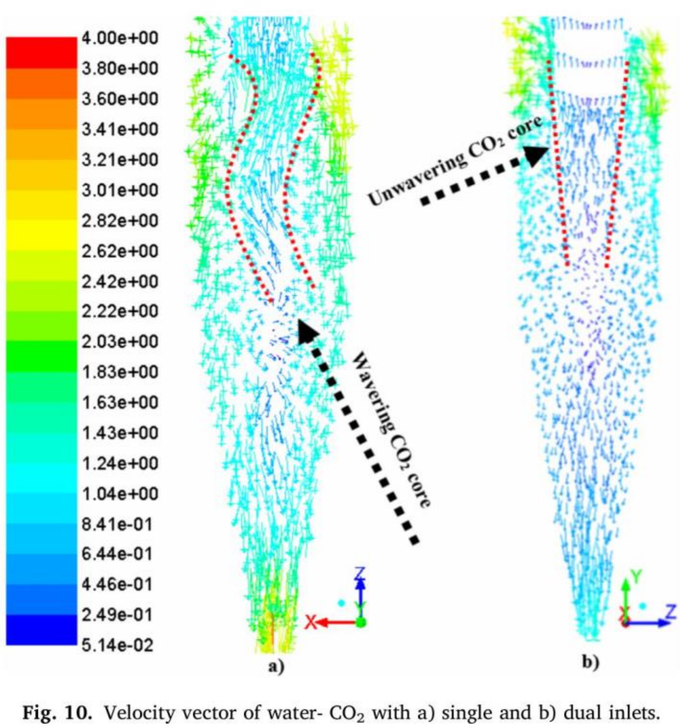

Fig. 10. Velocity vector of water- CO_2 with a) single and b) dual inlets.

Fig. 12 presents the separation efficiency and pressure drop across various cone sizes within a cyclone separator, with a water droplet diameter of 10^{-5}, a CO_2 mass flow rate of 12 $\left(\frac{g}{s}\right)$, and a liquid mass flow rate at the inlet of 100 $\frac{g}{s}$. As the cone size progresses from 0.2 to 0.5 (m), there is a consistent decline in the mass flow rate of water at the gas outlet, diminishing from approximately 0.022651 $\left(\frac{kg}{s}\right)$ for the smallest cone length to around 0.018986 $\left(\frac{kg}{s}\right)$ for the largest cone length. Concurrently, the pressure drop between the inlet and gas outlet of the cyclone shows a progressive increase, rising from 6.08 Pa for the smallest cone length to 10.91 Pa for the largest cone length. This augmentation in pressure drop signifies elevated flow resistance within the cyclone as the cone size expands. Notably, despite the augmented pressure drop associated with larger cone sizes, there is an overall enhancement trend in separation efficiency. Commencing at 77.30 % for the smallest cone size, the separation efficiency gradually rises and culminates at 80.98 % for the largest cone size. This trend implies that while larger cone sizes entail increased pressure drop, they also foster more efficient separation of CO_2 from water droplets, resulting in elevated separation efficiencies. The observed trend can be attributed to several factors. Firstly, larger cone sizes provide greater centrifugal forces, leading to more effective separation of CO_2 from water droplets due to enhanced particle inertia. Furthermore, the increase in pressure drop with larger cone sizes may promote better droplet coalescence, thereby enhancing separation efficiency. However, it is essential to consider the trade-off between separation efficiency and pressure drop, as higher pressure drops may translate to increased energy consumption and operational costs. Therefore, the selection of cyclone geometry should be guided by the specific objectives of the application. While longer cone lengths may be preferable for maximizing collection efficiency, shorter cone lengths may be favored to minimize pressure drop. In this study, where CO_2 purification at the gas outlet while considering a reasonable pressure drop is the primary criterion, a cone size of 0.5 (m) has been deemed optimal.

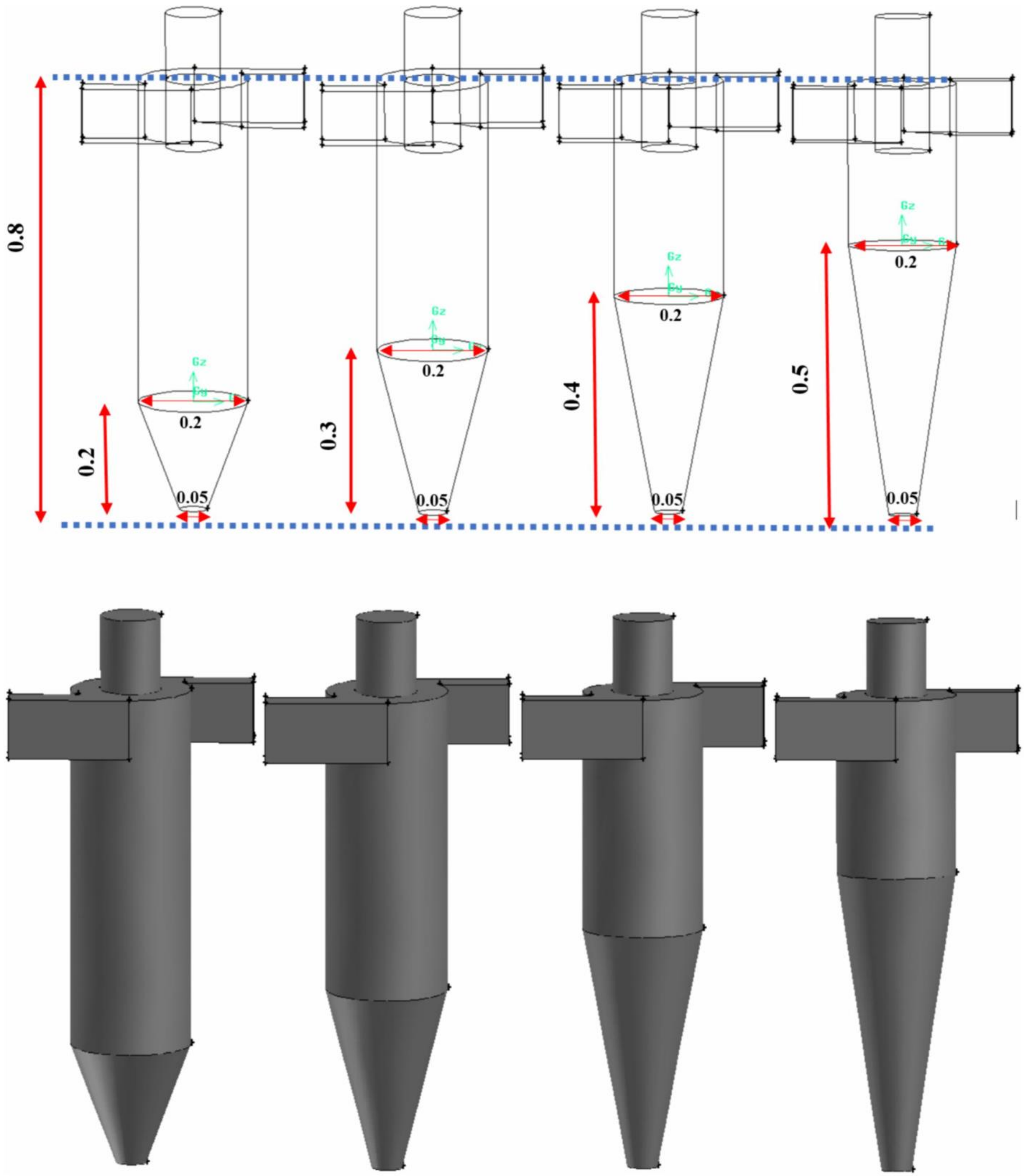

Fig. 11. Geometry and mesh of cyclone at different cones size (in m).

4.2. *Effect of mass flow rate of CO_2*

In our post-combustion carbon capture section, including SEC and cyclone separator, understanding how variations in CO_2 mass flow rate influence separation efficiency and pressure drop is key to enhancing overall system performance. Efficient CO_2 capture relies on maximizing separation efficiency while minimizing energy consumption and operational costs. By investigating the impact of CO_2 mass flow rate on separation efficiency, optimal operating conditions can be identified that ensure high CO_2 capture rates. Additionally, understanding how changes in CO_2 mass flow rate affect pressure drop within the carbon capture system is crucial for maintaining system integrity and minimizing energy requirements. The non-condensable nature of CO_2 presents a unique challenge in the design and operation of SEC within

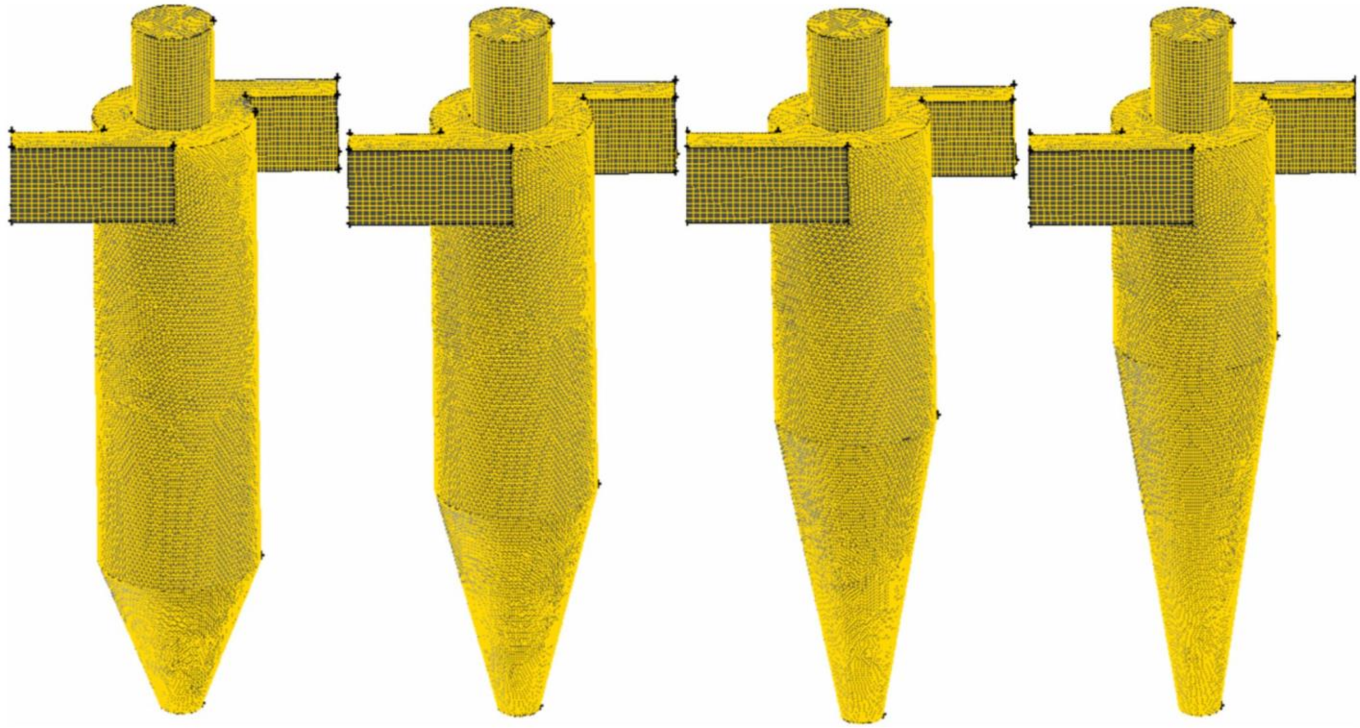

Fig. 11. (*continued*).

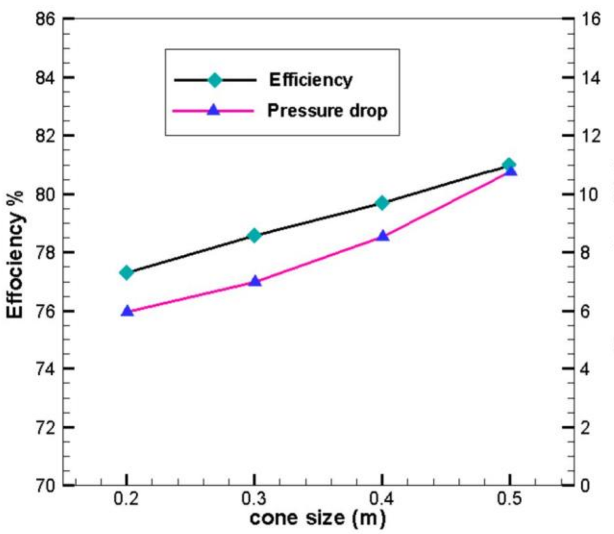

Fig. 12. Separation efficiency and pressure drop at different cone size with a water droplet diameter of 10^{-5} when $\dot{m}_{CO2} = 12\frac{g}{s}$, $\dot{m}_{liquidatinlet} = 100\frac{g}{s}$ and..$Re_m = 5 \times 10^4$

carbon capture systems. Unlike steam, which readily condenses into liquid form under appropriate temperature and pressure conditions, CO_2 remains in its gaseous state throughout the condensation process. This distinction is significant because SECs are typically designed to condense steam, with the assumption that the non-condensable gases present in the mixture, such as CO_2, will be separated and removed from the system. The presence of CO_2 as a non-condensable gas in SECs introduces several considerations for system design and performance. Firstly, the presence of CO_2 affects the overall mass and energy balance within the SEC, as it does not undergo condensation like steam. This necessitates careful consideration of the thermodynamic properties and behavior of CO_2 within the SEC to ensure accurate modeling and prediction of system performance. Additionally, CO_2 can impact the efficiency of steam condensation within the SEC by altering the thermodynamic properties of the gas–liquid mixture. The presence of CO_2 may affect the saturation pressure and temperature of the steam, as well as the heat transfer characteristics of the condensing fluid. This can result in changes to the overall condensation rate and efficiency of the SEC, potentially impacting the system's ability to capture CO_2 effectively. Furthermore, the presence of CO_2 as a non-condensable gas in the SEC necessitates the inclusion of separation and purification mechanisms to remove CO_2 from the condensed liquid stream. This typically involves additional processes, such as cyclone separators or distillation columns, to separate the CO_2 from the condensed water before it is discharged from the system. The efficiency and effectiveness of these separation mechanisms are critical for ensuring high-purity condensate and maximizing the overall performance of the carbon capture system. Therefore, the non-condensable nature of CO_2 presents both challenges

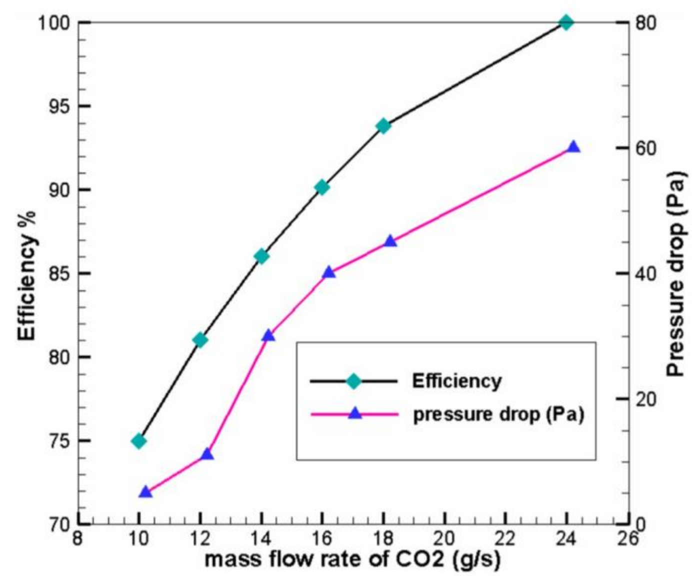

Fig. 13. Separation efficiency and pressure drop at different mass flow rate of CO_2 with a water droplet diameter of 10^{-5} and $l_{cone}0.5m$ at..$\dot{m}_{liquidatinlet} = 100\frac{g}{s}$

and opportunities in the design and operation of SECs within carbon capture systems. Fig. 13 illustrates the impact of varying mass flow rates of CO_2 on the separation efficiency and pressure drop within the cyclone separator, considering a water droplet diameter of 10^{-5} and a fixed cone size of 0.5 m, with a constant liquid mass flow rate at the inlet set to 100 $\frac{g}{s}$. An increase in the mass flow rate of CO_2 leads to an increase in the pressure drop across the cyclone separator. Specifically, the pressure drop values correspond to 5.1, 10.91, 30.2, 40.1, 44.9, and 60.1 Pa for CO_2 mass flow rates of 10, 12, 14, 16, 18, and 24 $\frac{g}{s}$, respectively. This phenomenon can be attributed to the higher volumetric flow rate of the gas mixture passing through the cyclone, resulting in increased resistance to flow and higher frictional losses within the cyclone geometry. Consequently, a higher mass flow rate of CO_2 correlates with a higher pressure drop across the cyclone separator. In addition, the provided data demonstrates a significant correlation between the mass flow rate of CO_2 and the separation efficiency of the cyclone separator. Firstly, as the mass flow rate of CO_2 increases from 10 $\frac{g}{s}$ to 24 $\frac{g}{s}$, there is a noticeable decrease in the mass flow rate of liquid at the gas outlet. This trend suggests that higher mass flow rates of CO_2 result in more efficient separation of CO_2 from the liquid phase, leading to reduced liquid carryover at the gas outlet. Secondly, the separation efficiency of the cyclone separator exhibits a corresponding increase with higher mass flow rates of CO_2. Specifically, as the mass flow rate of CO_2 increases from 10 $\frac{g}{s}$ to 24 $\frac{g}{s}$, the separation efficiency improves from 74.97 % to 100 %, respectively. This trend indicates that higher mass flow rates of CO_2 contribute to more effective separation of CO_2 from the liquid phase, resulting in higher separation efficiencies. Higher mass flow rates of CO_2 lead to increased turbulence and mixing within the cyclone separator. This enhanced interaction between the gas and liquid phases promotes more efficient contact. Also, as the mass flow rate of CO_2 increases, the momentum of the gas phase also increases, resulting in greater centrifugal forces within the cyclone separator. These centrifugal forces play a crucial role in driving the separation process by causing the denser water droplets to move towards the outer wall of the cyclone while allowing the lighter CO_2 to concentrate towards the center. With higher mass flow rates of CO_2, the stronger centrifugal forces facilitate more effective separation of CO_2 from the liquid phase, contributing to increased efficiency.

4.3. Impact of droplet break-up in SEC on separation efficiency

The process of primary droplet genesis within a SEC, underscoring the pivotal role of surface waves on the streaming medium. These undulations prompt the formation of primary droplets, with their size modulated by the magnitude of the wave and the endeavor to minimize surface energy. Under specific outflow conditions of the liquid jet, an optimal wavelength manifests. This wavelength surpasses the jet's circumference, inducing an augmentation in wave amplitude and consequentially resulting in the break-up of the liquid jet into smaller droplets. This observation underscores the intricate interplay between surface wave dynamics and jet attributes in dictating droplet dimensions within the SEC. To further deepen comprehension, scholarly inquiries may delve into how alterations in wave properties, such as wavelength and amplitude, influence droplet generation. Furthermore, investigating the impact of jet characteristics, including velocity and viscosity, on wave dynamics and droplet size distribution could furnish valuable insights into refining the design and efficacy of SECs across diverse applications. Following the initial production of droplets during primary atomization, a secondary breakup phenomenon occurs, yielding smaller droplets. Weber established a correlation to quantitatively characterize the size of these secondary droplets. Understanding the dynamics of secondary droplet formation holds paramount importance in optimizing SEC performance for vapor capture and condensation, thereby augmenting the efficacy of carbon capture processes. Moreover, delving into the mechanisms underpinning secondary droplet breakup can furnish valuable insights into methodologies for regulating droplet size and distribution, thus attaining desired separation efficiencies in carbon capture systems [18,50]:

$$\frac{d_d}{Dj} = 1.436\left(1 + 3\frac{We^{0.5}}{Re}\right)^{1/6} \tag{23}$$

$$We = \frac{\rho_l u_l^2 D_j}{\sigma_l} \tag{24}$$

$$Re = \frac{\rho_l u_l D_j}{\mu_l} \tag{25}$$

where Dj, ρ_l, σ_l, μ_l and u_l represent diameter of nozzle, water density, surface tension, dynamic viscosity and velocity of water, respectively.

In addition, the velocity of the droplets ejected from the water nozzle remains consistent with that of the liquid stream along the throat's length in the system. Consequently, the droplets generated exhibit a mass equivalent to that of the liquid throughout of the throat [18].

$$\dot{m}_d = \frac{\pi d_d^3 \rho_l}{6} n = \dot{m}_{l0} = \frac{\pi D^2}{4}(L - L_j)\rho_l \tag{26}$$

$$n = \frac{3}{2}\left(\frac{D}{d_d}\right)^2 \frac{(L - L_j)}{d_d} \tag{27}$$

where n, L, d_d and D indicate total number of droplet, mixing length, diameter of droplet and diameter of mixing length, respectively.

So, there is a direct relationship between number of droplet and diameter of droplet. Exploring the diameter of droplets within a SEC is imperative for the optimization of carbon capture processes. Droplet size directly influences the efficiency of condensation [18] and subsequent CO_2 separation. A detailed analysis of simulation outcomes offers valuable insights into the correlation between droplet diameter and cyclone efficiency. As droplet diameter increases from 1 to 20 (μm), a discernible trend emerges in the mass flow rate of water at the gas outlet (Tble.5). The downward trajectory in mass flow rate indicates that bigger droplets result in reduced water carryover in the separated gas stream, a critical factor for achieving heightened purity levels of captured CO_2.

Moreover, there is a notable enhancement in separation efficiency as droplet diameter increases. The escalation in separation efficiency from 50.98 % to 100 % as droplet diameter rises underscores the significance of droplet size in augmenting CO_2 capture efficacy (Table.8).

Fig. 14 provide insights into the distribution of water droplets at different diameters. Specifically, at a droplet diameter of 1 μm, where the separation efficiency is 50.98 %, the contour shows a relatively uniform distribution of water droplets throughout the cyclone separator, albeit with less concentration compared to higher efficiency scenarios. As the droplet diameter increases to 5 μm and the efficiency improves to 69.12 %, the contour depicts a more concentrated presence of water droplets, particularly towards the outer regions of the cyclone separator. At a droplet diameter of 10 μm and an efficiency of 89.24 %, the contour illustrates even greater concentration of water droplets, particularly along the walls of the cyclone separator. Finally, at a droplet diameter of 20 μm with 100 % efficiency, the contour demonstrates the highest

Table 8
Separation efficiency at different diameter of water when..$l_{cone} = 0.5m, \dot{m}_{CO2} = 16\frac{g}{s}, \dot{m}_{water} = 100\frac{g}{s}$

Diameter of water droplet (μm)	$\dot{m}_{liquidatgasoutlet}(\frac{Kg}{s})$	Separation efficiency,η%
1	0.0489	50.98
5	0.0308	69.12
10	0.010739	89.24
20	0	100

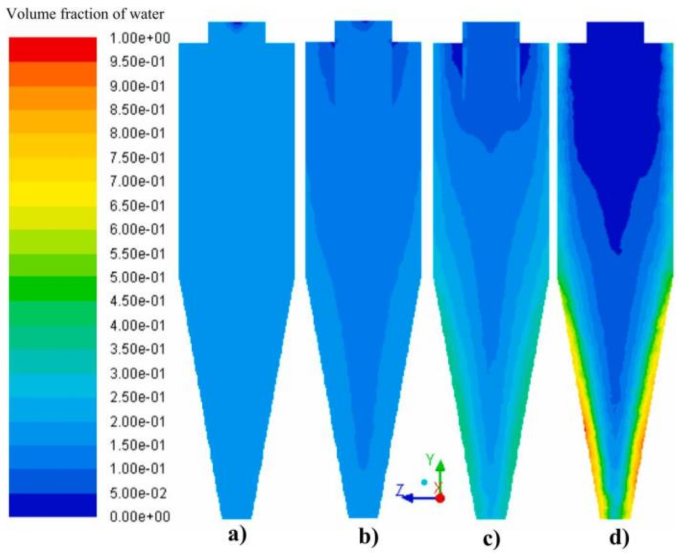

Fig. 14. Volume fraction of water at diameter of droplet of a) 1 μm, b) 5 μm, c) 10 μm and d) 20..μm

concentration of water droplets, densely packed towards the periphery of the cyclone separator, indicating optimal separation performance.

5. Conclusion

To improve the purging procedure within nCO_2PP, a comprehensive methodology was implemented, integrating experimental and analytical modeling of the SEC alongside numerical simulation of the cyclone separator. The integrated approach seeks to enhance the efficiency of the separation unit, guaranteeing the production of high-purity CO_2 in the post-combustion sector of nCO_2PP.

Key findings include the following insights:

- Integration of SEC and cyclone separator offers a practical solution for CO_2 purification, focusing on variables like steam mass flow rate and CO_2 volumetric flow rate to enhance heat transfer.
- Analyzing variations in cyclone cone size, CO_2 flow rate, and droplet breakup reveals trade-offs between separation efficiency and energy consumption.
- Higher CO_2 mass flow rates improve separation efficiency but increase pressure drop, crucial for effective CO_2 capture.
- Understanding droplet breakup in SEC highlights the impact of droplet size on CO_2 capture efficiency.

In conclusion, optimizing these variables is essential for maximizing CO_2 capture effectiveness while managing energy consumption in industrial applications.

6. Future research directions

In addition to the findings above, future research will focus on expanding the capabilities of the system. One avenue of exploration involves increasing the number and variety of nozzles used for water injection into the SEC. This enhancement aims to optimize the distribution and interaction of water and CO2 within the system, potentially improving overall purification efficiency. Furthermore, experimental studies are planned to complement the numerical simulations conducted on the cyclone separator. These experiments will provide a more robust foundation for industrial-scale applications. By integrating experimental data with computational models, the aim is to refine the design and operation of the cyclone separator, ensuring optimal performance in real-world conditions.

CRediT authorship contribution statement

Milad Amiri: Conceptualization, Methodology, Data curation, Formal analysis, Investigation, Resources, Software, Validation, Visualization, Writing – original draft, Writing – review & editing. **Paweł Ziółkowski:** Conceptualization, Data curation, Formal analysis. **Jarosław Mikielewicz:** Methodology, Investigation, Writing – review & editing. **Michał Klugmann:** Methodology, Investigation, Writing – review & editing. **Dariusz Mikielewicz:** Conceptualization, Methodology, Supervision, Project administration, Funding acquisition, Investigation, Writing – review & editing.

Declaration of competing interest

The authors declare that they have no known competing financial interests or personal relationships that could have appeared to influence the work reported in this paper.

Data availability

Data will be made available on request.

Acknowledgements

The research leading to these results has received funding from the Norway Grants 2014–2021 via the National Center for Research and Development. Article has been prepared within the frame of the project: "Negative CO_2 emission gas power plant" - NOR/POLNORCCS/NEGATIVE- CO_2 - PP/0009/2019–00 which is co-financed by programme "Applied research" under the Norwegian Financial Mechanisms 2014–2021 POLNOR CCS 2019 - Development of CO_2 capture solutions integrated in power and industry processes.

References

[1] Y. Shao, et al., Techno-economic evaluation of CO2 capture and storage retrofit in decarbonizing different thermal power plants: A case study in China, Appl. Therm. Eng. 242 (2024) 122380.
[2] S. Cloete, A. Giuffrida, M.C. Romano, A. Zaabout, Heat pump-driven adsorption CO2 capture for simple and cost-effective retrofits of coal power plants, Appl. Therm. Eng. 236 (2024) 121456.
[3] V.T. Skjervold, L.O. Nord, Thermal energy storage integration for increased flexibility of a power plant with post-combustion CO2 capture, Appl. Therm. Eng. 246 (2024) 122907.
[4] L.F. Vega, D. Bahamon, I.I. Alkhatib, Perspectives on Advancing Sustainable CO2 Conversion Processes: Trinomial Technology, Environment, and Economy, ACS Sustain. Chem. Eng. 12 (14) (2024) 5357–5382.
[5] R.S. Haszeldine, Carbon capture and storage: how green can black be? Science 325 (5948) (2009) 1647–1652.
[6] Q. Li, Z. Chen, J.-T. Zhang, L.-C. Liu, X. Li, L. Jia, Positioning and revision of CCUS technology development in China, Int. J. Greenhouse Gas Control 46 (2016) 282–293.
[7] H. Wu, X. Zhang, Q. Wu, Research progress of carbon capture technology based on alcohol amine solution, Sep. Purif. Technol. (2023) 125715.
[8] A. Skorek-Osikowska, K. Janusz-Szymańska, J. Kotowicz, Modeling and analysis of selected carbon dioxide capture methods in IGCC systems, Energy 45 (1) (2012) 92–100.
[9] C. Huang, et al., Influence of secondary air blade angle and oxygen-rich combustion characteristics of an improved Babcock swirl burner, Appl. Therm. Eng. 241 (2024) 122383.
[10] S. Dong, H. Cheng, Y. Niu, Space numerical simulation of full oxygen combustion flame in glass melting furnace based on flue gas preheating, Appl. Therm. Eng. 242 (2024) 122384.
[11] T. Yuan, et al., Computational fluid dynamics simulation on oxy-fuel combustion performance of a multiple-burner furnace firing coking dry gas, Appl. Therm. Eng. (2024) 123728.
[12] P. Ziółkowski, et al., Thermodynamic analysis of negative CO2 emission power plant using Aspen Plus, Aspen Hysys, and Ebsilon software, Energies 14 (19) (2021) 6304.
[13] P. Ziółkowski, K. Stasiak, M. Amiri, D. Mikielewicz, Negative carbon dioxide gas power plant integrated with gasification of sewage sludge, Energy 262 (2023) 125496.
[14] P. Ziółkowski, et al., Mathematical modelling of gasification process of sewage sludge in reactor of negative CO2 emission power plant, Energy 244 (2022) 122601.

[15] M. Amiri, J. Mikielewicz, D. Mikielewicz, CO2 capture using steam ejector condenser under electro hydrodynamic actuator with non-condensable gas and cyclone separator: A numerical study, Sep. Purif. Technol. 329 (2024) 125236.
[16] P. Madejski, M. Karch, P. Michalak, K. Banasiak, Conceptual Design of Experimental Test Rig for Research on Thermo-Flow Processes During Direct Contact Condensation in the Two-Phase Spray-Ejector Condenser, J. Energy Res. Technol. 146 (3) (2024) pp.
[17] M. Amiri, M. Klugmann, J. Mikielewicz, P. Ziółkowski, D. Mikielewicz, CO2 capture through direct-contact condensation in a spray ejector condenser and T-junction separator, Int. Commun. Heat Mass Transfer 156 (2024) 107596.
[18] D. Mikielewicz, M. Amiri, M. Klugmann, J. Mikielewicz, A novel concept of enhanced direct-contact condensation of vapour-inert gas mixture in a spray ejector condenser, Int. J. Heat Mass Transf. 216 (2023) 124576.
[19] T. Kuś, P. Madejski, Analysis of the Multiphase Flow With Condensation in the Two-Phase Ejector Condenser Using Computational Fluid Dynamics Modeling, J. Energy Res. Technol. 146 (3) (2024) pp.
[20] P. Madejski, et al., Development of a spray-ejector condenser for the use in a negative CO2 emission gas power plant, Energy 283 (2023) 129163.
[21] J. Yang, C. Liu, S. Li, B. Sun, J. Xiao, Y. Jin, A new pressure drop model of gas–liquid cyclone with innovative operation mode, Chem. Eng. Process. 95 (2015) 256–266.
[22] H. Safikhani, P. Mehrabian, Numerical study of flow field in new cyclone separators, Adv. Powder Technol. 27 (2) (2016) 379–387.
[23] W. Mazyan, A. Ahmadi, H. Ahmed, M. Hoorfar, Increasing efficiency of natural gas cyclones through addition of tangential chambers, J. Aerosol Sci 110 (2017) 36–42.
[24] C. Han, Y. Hu, W. Li, Q. Bie, Gas-solid separation performance and structure optimization in 3D printed guide vane cyclone separator, Adv. Powder Technol. 33 (11) (2022) 103815.
[25] M. Amiri, J. Mikielewicz, P. Ziółkowski, D. Mikielewicz, Optimising CO2 purification in a Negative CO2 Emission Power Plant, Chem. Eng. Technol. (2024), https://doi.org/10.1002/ceat.202300568.
[26] H. Yoshida, K. Fukui, K. Yoshida, E. Shinoda, Particle separation by Iinoya's type gas cyclone, Powder Technol. 118 (1–2) (2001) 16–23.
[27] F. Qian, J. Zhang, M. Zhang, Effects of the prolonged vertical tube on the separation performance of a cyclone, J. Hazard. Mater. 136 (3) (2006) 822–829.
[28] F. Kaya, I. Karagoz, Numerical investigation of performance characteristics of a cyclone prolonged with a dipleg, Chem. Eng. J. 151 (1–3) (2009) 39–45.
[29] A. Kępa, The effect of a counter-cone position on cyclone performance, Sep. Sci. Technol. 47 (16) (2012) 2250–2255.
[30] H. Yoshida, Y. Nishimura, K. Fukui, T. Yamamoto, Effect of apex cone shape on fine particle classification of gas-cyclone, Powder Technol. 204 (1) (2010) 54–62.
[31] L.S. Brar, R. Sharma, K. Elsayed, The effect of the cyclone length on the performance of Stairmand high-efficiency cyclone, Powder Technol. 286 (2015) 668–677.
[32] N. Prasanna, K. Subramanian, S. Ajay, T. Rajagopal, V. Vigneshwaran, CFD study on the performance of reducing pressure drop holes in cyclone separator, Mater. Today:. Proc. 43 (2021) 1960–1968.
[33] O. Hamdy, M.A. Bassily, H.M. El-Batsh, T.A. Mekhail, Numerical study of the effect of changing the cyclone cone length on the gas flow field, App. Math. Model. 46 (2017) 81–97.
[34] https://nco2pp.mech.pg.gda.pl/pl (accessed).
[35] E. Ganić, W. Rohsenow, Dispersed flow heat transfer, Int. J. Heat Mass Transf. 20 (8) (1977) 855–866.
[36] M. Amiri, D. Mikielewicz, Three-dimensional numerical investigation of hybrid nanofluids in chain microchannel under electrohydrodynamic actuator, Numerical Heat Transfer, Part a: Applications 83 (10) (2023) 1146–1173.
[37] M. Amiri, M.B. Ayani, P. Ziolkowski, D. Mikielewicz, Numerical analysis of vacuum drying of a porous body in the integrated domain, J. Food Process Eng 45 (4) (2022) e14006.
[38] M. Amiri, P. Ziółkowski, D. Mikielewicz, Synergistic effects of a swirl generator and MXene/water nanofluids used in a heat exchanger pipe of a negative CO2 emission gas power plant, Numerical Heat Transfer, Part a: Applications (2024) 1–27.
[39] O.E. Olaleye, B. Van Ombele, A.A. Olusola, X. Li, CFD modeling analysis of a vertical gas liquid separator, J. Pet. Sci. Eng. (2022) 110733.
[40] M.H. Purnanto, S.J. Zarrouk, J.E. Cater, CFD modelling of two-phase flow inside geothermal steam-water separators, IPENZ Transactions 40 (2013) 1–10.
[41] E. Yohana, M. Tauviqirrahman, B. Yusuf, K.-H. Choi, V. Paramita, Effect of vortex limiter position and metal rod insertion on the flow field, heat rate, and performance of cyclone separator, Powder Technol. 377 (2021) 464–475.
[42] A. Surjosatyo, A. Respati, H. Dafiqurrohman, Analysis of the influence of vortexbinder dimension on cyclone separator performance in biomass gasification system, Procedia Eng. 170 (2017) 154–161.
[43] J.V.N. Nejad, S. Kheradmand, The effect of fluctuating boundary on flow field and performance parameters of cyclone separator, Powder Technol. 390 (2021) 401–416.
[44] A. Hoekstra, J. Derksen, H. Van Den Akker, An experimental and numerical study of turbulent swirling flow in gas cyclones, Chem. Eng. Sci. 54 (13–14) (1999) 2055–2065.
[45] J.-H. Lim, S.-H. Oh, S. Kang, K.-J. Lee, S.-J. Yook, Development of cutoff size adjustable omnidirectional inlet cyclone separator, Sep. Purif. Technol. 276 (2021) 119397.
[46] R. Utikar *et al.*, "Hydrodynamic simulation of cyclone separators," in *Computational fluid dynamics*: InTech, 2010, pp. 241-266.
[47] Y. Song, L. Wang, L. Jia, X. Wang, Optimization and performance investigation of confocal twin-nozzle ejector for PEMFC hydrogen supply and recirculation system under actual variable operating conditions, Int. J. Hydrogen Energy 50 (2024) 1450–1464.
[48] "GAMBIT 2.2 Tutorial Guide " Fluent, Incorporated (accessed.
[49] B. Wang, D. Xu, K. Chu, A. Yu, Numerical study of gas–solid flow in a cyclone separator, App. Math. Model. 30 (11) (2006) 1326–1342.
[50] M. Jain, R.S. Prakash, G. Tomar, R. Ravikrishna, Secondary breakup of a drop at moderate Weber numbers, Proc. Royal Soc. A: Math. Phys. Eng. Sci. 471 (2177) (2015) 20140930.

Appendix 3. Article [C]

Milad Amiri[1],*
Jarosław Mikielewicz[2]
Paweł Ziółkowski[1]
Dariusz Mikielewicz[1]

Optimizing CO_2 Purification in a Negative CO_2 Emission Power Plant

In the pursuit of mitigating CO_2 emissions, this study investigates the optimization of CO_2 purification within a negative CO_2 emission power plant using a spray ejector condenser (SEC) coupled with a separator. The approach involves direct-contact condensation of vapor, primarily composed of an inert gas (CO_2), facilitated by a subcooled liquid spray. A comprehensive analysis is presented, employing a numerical model to simulate a cyclone separator under various SEC outlet conditions. Methodologically, the simulation, conducted in Fluent, encompasses three-dimensional, transient, and turbulent characteristics using the Reynolds stress model turbulent model and mixture model to replicate the turbulent two-phase flow within a gas–liquid separator. Structural considerations are delved into, evaluating the efficacy of single- and dual-inlet separators to enhance CO_2 purification efficiency. The study reveals significant insights into the optimization process, highlighting a notable enhancement in separation efficiency within the dual-inlet cyclone, compared to its single inlet counterpart. Specifically, a 90.7 % separation efficiency is observed in the former, characterized by symmetrical flow patterns devoid of wavering CO_2 cores, whereas the latter exhibits less desirable velocity vectors. Furthermore, the investigation explores the influence of key parameters, such as liquid volume fraction (LVF) and water droplet diameter, on separation efficiency. It is ascertained that a 10 % LVF with a water droplet diameter of 10 μm yields the highest separation efficiency at 90.7 %, whereas a 20 % LVF with a water droplet diameter of 1 μm results in a reduced efficiency of 50.79 %. Moreover, the impact of structural modifications, such as the addition of vanes, on separation efficiency and pressure drop is explored. Remarkably, the incorporation of vanes leads to a 9.2 % improvement in separation efficiency and a 16.8 % reduction in pressure drop at a 10 % LVF. The findings underscore the significance of structural considerations and parameter optimization in advancing CO_2 capture technologies, with implications for sustainable energy production and environmental conservation.

Keywords: Computational fluid dynamics, Cyclone separator, Gas–liquid separation, Separation efficiency, Vanes

Received: December 02, 2023; *revised:* June 06, 2024; *accepted:* July 01, 2024

DOI: 10.1002/ceat.202300568

1 Introduction

Carbon dioxide is widely recognized as a significant factor in the context of global warming [1–3]. Due to its substantial influence on climate change, there has been a growing focus on developing various strategies in recent years to control carbon emissions, encompassing techniques such as carbon dioxide capture [4] and storage [5]. Carbon capture and storage (CCS) is recognized as an essential technology, facilitating the efficient reduction of CO_2 emissions [6, 7] from fossil fuel-reliant power plants. In the long term, widespread adoption of carbon-negative emission technologies could bring atmospheric CO_2 levels back to pre-industrial concentrations [8] and could also provide sustainable solutions for heat generation [9]. Furthermore, there is increasing acknowledgment of the potential of integrated plants [10] in natural gas processing to address challenges such as gas

[1]Milad Amiri (milad.amiri@pg.edu.pl), Paweł Ziółkowski, Dariusz Mikielewicz
Faculty of Mechanical Engineering and Ship Technology, Gdańsk University of Technology, ul. Gabriela Narutowicza 11/12, Gdańsk 80-233, Poland.
[2]Jarosław Mikielewicz
Polish Academy of Science, Institute of Fluid-Flow Machinery ul, Fiszera 14, Gdańsk 80-231, Poland.

flaring and contribute to energy sustainability [11–15]. Concurrently, studies [16, 17] shed light on the exergetic sustainability, emissions patterns, and improvement potential of sectors like the Nigerian transport sector, underscoring the importance of addressing emissions and enhancing energy efficiency for future sustainable transport pathways. With these concerns in mind, innovative approaches for generating electricity with negative CO_2 emissions are gaining traction. One such method involves a combination of pre-combustion, oxy-combustion [18], and post-combustion technologies within a power plant setting. In this study, the focus lies particularly on post-combustion processes, which include the utilization of a spray ejector condenser (SEC) and cyclone separator to purify CO_2. Within this advanced negative CO_2 emission power plant cycle, multiple components play crucial roles. Following oxy-combustion within the wet combustion chamber, the resultant mixture of water and steam-CO_2 proceeds to the SEC, where complete condensation of steam occurs. Subsequently, the condensed mixture, comprising water and CO_2, exits the SEC and enters the cyclone separator for the purification of CO_2.

Cyclone separators find extensive applications across various industries, such as mineral processing, chemical engineering, environmental management, and petroleum refining, where they serve the purpose of efficiently separating gases from solids or liquids [19, 20]. There are various types of gas–liquid cyclones. The most commonly used type is the Stairmand cyclone [21], which features a cylindrical section, tangential inlet, vortex finder, and conical section. Cyclone separators can be classified into axial and tangential types based on the direction of the inlet flow toward the cyclone. A tangential cyclone has a tangential inlet flow that generates an outer vortex. The flow is then reversed at the end of the vortex and exits axially from the top. The existence of the density difference and two-phase interface allows for the separation of the mixture through centrifugal separation rather than relying on energy-consuming equipment like permeable membranes that consume significant energy resources. Therefore, using a cyclone separator is both practical and cost-effective. The liquid–gas flow in a cyclone is a complicated process that has garnered significant interest. The centrifugal force in a cone cyclone is the main factor in deaeration, although it results in some loss of flow pressure [22]. Different dimensions and types of cyclones result in varying pressure drops and centrifugal forces. The pressure distribution and tangential velocity in cyclones have been investigated in the literature, showing a drastic centrifugal effects and significant pressure changes in the cyclone [23]. Cyclones are devices that create a swirling flow by using high-velocity fluids entering through one or two (or more) tangential inlets. This generates a vortex core within the device. Mixing can be enhanced by this swirling flow through turbulence and vorticity effects, leading to the separation of higher-density particles or fluids from the base fluid. This refers to a cyclone separator, specifically a cone cyclone, which uses turbulence and physical instabilities to enhance mixing. The design consists of a cylinder with an outer cone, where the flow is injected tangentially into the cylinder, and the liquid exits through the underflow outlet, while gas exits through the overflow outlet.

The efficiency of a cyclone separator is impacted by a range of factors, encompassing its structural geometry [24–27] and operational variables like particle size, gas velocity, and properties of the phases being separated [28]. Vehmaanperä et al. [29] indicated that modifying the overflow pipe has a significant effect on the performance of the cyclone separator in terms of separating efficiency. Studies have also looked into the impact of the cone dimension on the performance of the cyclone separator [30, 31]. Studies have demonstrated that when the cone size is bigger than the gas outlet, decreasing the cone size improves collection efficiency without causing a noticeable increase in pressure drop. Yoshida et al. [32], examined a study using different types of apex cones at the inlet of the dust box. They discovered that the influence of the angle of the apex cone on the collection efficiency reduces when the inlet velocity is high. Studies have also delved into the impact of elongating a cyclone separator with a vertical tube on its efficiency [33, 34]. The impact of a counter-cone located at the bottom of a cyclone separator on its performance has been reported [35, 36]. Brar et al. [37] and Prasanna et al. [38] conducted studies to examine how the length of the cone and cylinder influences separation efficiency and pressure drop. Hamdy et al. [39] performed an investigation on the standard cyclone numerically, varying the length and angle of the cone gradually. The study concluded that the length and angle of the cone have a substantial influence on the separation efficiency of a cyclone separator and the internal flow pattern. The effect of adding a tangential cavity has been studied by Mazyan et al. [21]. Their experiment work showed that the separation efficiency of particles, particularly for small particles, can further be enhanced.

In addition, the use of a guide vane has been found to create a strong swirling effect, causing a small pressure drop, and providing the best separation performance. Umeny et al. proposed a cyclone separator design that separates multiphase flow by rotating it through guide vanes fixed at the inlet of the cyclone. Luping et al. confirmed that using a spindle structure or a better streamlined cone for the guide fluid can effectively reduce pressure loss resulting from the rapid change of speed [40]. Li et al. [41] analyzed steam–water separators equipped with wave-type vanes and the behavior of the droplets in wave-type flow channels. The results revealed that the most significant mechanism for the formation of secondary droplets under operating conditions is the breakup of droplets due to impingement on liquid film. Zhou et al. [42] conducted experimental and numerical studies on the impact of spiral guide vanes on the performance of a cyclone separator. The results showed that as the number of spiral guide vane turns increased, the turbulence intensity in the cyclones gradually decreased, particularly in the cylinder section.

However, notwithstanding the burgeoning enthusiasm surrounding CSS [43, 44], a notable lacuna persists in comprehending the intricacies of integrating and refining post-combustion methodologies within power plants [45–47] for the purposeful capture and sequestration of CO_2 emissions. This study aims to address these gaps by focusing on the post-combustion processes, especially the use of an SEC [48] and cyclone separator for the purification of CO_2 emissions from power plants. The study is motivated by the need to develop cost-effective and efficient solutions for CO_2 capture in power generation, with the ultimate goal of reducing greenhouse gas emissions and mitigating climate change. The novelty of this research lies in its thorough examination of the design and optimization of a tangential-flow CO_2–water separator, along with the investigation of

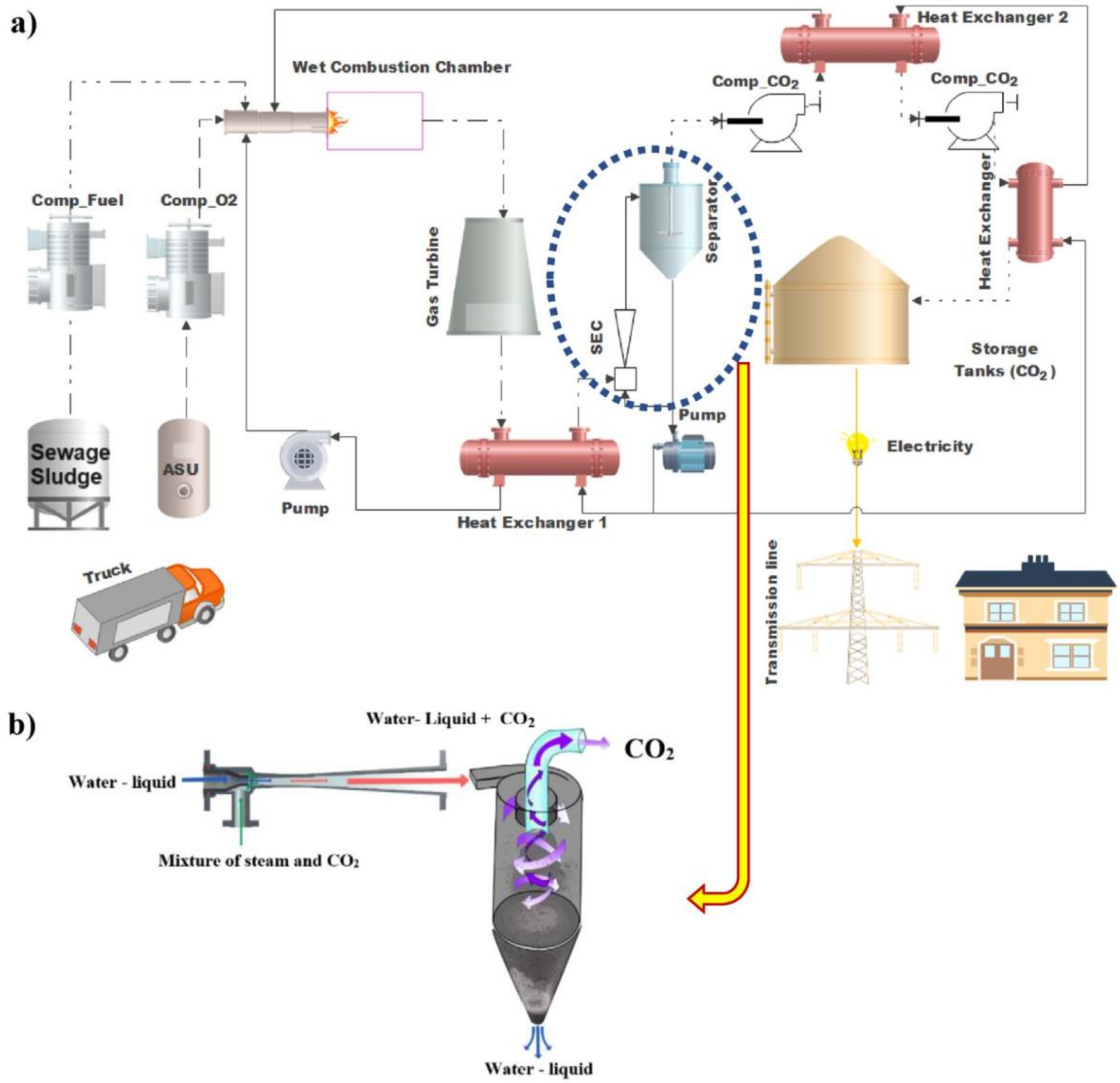

Figure 1. Process flow diagram (PFD) of the negative CO_2 emission gas power plant (nCO_2PP): (a) Overall plant layout, (b) CO_2 capture component (spray ejector condenser [SEC- and cyclone separator), (c) PFD simulation using Aspen HYSYS, and (d) Mixture 1 compositions in volume fraction [50, 51, 53]. ASU, air separation unit.

parameters such as volume fraction and droplet diameter of water for the SEC, specifically tailored for the negative CO_2 emission gas power plant (nCO_2PP) [49]. In order to establish a numerical model and enhance the separator's performance, the initial step involves defining single- and dual-inlet separators. Subsequently, an appropriate value for the liquid volume fraction (LVF) and the diameter of water droplets is determined based on the conditions of the SEC, utilizing the separation efficiency as a guiding parameter. This process allows for the execution of numerical simulations encompassing various LVF values. By considering volume fractions ranging from 10 % to 20 % for the water liquid and diameters of water droplets spanning from 1 to 10 µm, the model is comprehensively developed. After obtaining the model, the performance of the separator affected by vanes can be estimated. Finally, using vanes and dual inlets, the optimum value of the separation efficiency and pressure drop can be calculated.

2 Description of Negative CO_2 Emission Power Plant (nCO_2PP)

The schematic representation of the innovative gas power plant designed to achieve negative CO_2 emissions is depicted in Fig. 1 [50–52]. Fuel production commences with a thermochemical process within the gasifier (R), where dry sewage sludge interacts with a gasifying agent. Optionally, this agent can be released post-gas turbine from a carbon capture unit (CCU) operating at ambient pressure, with adjustable properties such as CO_2 and steam content, temperature, and pressure. Oxygen compression (C_{O2}) is achieved through an air separation unit. Within the process, exhaust from heat exchanger 1 enters an SEC, where the resulting condensed steam and CO_2 mixture undergoes separation in a cyclone separator. The separated CO_2 is directed to the CCU, with a portion available for use as a gasifying agent or in various chemical reactions, while the remainder can be stored

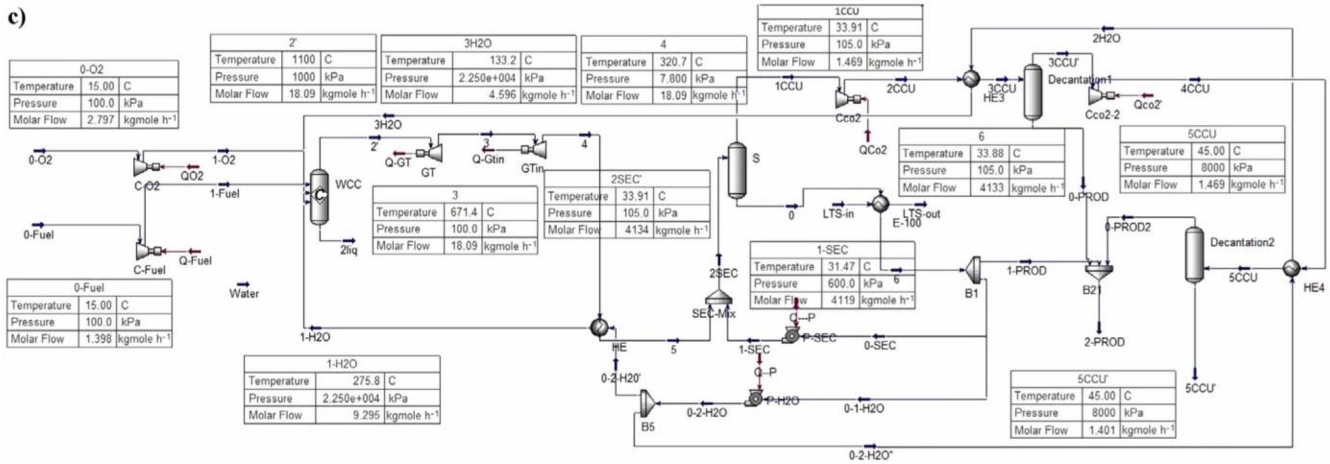

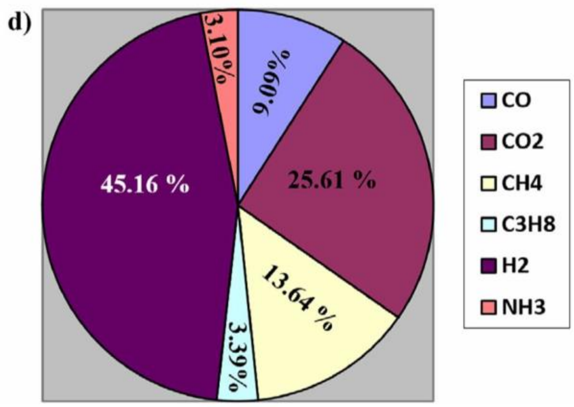

Figure 1. *Continued*

or utilized in processes like methanol production. Fig. 1b illustrates the composition of the separation unit in post-combustion section of nCO_2PP, consisting of the SEC and cyclone separator. The SEC's primary role is to efficiently condense water vapor from exhaust gases while maintaining a compact system design, featuring two inlets for suction and motive fluids and a single outlet. At the outlet of the SEC, both liquid water and CO_2 are directed into the cyclone separator to facilitate CO_2 purification. In our previous study [50], the illustrated process flow diagram was simulated using Aspen HYSYS (depicted in Fig. 1c) and subsequently validated against Aspen Plus and Ebsilon. Two fuel types, methane and mixture1, were utilized, with the composition of mixture1 detailed in Fig. 1d. A subset of the findings was then summarized in Tab. 1 [50].

3 Modeling

3.1 Cyclone Separator

Numerous factors influence the efficiency of cyclone separators, achieving optimal performance while minimizing pressure drop

Table 1. Results for Mixture 1 and methane in Aspen HYSYS [50].

Parameter	Symbol	Unit	Methane	Mixture 1
CO_2 mass flow in the exhaust	$\dot{m}_{2-CO_2}$	[g s^{-1}]	17.1	22.7
Turbine power output	N_t	[kW]	164	157.1
Chemical energy rate of combustion	$\dot{Q}_{CC}$	[kW]	311.8	284.9
Emission of carbon dioxide	eCO_2	[kg MWh^{-1}]	0.0	−720.0
Relative emissivity of carbon dioxide	$\eta_{net} \cdot eCO_2$	[%kg MWh^{-1}]	0.0	−286.70
Avoided emission of carbon dioxide	Avoid eCO_2	[kg MWh^{-1}]	475.33	1440
Avoided relative emissivity of carbon dioxide	Avoid $\eta_{net} \cdot eCO_2$	[%kg MWh^{-1}]	197.45	573.40
Net efficiency	η_{net}	[%]	41.5	39.9

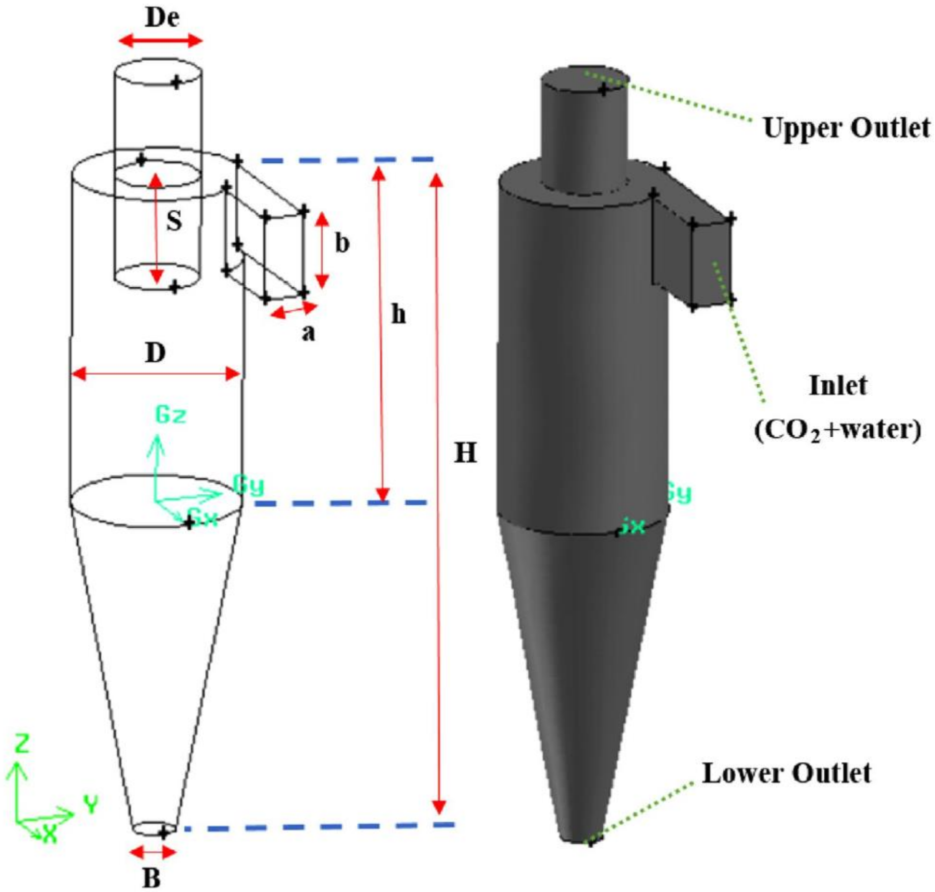

Figure 2. Cyclone separator's geometry and its dimensional details.

hinges on precisely calibrated component dimensions. Cyclone separators fall into two main categories based on their structural configurations: those featuring tangential inlets and those with axial inlets. Tangential inlet cyclone separators, renowned for their reliability and straightforward design, consist typically of cylindrical and conical sections. Illustrated in Fig. 2 is the intricate design of a three-dimensional cyclone separator with a tangential inlet. Upon entry, the CO_2–water mixture enters the separator with considerable velocity in a tangential trajectory, inducing rapid rotation within the annular space delineated by the exhaust pipe and the cylinder. Driven by centrifugal force, water droplets within the mixture are propelled toward the periphery, where they subsequently descend along the wall, aided by gravity and the mixture's momentum. Exiting through the underflow outlet, they leave behind purified CO_2, which ascends through the central region and is expelled via the exhaust pipe. Tab. 2 outlines the dimensions of the three-dimensional tangential single inlet cyclone separator, providing crucial insights into its structural specifications.

Table 2. Cyclone dimensions (D = 0.2 m).

$\frac{a}{D}$	$\frac{b}{D}$	$\frac{De}{D}$	$\frac{S}{D}$	$\frac{h}{D}$	$\frac{H}{D}$	$\frac{B}{D}$
0.25	0.5	0.5	0.625	2	4	0.25

3.1.1 Governing Equations

Computational fluid dynamics (CFD) offers a cost-efficient means to model fluid flow, complementing experimental and theoretical approaches in fluid dynamics [54–57]. Its extensive application in turbulent flow analysis renders it an indispensable facet of fluid dynamics research. CFD simulations offer several benefits, including enhanced performance optimization, the capability to replicate non-reproducible conditions, provision of comprehensive data and enhanced visualization, cost-effectiveness, and minimized environmental footprint [58]. Numerical modeling holds a pivotal role in conducting CFD simulations, facilitating the attainment of precise and comprehensive results. As a frontrunner in CFD, Fluent presents an advanced solution for simulating and analyzing fluid flow phenomena, including two-phase flow, which involves the concurrent movement of distinct phases like liquid and gas. Fluent offers two methodologies for multiphase flow simulation: the Euler–Lagrange and Euler–Euler approaches. The Euler–Lagrange method delineates a dispersed phase within a continuous fluid phase by tracking numerous particles, bubbles, or droplets throughout the flow field, computed using the Navier–Stokes equations. This method enables the exchange of momentum, mass, and energy between the two phases. However, it assumes a low volume fraction for the dispersed phase, typically below 10–12 %, despite its significantly higher mass loading. On the other hand, the Euler–Euler approach treats both phases as mutually penetrating continua, where the volume of one phase cannot be occupied by the other. This approach introduces the concept of volume fraction as a continuous function across space and time, summing up to one. Fluent offers three Euler–Euler multiphase models: volume of fluid (VOF), mixture, and Eulerian. The VOF model is well-suited for stratified or free-surface flows, while the mixture and Eulerian models are preferable for flows with dispersed-phase volume fractions surpassing 10 %. In scenarios involving simpler problems, the mixture model emerges as a more favorable option, compared to the Eulerian model, requiring the solution of fewer equations and consuming less computational resources [59].

In this study, we utilized the mixture model, also known as the algebraic slip model, as a simplified version of the Euler–Euler approach. This model is particularly well-suited for scenarios involving flows laden with droplets, bubbles, or particles, where the volume fraction of the dispersed phase exceeds 10 %, ensuring significant inter-particle collisions. The mixture model accommodates variations in fluid phase velocities, allowing for the interpenetration of fluid phases and facilitating the exchange of mass, momentum, and energy between them. Moreover, the mixture model has been applied in CFD simulations, especially in turbulent swirl two-phase flow within gas–liquid cyclone separators. However, the computation for the continuous and dispersed fluid phases is conducted using the following techniques:

The Reynolds-averaged Navier–Stokes equations, which include both the continuity and momentum equations, are utilized to solve for the continuous phase [60].

$$\frac{\partial \rho}{\partial t} + \frac{\partial(\rho u_i)}{\partial X_i} = 0 \quad (1)$$

$$\frac{\partial(\rho u_i)}{\partial t} + \frac{\partial(\rho u_i u_j)}{\partial X_j} = \frac{\partial P}{\partial X_i} + \frac{\partial}{\partial X_i}\left(\mu \frac{\partial^2 u_i}{\partial X_j^2} + \frac{\partial^2 u_j}{\partial X_i^2} - \frac{2}{3}\delta_{ij}\frac{\partial u_k}{\partial X_k}\right) + \frac{\partial}{\partial X_j}\left(-\rho\overline{u_I u_J}\right) \quad (2)$$

$$\left(-\rho\overline{u_I u_J}\right) = \mu_t\left(\frac{\partial^2 u_i}{\partial X_j^2} + \frac{\partial^2 u_j}{\partial X_i^2}\right) - \frac{2}{3}\left(\rho k + \mu_t \frac{\partial u_k}{\partial X_k}\right)\delta_{ij} \quad (3)$$

The equation describing the continuity of the mixture can be expressed as follows [60]:

$$\frac{\partial(\rho_m)}{\partial t} + \frac{\partial(\rho_m u_m)}{\partial x_i} = 0 \quad (4)$$

Mixture momentum is as follows [60]:

$$\frac{\partial(\rho_m u_{mi})}{\partial t} + \frac{\partial(\rho_m u_{mi} u_{mj})}{\partial x_i} = \frac{\partial P}{\partial x_i} + \frac{\partial}{\partial x_j}\mu_m\left(\frac{\partial u_{mi}}{\partial x_j} + \frac{\partial u_{mj}}{\partial x_j}\right) + \rho g_i + \frac{\partial}{\partial x_i}\left(\sum_{q=1}^{n}\alpha_q\rho_q u_{dr,qi} u_{dr,qj}\right) \quad (5)$$

where u_m represents the mass-averaged velocity, ρ_m stands for the mixture density, and μ_m denotes the viscosity of the mixture.

$$U_m = \frac{\sum_{q=1}^{n}\alpha_q\rho_q u_q}{\rho_m},\ \rho_m = \sum_{q=1}^{n}\alpha_q\rho_q\mu_m = \sum_{q=1}^{n}\alpha_q\mu_q, \quad (6)$$

The term $u_{dr,q}$ denotes the drift velocity for the secondary phase, which is determined by the equation $u_{dr,q} = u_q - u_m$.

Numerous researchers have explored the separation efficiency of cyclone separators using diverse methodologies, including numerical simulations, theoretical analyses, and experimental investigations. Presently, three primary approaches are employed for numerically examining the flow dynamics within cyclone separators: the Reynolds stress model (RSM) [61], RNG $k-\varepsilon$ numerical model [62], and the algebraic stress model (ASM) [63]. The $k-\varepsilon$ model assumes isotropic turbulence, rendering it unsuitable for cyclone flow characterized by anisotropic turbulence. Conversely, the ASM model proves inadequate in predicting the recirculation zone and Rankine vortex in instances of intense swirling flow. In contrast, the RSM model, which addresses a transport equation for each component of Reynolds stress, is widely considered the most suitable model for cyclone flow [64]. It comprehensively captures phenomena such as streamline curvature, swirling, rotation, and rapid strain rate changes, effectively capturing the anisotropic turbulence inherent in cyclone separators. Consequently, it is better suited for intricate, swirling, and rotational flows, providing more accurate predictions of complex flow phenomena in cyclones, albeit requiring greater computational resources. Moreover, when compared to large eddy simulation, RSM emerges as the preferred choice for modeling turbulence within cyclones, striking a balance between prediction accuracy and computational efficiency [65].

In the RSM with a time step of 0.001 s, the transport equation is expressed as follows [60].

$$\frac{\partial}{\partial t}\left(\rho\overline{u_i' u_j'}\right) + \frac{\partial}{\partial x_k}\left(\rho u_k \overline{u_i' u_j'}\right) = D_{ij} + P_{ij} + \Pi_{ij} + \varepsilon_{ij} + S \quad (7)$$

The equation encompasses two terms on the left side, delineating the local time derivative of stress and the convective transport term. On the right side, five terms are delineated, each encapsulating distinct facets [60]:

The stress diffusion term:

$$D_{ij} = -\frac{\partial}{\partial x_k}\left[\rho\overline{u_i' u_j' u_k'} + \overline{\left(P' u_j'\right)}\delta_{ik} + \overline{\left(P' u_i'\right)}\delta_{jk} - \mu\left(\frac{\partial}{\partial x_k}\overline{u_i' u_j'}\right)\right] \quad (8)$$

The shear production term: $P_{ij} = -\rho\left[\overline{u_i' u_k'}\frac{\partial u_j}{\partial x_k} + \overline{u_j' u_k'}\frac{\partial u_i}{\partial x_k}\right]$ (9)

The pressure-term: $\Pi_{ij} = \overline{p\left(\frac{\partial u_i'}{\partial x_j} + \frac{\partial u_j'}{\partial x_i}\right)}$ (10)

The dissipation term: $\varepsilon_{ij} = -2\mu\overline{\frac{\partial u_i'}{\partial x_k}\frac{\partial u_j'}{\partial x_k}}$ (11)

and S is the source term.

3.1.2 Numerical Simulation and Boundary Conditions

To capture the intricacies of the CO_2–water multiphase flow within the cyclone separator, the multiphase mixture model in ANSYS Fluent 2021 R1 was employed. This model was selected for its formidable robustness in managing the significant interactions between the CO_2 and water phases within the turbulent, swirling environment of the cyclone separator. Utilizing the interpenetrating continuum approach, CO_2 was designated as the primary (continuous) phase, ensuring an exhaustive representation of its dominant behavior, while water was treated as the secondary (dispersed) phase, facilitating a detailed analysis of droplet interactions and coalescence. The model integrated surface tension effects to accurately depict the interfacial dynamics between the two phases. The simulation utilized the SIMPLE algorithm to couple pressure and velocity in the continuity and

Table 3. Boundary conditions.

Boundary	Types
Inlet	Velocity inlet
Outlets	Pressure outlet
Wall	No slip wall

momentum equations, ensuring both stability and convergence. This method was paramount in attaining a stable and convergent solution, particularly for the intricate flow regimes within the cyclone separator. The PRESTO scheme was chosen for pressure interpolation due to its superior efficacy in handling high-speed swirling flows and flows within curved domains. This scheme was especially effective in mitigating numerical diffusion and preserving the integrity of the pressure field in regions of intense vorticity. For the discretization of the momentum, volume fraction, and kinetic energy equations, the QUICK method was employed. The QUICK method was favored over first- and second-order schemes due to its superior accuracy in capturing the rotational swirling flows characteristic of cyclone separators. This method significantly reduces numerical errors and enhances the reliability of the simulation results.

Boundary conditions were defined to emulate realistic operational scenarios [66]. The specific boundary conditions applied in the simulation are detailed in Tab. 3. The inlet boundary was set as a velocity inlet to accurately prescribe the inflow conditions, while the outlet boundaries were defined as pressure outlets to ensure the correct exit flow behavior. The walls of the cyclone separator were modeled as no-slip walls to guarantee that the tangential and normal velocities were zero at the boundaries, accurately reflecting the physical constraints of the separator.

3.2 SEC

Direct contact condensation involves the dynamic transfer of heat and mass across a moving vapor–liquid interface. Accurate predictions of the properties of direct contact condensation, especially phenomena near the interface like heat and mass transfer, are essential for upgrades and designs. This process entails complex interfacial mass and energy transfer, including turbulent transport, multiscale evolution, and pressure waves. The liquid–vapor interface, a thick layer of a few molecules, plays a crucial role in mass and energy transport. Condensation on a spray of droplets adds further complexity, requiring analysis of drop size distribution, velocity, and condensation behavior. Condensation occurs when saturated vapor contacts subcooled droplets exceeding a critical size, while evaporation occurs when droplets are smaller than this critical size. Building upon our prior analytical model [67, 68], we define the fluid properties at the inlet as the "inlet" state in Fig. 3. To determine the suction mass (mg) and pressure at the initiation of the mixing zone, we utilize equations derived from the flow conditions within the inlet region:

$$m_g = u_{g,in}\,\rho_g\,A_{g,in} = u_{g,0}\,\rho_g(A_0 - A_l) \tag{12}$$

From Bernoulli equation:

$$p_{g,in} + \frac{1}{2}\cdot\rho_{g,0}\,u_{g,in}^2 = p_{g,0} + \frac{1}{2}\cdot\rho_{g,0}u_{g,0}^2 + \Delta p_{loss,1} \tag{13}$$

The suction pressure ($p_{g,1}$) resulting from the interaction of the liquid jet with the gases can be determined by equating the momentum between the pre-mixing section (State 0) and the entrance to the mixing section (State 1).

$$p_{g,0}A_{g,0} + m_g u_{g,0} + p_l A_l + m_l\,u_l = p_{g,1}\,A_1 + (m_g + m_l)\,u_l \tag{14}$$

To determine the parameters at State 2, we apply conservation equations for mass, energy, and momentum within the context of an adiabatic process. In the presence of a non-condensable gas (CO_2), it becomes necessary to analyze both heat and mass transfer. We rely on equations and methodologies from our previous analytical investigations [67–69], including vapor condensation on a subcooled droplet stream, heat equilibrium of the droplet stream, and mass and heat balance for the vapor–gas mixture.

3.2.1 Effect of Diameter of Liquid Droplet

An essential parameter influencing the separation efficiency of the cyclone separator within the SEC is the diameter of droplets. As the discussion shifts to the internal dynamics of the SEC, it is notable that primary droplets originate from the formation of waves on the surface of the fluid stream. The volume of the wave and the need to minimize surface energy determine the droplet size. Under certain liquid jet outflow conditions, there is an optimal wavelength that, when greater than the jet circumference, results in an increase in wave amplitude and break-up of the liquid jet [70]:

$$\frac{D}{Dj} = 1.436\left(1 + 3\frac{We^{0.5}}{Re}\right)^{1/6} \tag{15}$$

where $We = \frac{\rho_l u_l^2 D_j}{\sigma_l}$ – Weber number, $Re = \frac{\rho_l u_l D_j}{\mu_l}$ – Reynolds number, Dj: diameter of jet, σ_l: surface tension, ρ_l: liquid density, u_l: liquid velocity, μ_l: dynamic viscosity.

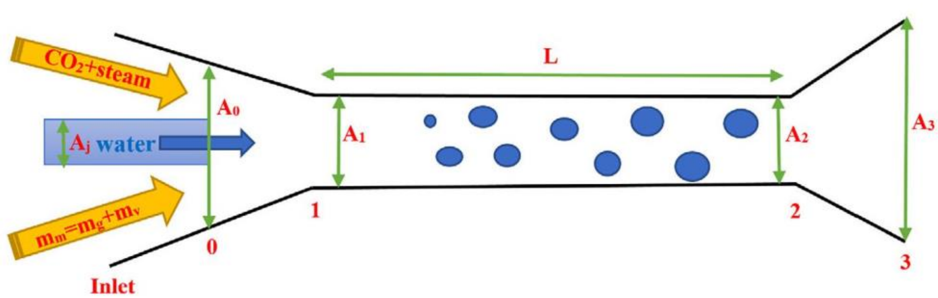

Figure 3. Schematic of the SEC [67–69].

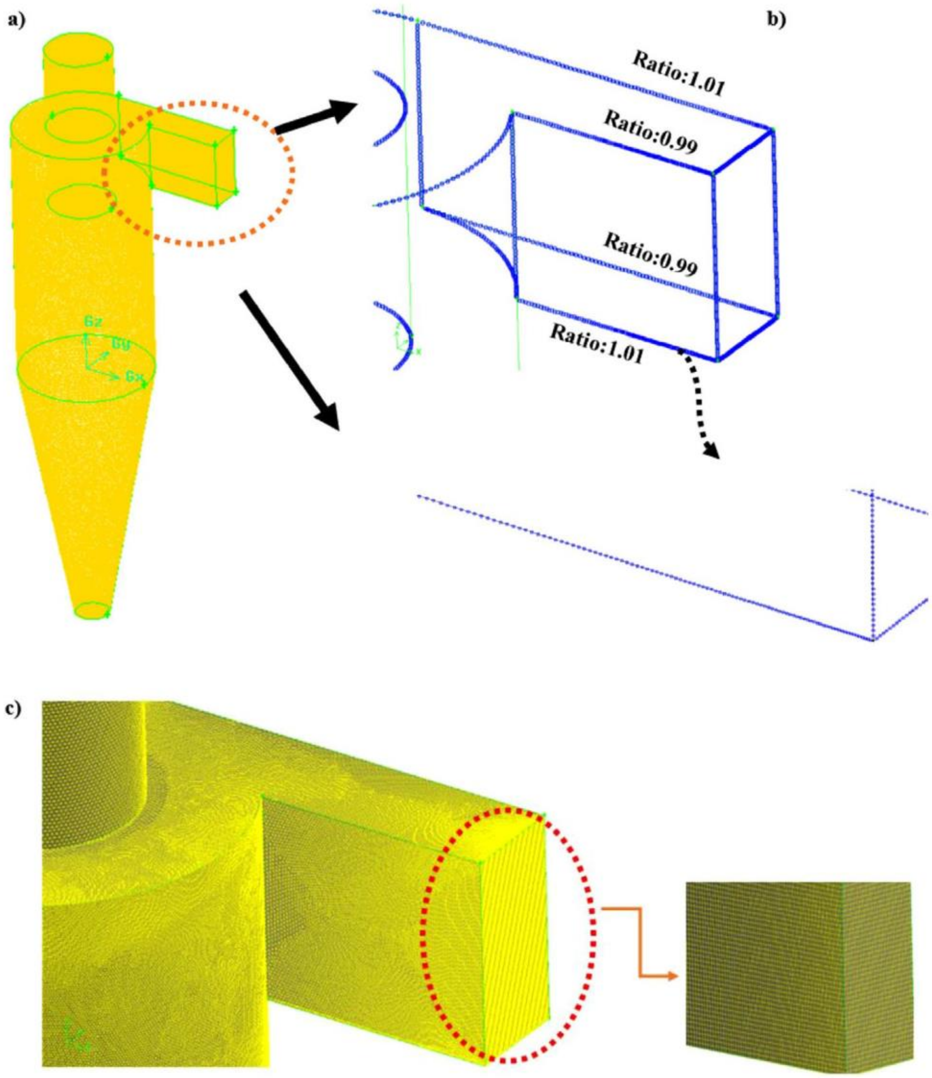

Figure 4. (a) Cyclone separator meshing, (b) line mesh, and (c) surface mesh.

In addition, the stream of drops from the water nozzle moves with the same velocity as the liquid stream, resulting in droplets with equal mass to the liquid along the throat length.

$$nm_{\mathrm{d}} = \frac{\pi\, d_{\mathrm{d}}^3 \rho_{\mathrm{l}}}{6} n = m_{\mathrm{l0}} = \frac{\pi D_{\mathrm{d}}}{4}\, l\rho_{\mathrm{l}} \tag{16}$$

where
$n = \frac{3}{2}\left(\frac{D_0}{d_{\mathrm{d}}}\right)^2 \frac{l}{d_{\mathrm{d}}}$ is total number of droplets, D_0: diameter of mixing length, l: mixing length, d_{d}: diameter of the droplet.

4 Evaluation of Numerical Model

The flow characteristics of the cyclone separator under scrutiny were scrutinized utilizing ANSYS Fluent 2021 R1. As a primary metric, the separation efficiency was ascertained, delineated as per Eq. (17) [60]:

$$\eta = \left(\frac{\dot{m}_{\text{liquid at inlet}} - \dot{m}_{\text{liquid at gas outlet}}}{\dot{m}_{\text{liquid at inlet}}}\right) \times 100 \tag{17}$$

where $\dot{m}$ represents the mass flow rate.

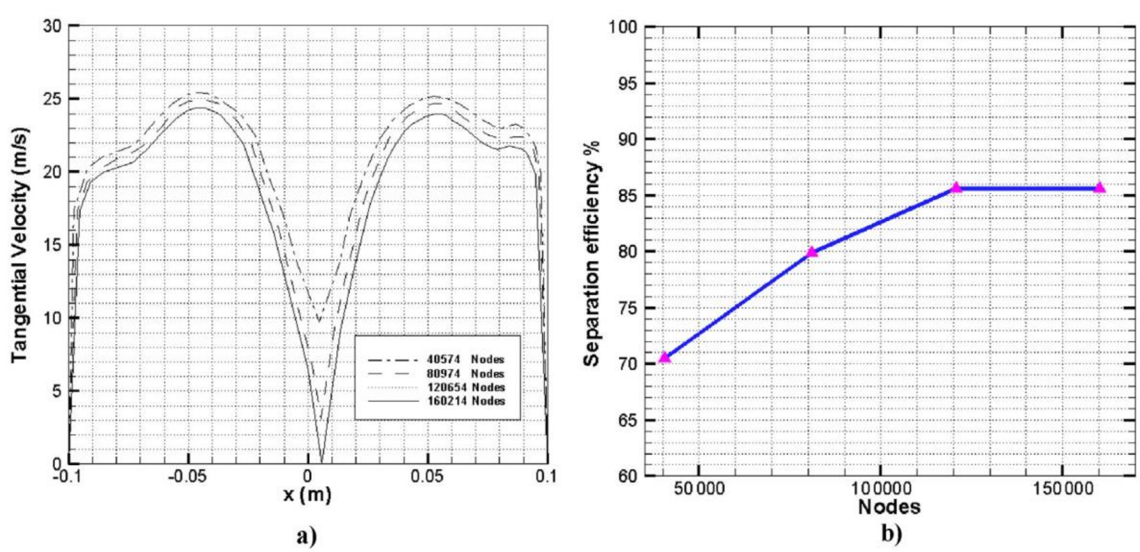

Figure 5. Grid independence for (a) tangential velocity and (b) separation efficiency of single inlet cyclone at 2.8 (kg s^{-1}) with a 10 % volume fraction of water.

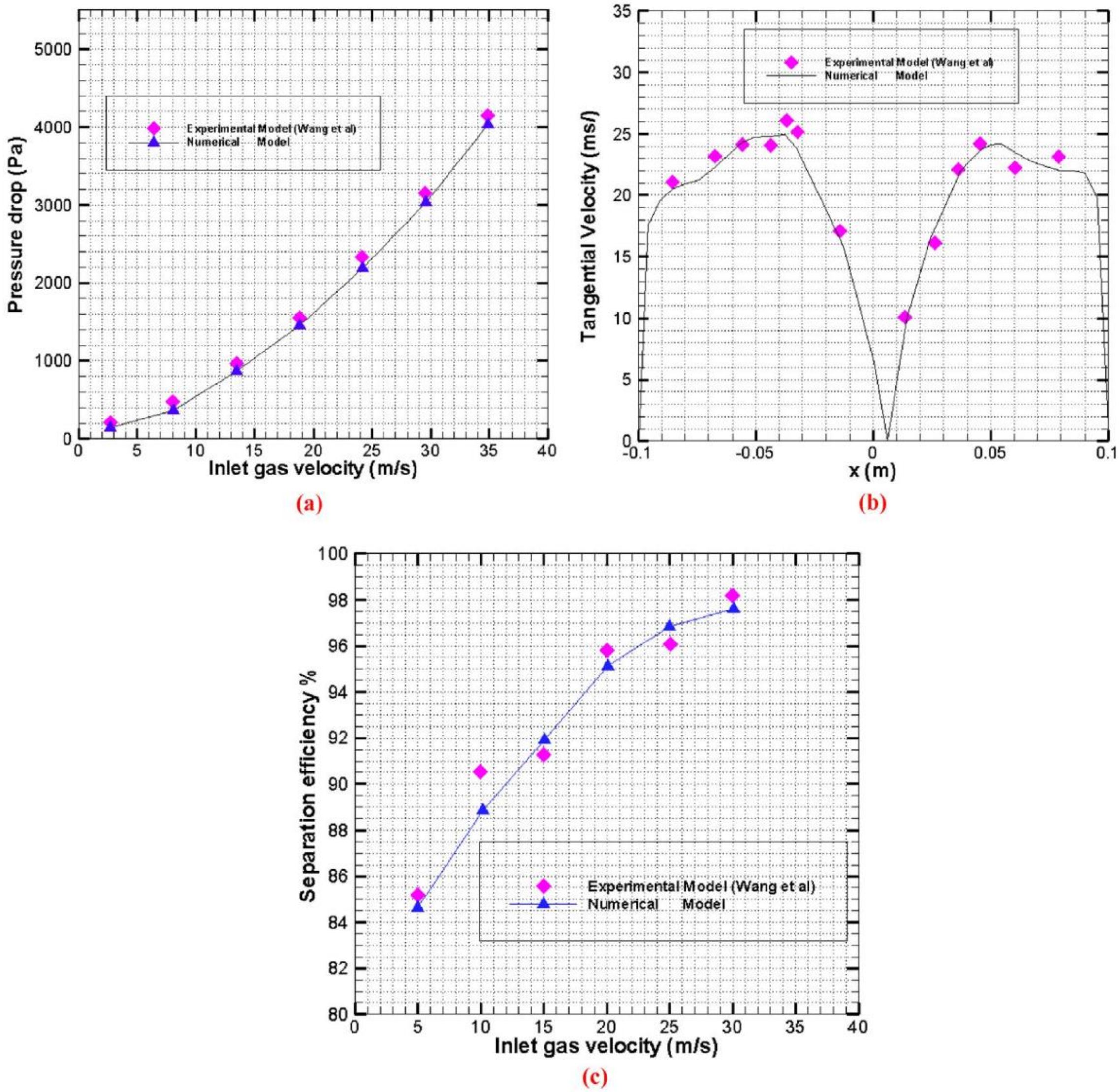

Figure 6. Comparison of experimental model (Wang et al.) and numerical simulation for (a) pressure drop, (b) tangential velocity, and (c) separation efficiency.

4.1 Grid Independence

The geometry and mesh of the cyclone separator, as created in Gambit 2.4.6, are depicted in Fig. 4. In order to ensure the precision of calculations, every edge within the model was meshed. Recognizing the sensitivity of specific regions, particularly the cyclone inlet, we applied a mesh refinement ratio in Gambit, setting it to 1.01 and 0.99 for the grid lines approaching the inlet (Fig. 4b). This adjustment aimed at achieving a finer mesh at the cyclone inlet. Subsequently, all faces and volumes were subjected to meshing. For this meshing process, Tet/Hybrid elements and the TGrid type were employed to generate cells that were well-suited for the geometry involved in CFD simulations. A high-quality mesh was deemed essential to mitigate errors stemming from numerical diffusion. To validate the independence of results from the grid size, we examined mesh-independent solutions for the cyclone separator by employing various grid configurations. The graph in Fig. 5 displays the variations in tangential velocity and separation efficiency for different node counts. Notably, the results obtained with 40 574 and 80 974 grids exhibit disparities, compared to the other grid configurations (120 654 and 160 214). While the outcomes for 120 654 and 160 214 nodes are approximately similar, we opted for the 120 654 nodes to reduce computational costs.

4.2 Model Validation

Fig. 6 illustrates the predicted variations in pressure drop, tangential velocity, and separation efficiency, which are compared to the findings reported by Wang et al. [71]. During the physical experiment, they introduced air into the cyclone's inlet and monitored its flow rate using a flowmeter. Both phases were flowing at a velocity of 20 m s^{-1} during the experiment. The outlet tube was exposed to the atmosphere, and the gas pressure at the top of the

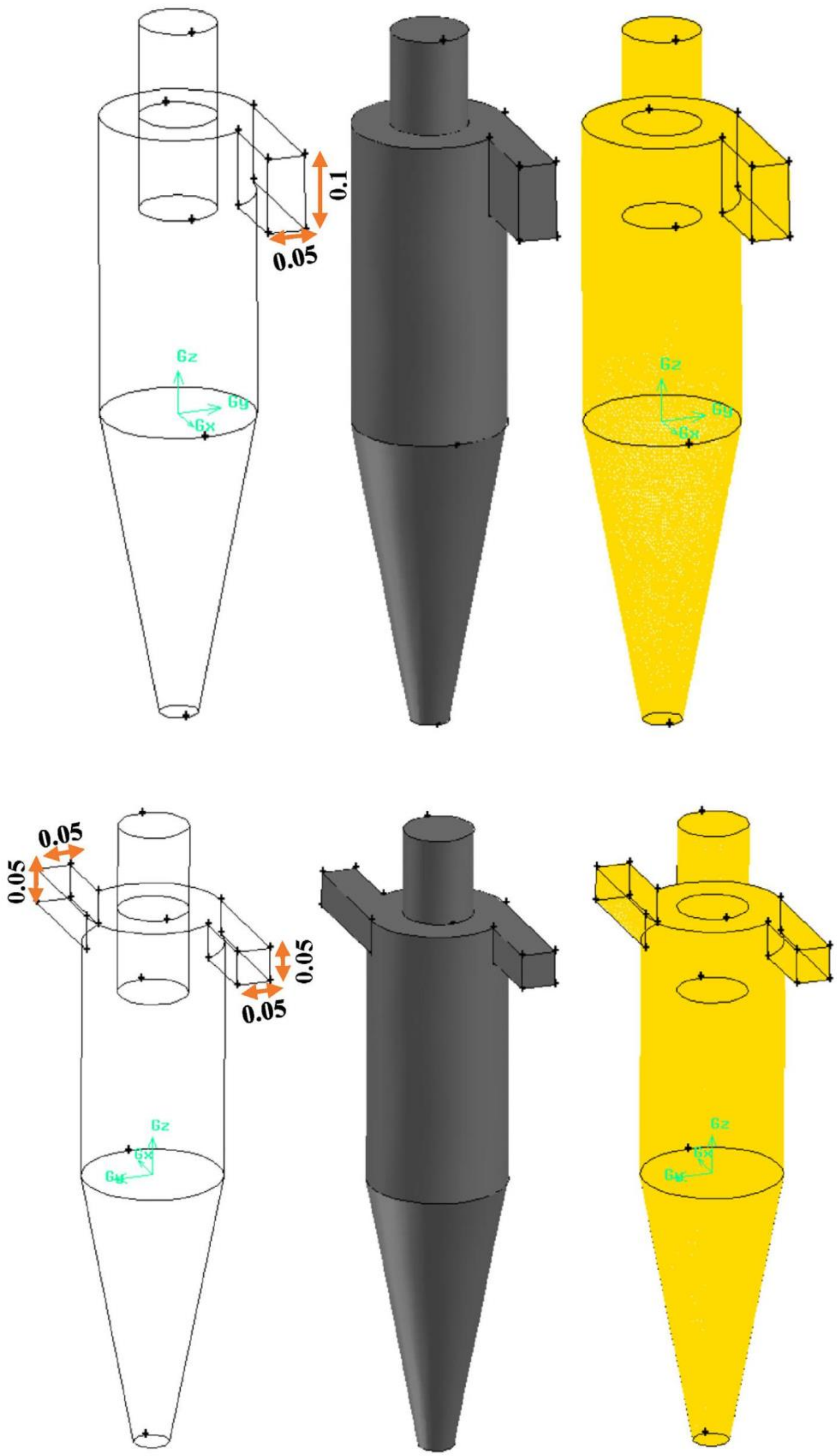

Figure 7. Geometry and mesh of dual-inlets cyclone.

vortex finder was kept at 1 atm. The volume fraction of the second phase was 10. Velocity and pressure measurements in the gas field were conducted using a five-hole probe, which consisted of an adjustable frame and five pressure transducers. The voltage signals produced by these five pressure transducers on the five-hole probe were amplified after being positioned within the gas flow field. The amplified voltage signals were gathered by a data acquisition system that was equipped with a microprocessor and a personal computer. As shown in Fig. 6, there was a good agreement between the experimental data and the numerical results obtained from Wang et al.'s studies.

4.3 Geometry and Mesh Configuration of Single and Dual Inlets

The efficiency of particle separation in various industrial applications heavily relies on the design and operation of cyclone separators. Among the design parameters influencing separator performance, the inlet configuration plays a crucial role. This section investigates the effect of single and dual inlets on cyclone separator efficiency. A single inlet configuration features one entrance for the incoming fluid, while a dual-inlet configuration includes two entrances. Our objective here is to assess how these inlet configurations affect particle separation efficiency. To achieve this, we conducted computational flow visualization to analyze the internal flow structure of cyclones. Two types of cyclones, with single and dual inlets, were created to elucidate the flow mechanism. Fig. 7 illustrates the geometry and mesh of the dual-inlet cyclone. Upon reviewing existing literature [72, 73], it becomes apparent that different design approaches have been employed for cyclone separators. Some studies have maintained a consistent total inlet area for

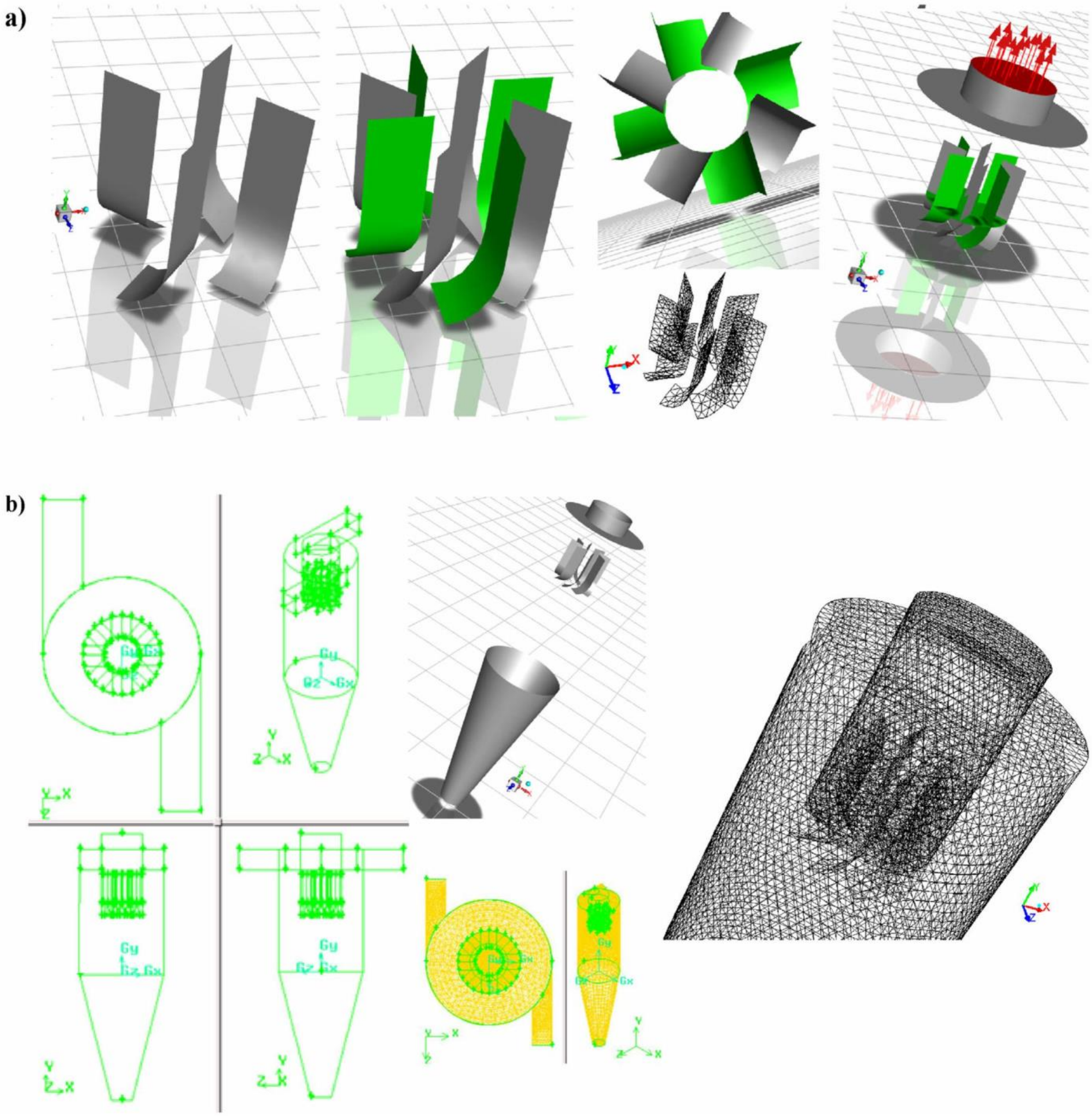

Figure 8. (a) Vanes and its meshing and (b) cyclone separator integrated with vanes and its meshing.

both single- and symmetric-inlet cyclones [74], while others have opted for equal inlet areas, resulting in the double inlet cyclone having twice the inlet area of the single inlet cyclone [75]. However, from an engineering perspective, it is often essential for cyclones to handle a uniform gas flow rate. Varying the total inlet area leads to inconsistent inlet gas velocities, impacting velocity distribution within the flow field and consequently influencing overall performance. In our study, we aimed to achieve a uniform total inlet area by exclusively modifying the inlet height.

4.4 Structural Layout and Meshing Details of a Cyclone Equipped with Vanes

Vanes and tangential inlets are not widely used features in industrial applications to improve the centrifugal separation of gas–liquid and liquid–liquid phases. However, when combined, as illustrated in Fig. 8, they offer a significant advantage by notably reducing the pressure drop experienced within the separator. This reduction in pressure drop is crucial for cyclones' efficient operation, as it leads to lower power requirements and

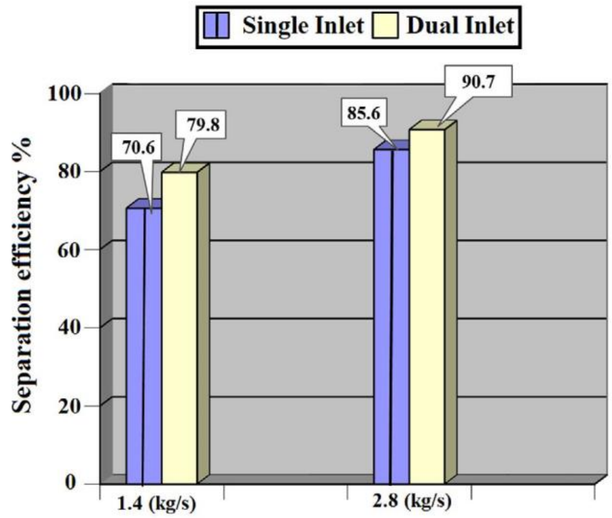

Figure 9. Separation efficiency of single- and dual-inlet cyclones at different flow rates with a 10 % water volume fraction.

more manageable fan specifications. Consequently, this configuration is particularly appealing for both new plant designs and the enhancement of existing systems. This section shows incorporating vanes within the cyclone separator. Fig. 8a visually represents the vanes installed inside the cyclone, showcasing their distinctive shape. Notably, Fig. 8b depicts the integration of eight vanes, each complete with its respective meshing.

5 Results and Discussion

5.1 Effect of Single and Dual Inlets

The performance of single- and dual-inlet cyclones was evaluated in terms of separation efficiency, with notable results favoring the dual-inlet cyclone configuration. At a flow rate of 1.4 (kg s^{-1}), the dual-inlet cyclone demonstrated an efficiency of 79.8 %, surpassing the 70.6 % efficiency achieved by the single inlet cyclone. Similarly, treatment of the CO_2–water feed at 2.8 (kg s^{-1}) showcased superior performance of the dual-inlet cyclone, yielding a separation efficiency of 90.7 %, compared to 85.6 % for the single inlet cyclone (Fig. 9). Several factors contribute to these compelling findings. First, the design of the dual-inlet cyclone enables improved control and distribution of the incoming gas mixture, facilitating more effective separation. The enhanced uniformity in flow distribution within the cyclone is a key factor driving the observed increase in separation efficiency. Moreover, the dual-inlet cyclone's versatility in accommodating varying flow rates, exemplified by its performance in treating the CO_2–water feed, underscores its suitability for applications requiring consistent and superior separation performance.

5.2 Assessment of Cyclone Separator Efficiency at Different SEC Outlets

In this section, we aim to optimize the separation efficiency of cyclone separator by investigating parameters within the SEC, such as volume fraction and droplet breakup.

5.2.1 Effect of Volume Fraction

The SEC and cyclone separator were integrated as the separation components of a negative CO_2 emission power plant to achieve high-purity CO_2 production through direct-contact condensation of vapor with inert gas (CO_2) on a subcooled liquid spray (water) within the SEC (Fig. 3). The ejector's performance is influenced by two choking phenomena: one occurring in the primary flow through the nozzle and the other in the entrained or suction flow. The latter arises from the acceleration of the entrained flow, transitioning it from a stagnant state at the suction port to a supersonic flow within the mixing chamber. Several factors affect the entrained flow rate or the entrainment ratio of an ejector, including supersonic flow, shock interactions, and turbulent mixing within the ejector enclosure. Additionally, the liquid jet exiting the nozzle undergoes dissipation and breakup, leading to the formation of droplets of varying sizes. The liquid stream disintegrates into droplets due to surface waves caused by

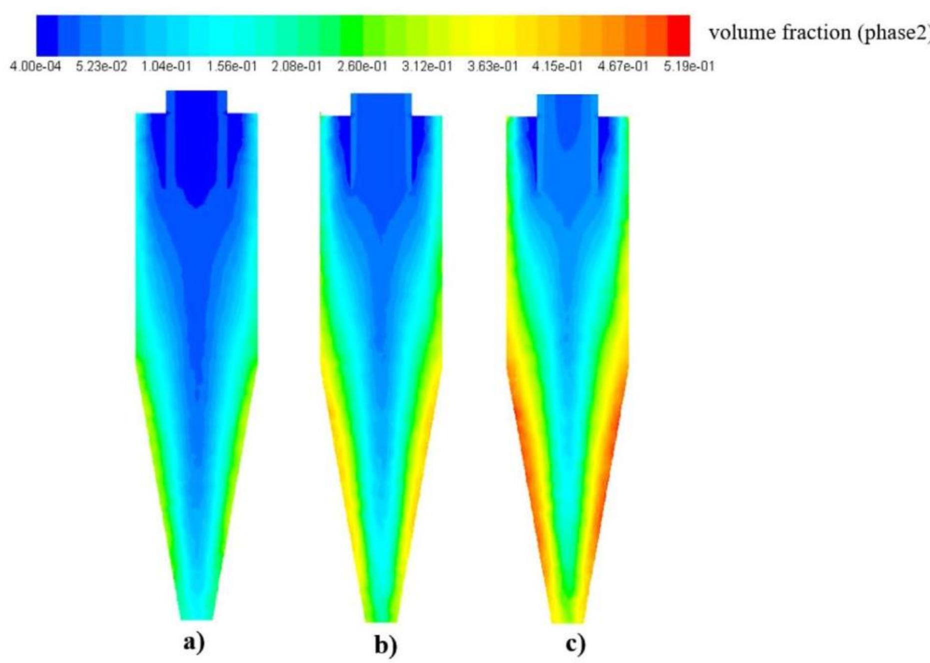

Figure 10. Contours of the liquid volume fraction (LVF) for an inlet mass flow rate of 2.8 (kg s^{-1}) at different feed stream LVFs: (a) 10 %, (b) 15 %, and (c) 20 %.

Table 4. The separation efficiency of a dual-inlet cyclone at different feed stream liquid volume fractions (LVFs) with a water droplet diameter of 10^{-5}.

LVF [%]	$\dot{m}_{\text{liquid at inlet}}$ [kg s^{-1}]	$\dot{m}_{\text{liquid at gas outlet}}$ [kg s^{-1}]	Separation efficiency [η %]
10	2.74649	0.254949	90.7
15	4.1197319	0.43964297	89.33
20	5.4929759	0.68230528	87.58

inherent instability, leading to initial droplet formation. Subsequently, secondary droplet breakup occurs due to aerodynamic forces, including aerodynamic drag and surface tension, which deform and break up the initial droplets. Consequently, the volume fraction of liquid water varies. In this section, we present the analysis conducted using a numerical model for various cyclone separator cases with different SEC outlet conditions. Specifically, we considered liquid water volume fractions of 10 %, 15 %, and 20 %. Fig. 10 illustrates the contour of liquid water volume fraction for a dual-inlet cyclone with an inlet mass flow rate of 2.8 (kg s^{-1}) under feed stream conditions of 10 %, 15 %, and 20 % LVF.

In order to comprehensively investigate the influence of the LVF on the internal configuration's separation performance, we conducted a rigorous assessment. The separation efficiency was computed at various LVFs using Eq. (17), and the resulting data were analyzed for meaningful insights. The results of this investigation, which included the assessment of separation efficiencies alongside the inlet and outlet liquid mass flow rates ($\dot{m}$), are thoughtfully presented in Tab. 4. An examination of the table reveals a noteworthy trend: As the LVF decreases, the separation efficiency improves. This trend is particularly evident in the data, where the highest separation efficiency was remarkably achieved at a LVF of 10 %, with an impressive efficiency rating of 90.7 %. A lower LVF translates to a higher gas-to-liquid ratio within the separator. This enhanced ratio is conducive to more effective phase separation, as it minimizes the chances of entrainment and promotes the swift ascent of gas bubbles within the cyclone. Additionally, the reduced LVF results in a less congested environment within the separator, allowing for a more streamlined and efficient separation process. Moreover, the decreased LVF minimizes the likelihood of liquid carryover to the gas outlet, further bolstering the overall separation performance. Furthermore, the ability to achieve a 90.7 % separation efficiency at a 10 % LVF underscores the remarkable adaptability and effectiveness of the internal configuration, particularly in scenarios where gas–liquid separation is crucial. This finding holds significant promise for industries and applications that demand optimal separation performance while operating with varying LVFs, as it highlights the potential for superior results under such conditions.

5.2.2 Effect of Diameter of Liquid Droplet

As mentioned in Sect. 3.2.1, there is a direct relationship between the number of droplet and the diameter of droplet. In this study 1, 5, and 10 (μm) of diameter of water droplet have been investigated based on the length and diameter of mixing length as well as number of droplets of SEC. Tab. 5 shows the mass flow rate of the liquid phase at the inlet and gas outlet for different diameter of water liquid and LVF.

Table 5. Mass flow rate of liquid phase at the inlet and gas outlet for different diameter of water liquid and LVF.

LVF [%]	Diameter of water droplet [μm]	$\dot{m}_{\text{liquid at inlet}}$ [kg s^{-1}]	$\dot{m}_{\text{liquid at gas outlet}}$ [kg s^{-1}]
	1	2.746488	1.3458184
10	5	2.746488	0.85150968
	10	2.746488	0.254949
	1	4.1197319	2.02284
15	5	4.1197319	1.3411002
	10	4.1197319	0.43964297
	1	5.4929759	2.7027527
20	5	5.4929759	1.8741025
	10	5.4929759	0.68230528

Having perused the data from Fig. 11, for 1, 5, and 10 (μm) of diameter of water droplet and 20 % of LVF, it can be understood that separation efficiency is 50.79 %, 65.88 %, and 87.58 %, respectively. For 15 % of LVF, separation efficiency has been faced with an increase of 0.1 %, 1.57 %, and 1.75 % for the aforementioned diameter of water droplets, respectively, while this rising for 10 % of LVF is 0.2 %, 3.11 %, and 3.12 % in comparison to 20 % of LVF. In addition, maximum and minimum of separation efficiency have been obtained at 10 % of LVF/10 (μm) of diameter of water droplet and 20 % of LVF/1 (μm) of diameter of water droplet so that their values are 90.7 % and 50.79 %, respectively.

5.3 Effect of Vanes

To gain insight into the flow dynamics facilitated by vanes, streamline and vector illustrations are presented in Fig. 12. The presence of two inlet ports generates a symmetrical flow field, promoting a relatively even distribution of flow throughout the guide channels. This innovative configuration of vanes and tangential inlets holds the promise of revolutionizing cyclone separator performance, providing a more energy-efficient and cost-effective solution for gas–liquid and liquid–liquid separation in industrial settings. Further exploration of the study will uncover how these components work in tandem to achieve enhanced separation efficiency while minimizing power consumption.

Tab. 6 provides a comparison of pressure drop and separation efficiency in dual-inlet cyclones, both with and without vanes. Upon examination of the data presented in Tab. 6, the incorporation of vanes into the cyclone setup leads to a notable reduction of 16.8 % in pressure drop while simultaneously yielding a 9.2 % improvement in separation efficiency, a particularly striking result when observing the conditions at a 10 % LVF. The calculation of pressure drop, representing the difference between inlet and CO_2 outlet pressures, is fundamental in evaluating the performance

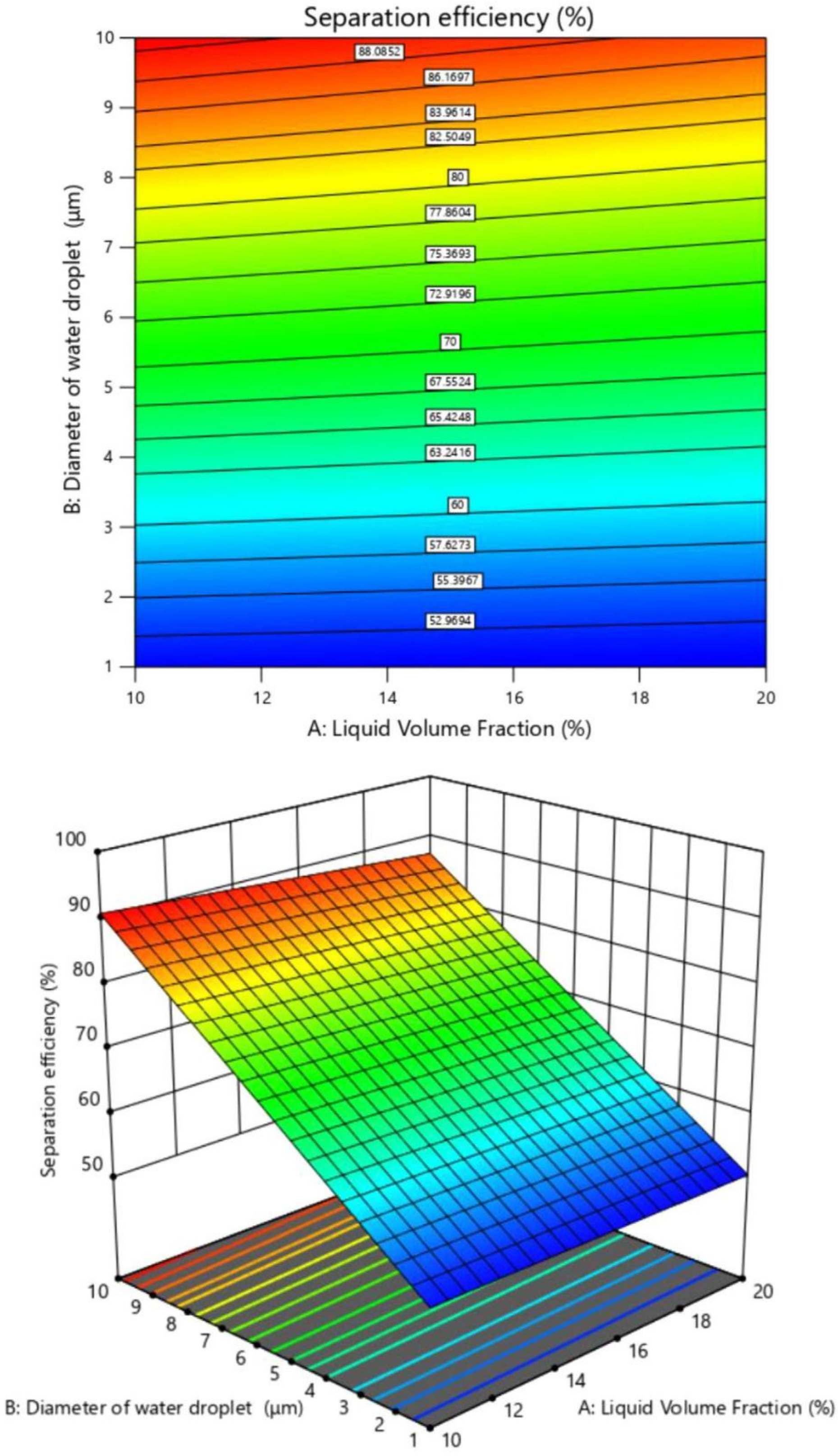

Figure 11. Separation efficiency of dual-inlet cyclone at different diameters of water liquid and LVF.

enhancement brought about by the introduction of vanes. This calculation is executed as follows:

$$\Delta P = P_{\text{in}} - P_{\text{out}} \tag{18}$$

where P_{in} and P_{out} are static pressure at the inlet and pressure of CO_2 outlet, respectively.

One of the key observations from Tab. 6 is the substantial reduction in pressure drop when vanes are employed. Pressure drop is a critical parameter in cyclone separators, directly affecting the energy requirements of the system. By minimizing pressure drop, as demonstrated by the data, less energy is needed to maintain desired flow rates and separation efficiency. This reduction in pressure drop results in lower power consumption, contributing to improved energy efficiency. Simultaneously, the presence of vanes leads to an enhancement in separation efficiency, a crucial aspect for any separation process, directly influencing the quality of the separated components and the overall effectiveness of the cyclone separator. The data clearly indicate that the addition of vanes contributes to a more efficient separation process, allowing a higher percentage of the desired component (CO_2) to be purified. This improved efficiency means that fewer resources are wasted, and the desired product can be obtained with less energy input.

Combining the reduced pressure drop and improved separation efficiency, it becomes evident that the use of vanes contributes to substantial energy savings. When less energy is required to achieve the desired separation, operational costs associated with power consumption are reduced. This is particularly significant for industries where energy costs constitute a substantial portion of operational expenses.

6 Conclusion

A numerical simulation was performed to enhance the efficiency of the design for a tangential-flow vanes

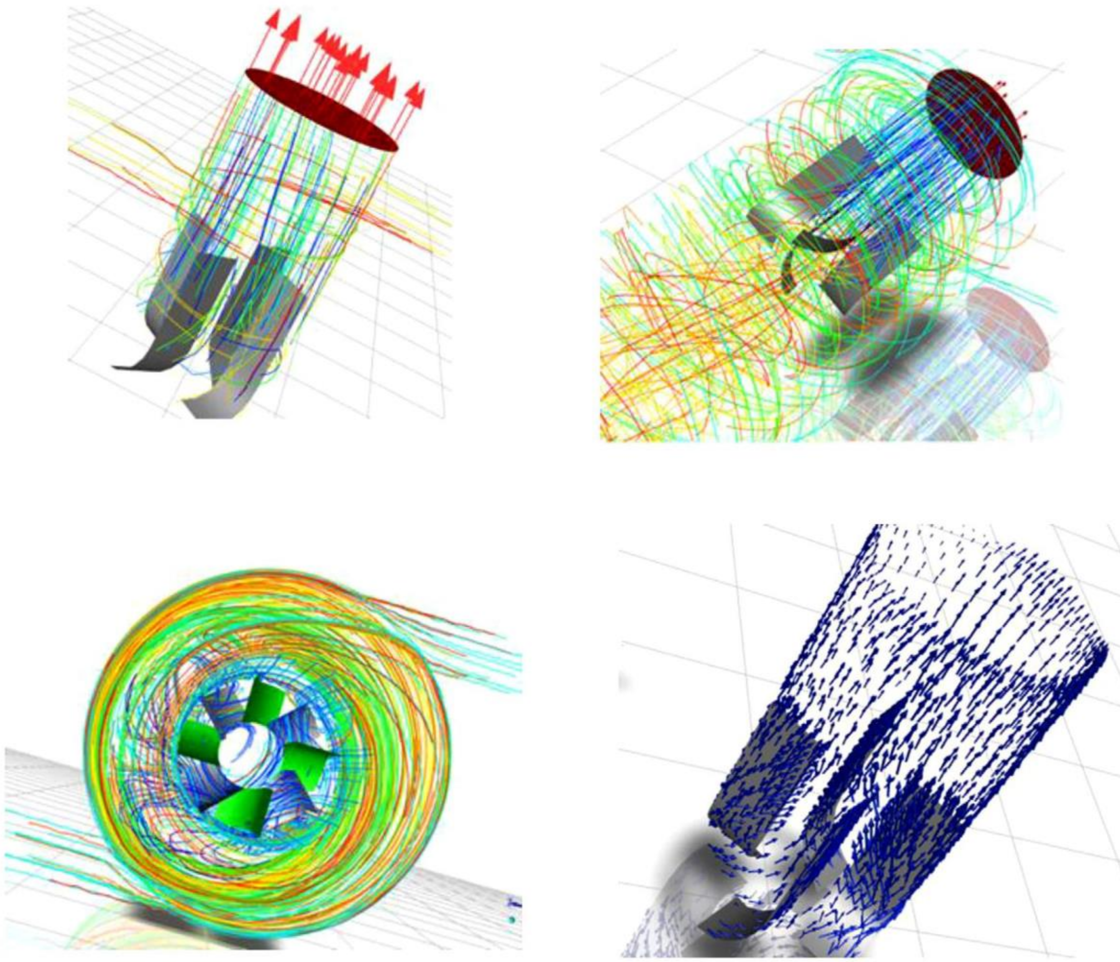

Figure 12. Streamline and vector around the vanes.

CO_2–water separator in the context of a nCO_2PP. This optimization aimed to achieve a high-purity CO_2 output. The simulation employed a transient RSM for turbulence and utilized a three-dimensional model. The impact of single and dual inlets on separation efficiency was analyzed, and the effects of SEC outlet conditions, such as water LVF and diameter of water droplets, on separator performance were studied. The optimized conditions were then used in a simulation of the separator with added vanes.

The key findings are outlined as follows:

- The analysis of single- and dual-inlet cyclones revealed significant differences in their performance. The dual-inlet cyclone demonstrated superior efficiency, particularly at higher flow rates, by effectively separating CO_2-rich and water-rich cores. This insight underscores the importance of inlet configuration in optimizing separator performance.
- The study delved into the influence of outlet conditions of SEC, specifically focusing on LVF and water droplet diameter. These parameters were found to play a crucial role in shaping separator performance, with lower LVFs and larger water droplet diameters contributing to enhanced separation efficiency.
- The research identified optimal operating conditions for the separator, highlighting that a LVF of 10 % yielded the highest separation efficiency of 90.7 %. Additionally, variations in water droplet diameter further underscored the importance of parameter tuning for achieving desired performance outcomes.
- The adding of vanes within the cyclone separator emerged as a pivotal factor in the quest for improved performance. The presence of vanes led to a notable reduction in pressure drop by 16.8 %, lowering energy requirements and operational costs. Simultaneously, it boosted separation efficiency by 9.2 % at a LVF of 10 %, ensuring that a higher percentage of CO_2 was efficiently captured.

Table 6. Comparison of pressure drop and separation efficiency of dual-inlet cyclone without/with vanes at 10 % LVF and 10^{-5} of diameter of the water droplet.

Separator performance	Without vanes	With vanes
ΔP [kPa]	54.31	45.2
Separation efficiency [%]	90.7	99.9

In conclusion, this study provides valuable insights into the optimization of CO_2–water separators in the context of nCO_2PP. The findings presented here underscore the significance of inlet configuration, outlet conditions of SEC, and vane integration in enhancing separator performance. These insights have important implications for industries seeking to improve gas–liquid separation processes, reduce energy consumption, and promote more sustainable CO_2 capture practices. The knowledge gained from this research contributes to the ongoing efforts to address environmental challenges and advance the development of cleaner energy solutions.

Author contributions

Milad Amiri: Conceptualization, methodology, data curation, formal analysis, investigation, resources, software, validation, visualization, writing—original draft, writing—review and editing. **Jaroslaw Mikielewicz**: Methodology, writing—review and editing. **Paweł Ziółkowski**: Investigation, data curation, formal analysis, resources. **Dariusz Mikielewicz**: Conceptualization, Methodology, supervision, project administration, funding acquisition, investigation, writing—review and editing.

Acknowledgments

The research leading to these results has received funding from the Norway Grants 2014-2021 via the National Center for Research and Development. Article has been prepared within the frame of the project: "Negative CO_2emission gas power plant"—NOR/POLNORCCS/NEGATIVE- CO_2- PP/0009/2019-00, which is co-financed by program "Applied Research" under the Norwegian Financial Mechanisms 2014-2021 POLNOR CCS 2019–Development of CO_2 capture solutions integrated in power and industry processes.

Symbols used

Dj	[m]	Diameter of jet
D_{ij}	$[kg \cdot m^{-1} \cdot s^{-2}]$	Stress diffusion term
D_0	[m]	Diameter of mixing length
d_d	[m]	Diameter of droplet
l	[m]	Mixing length
m_g	$[kg\ s^{-1}]$	Suction mass
n	[–]	Total number of droplet
P	[pa]	Static pressure
P_{ij}	$[N\ m^{-3}]$	Shear production term
$p_{g,l}$	[pa]	Suction pressure
Re	[–]	Reynolds number
S	[–]	Source term
$\vec{u}$	$[m\ s^{-1}]$	Velocity vector
$u_{dr,q}$	$[m\ s^{-1}]$	Drift velocity

Greek letters

ρ_l	$[kg\ m^{-3}]$	liquid density
ρ	$[kg\ m^{-3}]$	density
ρ_m	$[kg\ m^{-3}]$	mixture density
μ_m	$[kg \cdot m^{-1} \cdot s^{-1}]$	viscosity of the mixture
Π_{ij}	$[kg \cdot m^{-1} \cdot s^{-2}]$	pressure-strain term
μ_l	$[kg \cdot m^{-1} \cdot s^{-1}]$	dynamic viscosity
ε_{ij}	$[kg \cdot m^{-1} \cdot s^{-3}]$	dissipation term
η	[%]	separation efficiency
σ_l	$[N\ m^{-1}]$	surface tension
$\Delta p_{loss,l}$	[pa]	pressure drop

References

[1] C. Pelletier, Y. Rogaume, L. Dieckhoff, G. Bardeau, M.-N. Pons, A. Dufour, *Appl. Energy* **2019**, *235*, 1381–1388. DOI: https://doi.org/10.1016/j.apenergy.2018.11.060

[2] G. G. Esquivel Patiño, F. Nápoles Rivera, *J. Cleaner Prod.* **2019**, *208*, 11–18. DOI: https://doi.org/10.1016/j.jclepro.2018.10.098

[3] H. Kawahata, K. Fujita, A. Iguchi, M. Inoue, S. Iwasaki, A. Kuroyanagi, A. Maeda, T. Manaka, K. Moriya, H. Takagi, T. Toyofuku, T. Yoshimura, A. Suzuki, *Prog. Earth Planet. Sci.* **2019**. *6* (*1*), 1–37. DOI: https://doi.org/10.1186/s40645-018-0239-9

[4] Y. Zhang, Y. Gao, B. Louis, Q. Wang, W. Lin, *J. Energy Chem.* **2019**, *33*, 81–89. DOI: https://doi.org/10.1016/j.jechem.2018.08.014

[5] E. Lee, J. S. Hornafius, E. Dean, H. Kazemi, *Int. J. Greenhouse Gas Control* **2019**, *81*, 137–156. DOI: https://doi.org/10.1016/j.ijggc.2018.11.013

[6] K. V. Sterkhov, D. A. Khokhlov, M. N. Zaichenko, *Energy* **2024**, *294*, 130958. DOI: https://doi.org/10.1016/j.energy.2024.130958

[7] M. Abdollahzadeh Delazi, R. Amiri Chayjan, M. Kaveh, *Clean Technol. Environ. Policy*, in press. DOI: https://doi.org/10.1007/s10098-024-02778-2

[8] J. M. Ahlström, V. Walter, L. Göransson, S. Papadokonstantakis, *Renew. Energy* **2022**, *190*, 596–605. DOI: https://doi.org/10.1016/j.renene.2022.03.100

[9] S. Sanaye, P. Alizadeh, M. Yazdani, *Renew. Energy* **2022**, *190*, 524–539. DOI: https://doi.org/10.1016/j.renene.2022.03.086

[10] P. A. Aigba, I. Emovon, O. D. Samuel, C. Chintua Enweremadu, T. Abdeljawad, Q. M. Al-Mdallal, A. Afzal, *Front. Energy Res.* **2022**, *9*, 798896. DOI: https://doi.org/10.3389/fenrg.2021.798896

[11] F. I. Abam, O. I. Inah, S. O. Effiom, D. I. Ntunde, H. U. Ugwu, M. C. Ndukwu, O. D. Samuel, *Sci. Afr.* **2022**, *16*, e01175. DOI: https://doi.org/10.1016/j.sciaf.2022.e01175

[12] O. D. Samuel, P. A. Aigba, T. K. Tran, H. Fayaz, C. Pastore, O. Der, A. Erçetin, C. C. Enweremadu, A. Mustafa, *Sustainability* **2023**, *15*, 16287. DOI: https://doi.org/10.3390/su152316287

[13] A. Mustafa, S. Fathy, O. Kutlu, F. Niikura, A. Inayat, M. Mustafa, T. M. M. Abdellatief, A. Bokhari, O. D. Samuel, C. Pastore, L. Di Bitonto, M. A. Tawfik, M. Munir, R. Mohsen, *Clean Technol. Environ. Policy* **2023**, *25* (*10*), 3263–3283. DOI: https://doi.org/10.1007/s10098-023-02577-1

[14] F. I. Abam, O. E. Diemuodeke, E. B. Ekwe, M. Alghassab, O. D. Samuel, Z. A. Khan, M. Imran, M. Farooq, *Energies* **2020**, *13* (*22*), 6018. DOI: https://doi.org/10.3390/en13226018

[15] T. S. Singh, U. Rajak, O. D. Samuel, P. K. Chaurasiya, K. Natarajan, T. N. Verma, P. Nashine, *Fuel* **2021**, *285*, 119103. DOI: https://doi.org/10.1016/j.fuel.2020.119103

[16] A. Taheri-Garavand, A. Heidari-Maleni, T. Mesri-Gundoshmian, O. D. Samuel, *Energy Convers. Manage:*

X **2022**, *16*, 100304. DOI: https://doi.org/10.1016/j.ecmx.2022.100304

[17] L. Agberegha, P. Aigba, S. Nwigbo, F. Onoroh, O. Samuel, T. Bako, O. Der, A. Ercetin, R. Sener, *Energies* **2024**, *17*, 1295. DOI: https://doi.org/10.3390/en17061295

[18] M. Amiri, P. Ziółkowski, K. Stasiak, M. Ditaranto, S. Wiseman, D. Mikielewicz, Numerical simulation of cold flow and combustion in a swirl stabilized combustor, Nordic Flame Days, Trondheim, Norway, November **2023**.

[19] J. Yang, C. Liu, S. Li, B. Sun, J. Xiao, Y. Jin, *Chem. Eng. Process. Process Intensif.* **2015**, *95*, 256–266. DOI: https://doi.org/10.1016/j.cep.2015.06.017

[20] H. Safikhani, P. Mehrabian, *Adv. Powder Technol.* **2016**, *27* (*2*), 379–387. DOI: https://doi.org/10.1016/j.apt.2016.01.011

[21] W. I. Mazyan, A. Ahmadi, H. Ahmed, M. Hoorfar, *J. Aerosol Sci.* **2017**, *110*, 36–42. DOI: https://doi.org/10.1016/j.jaerosci.2017.05.007

[22] L. E. Wiesegger, R. P. Knauss, G. E. Guntschnig, J. J. Brandner, R. J. Marr, *Chem. Eng. Sci.* **2013**, *93*, 32–46. DOI: https://doi.org/10.1016/j.ces.2013.01.030

[23] X. Xu, Q. Yang, C. Wang, H. Wang, *Sep. Purif. Technol.* **2015**, *152*, 80–86. DOI: https://doi.org/10.1016/j.seppur.2015.07.058

[24] J. Z. Duran, R. T. G. Gabon, M. O. Licdan, E B. Caldona, *Chem. Eng. Technol.* **2024**, *47* (*4*), 692–698. DOI: https://doi.org/10.1002/ceat.202300076

[25] Z. Fu, H. Wu, M. Liang, Z. Guo, L. Hou, Z. Xing, *Chem. Eng. Technol.* **2024**, *47* (*3*), 520–530. DOI: https://doi.org/10.1002/ceat.202300372

[26] C. Song, J. Wang, S. Wang, J. Wen, *Chem. Eng. Technol.* **2022**, *45* (*9*), 1691–1700. DOI: https://doi.org/10.1002/ceat.202200242

[27] X. Xu, C. Gong, S. Wang, Q. Yang, Z. Xi, *Chem. Eng. Technol.* **2024**, *47* (*1*), 68–78. DOI: https://doi.org/10.1002/ceat.202300204

[28] C. Han, Y. Hu, W. Li, Q. Bie, *Adv. Powder Technol.* **2022**, *33* (*11*), 103815. DOI: https://doi.org/10.1016/j.apt.2022.103815

[29] P. Vehmaanperä, D. Safonov, T. Kinnarinen, A. Häkkinen, *Miner. Eng.* **2018**, *128*, 133–140. DOI: https://doi.org/10.1016/j.mineng.2018.08.042

[30] R. B. Xiang, K. W. Lee, *Part. Sci. Technol.* **2001**, *19* (*4*), 327–338. DOI: https://doi.org/10.1080/02726350290057868

[31] T. G. Chuah, J. Gimbun, T. S. Y. Choong, *Powder Technol.* **2006**, *162* (*2*), 126–132. DOI: https://doi.org/10.1016/j.powtec.2005.12.010

[32] H. Yoshida, K. Fukui, K. Yoshida, E. Shinoda, *Powder Technol.* **2001**, *118* (*1*), 16–23. DOI: https://doi.org/10.1016/S0032-5910(01)00290-X

[33] F. Qian, J. Zhang, M. Zhang, *J. Hazard. Mater.* **2006**, *136* (*3*), 822–829. DOI: https://doi.org/10.1016/j.jhazmat.2006.01.028

[34] F. Kaya, I. Karagoz, *Chem. Eng. J.* **2009**, *151* (*1*), 39–45. DOI: https://doi.org/10.1016/j.cej.2009.01.040

[35] A. Kępa, *Sep. Sci. Technol.* **2012**, *47* (*16*), 2250–2255. DOI: https://doi.org/10.1080/01496395.2012.671878

[36] H. Yoshida, Y. Nishimura, K. Fukui, T. Yamamoto, *Powder Technol.* **2010**, *204* (*1*), 54–62. DOI: https://doi.org/10.1016/j.powtec.2010.07.006

[37] L. S. Brar, R. P. Sharma, K. Elsayed, *Powder Technol.* **2015**, *286*, 668–677. DOI: https://doi.org/10.1016/j.powtec.2015.09.003

[38] N. Prasanna, K. Subramanian, S. Ajay, T. Rajagopal, V. Vigneshwaran, *Mater. Today Proc.* **2021**, *43*, 1960–1968. DOI: https://doi.org/10.1016/j.matpr.2020.11.425

[39] O. Hamdy, M. A. Bassily, H. M. El-Batsh, T. A. Mekhail, *Appl. Math. Modell.* **2017**, *46*, 81–97. DOI: https://doi.org/10.1016/j.apm.2017.01.069

[40] L. Wang, C. Xie, Z. Wang, K. Chen, *Adv. Mech. Eng.* **2022**, *14* (*9*), 168781322211199. DOI: https://doi.org/10.1177/16878132221119951

[41] J. Li, S. Huang, X. Wang, *Chin. J. Chem. Eng.* **2007**, *15*(*4*), 492–498. DOI: https://doi.org/10.1016/S1004-9541(07)60114-1

[42] F. Zhou, G. Sun, X. Han, Y. Zhang, W. Bi, *Adv. Powder Technol.* **2018**, *29* (*12*), 3394–3403. DOI: https://doi.org/10.1016/j.apt.2018.09.022

[43] B. Chu, B. Lin, L. Tian, C. Zheng, N. Ye, Y. Zhu, Z. Tan, *Appl. Energy* **2024**, *358*, 122567. DOI: https://doi.org/10.1016/j.apenergy.2023.122567

[44] Z. Wang, S. Chen, X. Zhang, Y. Zhou, Z. Wei, *Energy* **2024**, *291*, 130480. DOI: https://doi.org/10.1016/j.energy.2024.130480

[45] S. Park, H. Mun, J. Park, I. Lee, *J. Cleaner Prod.* **2024**, *434*, 139887. DOI: https://doi.org/10.1016/j.jclepro.2023.139887

[46] F. Yulia, R. Sofianita, K. Prayogo, N. Nasruddin, *Case Stud. Therm. Eng.* **2021**, *26*, 101093. DOI: https://doi.org/10.1016/j.csite.2021.101093

[47] N. Subramanian, P. Madejski, *Energy* **2023**, *282*, 128311. DOI: https://doi.org/10.1016/j.energy.2023.128311

[48] P. Madejski, K. Banasiak, P. Ziółkowski, D. Mikielewicz, J. Mikielewicz, T. Kuś, M. Karch, P. Michalak, M. Amiri, P. Dąbrowski, K. Stasiak, N. Subramanian, T. Ochrymiuk, *Energy* **2023**, *283*, 129163. DOI: https://doi.org/10.1016/j.energy.2023.129163

[49] https://nco2pp.mech.pg.gda.pl/pl (Accessed 2020).

[50] P. Ziółkowski, P. Madejski, M. Amiri, T. Kuś, K. Stasiak, N. Subramanian, H. Pawlak-Kruczek, J. Badur, Ł. Niedźwiecki, D. Mikielewicz, *Energies* **2021**, *14* (*19*), 6304. DOI: https://doi.org/10.3390/en14196304

[51] P. Ziółkowski, K. Stasiak, M. Amiri, D. Mikielewicz, *Energy* **2023**, *262*, 125496. DOI: https://doi.org/10.1016/j.energy.2022.125496

[52] P. Ziółkowski, J. Badur, H. Pawlak-Kruczek, K. Stasiak, M. Amiri, L. Niedzwiecki, K. Krochmalny, J. Mularski, P. Madejski, D. Mikielewicz, *Energy* **2022**, *244*, 122601. DOI: https://doi.org/10.1016/j.energy.2021.122601

[53] M. Amiri, M. Klugmann, J. Mikielewicz, P. Ziółkowski, D. Mikielewicz, *Int. Commun. Heat Mass Transfer* **2024**, *156*, 107596. DOI: https://doi.org/10.1016/j.icheatmasstransfer.2024.107596

[54] Z. Sayyah Alborzi, Y. Amini, P. Amirabedi, S. Raveshiyan, A. Hassanvand, *Chem. Eng. Technol.* **2023**, *46* (*10*), 2034–2045. DOI: https://doi.org/10.1002/ceat.202300102

[55] M. Bagi, M. V. Razlighi, M. Shanbedi, A. Karim, *Chem. Eng. Technol.* **2024**, *47* (*4*), 732–738. DOI: https://doi.org/10.1002/ceat.202300504

[56] M. Amiri, D. Mikielewicz, *Numer. Heat Transfer, Part A* **2023**, *83* (*10*), 1146–1173. DOI: https://doi.org/10.1080/10407782.2022.2150342

[57] M. Amiri, M. B. Ayani, P. Ziolkowski, D. Mikielewicz, *J. Food Process Eng.* **2022**, *45* (*4*), e14006. DOI: https://doi.org/10.1111/jfpe.14006

[58] O. E. Olaleye, B. Van Ombele, X. Li, O. A. Adeshina, *J. Pet. Sci. Eng.* **2022**, *216*, 110733. DOI: https://doi.org/10.1016/j.petrol.2022.110733

[59] M. H. Purnanto, S. J. Zarrouk, J. E. Cater, *IPENZ Trans.* **2013**, *40*, 1–10. DOI: https://search.informit.org/doi/10.3316/informit.366967552564856
[60] M. Amiri, J. Mikielewicz, D. Mikielewicz, *Sep. Purif. Technol.* **2024**, *329*, 125236. DOI: https://doi.org/10.1016/j.seppur.2023.125236
[61] E. Yohana, M. Tauviqirrahman, B. Yusuf, K.-H. Choi, V. Paramita, *Powder Technol.* **2021**, *377*, 464–475. DOI: https://doi.org/10.1016/j.powtec.2020.09.014
[62] A. Surjosatyo, A. Respati, H. Dafiqurrohman, Muammar, *Procedia Eng.* **2017**, *170*, 154–161. DOI: https://doi.org/10.1016/j.proeng.2017.03.036
[63] J. Vaziri Naeen Nejad, S. Kheradmand, *Powder Technol.* **2021**, *390*, 401–416. DOI: https://doi.org/10.1016/j.powtec.2021.05.055
[64] A. J. Hoekstra, J. J. Derksen, H. E. A. Van Den Akker, *Chem. Eng. Sci.* **1999**, *54* (*13-14*), 2055–2065. DOI: https://doi.org/10.1016/S0009-2509(98)00373-X
[65] J.-H. Lim, S.-H. Oh, S. Kang, K.-J. Lee, S.-J. Yook, *Sep. Purif. Technol.* **2021**, *276*, 119397. DOI: https://doi.org/10.1016/j.seppur.2021.119397
[66] R. Utikar, N. Darmawan, M. Tade, Q. Li, G. Evans, M. Glenny, V. Pareek, in *Computational Fluid Dynamics* (Eds: H. W. Oh), InTech, Rijeka **2010**, 241–266.
[67] D. Mikielewicz, M. Amiri, M. Klugmann, J. Mikielewicz, *Int. J. Heat Mass Transfer* **2023**, *216*, 124576. DOI: https://doi.org/10.1016/j.ijheatmasstransfer.2023.124576
[68] D. Mikielewicz, M. Amiri, J. Mikielewicz, Direct-contact condensation from vapour-gas mixture in a spray ejector condenser for negative CO_2 power plant, 2nd Int. Conf. on Negative CO_2 Emissions, Götenborg, Sweden, June, **2022**.
[69] D. Mikielewicz, M. Amiri, J. Mikielewicz, A simple analytical model of direct-contact condensation from vapour- inert gas mixture in a spray ejector condenser, **2022**. Available at SSRN: DOI: https://doi.org/10.2139/ssrn.4147312
[70] M. Jain, R. S Prakash, G. Tomar, R. V. Ravikrishna, *Proc. R. Soc. A* **2015**, *471* (*2177*), 20140930. DOI: https://doi.org/10.1098/rspa.2014.0930
[71] B. Wang, D. L. Xu, K. W. Chu, A. B. Yu, *Appl. Math. Modell.* **2006**, *30* (*11*), 1326–1342. DOI: https://doi.org/10.1016/j.apm.2006.03.011
[72] B. Zhao, H. Li, D. Wang, Q. Liu, Y. Su, *Powder Technol.* **2022**, *395*, 122–132. DOI: https://doi.org/10.1016/j.powtec.2021.09.047
[73] J. Yang, Z. Dong, C. Shen, W. Zhang, X. Hao, G. Guan, *Powder Technol.* **2019**, *356*, 871–879. DOI: https://doi.org/10.1016/j.powtec.2019.09.013
[74] Z. Wang, G. Sun, S. Yuan, Z. Qian, Z. Song, *Asia-Pac. J. Chem. Eng.* **2022**, *17* (*6*), e2836. DOI: https://doi.org/10.1002/apj.2836
[75] S. M. Vahedi, F. Parvaz, M. Kamali, H. J Jebeli, *Iranian J. Oil Gas Sci. Technol.* **2018**, *7* (*4*), 59–78. DOI: https://doi.org/10.22050/ijogst.2018.98556.1409

International Communications in Heat and Mass Transfer 156 (2024) 107596

Contents lists available at ScienceDirect

International Communications in Heat and Mass Transfer

journal homepage: www.elsevier.com/locate/ichmt

CO_2 capture through direct-contact condensation in a spray ejector condenser and T- junction separator

Milad Amiri [a,*], Michal Klugmann [a], Jaroslaw Mikielewicz [b], Paweł Ziółkowski [a], Dariusz Mikielewicz [a]

[a] Faculty of Mechanical Engineering and Ship Technology, Gdańsk University of Technology, ul. Gabriela Narutowicza 11/12, 80-233 Gdańsk, Poland
[b] Polish Academy of Science, Institute of Fluid-Flow Machinery ul, Fiszera 14, 80-231 Gdańsk, Poland

ARTICLE INFO

Keywords:
Direct-contact condensation
Spray ejector condenser
Separator efficiency
CO_2 capture

ABSTRACT

The design principle underlying the steam condensation and CO2 purification in a gas power plant with a focus on reducing CO2 emissions encompasses the deployment of a spray ejector condenser (SEC) and separator. This innovative system facilitates direct-contact condensation of steam with non-condensable gas (CO2) by interacting with a spray of subcooled water, seamlessly integrated with a T-junction separator mechanism aimed at yielding pure CO2. Because of decreased convective heat transfer and heightened diffusion resistance between the subcooled water and steam phases caused by CO2, the research examined the effects of various thermophysical parameters of the injected water, specifically temperature (20–40 $^{\circ}C$) and pressure (12–16 bar) along with steam mass flow rates (2.2–4.6 $\frac{g}{s}$) to improve heat transfer rates within the SEC. The SEC utilizes a Eulerian-Eulerian multiphase model, wherein water is considered the continuous phase while the mixture of steam and CO2 constitutes the dispersed phase. Turbulence within the ejector is represented applying standard k-ε model. Furthermore, the separator employs turbulence and operates in three dimensions using the control volume method. The simulation of turbulent two-phase flow in the gas-liquid T-junction separator is conducted utilizing standard k-ε turbulence model and a mixture model. The results imply that the maximum temperature difference (ΔT) between inlet and outlet of SEC is observed when the steam mass flow rate is 2.2 (g/s) without CO2, while the presence of CO2 leads to a reduction in ΔT. Additionally, the performance of the SEC is notably affected by the optimal settings of water temperature and pressure, where lower coolant water temperatures (20$^{\circ}C$) and higher water pressures (16 bar) contribute to improved condensation performance. Furthermore, the study explores the decrease in separation efficiency associated with elevated inlet mass flow rate, attributed to maldistribution in the vertical impact T-junction separator.

1. Introduction

Reducing the release of CO2 from fossil fuel combustion in power generation plays an indispensable role in addressing global climate change [1]. Implementing effective carbon capture methodologies in power generation facilities is crucial to alleviate CO2 emissions. Currently, researchers are exploring three distinct methods for capturing CO2 emissions from power plants: 1. pre-combustion 2. oxy-combustion 3. post-combustion, so that Pre-combustion capture focuses on extracting CO2 before combustion initiates. Hence, this method is impractical in traditional steam power facilities but finds application in Integrated Gasification Combined Cycle (IGCC) plants. These plants operate by gasifying fuel, purifying the gas, and incorporating the resultant gas into a combined cycle system. Pre-combustion is primarily employed in power plants handling natural gas or coal. These processes involve intricate and costly initial fuel conversions. However, pre-combustion offers advantages such as elevated CO_2 concentrations and heightened pressure in the discharge flow, which streamline subsequent CO_2 separation steps [2]. The elevated CO_2 concentration achieved through pre-combustion enables the use of sorbents of a physical nature, simplifying separations compared to post-combustion methods that rely on chemical absorbents like amine-based solvents. Typically, due to its operation at higher pressure resulting in elevated CO_2 concentrations, the operational costs associated with CO_2 capture in pre-combustion are substantially lower compared to post-combustion methods [3]. The oxy-fuel method, another carbon capture and storage (CCS) strategy,

* Corresponding author.
E-mail address: milad.amiri@pg.edu.pl (M. Amiri).

https://doi.org/10.1016/j.icheatmasstransfer.2024.107596

Available online 21 May 2024

circumvents the challenges of capturing CO2 from large flue gas streams by burning pure oxygen with fuel. Consequently, the concentration of other gas constituents in the flue gas can be minimized, allowing for the recovery of CO2 through water condensation. To control the combustion temperature, cold recycling of flue gas is necessary. Nevertheless, this method significantly affects the power plant's operation and complicates the process of retrofitting existing plants. Oxyfuel is applicable for power generation in facilities utilizing solid coal, syngas, natural gas and liquid petroleum fractions up to medium hydrocarbons. The key features of employing oxyfuel combustion for CO_2 capture involves enhancing CO_2 concentration, eliminating NOx with pure oxygen [4]. The post-combustion capture of CO2 method involves extracting CO2 and other gases emitted from the combustion of fossil fuels through either physical or chemical adsorption/absorption processes [5]. Post-combustion CO2 mitigation represents a direct method and serves as the foundation of the existing infrastructure in CCS. Although pre-combustion and oxy-fuel capture offer unique benefits, it's improbable that these techniques will entirely supplant post-combustion capture worldwide. A recent in-depth analysis delved into the core principles of these varied approaches and their economic ramifications [6]. This study provides a post-combustion carbon capture technology including a SEC and T-Junction separator.

The spray ejector condenser (SEC) functions by employing direct contact condensation to convert water vapor from exhaust gases into liquid form. Direct contact condensation (DCC) is a prevalent technique applied across diverse industries, and direct contact condensers represent apparatuses that employ this method for condensation purposes. For more than a century, DCC has found extensive application across various industrial sectors including chemical and petroleum engineering, desalination plants, and power generation facilities [7]. Direct-contact condensers facilitate direct interaction between liquid and gas phases. Cooling liquid can be introduced into the gas zone via spraying, initiating rapid condensation to optimize the performance of condensers in terms of heat transfer. The presence of other gases significantly affects the rate of heat transfer and condensation efficiency [8]. Sideman and Moalem-Maron [9] noted that the benefits of DCC over traditional methods employing metal transfer surfaces stem from its simpler design, reduced issues with scaling and corrosion, decreased maintenance expenses, enhanced transfer rates and greater specified transfer areas. Recent researches have focused on optimizing condensation processes to improve efficiency and reduce mechanical damage caused by droplets. Studies have explored innovative methods such as determining optimal surface heating and wetness at the inlet of turbines using the TOPSIS method [10], optimizing inlet steam superheat degree and blade pitch [11], implementing drainage grooves on turbine blades [12], and optimizing hot steam injection into turbine cascades [13]. These approaches aim to enhance condensation efficiency, reduce condensation losses, and minimize erosion rates, ultimately leading to improved performance and lower operational costs. Amiri et al. [5] examined how the implementation of an electrohydrodynamic actuator (EHD) in a steam ejector condenser enhances convective transfer for DCC by mitigating resistance. Mikielewicz et al. [14] explored an innovative approach to enhance DCC of a vapor-inert gas mixture within a SEC. Their research delved into the breakup of droplets and heat and mass transfer mechanism. Findings indicated that an increased quantity of droplets at identical mass flow rates led to improved DCC effectiveness because of the increased surface of heat transfer. Ghazi [15] conducted experimental research to explore heat transfer mechanism through direct contact, which involved injecting air via bubbling at a constant temperature. This study revealed a significant rise in air temperature, ranging from approximately 100% to 200%. Zong et al. [16] and Fu et al. [17] investigated experiments to examine the influence of steam-water variables on flow patterns. Reddick et al. [18] reported the findings from an experimental assessment on the efficacy of a steam ejector in managing CO2 and steam.

In this study, the T-junction separator serves as the second component of the carbon capture technology under investigation. T-junctions are commonly employed across various engineering applications, including petroleum [19], refrigeration systems [20], nuclear reactors [21], owing to their uncomplicated design, compact size, and affordability. The injection of fluids into the primary conduit via the bypass pipeline results in varied flow patterns, influenced by the differing rates of flow for two-phase fluids and properties [22,23]. When a two-phase flow of liquid and vapor enters a T-junction, there's an inevitable uneven distribution of vapor and liquid, which can potentially lead to harmful consequences downstream due to mass flow rate and gas quality disparities. Conversely, this maldistribution can also serve as a means for separating the phases. Azzopardi et al. [24] examined how T-junctions perform in separating phases for air–water mixtures, particularly in chemical plant settings. Tuo et al. [20] utilized T-junctions for separating two-phase refrigerants within refrigeration systems based on vapor compression. Śliwicki and Mikielewicz [25] examined the behavior of two-phase flow within a horizontal T-junction, considering an annular mist flow distribution at the inlet of T-junction. Xu et al. [26] introduced an innovative approach to constructing a thermodynamic cycle utilizing T-junctions as component separators, resulting in a 22% [27] improvement in cycle efficiency compared to traditional thermodynamic cycles. Numerous factors influence phase separation process in T-junctions. The contributing factor factors were classified by Yang et al. [28] into fundamental and direct categories. Direct factors encompass operational conditions and geometric aspects, while fundamental factors consist of gravity, surface tension, centrifugal force and inertia. The efficiency of phase separation in a T-junction, especially one with horizontal branching, is limited. Several studies [28,29] suggest that augmenting the quantity of branches may enhance the efficiency of phase separation. Mohamed et al. [30] conducted experimental investigations on full separation of air-water mixtures using a single impacting T-junction. Their findings suggested that achieving full separation through a single T-junction at elevated inlet flow rates might not be feasible, but it could potentially be accomplished by employing multiple T-junctions. Soliman and Noor [31] divided the annular flow of air-water into two vertically impacting T-junctions to investigate the inlet velocities of the two phases required for complete phase separation. At the constant inlet air velocity, the range of liquid phase velocities for achieving full phase separation in the two T-junctions is nearly double that of a single T-junction. While numerous scholars have explored separation in T-junctions, the majority of these investigations utilize steam-water or air-water mixtures. Only a handful of investigations delve into the separation of CO2-water, which could hold practical significance for integration into advanced negative CO2 emission gas power plant (nCO2PP), [32–34] as depicted in Fig. 1. The concept of nCO2PP relies on the utilization of sewage sludge, which is converted into syngas and then combusted in a wet combustion chamber (WCC). Following this, CO2 is separated from the moist exhaust gases in a SEC and subsequently sequestered in cyclone or T-junction separators. It's noteworthy that syngas is considered a renewable fuel, resulting in a net reduction of CO2 emissions in the power plant.

This paper presents the design of a SEC, both experimentally and numerically, as well as a T-junction separator (numerically) to achieve the intended high-purity CO2 stream. The integration of a spray ejector condenser with a removed diffuser section and T-junction separator for CO2 separation in negative gas power plants represents an innovative approach that has not been previously explored or extensively researched in existing literature. While prior studies, such as those conducted by Madejski et al. [35,36] and Kus and Madejski [37], have investigated aspects of vapor condensation using a SEC with a diffuser section, the specific combination of components in our study presents a unique solution for enhancing CO2 capture efficiency within power generation facilities. This study addresses a significant research gap by examining the performance of this novel combination and elucidating the intricate dynamics within the ejector. Through a comprehensive examination employing computational analyses and precise

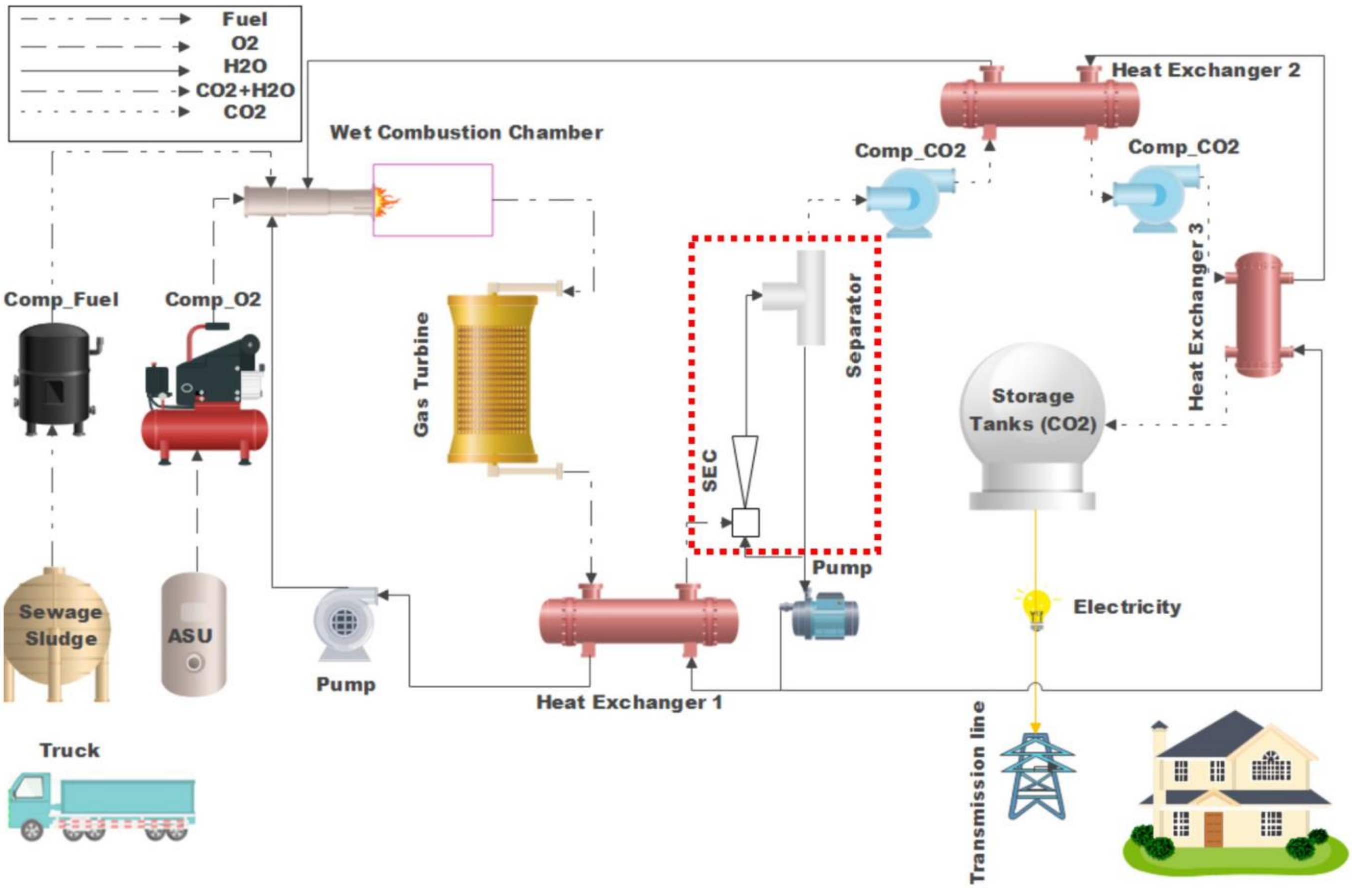

Fig. 1. Flowchart of the Gas Power Plant with Negative CO2 Emissions [32,33].

experimental methods, we aim to deepen our understanding of ejector dynamics and contribute valuable insights to the field of carbon capture and power generation. By addressing these research gaps, this study makes significant contributions to the development of more efficient and environmentally sustainable power generation practices. The implementation of our proposed SEC and T-junction separator in negative gas

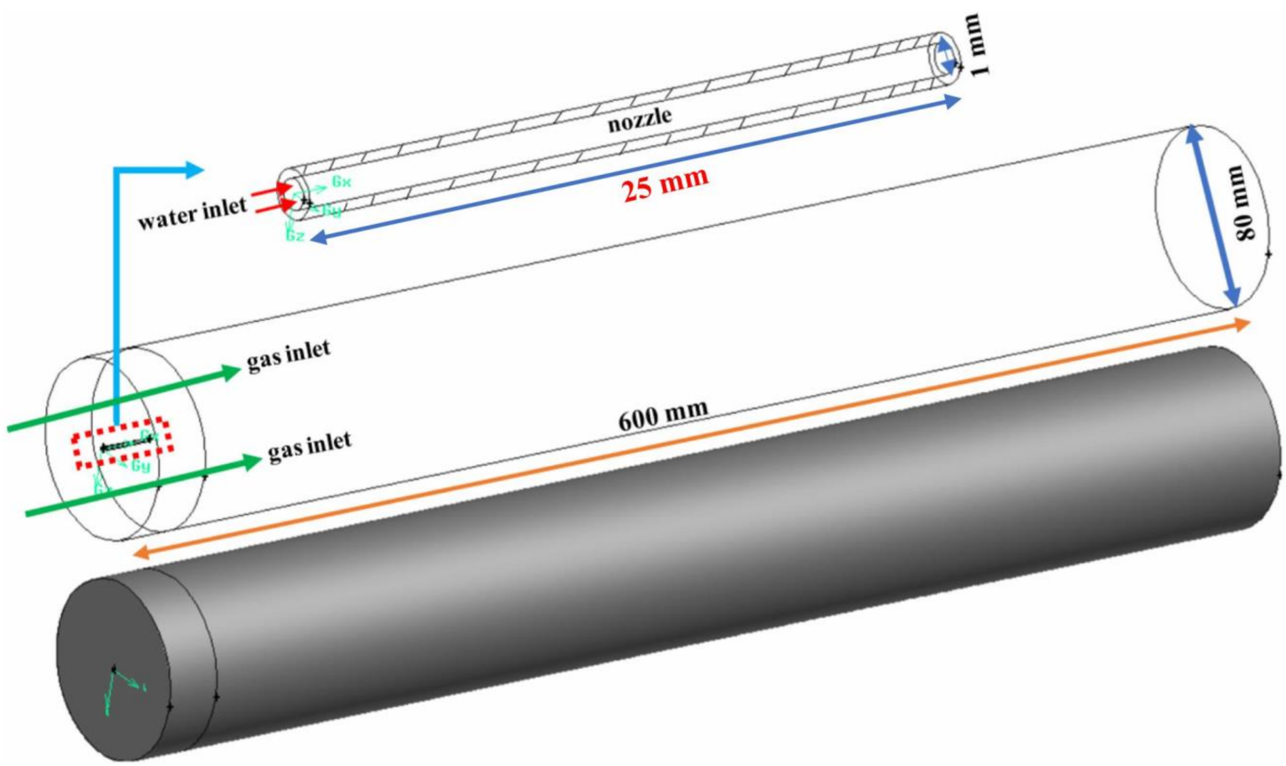

Fig. 2. Geometry of a spray ejector condenser and its dimensions.

power plants holds promise for significantly reducing greenhouse gas emissions, thereby advancing efforts towards a cleaner and more sustainable energy future. For this purpose, initially, a numerical model is developed to enhance the efficiency of the CO2 capture unit. The impact of varying steam inlet mass flow rates on the water volume fraction is examined. Subsequently, the effect of steam mass flow rate and the volumetric flow rate of non-condensable gas (CO2) on the inlet and outlet temperatures of the SEC is investigated. Numerical simulations are conducted for varying values of inlet mass flow rate of steam (ranging from 2.2 to 4.6 $\frac{g}{s}$) and volumetric flow rate of CO2 (ranging from 0 to 10 $\frac{m^3}{h}$). By examining the effects of water temperature and pressure, a comprehensive model for the SEC is derived. Once the SEC model is obtained, the efficiency of the vertical impact T-junction separator can be assessed.

2. Modeling

2.1. SEC

An experimental and computational investigation was undertaken to examine the DCC process involving a subcooled water jet interacting with steam and CO2 within an ejector. This investigation was conducted following the layout of the water-steam/CO2 ejector depicted in Fig. 2. The ejector comprises a central water nozzle surrounded by a steam/CO2 region. A motive fluid has been introduced through a 1 mm nozzle, where it makes direct contact with the steam/CO2 mixture in the chamber. This interaction leads to condensation. Fig. 2 provides a schematic depiction along with the dimensional specifications of the ejector.

2.2. T- junction

The geometries of the 3D horizontal and vertical T-junctions are depicted in Fig. 3. In the validation section, separation efficiency of the vertical impact T-junction separator compared with experimental results. However, the authors emphasize the importance of validating the fluid flow in numerical simulations. Therefore, the pressure drop of the horizontal T-junction separator was also compared with experimental results. Consequently, both the horizontal and vertical geometries of the T-junction separators are discussed in this section. In order to ensure the reliability of our simulation results, regarding pressure drop and separation efficiency, we began by implementing the boundary conditions outlined in the corresponding experimental study. This step was crucial to verify the fidelity of our simulation approach within the Ansys Fluent 2021 R1. By aligning our computational setup with the experimental conditions, we aimed to enhance the confidence in the validity of our simulation outcomes. Therefore, the primary objective of this investigation is on the vertical T-junction geometry. However, the inclusion of the horizontal T-junction is intended solely to validate the simulation process in Ansys Fluent 2021R1. For the horizontal configuration, each leg has a length of 0.5 m, and the diameter is 3.81 cm, following the parameters outlined in Saba et al. [38]. While Saba et al. examined the pressure drop in a horizontal T-junction separator experimentally, validation of the separation efficiency in the vertical impact T-junction separator involved an experimental investigation conducted by Tuo and Hrnjak [20].

3. Governing equations

3.1. SEC

In this investigation, the flow pattern reveals an irregular distribution of both liquid and gas phases, creating a significant discrepancy between them. In order to precisely depict the phenomenon, a Eulerian-Eulerian multiphase model was utilized, allowing for separate treatment

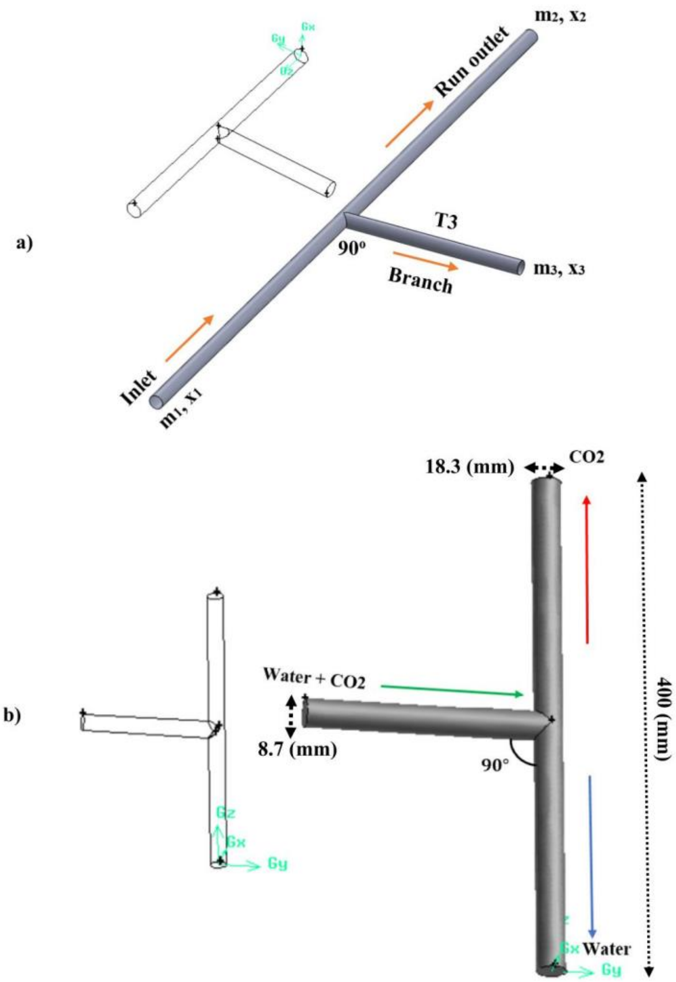

Fig. 3. a) horizontal T-junction geometry and b) vertical impact T-junction separator.

of the gas and liquid phases. Here, water serves as the representative of the continuous phase, whilst the dispersed phase comprises a mixture of gas including CO2 and steam. The standard k - ε model is applied to characterize the turbulent dynamics within the ejector. In this model, the liquid phase (α) corresponds to the liquid water, while the dispersed gas phase (β) is considered. The modeling of the liquid phase involves the equations for turbulent kinetic energy (k) and its dissipation rate (ε) that are characteristic of the standard k - ε turbulence model, enabling a detailed examination of the flow dynamics within the system.

$$\frac{\partial}{\partial t}(r_\alpha\rho_\alpha k_\alpha) + \nabla(r_\alpha\rho_\alpha \boldsymbol{U}_\alpha k_\alpha) = \nabla\left(r_\alpha\left(\mu_\alpha + \frac{\mu_{t\alpha}}{\sigma_k}\right)\nabla k_\alpha\right) + r_\alpha(P_\alpha - \rho_\alpha\varepsilon_\alpha) \quad (1)$$

$$\frac{\partial}{\partial t}(r_\alpha\rho_\alpha\varepsilon_\alpha) + \nabla(r_\alpha\rho_\alpha \boldsymbol{U}_\alpha\varepsilon_\alpha) = \nabla\left(\mu_\alpha + \frac{\mu_{t\alpha}}{\sigma_\varepsilon}\right)\nabla\varepsilon_\alpha + r_\alpha\frac{\varepsilon_\alpha}{k_\alpha}(C_{\varepsilon1}P_\alpha - C_{\varepsilon2}\rho_\alpha\varepsilon_\alpha) \quad (2)$$

The equations provided utilize symbols representing various properties: density (ρ), volume fraction (r), velocity vector ($\boldsymbol{U}$), turbulent kinetic energy (k), and turbulent dissipation rate (ε). The turbulent viscosity of the liquid phase ($\mu_{t\alpha}$) can be calculated using the following formula:

$$\mu_{t\alpha} = \frac{C_\mu\rho_\alpha k_\alpha^2}{\varepsilon_\alpha} \quad (3)$$

In this context, the parameters $C_{\varepsilon1}$, $C_{\varepsilon2}$, C_μ, σ_k and σ_ε are assigned values of 1.44, 1.92, 0.09, 1.0, and 1.3, respectively [39]. To calculate the turbulent kinematic viscosity for the gas phase, which encompasses α and β phases, the equation mentioned below is employed:

$$\sigma = \frac{\nu_{ta}}{\nu_{t\beta}} \tag{4}$$

In this formula, σ denotes a parameter termed the turbulent Prandtl number, fixed at a value of 1 within the model [40]. Derived from the turbulent viscosity of the liquid phase, the turbulent viscosity for the gas phase is determined.

$$\mu_{t\beta} = \frac{\rho_\beta \mu_{t\alpha}}{\rho_\alpha} \tag{5}$$

3.1.1. Interfacial surface density between water and steam

In this study, the analysis of steam condensation rate delves into the significance of the heat transfer surface area shared between the steam and water phases, which serves as a focal point of investigation. To model the dispersed phase accurately, it is represented as clusters comprising standard spherical particles. Furthermore, the assumption of minute gas bubbles as spherical entities aids in determining the density of interfacial area. This calculation is pivotal for understanding the interphase interaction dynamics and optimizing the efficiency of steam condensation processes. The equation elucidating the computation of interfacial area density is provided below, offering a quantitative approach to evaluate this critical parameter.

$$A_{sw} = \frac{6\gamma_\beta}{d_\beta} \tag{6}$$

In this formula, d_β signifies the average diameter of bubbles within the dispersed phase, whereas γ_β denotes the fraction of gas volume within the liquid phase [41,42].

3.1.2. Momentum transfer of interphase

In this context, the exchange of momentum between the liquid and gas phases is examined through two distinct mechanisms: the drag force ($\mathbf{M}_{D\alpha}$) and turbulent dispersion force ($\mathbf{M}_{TD\alpha}$). $\mathbf{M}_{D\alpha}$ acts as a resistive force opposing the motion of the dispersed phase within the continuous phase. It arises due to the interaction between the fluid phases and is crucial for understanding the overall momentum transfer dynamics in multiphase flows [43]:

$$\mathbf{M}_{D\alpha} = -\mathbf{M}_{D\beta} = \frac{3}{4}\frac{C_D}{D_\beta} r_\beta \rho_\alpha \left|\mathbf{U}_\beta - \mathbf{U}_\alpha\right| \left(\mathbf{U}_\beta - \mathbf{U}_\alpha\right) \tag{7}$$

The integration of the drag force coefficient, symbolized as C_D, into the Schiller-Naumann drag force model is feasible.

$$C_D = max\left(\left(\frac{24}{Re}\left(1 + 0.15Re^{0.687}\right), 0.44\right)\right) \tag{8}$$

The Lopez-de-Bertodano model is utilized to compute the $\mathbf{M}_{TD\alpha}$:

$$\mathbf{M}_{TD\alpha} = -\mathbf{M}_{TD\beta} = -C_{TD}\rho_\alpha \kappa_\alpha \nabla_{r_\alpha} \tag{9}$$

The κ_α represents the turbulent kinetic energy, a crucial parameter in turbulent flow analysis. Meanwhile, C_{TD} refers to the coefficient governing the turbulent dispersion force, which remains consistently 0.3 throughout this particular analysis, providing a standardized basis for calculations and simulations.

3.1.3. Heat and mass transfer of interphase

In the context of the SEC system, the introduction of CO2 results in the formation of a gas layer adjacent to the phase interface, which impedes the diffusion of steam into subcooled water and reduces convective heat transfer between the phases. To address these challenges, a two-resistance model, grounded in the diffusion-conduction principle, is employed [44]. On the gas side, CO2 creates a barrier layer hindering direct contact between subcooled water and steam, resulting in a reduced density of the interfacial area in comparison to a pure steam flow. However, typically, the heat transfer coefficient overcomes this resistance [45]. On the contrary, within the liquid domain, the existence of undercooled water encourages the condensation of steam, whereas the occurrence of non-condensable gas hinders this phenomenon. The conveyance of overall heat flow from steam to the phase interface is delineated as follows [40]:

$$\dot{Q}_s = \dot{m}_{sw} \mathrm{H_s} \tag{10}$$

The steam condensation rate, denoted as $\dot{m}_{sw}$, contributes to the complete heat flow from the interface of phases to the subcooled water, encompassing both the enthalpy of convective heat exchange and water between interface and water.

$$\dot{Q}_w = \dot{m}_{sw}\mathrm{H_w} + \mathrm{h_w A_{sw}}(\mathrm{T_{sat}} - \mathrm{T_w}) \tag{11}$$

The determination of the coefficient of heat transfer (liquid phase), denoted as h_w, relies on the physical properties inherent to the mixture as well as the Nusselt number:

$$h_w = \frac{\lambda_{wa} Nu_{wa}}{d_g} \tag{12}$$

The Nusselt number of the liquid phase [45]:

$$\mathrm{Nu_{wa}} = \begin{cases} 2 + 0.6Re_\mathrm{r}^{0.5} Pr_\mathrm{wa}^{0.33}\ 0 \le Re_\mathrm{r} < 776\ 0 < Pr_\mathrm{wa} < 250 \\ 2 + 0.27Re_\mathrm{r}^{0.62} Pr_\mathrm{wa}^{0.33}\ Re_\mathrm{r} \ge 776\ 0 < Pr_\mathrm{wa} < 250 \end{cases} \tag{13}$$

Relative motion and shear effect between the gas and liquid phases defined as [40]:

$$Re_r = \frac{\rho_{wa}\left|\mathbf{U}_g - \mathbf{U}_{wa}\right| d_g}{\mu_{wa}} \tag{14}$$

The following correlations are utilized to determine the physical properties [40]:

$$\lambda_{wa} = \frac{\alpha_w \lambda_w + \alpha_a \lambda_a}{\alpha_w + \alpha_a} \tag{15}$$

$$\mu_{wa} = \frac{\alpha_w \mu_w + \alpha_a \mu_a}{\alpha_w + \alpha_a} \tag{16}$$

$$Pr_{wa} = \frac{\alpha_w Pr_w + \alpha_a Pr_a}{\alpha_w + \alpha_a} \tag{17}$$

Mass-weighted average velocity determines the velocity of the mixture, considering the momentum transfer between CO2 and water [40].

$$\mathbf{U}_{wa} = \frac{\alpha_w \rho_w \mathbf{U}_w + \alpha_a \rho_a \mathbf{U}_a}{\alpha_w \rho_w + \alpha_a \rho_a} \tag{18}$$

Using the previously mentioned equations, it's noted that the dynamic viscosity, Prandtl number and thermal conductivity of the gas mixture decline with an increase in the CO2 mass fraction, in line with theoretical [44] and experimental [46] data. In accordance with two-resistance model, thermal equilibrium has been achieved at the phase interface, where $\dot{Q}_s$ equals $\dot{Q}_w$. The combination of Eqs. (10) and (11) allows for the determination of the rate of condensation per time and unit volume.

$$\dot{m}_{sw} = \frac{h_w A_{sw}(T_{sat} - T_w)}{H_s - H_w} \tag{19}$$

T_{sat} denotes the temperature at which water reaches its saturation point corresponding to the local steam partial pressure. The steam partial pressure of steam has been determined using the following procedure:

$$P_s = P_{stat}\left(\frac{\alpha_s}{\alpha_s + \alpha_a}\right) \tag{20}$$

3.2. T-junction separator

The modeling approach adopted in this study, employing a Eulerian-Eulerian model, treats both phases as continuous entities and integrates phase coupling into the analysis. Within this framework, there is no exchange of mass or heat between the phases, and an assumption of a smooth, adiabatic wall serves as the boundary condition. Furthermore, the computation of near-wall flow dynamics incorporates the use of the non-equilibrium equation, providing a comprehensive understanding of the system's behavior near the boundaries.

Formulated below are the continuity equations:

$$\nabla.\left(\alpha_{ph}\rho_{ph}\mathbf{V}_{ph}\right) = 0 \tag{21}$$

The correlation between the two phases is articulated as follows:

$$\sum \alpha_{ph} = 1 \tag{22}$$

The term α_{ph} signifies the fraction of voids, with "ph" denoting either the gas or liquid phases. The equations governing the conservation of momentum have been deduced as outlined in the reference [47]:

$$\nabla.\left(\alpha_{ph}\rho_{ph}\mathbf{V}_{ph}\mathbf{V}_{ph}\right) = -\alpha_{ph}\nabla p + \nabla.\boldsymbol{\tau}_{ph} + \alpha_{ph}\rho_{ph}\mathbf{g} + \mathbf{f} + \mathbf{S}$$

$$\boldsymbol{\tau}_{ph} = \alpha_{ph}\left(\mu_{ph} + \mu_{t,m}\right)\left(\nabla\mathbf{V}_{ph} + \nabla\mathbf{V}_{ph}^{T}\right) + \alpha_{ph}\left(\lambda_{ph} - \frac{2}{3}\left(\mu_{ph} + \mu_{t,m}\right)\right)\nabla.\mathbf{V}_{ph}\mathbf{I} \tag{23}$$

P denotes static pressure, S stands for surface tension, g represents gravitational acceleration, and drag force coefficient defines as f. The drag force coefficient has been computed using the formula:

$$C_D = \begin{cases} 24\left(1 + 0.15Re^{0.678}\right)/Re & Re \le 1000 \\ 0.44 & Re \ge 1000 \end{cases}$$

$$f = \frac{C_D Re}{24}$$

$$Re = \rho_G|\upsilon_L - \upsilon_G|d_p/\mu_G \tag{24}$$

The droplet diameter, represented by d_p, is assumed to be 10^{-5}. Boundary conditions consist of velocity inlet and outflow. The following equations determine the inlet velocity:

$$\upsilon_G = m_1 x_1/\rho_G\alpha_G$$

$$\upsilon_L = m_1(1 - x_1)/\rho_L\alpha_L \tag{25}$$

The flow simulation utilizes the standard k-ε turbulence model.

$$\nabla.\left(\rho_m\mathbf{V}_m\mathbf{k}\right) = \nabla.\left(\left(\mu_m + \frac{\mu_{t,m}}{\sigma_k}\right)\nabla k\right) + G_{k,m} - \rho_m\varepsilon$$

$$\nabla.\left(\rho_m\mathbf{V}_m\varepsilon\right) = \nabla.\left(\left(\mu_m + \frac{\mu_{t,m}}{\sigma_\varepsilon}\right)\nabla\varepsilon\right) + \frac{\varepsilon}{k}\left(C_1G_{k,m} - C_2\rho_m\varepsilon\right) - R_\varepsilon \tag{26}$$

The parameters σ_ε and σ_k have been assigned specific values crucial for characterizing turbulent flow behavior: 1.3 and 1, respectively. Also, $C_1$and C_2 are 1.44, and 1.92, respectively. $\mu_{t,m}$ defines the turbulent viscosity of the mixture, ρ_m represents mixture density, $\mathbf{V}_m$ indicates the mixture velocity. Their definitions are as follows:

$$\rho_m = \sum_{ph=1}^{N}\alpha_{ph}\rho_{ph}$$

$$\mu_m = \sum_{ph=1}^{N}\alpha_{ph}\mu_{ph}$$

$$\mathbf{V}_m = \sum_{ph=1}^{N}\alpha_{ph}\rho_{ph}\mathbf{V}_{ph} \Big/ \sum_{ph=1}^{N}\alpha_{ph}\rho_{ph}$$

$$\mu_{t,m} = \rho_m C_\mu k^2/\varepsilon \tag{27}$$

In Eq. (27), N encompasses 1 (for gas) and 2 (for liquid) and the value of C_μ is 0.0845 [47]. The formulation for turbulent kinetic energy $\left(G_{k,m}\right)$ from the average gradient is:

$$G_{k,m} = \mu_{t,m}\left[\nabla\mathbf{V}_m + \nabla\mathbf{V}_m^T\right]/\nabla\mathbf{V}_m \tag{28}$$

4. Experimental feasibility study of a spray ejector condenser

DCC process occurs within the primary section of the SEC, specifically within the throat. This study exclusively focuses on examining the physical phenomena within this throat region, given the extensive documentation of processes within the Venturi nozzle's converging and diverging sections for both single and multi-phase flow scenarios [48]. Utilizing a transparent tube with an 80 mm internal diameter, the experimental setup serves as the SEC's test section, as illustrated in Fig. 4. A 1 mm nozzle delivers the motive fluid, comprising water with an average inlet temperature of 8 °C and pressures ranging from 5.68 to 10.17 bars, corresponding to water mass flow rates between 17.56 and 22.90 g per second. The minimum inlet pressure required for drop spray formation and jet breakup is noted at 5.68 bar. The throat extends over a length of 600 mm. Introduction of the steam and CO2 mixture occurs through an inlet manifold and mixing chamber within the mixing length. Sourced from the Battistella Saturno MAX/S generator, the wet vapor, regulated at near-atmospheric pressure and approximately 100 °C, has a maximum feed rate of 6 g/s, with the CO2 reaching a maximum feed rate of 8.7 $\frac{m^3}{h}$. The mixing chamber (2.4×10^{-3} m^3) aids in mixing, equalizing temperatures, and eliminating excess water condensate. As the gas-steam mixture enters the throat, it interacts with a spray of droplets to initiate DCC process. Jet breakup occurs after some distance from the throat inlet, contingent upon inlet pressure of water. Information regarding the condensed vapor within the process is obtained by subtracting the known quantity of water from the total volume at the nozzle. An outlet at the upper section of the separation chamber (9) is employed to release excess CO2 and any non-condensed vapor into the atmosphere. Water sourced from the municipal supply, regulated by the Lead Fluid model CT3001S gear pump, is delivered to the nozzle under a pressure of 3 bars, ensuring a pulse-free flow and stabilizing with an accuracy of ±5 ml/min. Flow rate measurements utilize a mass flowmeter (Atrato AT740), independently confirmed via titration performed at the onset and conclusion of each measurement series. During these series, the entirety of the vapor input range is explored while maintaining a constant feed of spray droplets, and optionally, constant flow rate of CO2. Alternatively, entire range of CO2 input is examined while maintaining a constant vapor and spray droplets rate. Water pressure measured (by Trafag NAH type 8253.80.2317 transducer) at the nozzle inlet, while temperature measurements employ type T thermocouples with an accuracy of ±0.3 K, their positions indicated in Fig. 4. The flow rates of CO2 and vapor are measured using calibrated Krohne glass rotameters.

5. Computational modeling and boundary conditions

5.1. SEC

The water-steam/CO2 ejector condenser incorporating CO2 is also subject to numerical simulation using Ansys Fluent 2021 R1. Boundary conditions for mass flow rates are prescribed at the inlet for both steam and water streams. The ejector wall is set to adhere to no-slip adiabatic conditions, and the simulation of flow within the boundary layer grids employs a scalable wall function. To address interphase momentum transfer, utilizing the drag force model proposed by Schiller and Naumann [49] and the turbulent dispersion model introduced by Lopez de Bertodano [50] and the turbulent dispersion model introduced by Lopez

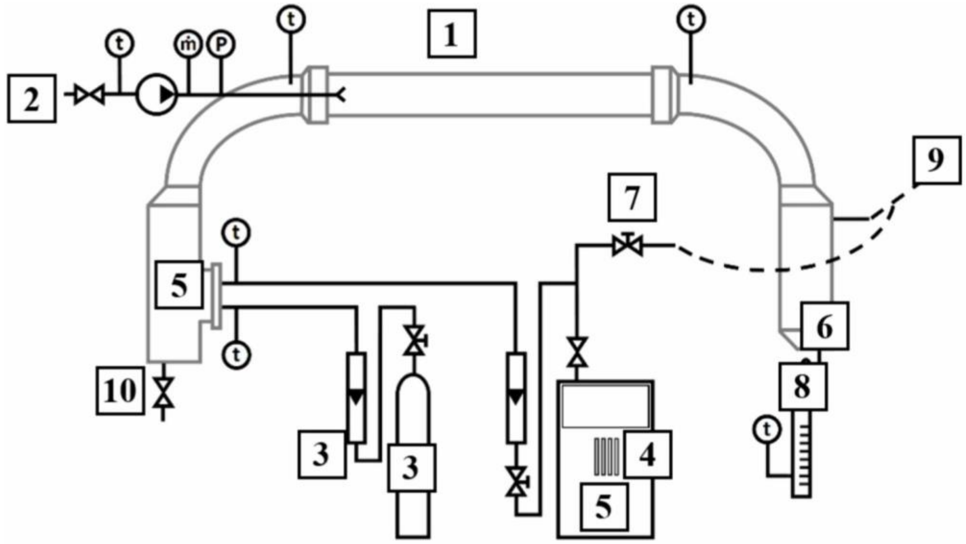

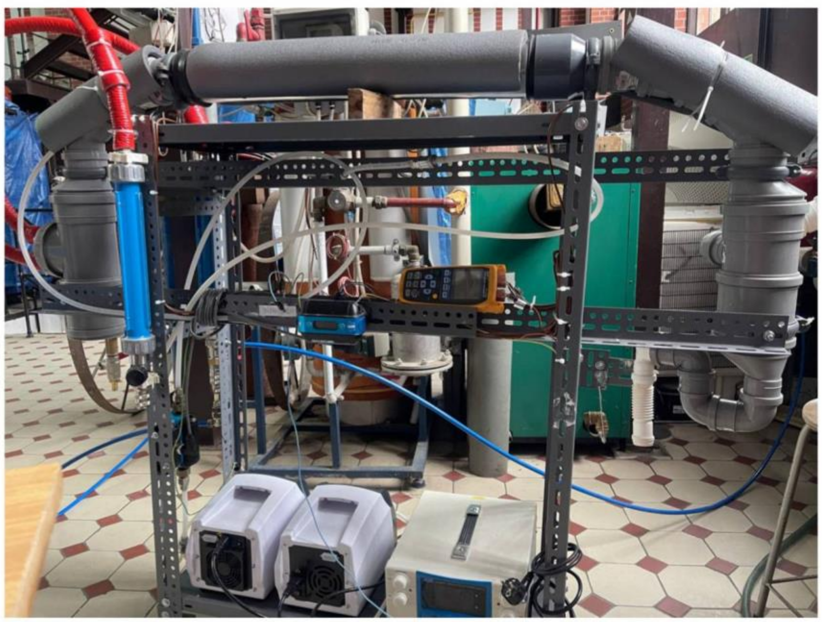

Fig. 4. Illustrative layout of the experimental setup: 1 – measurement segment, 2 – motive water supply, nozzle and pump, 3 – pressurized carbon dioxide, 4 – steam generator, 5 – blending chamber, 6 – separation unit, 7 – steam bypass, 8 – water discharge and condensation for titration, 9 – CO2 and steam release into the atmosphere.

de Bertodano The proposed approach in [44] to model forces in the flow proved to be suitable in modeling of hydrodynamics in bubbly two-phase flow [51]. Also, time step is 0.001 s.

5.2. T-junction separator

To precisely replicate the CO2-water flow within the T-junction, the mixture model within Fluent 2021 R1 utilized. This model was specifically selected to capture the significant interaction between the CO2 and water phases. The boundary conditions encompass both outflow and velocity inlet specifications. The outlet and branch pipe exit boundary conditions are outlined as follows:

$$\frac{du}{ds} = 0$$

$$\frac{dp}{ds} = constant \tag{29}$$

The variables u, s, and p represent the velocity along the flow direction, a direction parallel to u, and the static pressure, respectively. At the terminations of the exit and branch pipe, outflow boundary conditions are enforced, mandating a zero diffusion flux while incorporating a correction mechanism to ensure overall mass balance. This process guarantees that conditions at the outflow plane are meticulously extrapolated from the internal domain, effectively insulating them from any upstream influence. Consequently, adjustments to the outflow velocity and pressure are orchestrated to conform with the presumption of fully-developed flow. Furthermore, all solid boundary walls are presupposed to exhibit adiabatic and smooth characteristics, thereby upholding a no-slip boundary conditions. Additionally, the simulation integrates gravitational acceleration, precisely set at 9.81 $\frac{m}{s^2}$. The boundary conditions for both the SEC and T-junction separator are detailed in Table 1.

The coupling of pressure and velocity was accomplished utilizing the SIMPLE (Semi-Implicit Method for Pressure Linked Equations) algorithm [52,53], ensuring strong convergence in the modeling. To precisely capture high-velocity swirling flow, particularly in bent domains, the PRESTO (PREssure STaggering Option) scheme was employed,

Table 1
Parameters for SEC and T-junction separator

T-junction		SEC		
Boundary	Types	Boundary	unit	Values
Inlet	Velocity inlet	Steam inlet temperature	(K)	383
Outlets	Outflow	Water inlet pressure	(bar)	12–16
Wall	No Slip wall	Water inlet temperature	(K)	293–313
		Water mass flow rate	$(\frac{g}{s})$	29

enhancing the faithfulness of the results. Discretization of key variables including kinetic energy, volume fraction, and momentum equations executed utilizing the QUICK (Quadratic Upstream Interpolation for Convective Kinematics) technique. This method offers superior accuracy, especially in modeling rotational swirling flows, surpassing the limitations of traditional 1st and 2nd order schemes. It is essential to avoid dependence on first-order discretization techniques, as they can introduce Greater inaccuracies and yield unreliable outcomes [54]. As a convergence criterion, the residual was meticulously reduced to 10^{-5}, ensuring the stability of the simulation. Additionally, maintaining a stable mass flow rate at each outlet throughout the computation is crucial for obtaining trustworthy results. The summarized multiphase model and discretization are presented in Table 2.

6. Assessment of numerical model

6.1. Mesh Independence

SEC and T-junction separator geometry and mesh were meticulously crafted using Gambit 2.4.6, as illustrated in Fig. 5. To uphold precision in the computations, meshing was performed on all sides of the model, followed by meshing of surfaces and three-dimensional shapes. Tet/Hybrid elements, coupled with the TGrid format, were employed for volumetric meshing, guaranteeing the production of cells suitable for computational fluid dynamics (CFD) analyses. Ensuring a top-notch mesh quality is crucial to minimize errors stemming from numerical diffusion. Consequently, the independence of mesh solutions concerning the SEC and T-junction separator was validated through simulations using diverse grid setups.

In order to assess the independence of the mesh and its impact on the results of the SEC, an evaluations were carried out on condensation mass flow rate and temperature distribution across various nods (Fig. 6). The investigation unveiled notable differences between the outcomes derived from the 500,222 and 750,124 node setups compared to those at 1000036 and 1,250,328 node setups. Furthermore, results obtained from the 1,000,036 and 1,250,328 node setups demonstrated a substantial level of concurrence. Hence, considering computational efficiency and precision concerns, the configuration comprising 1,000,036 nodes identified as the best choice. This selection ensures enhanced computational efficiency while maintaining simulation accuracy.

The concept of grid independence refers to the consistency of calculation results despite variations in grid density, where the impact of truncation error becomes negligible in numerical simulations. It's crucial to emphasize that grid independence analysis should be conducted in areas pivotal to the simulation's objectives or where outcomes are significantly influenced. To ascertain the solution's robustness against mesh resolution, an analysis of mesh sensitivity was conducted for the T-junction separator. Four distinct meshes, as outlined in Table 3, underwent thorough investigation. Notably, there were no discernible alterations in the pressure drop and separation efficiency between Mesh 3 and Mesh 4. Consequently, Mesh 3 with 10^6 number of nodes was identified as the optimal computational mesh for further calculations. The boundary conditions used for the results obtained in this table are explained in the following section.

Table 2
Summarized multiphase model and discretization

Components	Solution Method
multiphase model	mixture model
pressure-velocity coupling	SIMPLE
pressure	PRESTO
kinetic energy	QUICK
volume fraction	QUICK
momentum	QUICK

6.2. Model validation

6.2.1. SEC

To ensure the precision and reliability of the model, a comprehensive comparison was conducted between simulation results incorporating CO2 and those without it, as depicted in Fig. 7. Initially, numerical results without CO2 juxtaposed against the experimental data collected in our laboratory. The experimental conditions encompassed $\dot{m}_{water} = 29\left(\frac{g}{s}\right), T_{water} = 18^{\circ}C, P_{water} = 14.7\ bar\ and\ T_{steam} = 100^{\circ}C$. The examination of the outlet temperature of the SEC under assorted steam mass flow rates, depicted in Fig. 7a, reveals a satisfactory alignment between the simulated and experimental findings.

Following this, a computational analysis was conducted to authenticate the robustness of the model when considering various volumetric flow rate of CO2. Illustrated in Fig. 7b is the experimental determination of the inlet temperature of the SEC across various volumetric flow rates of CO2, revealing a noteworthy consistency with the distribution derived from the simulated model. Furthermore, numerical and experimental investigations were conducted to analyze the condensation mass flow rates at different steam mass flow rates, with the water mass flow rate set at 29 $\left(\frac{g}{s}\right)$ and the CO2 volumetric flow rate at 2.6 $\left(\frac{m^3}{h}\right)$, as illustrated in Fig. 7c. Notably, a commendable alignment between the numerical outcomes and experimental observations is evident.

In addition, the breakup of droplets plays a crucial role in the condensation process and overall system performance. Droplet breakup in a SEC occurs due to several mechanisms, including aerodynamic forces, surface tension effects, and shear forces induced by the surrounding gas or vapor flow. As the droplets travel through the chamber, they are subjected to high-velocity gas flow, which can cause deformation and fragmentation of the droplets. Aerodynamic drag forces acting on the droplets can lead to elongation and distortion, eventually resulting in breakup into smaller droplets or ligaments. Surface tension effects also contribute to droplet breakup, particularly at small length scales where surface tension dominates over inertial forces. Variations in surface tension across the droplet surface can lead to instability and the formation of surface waves, ultimately causing breakup into smaller droplets. Additionally, shear forces induced by turbulent gas flow can exert stresses on the droplets, causing deformation and breakup. Our previous study [14] thoroughly analyzed the breakup behavior of droplets, employing detailed analytical techniques. In Fig. 8, a comparison is made between the numerical simulations and the analytical results [14] concerning the temperature at the outlet of the SEC. The comparison reveals a noteworthy concurrence between the numerical and analytical outcomes, indicating a strong agreement between the two methodologies.

6.2.2. T-junction

Validation of the T-junction separator involves two parts: the horizontal T-junction and the vertical impact T-junction separator. The simulation of the horizontal T-junction separator was conducted, and the outcomes were contrasted with the experimental research carried out by Saba et al. [38] for validation. The experimental investigation emphasized the importance of accurately determining two-phase flow patterns within complex, branching conduits for analysing loss-of-

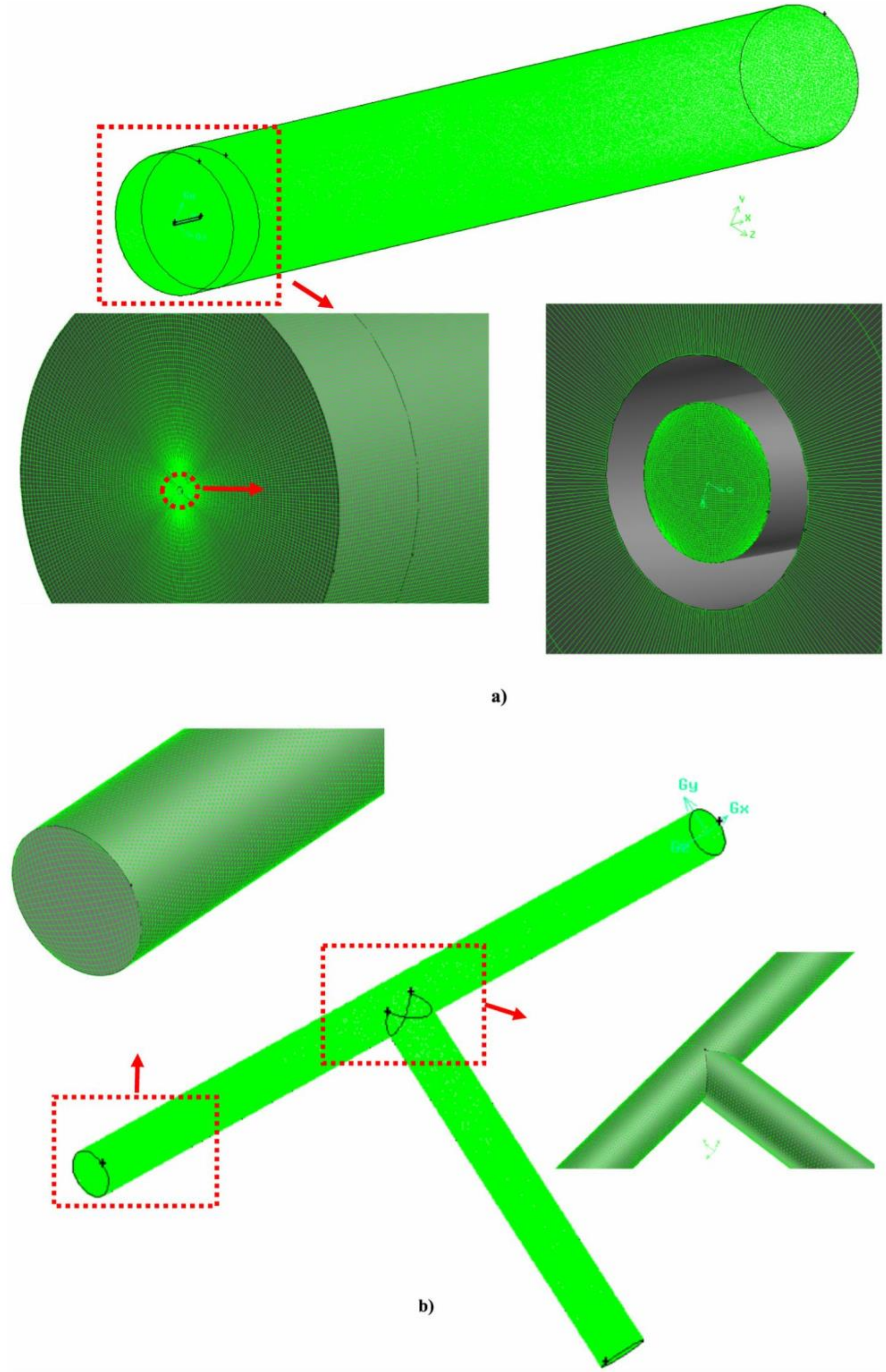

Fig. 5. Meshing of a) SEC and b) T-junction separator.

coolant accidents (LOCAs) in light water nuclear reactors (LWRs). To facilitate observation of phenomena, a tee test made of Plexiglas was specially designed. This section was horizontally installed within a sizable liquid/gas loop at Rensselaer Polytechnic Institute (RPI) [38].

The dataset included various liquid and gas inlet and outlet flow rates, inlet pressures and pressure drop. The pressure variance at the tee junction derived through extrapolation based on the measured pressure drop. In every instance, side 1 serves as the entrance, side 2 acts as the run, and side 3 pertains to the branch. Out of the 45 distinct experimental runs conducted, two were chosen to validate our numerical horizontal modeling against the experimental conditions. For this validation, run 1 and run 10 (Table 4) were selected. The flow regime in Run1 indicates a single-phase scenario, indicating that only the liquid phase (water) is simulated. Conversely, in Run10, both the liquid and gas phases have been considered.

Static pressure distribution along the inlet and run sections for Runs 1 and 10 is illustrated in Fig. 9, respectively. Based on the data available in Table 4, the pressure differential (ΔP_{2-1_j}) is 890 Pa for Run 1 and 3510 Pam for Run 10. There is a notable consistency between the numerical and experimental results for both single-phase flow (Run 1) and two-phase flow (Run 10).

The second part of the validation process for the T-junction involves

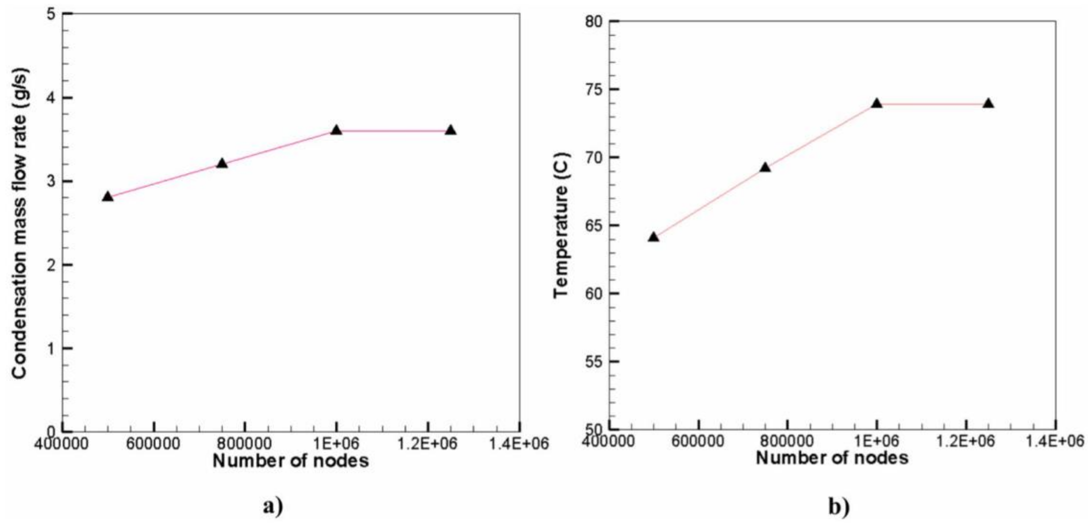

Fig. 6. Grid independence of SEC at $\dot{m}_{water} = 29\ \frac{g}{s}$ and $\dot{m}_{steam} = 3.6\ \frac{g}{s}$ for a) mass flow rate of condensation at $\dot{m}_{CO2} = 2.6\ \frac{m^3}{h}$, b) temperature of mixture at the outlet of SEC.

Table 3
Mesh independency

Grids	Mesh 1	Mesh 2	Mesh 3	Mesh 4
Nodes	500,000	750,000	1,000,000	1,250,000
$(\Delta p_{2-1})_j$	3180	3360	3510	3510
Separation efficiency	84.3	88.12	91.5	91.5

comparing our numerical vertical impact T-junction simulation with an experimental research conducted by Tuo and Hrnjak [20]. They performed an experimental study on the segregation of gas and liquid in vertical impacting T-junctions for a gas pressurization system. The study involved exploring various mass flow rates ranging from 10 to 35 $\left(\frac{g}{s}\right)$, aiming to replicate the operations seen in air-conditioning systems integrating with cooling capacities ranging from approximately 1.5 to 6 kW. Their experimental setup comprised a test section, specifically vertical impacting T-junctions, along with a storage container, an electric heater and mass flow meters for gas and liquid (MFl and MFv). Fig. 10 demonstrates the alignment between experimental data [20] and numerical simulations concerning separation efficiency at an inlet mass flow rate of 25 $\left(\frac{g}{s}\right)$ affirming a robust agreement between the two datasets. The discrepancy between experimental and numerical results for five various input quality (ranging from 0.11 to 0.3) is 01%, 0.8%, 1.2%, 1.4%, and 1.89%, respectively.

7. Results and discussion

7.1. Impact of steam inlet mass flow rate

The water plume is a pivotal component in comprehending the intricate dynamics of mass, momentum and heat transfer within a SEC. Its characteristics vary significantly based on the particular properties of inlet steam. Upon injection of subcooled water into the steam flow, a closed water cavity, known the water plume, forms at the outlet of the nozzle. It is imperative to acknowledge that the dynamics of the water column are significantly impacted by the mass flow rate of the incoming steam, especially as it nears sonic or supersonic speeds. Continuously replenished by the nozzle's water supply, the water column experiences condensation while engaging with the entrapped steam. Evaluating the water plume involves a thorough examination of contours representing the volume fraction of water. From these contours (Fig. 11), Diverse variables could be derived, with particular emphasis on the maximum penetration length.

By examining the outlines of water volume proportion and taking into account the maximum penetration distance, valuable observations can be acquired regarding the conduct and qualities of the water plume amid changing inlet mass flow rates. By examining the volume fraction of water, insights into how effectively water vapor is mixed with the injected subcooled water and how efficiently condensation occurs can be gained. Variations in the volume fraction of water across different mass flow rates of steam can indicate areas of optimal mixing and condensation efficiency within the SEC. Also, the volume fraction of water contours provides valuable information about the distribution and extent of condensation within the SEC. Analysing these contours at varoius steam flow rates leads to assess the dynamics of phase change processes under varying operating conditions. This understanding is crucial for optimizing SEC performance and enhancing its fully condensation capabilities. Fully condensed water refers to the state where all water vapor within the SEC has undergone condensation, resulting in the complete conversion of vapor into liquid water. Achieving fully condensed water is a desirable outcome in SEC operation as it maximizes heat transfer efficiency and ensures optimal performance for carbon capture. As depicted in Fig. 11, it is evident that the configuration of the water plume is directly correlated with the inlet mass flow rate of the steam. When the steam mass flow rate at the inlet is 2.21 $\left(\frac{g}{m^2.s}\right)$, the penetration shape adopts an ellipsoidal form. Nevertheless, fully condensation is observed across all three scenarios.

7.2. Impact of CO_2 and steam on inlet and outlet temperatures of SEC

The inlet temperature of SEC provides insights into the system's initial thermal state. Understanding the temperature of steam and CO2 streams leads to assess the energy input into the condensation process. Deviations from the expected inlet temperature can indicate variations in operating conditions or potential issues in the upstream processes. Also, the outlet temperature of the SEC is a crucial indicator of the effectiveness of the condensation process within the system. It reflects the thermal state of the effluent leaving the condenser after the condensation of water vapor into liquid form. At a given inlet temperature, a lower outlet temperature indicates that the condensation process has efficiently removed thermal energy from the system, causes to a cooler effluent. Efficient heat transfer, as indicated by a lower outlet temperature at a given inlet temperature, is vital for several reasons. Firstly, it ensures that the SEC effectively meets its primary objective of removing heat from the incoming steam and CO2 streams, facilitating

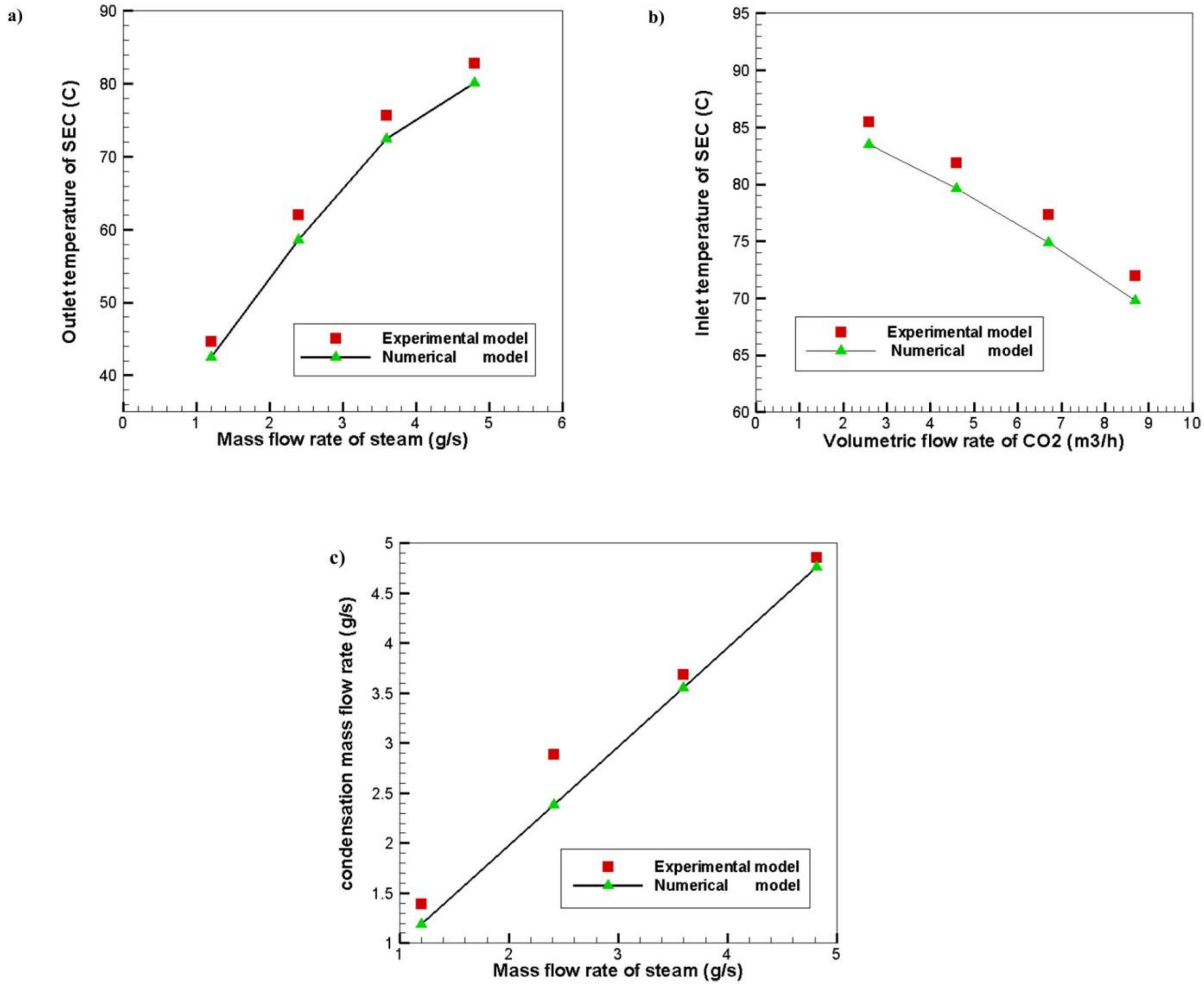

Fig. 7. Validation of SEC at $\dot{m}_{water} = 29 \left(\frac{g}{s}\right), T_{water} = 18^{\circ} C, P_{water} = 14.7\ bar, T_{steam} = 100^{\circ} C$ a) outlet temperature of SEC without non-condensable gas (CO_2) and b) inlet temperature of SEC with condensable gas (CO_2) at $\dot{m}_{steam} = 2.4 \left(\frac{g}{s}\right)$, c) condensation mass flow rate at volumetric flow rate of $CO_2 = 2.6 \left(\frac{m^3}{h}\right)$.

their transition from vapor to liquid phase. This is particularly important in applications where maintaining specific temperature conditions is critical for downstream processes or equipment. Furthermore, efficient condensation and heat transfer contribute to the overall energy efficiency of the system. By effectively removing thermal energy from the incoming streams, the SEC helps minimize energy losses and maximizes the utilization of available resources. This is especially relevant in energy-intensive industries where optimizing energy usage is paramount for reducing operational costs and environmental impact. Monitoring outlet temperature variations over time or under different operating conditions provides valuable insights for engineers. It allows them to assess the performance of the SEC and identify any deviations from expected behavior. For example, at a specified inlet temperature, an increase in outlet temperature beyond expected levels may indicate inefficiencies in the condensation process, such as inadequate cooling or reduced heat transfer efficiency. By closely monitoring outlet temperature variations, engineers can identify potential issues early on and take corrective actions to optimize operating parameters. This may involve adjusting parameters such as steam and CO2 flow rates, temperature settings, or the design of heat exchange surfaces to improve condensation efficiency and overall SEC performance. Figs. 12 and 13 illustrate the distribution of inlet and outlet temperatures of SEC across varying mass flow rates of steam and CO2, under constant conditions of $T_{water} = 20^{\circ} C$, $P_{water} = 12\ bar\ and\ \dot{m}_{water} = 29 \left(\frac{g}{s}\right)$. The investigation covered a range of steam mass flow rates, including 2.2, 3.4, and 4.6 $\left(\frac{g}{s}\right)$, alongside varying volumetric flow rates of CO2 (0, 2, 4, 6, 8, and 10 $\frac{m^3}{h}$). The results indicate a clear correlation between steam mass flow rates and the inlet and outlet temperatures of the SEC. Decreasing steam mass flow rates lead to a decrease in both inlet and outlet temperatures, resulting in a lower mixture temperature overall. This situation can be explained to the reduced condensation of steam due to lower mass flow rates, thereby limiting the amount of thermal energy transferred to the system. On the other hand, the investigation revealed that decreasing the volumetric flow rate of CO2 corresponded to an increase in both inlet and outlet temperatures of SEC. For instance, the minimum inlet temperature of 70 °C was observed when the steam mass flow rate was 2.2 $\left(\frac{g}{s}\right)$ and the volumetric flow rate of CO2 was 10 $\left(\frac{m^3}{h}\right)$, whereas the absence of CO2 resulted in the maximum inlet temperature of 102 °C. This trend can be attributed to the thermal properties of CO2, which acts as a cooling agent when present in the mixture. Further analysis revealed that the minimum outlet temperature of 55 °C occurred when the steam mass flow rate was at its minimum (2.2 $\frac{g}{s}$) and the volumetric flow rate of CO2 was at its maximum (10 $\frac{m^3}{h}$). Conversely, the maximum

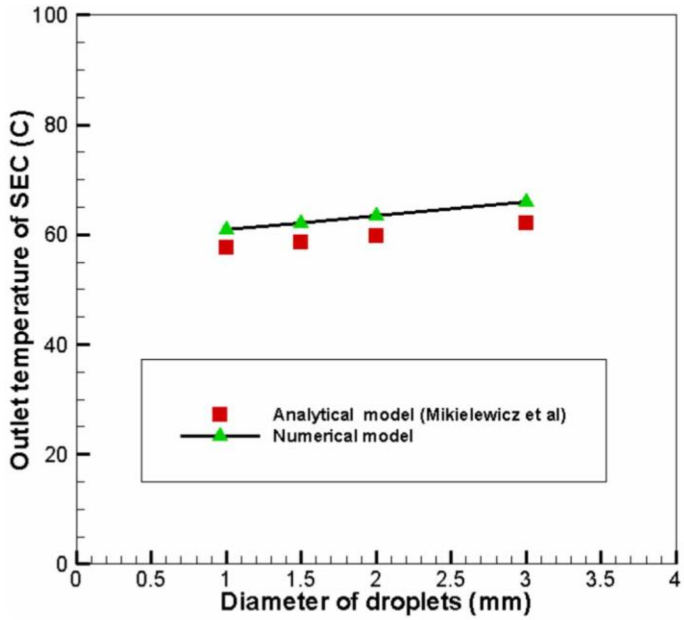

Fig. 8. Comparison of numerical and analytical model of temperature at the outlet of SEC for different diameter of droplet

Table 4
Data regarding phase separation in a horizontal T-junction separator [38].

Run	$G_1 \times 10^6$ $\left(\frac{kg}{hr.m^2}\right)$	$x_1(\%)$	$x_2(\%)$	$x_3(\%)$	$\frac{w_2}{w_1}$	$p_1(kPa)$	$(\Delta p_{2-1})_j$ (kPa)
1	4.88	0	0	0	0.3	41.37	0.89
10	4.88	0.5	0.0130	0.695	0.3	48.26	3.51

outlet temperature of 87 °C was observed in the absence of CO2 and with the maximum steam mass flow rate of 4.6 $\left(\frac{g}{s}\right)$. In this scenario, the absence of CO2 eliminates the cooling effect, while the high steam mass flow rate increases the thermal energy input into the system, resulting in higher outlet temperatures. But, the temperature difference (ΔT) between the inlet and outlet of the SEC is a critical parameter in assessing heat transfer efficiency within the system. A larger ΔT typically indicates a more effective heat transfer process, as it implies that a greater amount of thermal energy is being removed from the steam and CO2 streams, leading to a cooler effluent. In the context of the SEC, achieving a significant ΔT is desirable as it reflects the system's ability to efficiently condense steam and remove thermal energy, ultimately contributing to enhanced performance and energy efficiency. Fig. 14 depicts the distribution of temperature difference (ΔT) of the SEC at various mass flow rate of steam and CO_2 for $T_{water} = 20^{\circ}C$, $P_{water} = 12\ bar$ and $\dot{m}_{water} = 29\left(\frac{g}{s}\right)$. It can be seen vividly that the maximum ΔT can be obtained at $\dot{m}_{steam} = 2.2\left(\frac{g}{s}\right)$ and in the absence of CO2. For instance, examining the specific data for $\dot{m}_{steam} = 2.2\left(\frac{g}{s}\right)$, it is observed that with CO2 volumetric flow rate of 0, 2,4, 6, 8 and 10 $\frac{m^3}{h}$, the ΔT values are 29.1, 22.7, 21.3, 19.9, 16.8 and 12.9, respectively. As Fig. 14 shows, the presence of CO2 induces a reduction in ΔT, primarily due to increased diffusion hindrance and reduced convective heat transfer between the subcooled water and steam phases.

Fig. 15 displays the volume fraction contour of steam at 4.6 $\left(\frac{g}{s}\right)$ and temperature contours for the SEC under varying steam mass flow rates, while keeping the CO2 mass flow rate constant at 2 $\left(\frac{m^3}{h}\right)$, with an inlet water temperature of $18^{\circ}C$ and a water pressure of 18 *bar*, along with a water mass flow rate of 29 $\left(\frac{g}{s}\right)$ as well as consistent chamber inlet temperature of 113 °C. Fig. 15a demonstrates complete condensation of

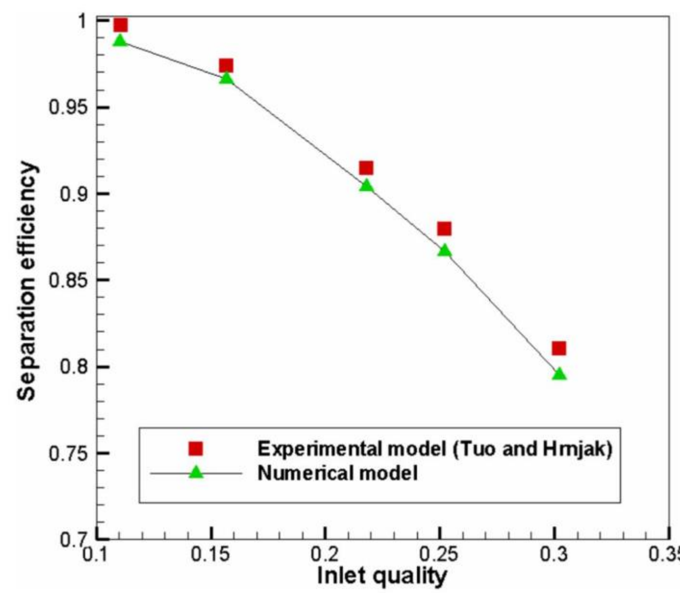

Fig. 10. Comparison of separation efficiency between experimental [20] and numerical results at an inlet mass flow rate of 25 $\left(\frac{g}{s}\right)$.

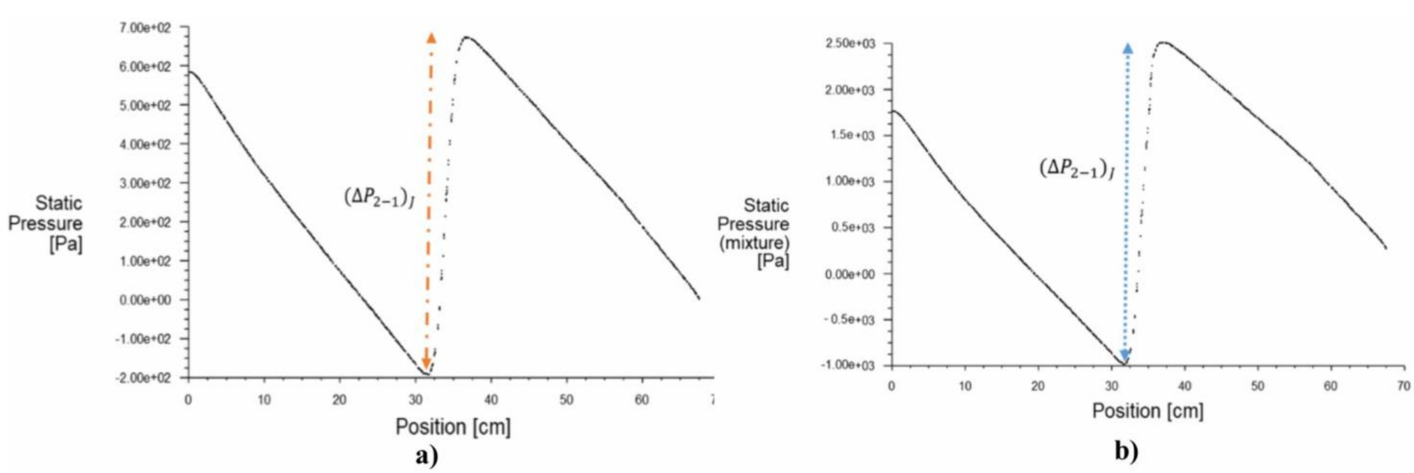

Fig. 9. Distribution of static pressure of a) Run1 and b) Run10 in numerical simulation.

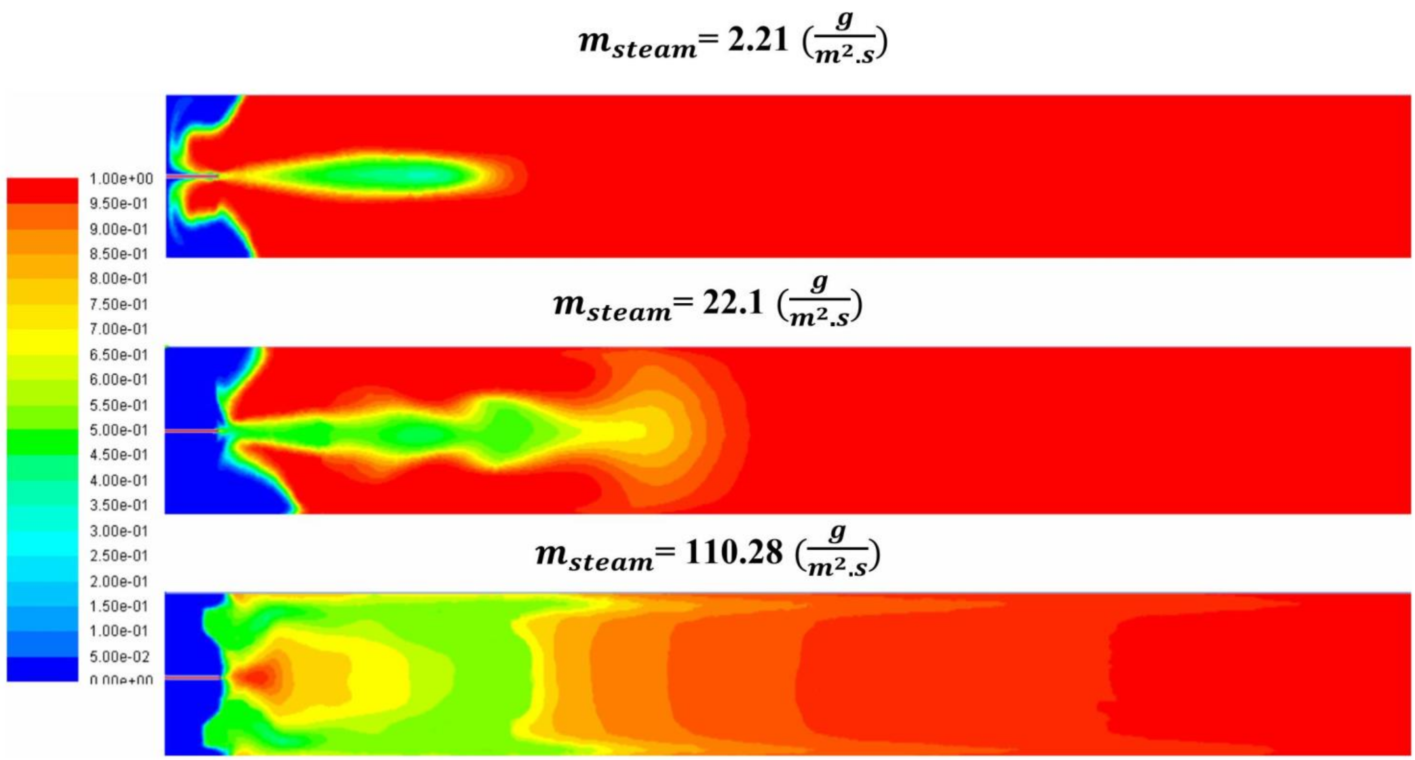

Fig. 11. Water volume fractions at varying inlet flow rates of steam.

steam into water, while CO2 is treated as a non-condensable gas, with the assumption that the inlet mass flow rate of CO2 equals the outlet mass flow rate of CO2. Fig. 15b serves to elucidate how alterations in steam mass flow rates impact the overall cooling performance of the SEC and its steam condensation efficiency. The findings indicate that with a consistent chamber inlet temperature of 113 °C, the outlet temperatures vary, with values of 55.92 °C, 60.69 °C, and 65.40°C corresponding to steam mass flow rates of 2.2, 3.4, and 4.6 $\left(\frac{g}{s}\right)$, respectively. This observation suggests that an increase in steam mass flow rate correlates with a reduction in ΔT, highlighting the influence of steam flow dynamics on thermal behavior.

7.3. Effect of water temperature on outlet temperature of SEC

Water temperature plays a critical role in regulating the temperature discrepancy between the incoming steam and CO2 streams and the coolant water within the SEC. A lower coolant water temperature facilitates more efficient heat transfer from the steam and CO2 streams to the coolant water, resulting in a lower outlet temperature (at constant inlet temperature and specific CO2 flow rate). Conversely, higher coolant water temperatures may reduce the temperature difference and hinder heat transfer efficiency, leading to higher outlet temperatures. In addition, the outlet temperature of the SEC is closely tied to the extent of condensation occurring within the system. As mentioned earlier, lower outlet temperatures at constant inlet temperature and specific CO2 flow rate indicate more effective removal of thermal energy from the steam and CO2 streams, resulting in higher rates of condensation and greater liquid formation. By investigating how water temperature influences outlet temperature, coolant water conditions to maximize condensation efficiency and enhance overall SEC performance can be optimized. Moreover, monitoring outlet temperature variations helps prevent thermal overload within the SEC. Excessive outlet temperatures can indicate inadequate heat transfer or cooling capacity, potentially leading to system overheating and operational issues. The relationship between water temperature and outlet temperature (at constant inlet temperature and specific CO2 flow rate) can be understood, and measures can be implemented to maintain optimal operating conditions and prevent thermal overload, ensuring the reliability and safety of the SEC. Also, optimizing water temperature can contribute to improved energy efficiency of the SEC. Lower outlet temperatures (at constant inlet temperature and specific CO2 flow rate) result in reduced energy consumption for cooling purposes, as less energy is required to maintain the desired outlet temperature. By fine-tuning water temperature settings based on the investigation results, energy consumption can be minimized while condensation efficiency is maximized, ultimately enhancing the overall energy efficiency of the SEC. Figs. 16 and 17 depict the distribution of outlet temperature of the SEC across various water temperature and mass flow rates of CO2, maintaining a constant water pressure ($P_{water} = 12\ bar$) and mass flow rate ($\dot{m}_{water} = 29\ \frac{g}{s}$) while varying the mass flow rates of steam ($\dot{m}_{steam} = 2.2\ and\ 3.4\ \frac{g}{s}$). Inlet temperature for 0, 2, 4, 6, 8 and 10 $\frac{m^3}{h}$ of CO2 volumetric flow rate is 102, 92, 85, 80, 75 and 70 °C, respectively. The findings reveal a direct correlation between the temperature of water and the outlet temperature of SEC. As the water temperature decreases, there is a corresponding decrease in outlet temperature of the SEC. For instance, when the mass flow rate of steam is 2.2 $\left(\frac{g}{s}\right)$ and without presence of CO2, the outlet temperature of the SEC decreases from 80.2 °C to 72.8 °C as the water temperature decreases from 40°C to 20°C. Similarly, when a volumetric flow rate of 10 $\left(\frac{m^3}{h}\right)$ of CO2 is introduced, the outlet temperature decreases further, ranging from 60.9 °C to 57.3 °C across the same temperature range. In the case of a mass flow rate of steam of 3.4 $\left(\frac{g}{s}\right)$ and in the absence of CO2, the outlet temperature of the SEC varies from 91.6 °C to 80.8 °C as the water temperature decreases from 40 °C to 20°C. Introducing a volumetric flow rate of 10 $\left(\frac{m^3}{h}\right)$ of CO2 leads to additional reductions in outlet temperature, ranging from 70.3 °C to 60 °C over the same temperature range. These results underscore the significance of water temperature in influencing the outlet temperature of the SEC at constant inlet temperature and specific CO2 flow rate.

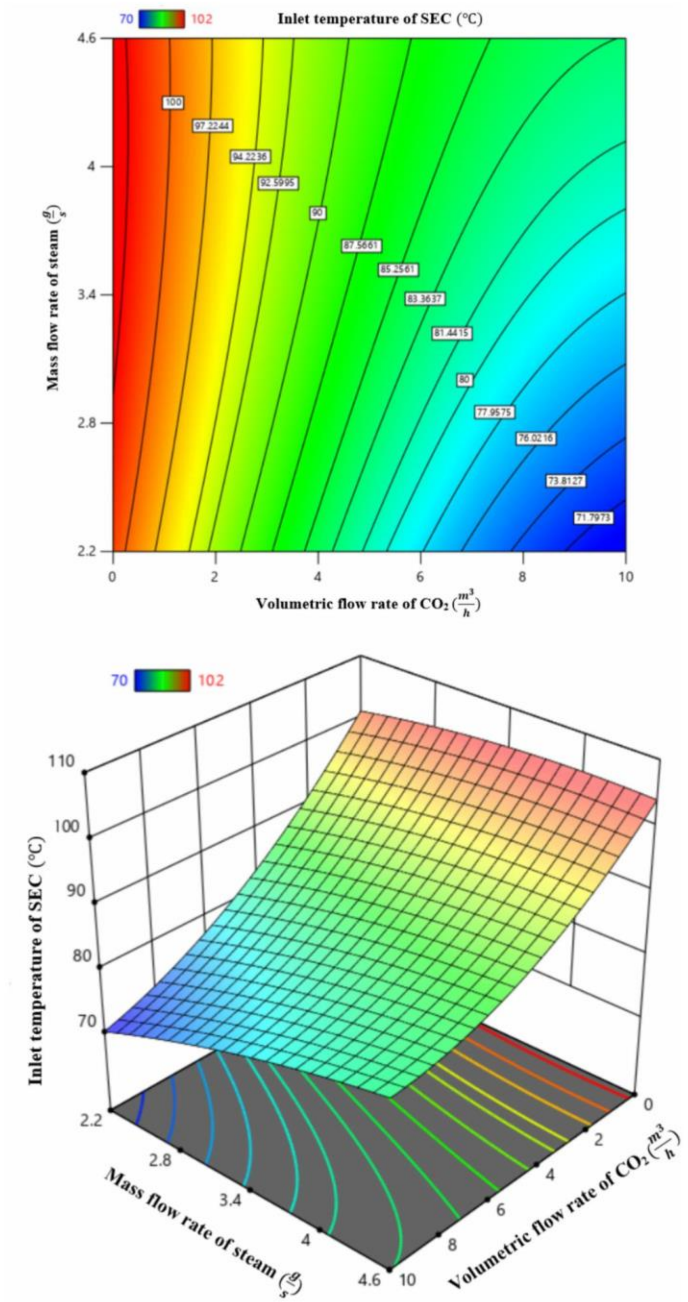

Fig. 12. Inlet temperature of SEC at different mass flow rate of steam and CO_2 for $T_{water} = 20^{\circ} C$, $P_{water} = 12\ bar$ and $\dot{m}_{water} = 29\ \left(\frac{g}{s}\right)$.

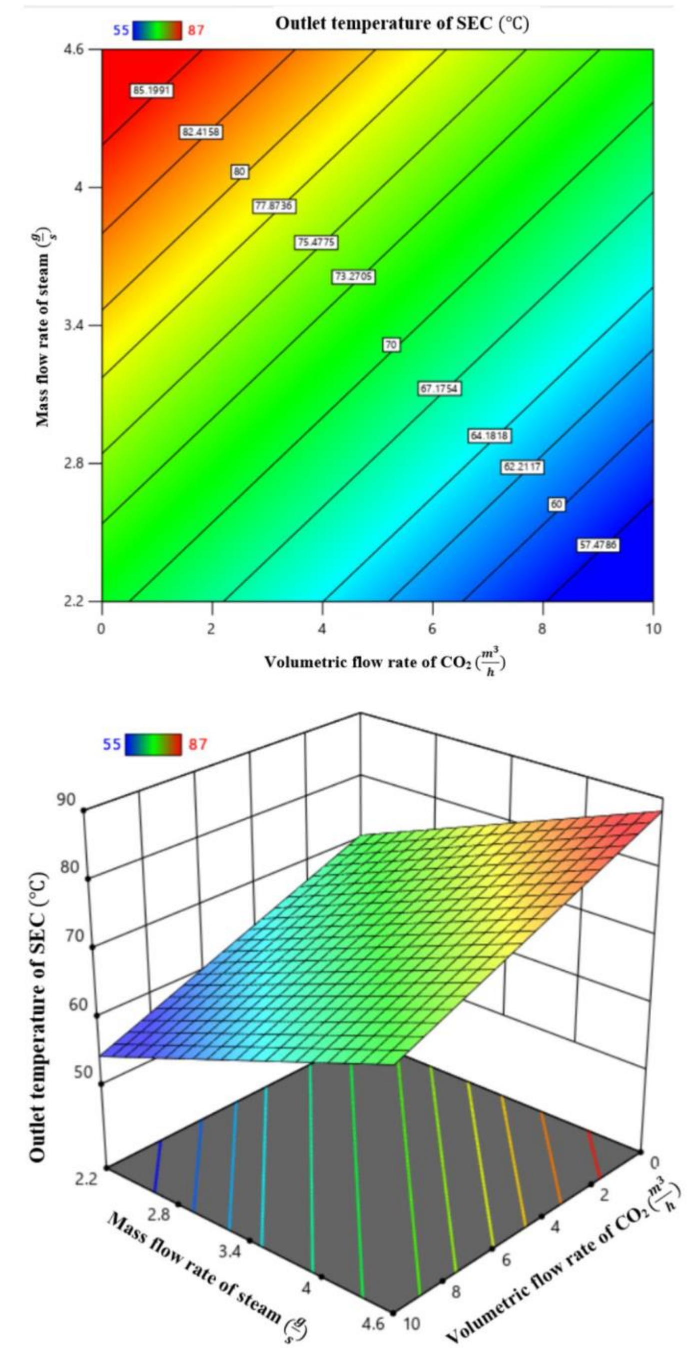

Fig. 13. Distribution of outlet temperature for SEC at various mass flow rate of steam and CO_2 for $T_{water} = 20^{\circ} C$, $P_{water} = 12\ bar$ and $\dot{m}_{water} = 29\ \left(\frac{g}{s}\right)$.

7.4. Effect of water pressure on outlet temperature of SEC

Water pressure directly affects the boiling point of water, which influences the heat transfer characteristics of the SEC. Higher water pressures result in higher boiling points, facilitating more efficient heat transfer from the steam and CO2 streams to the coolant water. By investigating how changes in water pressure affect temperature difference, water pressure settings can be optimized to maximize heat transfer efficiency and enhance overall SEC performance. Also, investigating water pressure's effect on ΔT contributes to overall system reliability. By identifying optimal pressure conditions, the risk of temperature-related equipment failures or performance degradation can be minimized, ensuring consistent and reliable operation of the SEC over time. Fig. 18 depicts the distribution of temperatures difference between inlet and outlet of SEC across various water pressures (P_{water}) and mass flow rates of CO2, under constant conditions of water temperature ($T_{water} = 20^{\circ} C$), water mass flow rate ($\dot{m}_{water} = 29\ \frac{g}{s}$), and steam mass flow rate ($\dot{m}_{steam} = 2.2\ \frac{g}{s}$). The data reveals a distinct pattern in the impact of pressure on temperature difference (ΔT). Increasing pressure from 12 bar to 14 bar and 16 bar generally results in an upward trend in ΔT across corresponding CO2 flow rates. At 12 bar, as CO2 flow rate rises from 0 to 10 m3/h, ΔT gradually declines from 30.5 to 14.5, suggesting lower pressures correlate with reduced ΔT and potentially decreased heat transfer efficiency. Also, at 14 bar and 16 bar, with ΔT decreasing from 35.6 to 17.85 at 14 bar and further from 41 to 19.6 at 16 bar across the same CO2 flow rate range. This indicates that higher pressures promote a larger temperature difference between inlet and outlet, thereby enhancing heat transfer efficiency.

Overall, both coolant water and a mixture of steam and CO2 are introduced into the SEC. The findings indicate that complete

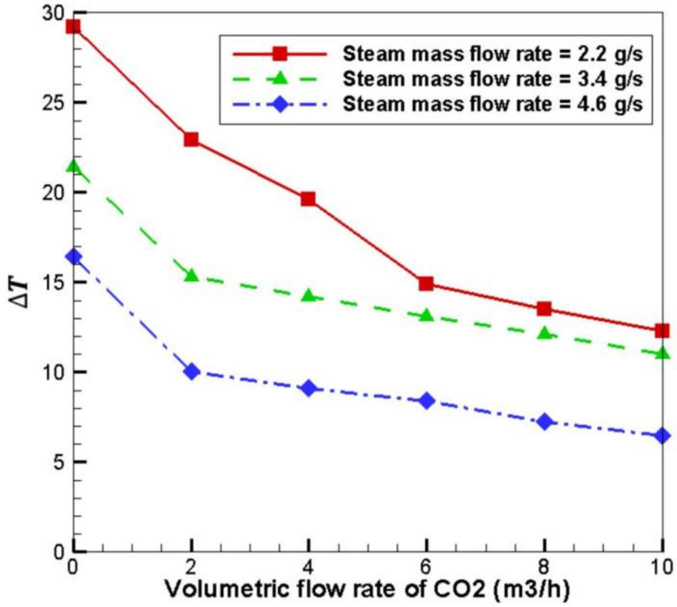

Fig. 14. Distribution of temperature difference for SEC at various mass flow rate of steam and CO_2 for $T_{water} = 20^{\circ} C$, $P_{water} = 12\ bar\ and\ \dot{m}_{water} = 29\left(\frac{g}{s}\right)$.

condensation occurs under the specified boundary conditions, resulting in the complete condensation of steam. Consequently, at the SEC outlet, the components present are CO2 and water. Hence, a separator is essential to separate the CO2 from the water, aligning with the objective of this study, which aims to capture CO2. The subsequent section will

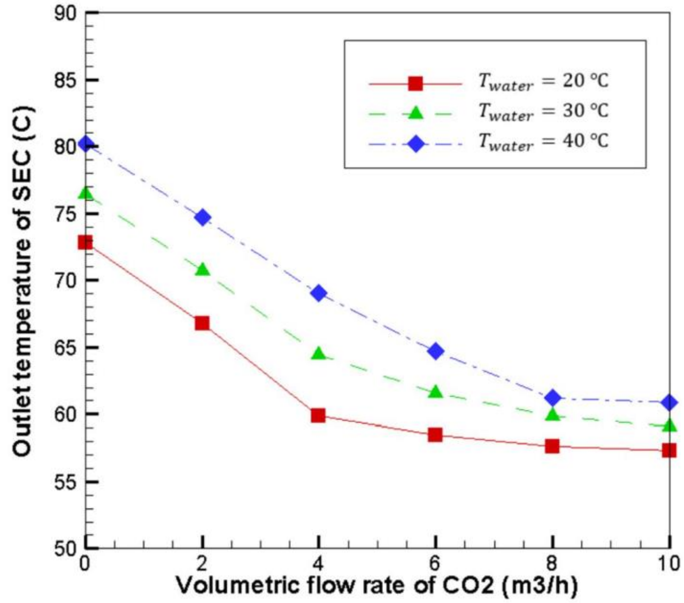

Fig. 16. Outlet temperature of SEC at different T_{water} and mass flow rate of CO_2 for $P_{water} = 12\ bar, \dot{m}_{water} = 29\left(\frac{g}{s}\right)$ and $\dot{m}_{steam} = 2.2\left(\frac{g}{s}\right)$.

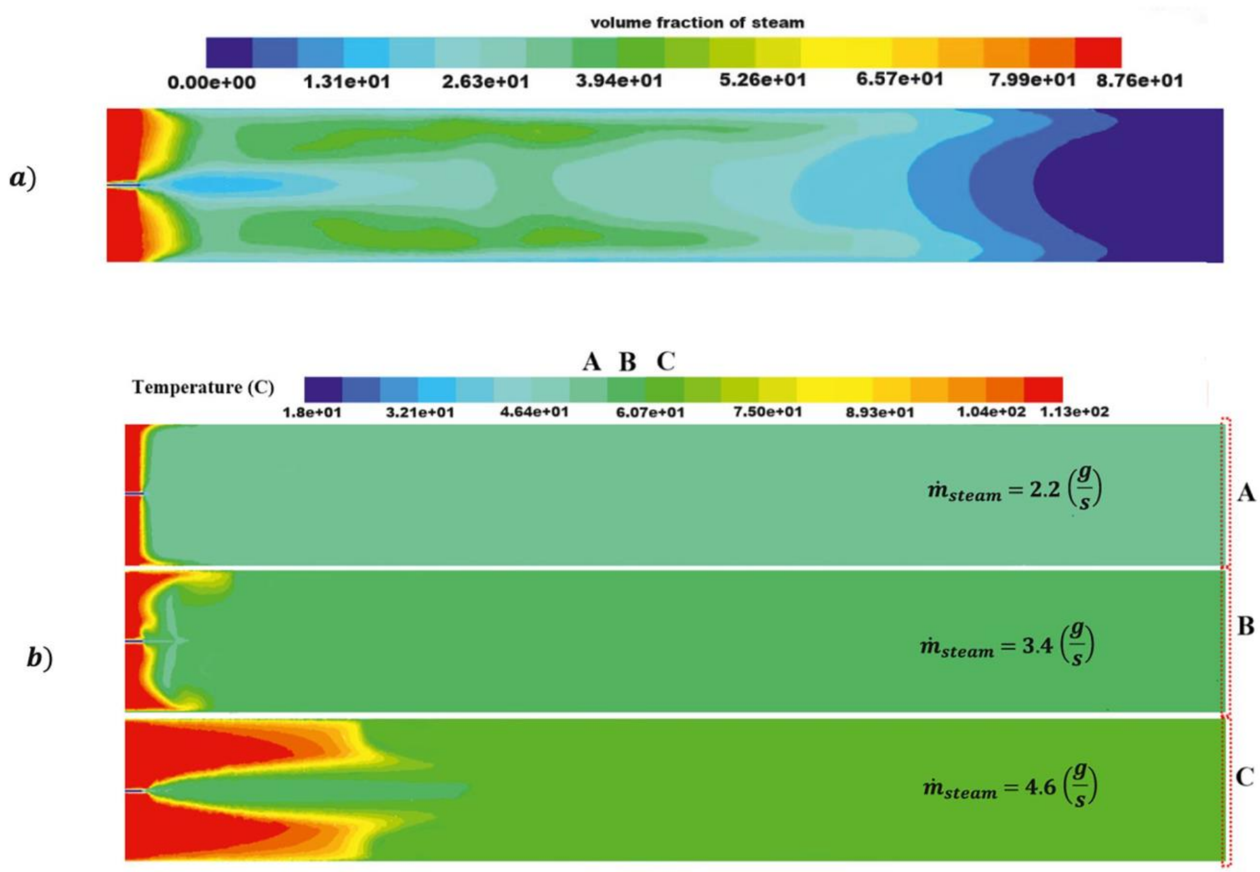

Fig. 15. Contour of a) volume fraction of 4.6 $\left(\frac{g}{s}\right)$ of steam and b) temperature for SEC at various mass flow rate of steam for $\dot{m}_{CO2} = 2\left(\frac{m^3}{h}\right)$, $T_{water} = 18^{\circ} C$, $P_{water} = 18\ bar\ and\ \dot{m}_{water} = 29\left(\frac{g}{s}\right)$.

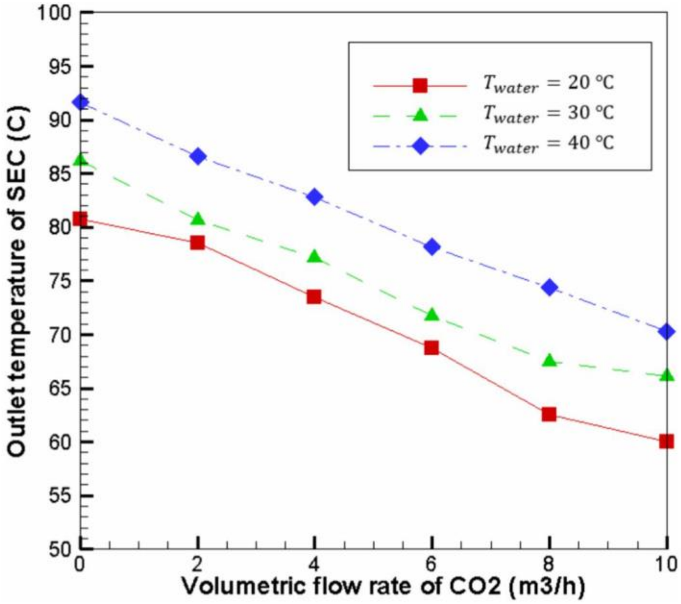

Fig. 17. Outlet temperature of SEC at various T_{water} and flow rates of CO_2 for $P_{water} = 12\ bar, \dot{m}_{water} = 29\ \left(\frac{g}{s}\right)$ and $\dot{m}_{steam} = 3.4\ \left(\frac{g}{s}\right)$.

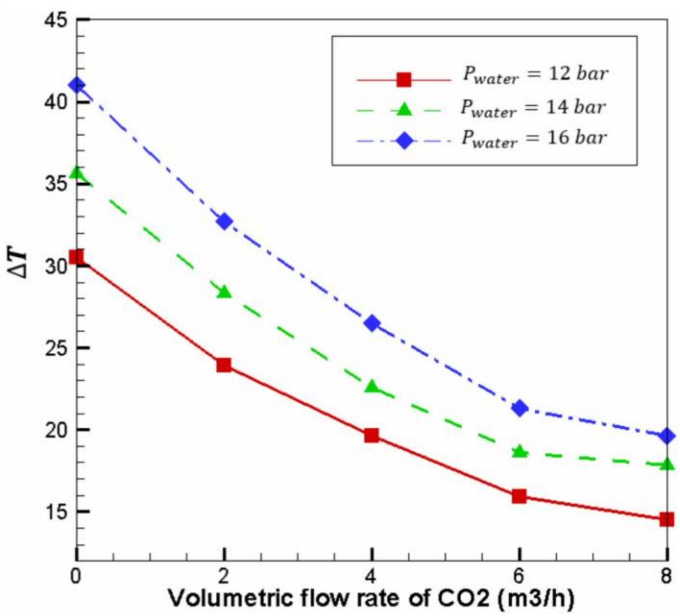

Fig. 18. Distribution of temperature difference of SEC at different P_{water} and volumetric flow rate of CO_2 for $T_{water} = 20^{\circ}C, \dot{m}_{water} = 29\ \left(\frac{g}{s}\right)$ and $\dot{m}_{steam} = 2.2\ \left(\frac{g}{s}\right)$.

delve into the detailed utilization of a T-junction separator for this purpose.

7.5. T-junction

7.5.1. Classification of T-junctions

T-junctions, with their versatile capabilities, offering the flexibility to either combine or divide fluid streams as needed. As a combining T, they efficiently merge two inlet streams into a single outlet, streamlining flow paths and simplifying system configurations. Conversely, as a dividing T, they facilitate the separation of a single inlet stream into two distinct outlets, enabling precise control over fluid distribution. However, in applications where a gas-liquid mixture encounters a dividing T-junction, challenges arise due to inevitable maldistribution. This phenomenon leads to variations in the qualities of the outlet streams, potentially resulting in undesirable scenarios such as uneven liquid or gas distribution across outlets. Remarkably, in certain cases, intentional maldistribution proves advantageous, particularly when the tee functions as a separator, allowing for selective extraction of specific components. Comprehend the alignment of inflowing streams concerning the outgoing flows is important for the classification of T-junctions. Two primary types emerge: the run type and the impact type (Fig. 19). In the run type, the inlet branch aligns with one of the outlet branches, promoting a smooth flow transition. Conversely, impact type is characterized by outlet branches diverging in opposite directions, while the inlet flow directly strikes the junction of the outlet branches, resulting in unique flow behaviors. Fig. 20elucidates the pathlines and vectors associated with both types of T-junction separators. In Fig. 20, it is crucial to delve deeper into the underlying principles driving the separation phenomenon and elucidate the key parameters influencing this process. The separation mechanism within the T-junction separator is multifaceted and warrants a comprehensive analysis to better understand its intricacies. Specifically, exploring the factors contributing to the selective extraction of CO2 from the water stream is paramount in discerning the efficiency and effectiveness of the separation process. One critical aspect to consider is the flow dynamics within the T-junction separator, including factors such as flow velocity, pressure gradients, and fluid properties [55]. These parameters play a pivotal role in determining the distribution of CO2 and water across the outlet branches, influencing the overall separation efficiency. Additionally, the design characteristics of the T-junction separator, such as the geometry of the junction and the orientation of the inlet and outlet branches, can significantly impact the separation performance [56]. Furthermore, it is essential to assess the influence of operational conditions, such as inlet flow rates, on the separation process [57]. Variations in these parameters can alter the phase behavior of the fluid mixture and affect the degree of CO2 extraction from the water stream. By analysing the interplay between these factors, optimizing the design and operation of T-junction separators for enhanced CO2 capture efficiency can be gained. Moreover, practical considerations related to the implementation of T-junction separators in real-world applications can be discussed [24]. Factors such as scalability, reliability, and maintenance requirements can be addressed to assess the feasibility of integrating these separators into larger-scale carbon capture systems [58]. Additionally, considerations regarding energy consumption and cost-effectiveness can be evaluated to ensure the economic viability of utilizing T-junction separators for CO2 separation [24].

As described in preceding sections, a mixture comprising steam, CO2, and water is introduced into the SEC. With the complete condensation of steam, the resultant output in SEC comprises water and CO2. Subsequently, a T-junction separator is utilized to capture the CO2 from the water. The purified CO2 is directed to the compressor, while the water is routed to the pump and the wet combustion chamber [59] to decrease the temperature of the products of oxy-fuel combustion (Fig. 1).

7.5.2. Separation efficiency

T-junction separators offer several advantages, including their compact size, cost-effectiveness and simple geometry in comparison to conventional separators. However, existing literature predominantly focuses on single via type T-junctions or combinations of multiple ones. [47,60,61]. Mohamed et al. [60] executed a study investigating to explore how the efficiency of complete separation in an impact T-junction is affected by the superficial velocities of the inlet gas and liquid, varying the outlet inclination angle from 0 to 90°. Notably, their findings underscored that a 90-degree angle, where two outlet tubes are positioned vertically, yielded optimal separation performance across various inlet conditions.

The separation efficiency, concerning both liquid (water) and non-

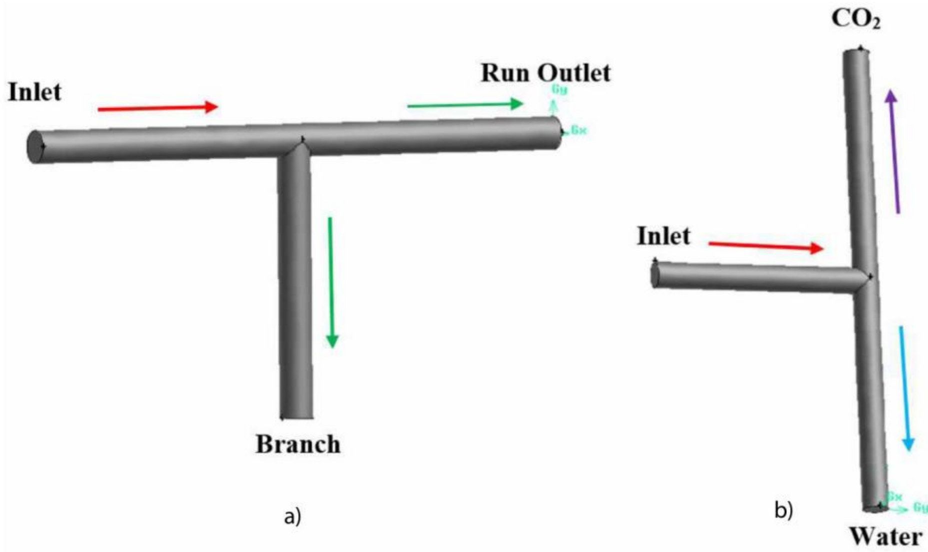

Fig. 19. Categorization of T-junctions, a) run type, b) impact type.

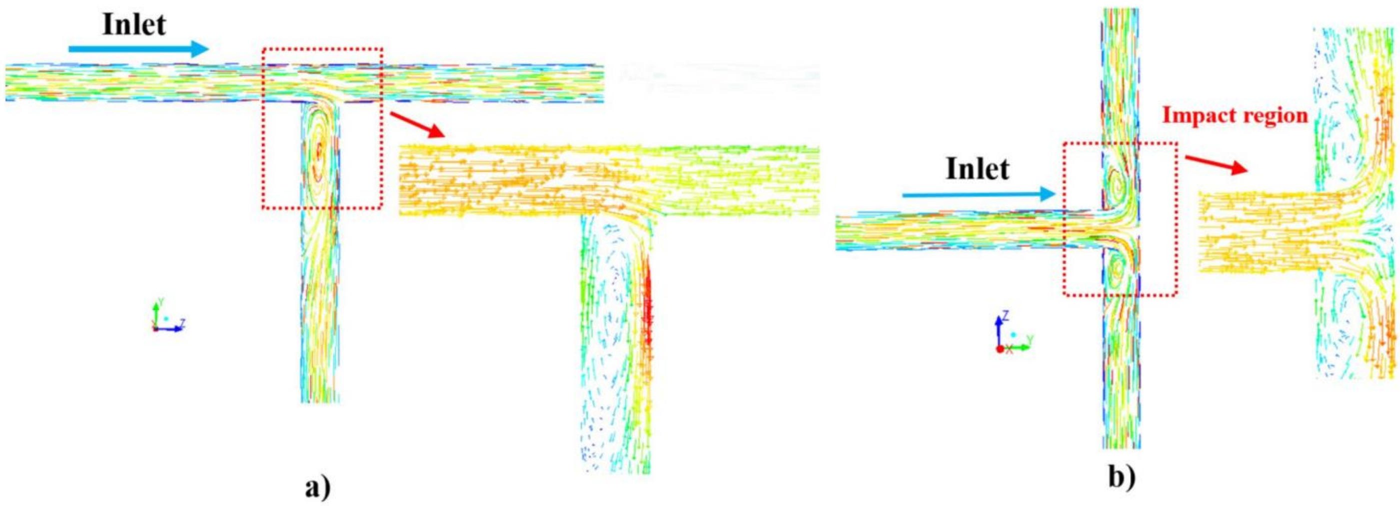

Fig. 20. Pathline and vector of mixture of water and CO2 for a) run type, b) impact type T-junction separator.

condensable gas (CO2), was quantified as follows [5]:

$$\eta = \left(\frac{\dot{m}_{liquid\ at\ inlet} - \dot{m}_{liquid\ at\ gas\ outlet}}{\dot{m}_{liquid\ at\ inlet}} \right) \times 100 \tag{30}$$

As previously noted in this study, a lower outlet temperature signifies efficient removal of thermal energy during the condensation process, resulting in a cooler effluent. The lowest outlet temperature is achieved with a volumetric flow rate of 10 $\left(\frac{m^3}{h}\right)$ of CO2 and 2.2 $\left(\frac{g}{s}\right)$ of steam. Considering fully condensation of steam, the mass flow rate of water would be 31.2 $\left(\frac{g}{s}\right)$. Fig. 21 illustrates the separation efficiency at diverse inlet mass flow rates. As the inlet mass flow rate augments, the separation efficiency reduces. This decline is attributed to the higher velocities of liquid and gas flow at the T-junction. The elevated velocity results in gas phase drag force and stronger liquid inertial force, both of which contribute to the entrainment of liquid towards the top outlet, opposing the downward gravity. When the incoming liquid jet collides with the vertical pipe, it splits into downward and upward directions, with the distribution between the two primarily determined by gravity forces and relative magnitudes of inertial.

To put it in a nutshell, direct contact condensation (DCC) in the SEC and T-junction separation are two distinct methods employed in thermal systems for phase separation and component extraction. DCC in the SEC involves the direct interaction between two fluid streams of different temperatures, leading to the condensation of vapor and subsequent separation of phases. On the other hand, T-junction separation utilizes a geometric configuration to divert a single-phase fluid stream into two separate outlets, enabling the selective extraction of specific components. In terms of efficiency, DCC offers a straightforward approach to phase separation, leveraging the natural thermodynamic properties of the fluid streams to achieve condensation. This method is particularly effective for systems where a mixture undergoes a phase change, such as the condensation of steam in a power plant. DCC typically requires minimal additional equipment and can be implemented with relatively low energy consumption, making it a cost-effective solution for many applications. In contrast, T-junction separation provides a more controlled approach to phase separation, allowing for the selective extraction of specific components from a fluid stream. By diverting the flow into multiple outlets, T-junction separators enable precise control over the distribution of phases and components, making them well-suited for applications requiring high purity separations or complex phase behavior. In this study, a mixture of steam and a non-condensable gas (CO2) is introduced into the SEC. Following the complete

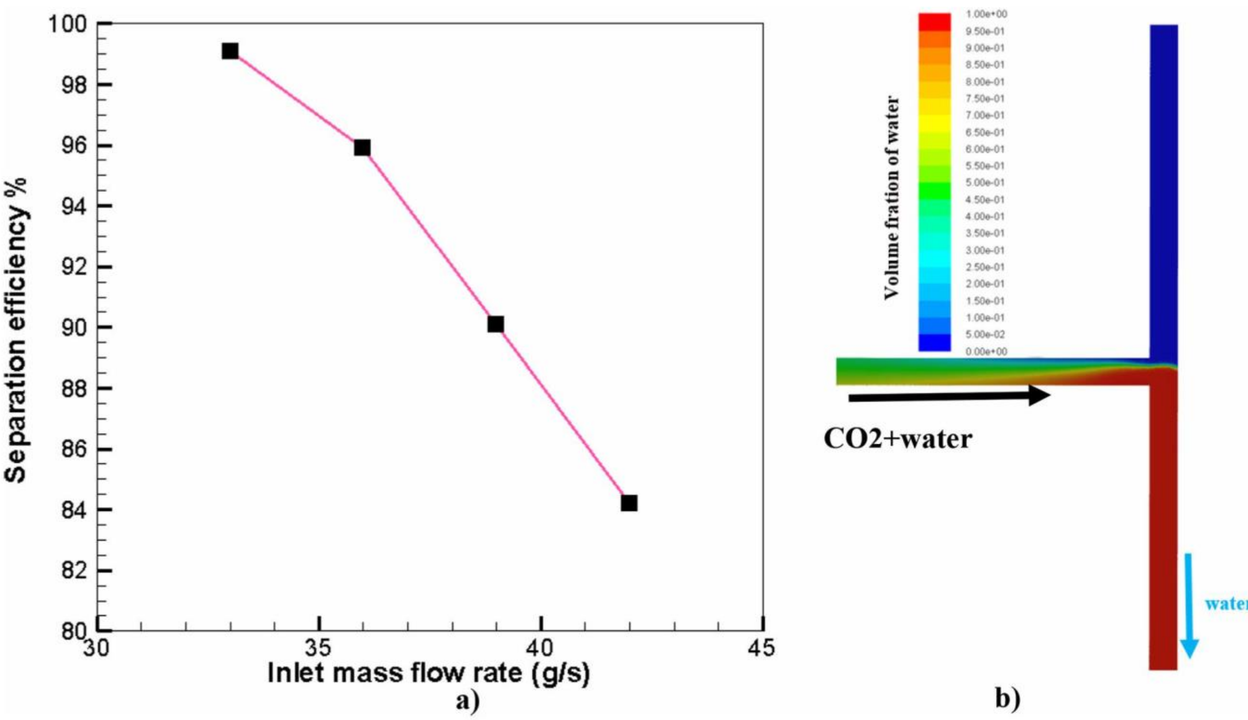

Fig. 21. a) Separation efficiency for different inlet mass flow rate and b) contour of volume fraction of water.

condensation of steam into water within the SEC, a T-junction is employed to separate the water and CO2 components, facilitating the purification of CO2.

8. Conclusion

To enrich the purging process in negative CO2 emission power plants (nCO2PP), a comprehensive approach was undertaken involving both numerical and experimental modeling of SEC and numerical simulation of the T-junction separator. This integrated strategy aims to optimize the separation section, ensuring the generation of CO2 with high-purity in the post-combustion part of nCO2PP. By combining the SEC and T-junction separator, a practical solution is proposed for CO2 purification. This approach addresses key factors such as optimizing steam condensation, controlling water temperature and pressure to regulate the outlet temperature of the SEC, and assessing the impact of non-condensable gas (CO2) and steam mass flow rate on both inlet and outlet temperatures of SEC, as well as enhancing separation efficiency. The results from the calculations confirm that the proposed model closely aligns with experimental observations.

Through numerical and experimental investigations on the SEC and numerical simulations of the vertical impact T-junction separator, the ensuing outcomes were derived:

- Understanding the water plume's behavior within the SEC, influenced by parameters like steam mass flow rate, is crucial for optimizing performance, enhancing condensation efficiency, and achieving fully condensed water, thus maximizing heat transfer and carbon capture efficiency.
- Monitoring inlet and outlet temperatures of the SEC provides crucial insights into the system's initial thermal conditions and the effectiveness of condensation.
- Water temperature of jet profoundly influences outlet temperature of the SEC at constant inlet temperature and specific CO2 flow rate, with lower coolant water temperatures enhancing heat transfer efficiency (at constant inlet temperature and specific CO2 flow rate), lowering outlet temperatures, and optimizing condensation efficiency, thereby improving energy efficiency and operational reliability. For example, the outlet temperature of the SEC decreases by approximately 9.22% without CO2 and by approximately 5.89% with a CO2 volumetric flow rate of 10 $\left(\frac{m^3}{h}\right)$ as the water temperature decreases from 40 °C to 20 °C.
- Investigating the impact of water pressure on the temperature difference reveals that higher pressures enhance heat transfer efficiency, which has practical implications for optimizing SEC operation in industries reliant on efficient heat exchange processes. For instance, in the absence of CO2, ΔT increased by approximately 34.43% (from 30.5 to 41), and when CO2 $= 10 \left(\frac{m^3}{h}\right)$, ΔT increased by about 34.48% (from 14.5 to 19.6).
- Understanding the decrease in separation efficiency with higher inlet mass flow rates due to maldistribution in vertical impact T-junction separator provides valuable insights for industries reliant on efficient separation processes. Implementing strategies to mitigate maldistribution can enhance the performance and reliability of separation systems in various industrial applications.

Nomenclature

C_D	Drag force coefficient
d_β	Mean bubble diameter (m)
H	Enthalpy (J/kg)
h_w	Heat transfer coefficient on liquid side (w/m^2.k)
k	Turbulent kinetic energy (J/kg)
$\dot{m}_{sw}$	Steam condensation rates
$\mathbf{M}_{D\alpha}$	Drag force
$\mathbf{M}_{TD\alpha}$	Turbulent dispersion force
Re_r	Relative Reynolds number
$\dot{Q}_s$	Total heat flux transfers from steam to phase interface (W)
r	Volume fraction
$\boldsymbol{U}$	velocity vector (m/s)

Greek symbols

σ	Turbulent Prandtl number
ρ	Density (kg/m^3)
μ_m	Viscosity of the mixture $(kg.m^{-1}.s^{-1})$
$\mu_{t\alpha}$	turbulent viscosity in the liquid phase $(kg.m^{-1}.s^{-1})$
$\mu_{t\beta}$	Turbulent viscosity in the gas side $(kg.m^{-1}.s^{-1})$
ε	Turbulent dissipation rate (J/kg/s)
γ_β	gas volume fraction in the liquid phase

CRediT authorship contribution statement

Milad Amiri: Writing – review & editing, Writing – original draft, Visualization, Validation, Software, Resources, Methodology, Investigation, Data curation, Conceptualization, Formal analysis. **Michal Klugmann:** Validation, Methodology, Investigation, Formal analysis. **Jaroslaw Mikielewicz:** Investigation. **Paweł Ziółkowski:** Investigation. **Dariusz Mikielewicz:** Writing – review & editing, Supervision, Project administration, Funding acquisition, Conceptualization, Investigation, Methodology.

Declaration of competing interest

The authors declare that they have no known competing financial interests or personal relationships that could have appeared to influence the work reported in this paper.

Data availability

Data will be made available on request.

Acknowledgements

The research leading to these results has received funding from the Norway Grants 2014–2021 via the National Center for Research and Development. Article has been prepared within the frame of the project: “Negative CO2 emission gas power plant” - NOR/POLNORCCS/NEGATIVE-CO2- PP/0009/2019–00 which is co-financed by programme “Applied research” under the Norwegian Financial Mechanisms 2014–2021 POLNOR CCS 2019 - Development of CO2 capture solutions integrated in power and industry processes.

References

[1] L. Guo, H. Jin, Y. Lu, Supercritical water gasification research and development in China, J. Supercrit. Fluids 96 (2015) 144–150.
[2] C. Kunze, H. Spliethoff, Assessment of oxy-fuel, pre-and post-combustion-based carbon capture for future IGCC plants, Appl. Energy 94 (2012) 109–116.
[3] F. Wu, P.A. Dellenback, M. Fan, Highly efficient and stable calcium looping based pre-combustion CO2 capture for high-purity H2 production, Mater. Today Energy 13 (2019) 233–238.
[4] H. Hekmatmehr, et al., Carbon capture technologies: a review on technology readiness level, Fuel 363 (2024) 130898.
[5] M. Amiri, J. Mikielewicz, D. Mikielewicz, CO2 capture using steam ejector condenser under electro hydrodynamic actuator with non-condensable gas and cyclone separator: a numerical study, Sep. Purif. Technol. 329 (2024) 125236.
[6] M.B. Toftegaard, J. Brix, P.A. Jensen, P. Glarborg, A.D. Jensen, Oxy-fuel combustion of solid fuels, Prog. Energy Combust. Sci. 36 (5) (2010) 581–625.
[7] P. Madejski, M. Karch, P. Michalak, K. Banasiak, Conceptual design of experimental test rig for research on thermo-flow processes during direct contact condensation in the two-phase spray-ejector condenser, J. Energy Resour. Technol. 146 (3) (2024).
[8] P. Madejski, T. Kuś, P. Michalak, M. Karch, N. Subramanian, Direct contact condensers: a comprehensive review of experimental and numerical investigations on direct-contact condensation, Energies 15 (24) (2022) 9312.
[9] S. Sideman, D. Moalem-Maron, Direct contact condensation, in: Advances in Heat Transfer vol. 15, Elsevier, 1982, pp. 227–281.
[10] E. Lakzian, D. Dadpour, M.R. Aghdasi, M. Gholami, H.D. Kim, Multi-objective optimization of the wet at the blade's inlet and surface heating for wet steam flow in turbine blade cascade by TOPSIS method, Int. J. Heat Mass Transf. 224 (2024) 125372.
[11] S.A. Hosseini, M.R. Aghdasi, E. Lakzian, H.D. Kim, Multi-objective optimization of the effects of superheat degree and blade pitch on the wet steam parameters, Int. J. Heat Mass Transf. 213 (2023) 124337.
[12] S.A. Hosseini, M. Nakisa, E. Lakzian, Reducing the condensing flow effects on the steam turbine blades through modified design geometry, Phys. Fluids 35 (9) (2023).
[13] M. Ghodrati, E. Lakzian, H.D. Kim, Optimization of inlet conditions of hot steam injection into the non-equilibrium condensing steam, Phys. Fluids 35 (8) (2023).
[14] D. Mikielewicz, M. Amiri, M. Klugmann, J. Mikielewicz, A novel concept of enhanced direct-contact condensation of vapour-inert gas mixture in a spray ejector condenser, Int. J. Heat Mass Transf. 216 (2023) 124576.
[15] H. Ghazi, Direct-Contact Heat Transfer for Air Bubbling through Water, 1991.
[16] X. Zong, J.-P. Liu, X.-P. Yang, J.-J. Yan, Experimental study on the direct contact condensation of steam jet in subcooled water flow in a rectangular mix chamber, Int. J. Heat Mass Transf. 80 (2015) 448–457.
[17] P. Fu, Y. Zhou, X. Yang, J. Yan, J. Liu, Experimental study on the effect of non-condensable gas dissolved in sub-cooled water on steam jet condensation in a rectangular channel, Int. J. Heat Mass Transf. 134 (2019) 668–679.
[18] C. Reddick, M. Sorin, H. Sapoundjiev, Z. Aidoun, Effect of a mixture of carbon dioxide and steam on ejector performance: an experimental parametric investigation, Exp. Thermal Fluid Sci. 92 (2018) 353–365.
[19] M. Abbad, S. Dyer, P. Ligneul, M. Badri, In-line water separation: A new promising concept for water debottlenecking close to the wellhead, in: SPE Middle East Oil & Gas Show and Conference, OnePetro, 2015.
[20] H. Tuo, P. Hrnjak, Vapor–liquid separation in a vertical impact T-junction for vapor compression systems with flash gas bypass, Int. J. Refrig. 40 (2014) 189–200.
[21] K. Welter, et al., Experimental investigation and theoretical modeling of liquid entrainment in a horizontal tee with a vertical-up branch, Int. J. Multiphase Flow 30 (12) (2004) 1451–1484.
[22] W. Lou, Z. Wang, J. Zhang, H. Liu, B. Sun, F. Zhang, Flow regime evolution mechanism and falling flux prediction model for bypass injection of viscous liquid in vertical T-junction, Chem. Eng. J. 476 (2023) 146601.
[23] L. Liu, S. Jiang, C. Zhu, Y. Ma, T. Fu, Distribution of liquid–liquid two-phase flow in branching T-junction microchannels, Chem. Eng. J. 431 (2022) 133939.
[24] B. Azzopardi, D. Colman, D. Nicholson, Plant application of a T-junction as a partial phase separator, Chem. Eng. Res. Des. 80 (1) (2002) 87–96.
[25] E. Sliwicki, J. Mikielewicz, Analysis of an annular-mist flow model in a T-junction, Int. J. Multiphase Flow 14 (3) (1988) 321–331.
[26] W. Xu, S. Deng, W. Su, Y. Zhang, L. Zhao, Z. Yu, How to approach Carnot cycle via zeotropic working fluid: research methodology and case study, Energy 144 (2018) 576–586.
[27] W. Xu, S. Deng, L. Zhao, Y. Zhang, S. Li, Performance analysis on novel thermodynamic cycle under the guidance of 3D construction method, Appl. Energy 250 (2019) 478–492.
[28] B. Yang, W. Su, S. Deng, L. Zhao, P. Lu, State-of-art of branching T-junction: experiments, modeling, developing prospects and applications, Exp. Thermal Fluid Sci. 109 (2019) 109895.
[29] L. Yang, J. Wang, Z. Zhao, S. Xu, B.J. Azzopardi, H. Wang, Phase separation of gas–liquid two-phase stratified and plug flows in multitube T-junction separators, AICHE J. 63 (6) (2017) 2285–2292.
[30] M. Mohamed, H. Soliman, G. Sims, Conditions for complete phase separation in an impacting tee junction at various inclinations of the outlet arms, Int. J. Multiphase Flow 47 (2012) 66–72.
[31] S. Noor, H.M. Soliman, Experimental investigation of phase-separation effectiveness of combined impacting tee junctions, Int. J. Mech. Eng. Robot. Res. 8 (3) (2019).
[32] P. Ziółkowski, et al., Thermodynamic analysis of negative CO2 emission power plant using Aspen plus, Aspen Hysys, and Ebsilon software, Energies 14 (19) (2021) 6304.
[33] P. Ziółkowski, K. Stasiak, M. Amiri, D. Mikielewicz, Negative carbon dioxide gas power plant integrated with gasification of sewage sludge, Energy 262 (2023) 125496.
[34] P. Ziółkowski, et al., Mathematical modelling of gasification process of sewage sludge in reactor of negative CO2 emission power plant, Energy 244 (2022) 122601.
[35] P. Madejski, et al., Development of a spray-ejector condenser for the use in a negative CO2 emission gas power plant, Energy 283 (2023) 129163.
[36] P. Madejski, P. Michalak, M. Karch, T. Kuś, K. Banasiak, Monitoring of thermal and flow processes in the two-phase spray-ejector condenser for thermal power plant applications, Energies 15 (19) (2022) 7151.
[37] T. Kuś, P. Madejski, Analysis of the multiphase flow with condensation in the two-phase ejector condenser using computational fluid dynamics modeling, J. Energy Resour. Technol. 146 (3) (2024).
[38] N. Saba, R.T. Lahey Jr., The analysis of phase separation phenomena in branching conduits, Int. J. Multiphase Flow 10 (1) (1983) 1–20.
[39] B.E. Launder, D.B. Spalding, The numerical computation of turbulent flows, in: Numerical Prediction of Flow, Heat Transfer, Turbulence and Combustion, Elsevier, 1983, pp. 96–116.
[40] Y. Zhou, et al., Numerical simulation on the direct contact condensation in a steam-water two-phase ejector with non-condensable gas, Int. J. Therm. Sci. 185 (2023) 108030.
[41] Q. Xu, L. Liang, Y. She, X. Xie, L. Guo, Numerical investigation on thermal hydraulic characteristics of steam jet condensation in subcooled water flow in pipes, Int. J. Heat Mass Transf. 184 (2022) 122277.

[42] Q. Xu, C. Liu, Q. Liu, Y. Zhu, H. Zhou, L. Guo, Interfacial characteristics of steam jet condensation in subcooled water pipe flow–an experimental and numerical study, Chem. Eng. Sci. 251 (2022) 117457.

[43] X. Chen, M. Tian, G. Zhang, H. Liu, Numerical Simulation on interfacial characteristics in supersonic steam–water injector using particle model method, Energies 12 (6) (2019) 1108.

[44] K.-S. Liang, Experimental and analytical study of direct contact condensation of steam in water, Nucl. Eng. Des. 147 (3) (1994) 425–435.

[45] X. Chen, M. Tian, X. Qu, Y. Zhang, Numerical investigation on the interfacial characteristics of steam jet condensation in subcooled water flow in a restricted channel, Int. J. Heat Mass Transf. 137 (2019) 908–921.

[46] X. Yang, D. Chong, J. Liu, X. Zong, J. Yan, Experimental study on the direct contact condensation of the steam–air mixture in subcooled water flow in a rectangular channel, Int. J. Heat Mass Transf. 88 (2015) 424–432.

[47] M. Bai, R. Zhao, P. Lu, B. Yang, L. Zhao, Y. Zhang, Simulation study on phase separation and pressure distribution of refrigerant in horizontal double T-junctions, Int. J. Refrig. 126 (2021) 88–98.

[48] E. Ganić, W. Rohsenow, Dispersed flow heat transfer, Int. J. Heat Mass Transf. 20 (8) (1977) 855–866.

[49] L. Schiller, A drag coefficient correlation, Zeit. Ver. Deutsch. Ing. 77 (1933) 318–320.

[50] M.A.L. De Bertodano, Two fluid model for two-phase turbulent jets, Nucl. Eng. Des. 179 (1) (1998) 65–74.

[51] D. Mikielewicz, Hydrodynamics and heat transfer in bubbly flow in the turbulent boundary layer, Int. J. Heat Mass Transf. 46 (2) (2003) 207–220.

[52] S. Patankar, Numerical Heat Transfer and Fluid Flow, Taylor & Francis, 2018.

[53] H.K. Versteeg, W. Malalasekera, An Introduction to Computational Fluid Dynamics: The Finite Volume Method, Pearson education, 2007.

[54] R. Utikar, et al., Hydrodynamic simulation of cyclone separators, in: Computational Fluid Dynamics, InTech, 2010, pp. 241–266.

[55] N. Zheng, L. Zhao, Y. Hwang, J. Zhang, X. Yang, Experimental study on two-phase separation performance of impacting T-junction, Int. J. Multiphase Flow 83 (2016) 172–182.

[56] B. Yang, W. Su, S. Deng, L. Zhao, P. Lu, State-of-art of impacting T-junction: phase separation, constituent separation and applications, Int. J. Heat Mass Transf. 148 (2020) 119067.

[57] Z.Q. Memon, W. Pao, F.M. Hashim, H.M. Ali, Experimental investigation of two-phase separation in T-junction with combined diameter ratio, J. Nat. Gas Sci. Eng. 73 (2020) 103048.

[58] B. Azzopardi, The effect of side arm diameter on phase split at T-junctions, in: SPE Annual Technical Conference and Exhibition?, SPE, 1999 pp. SPE-56707-MS.

[59] M. Froissart, T. Ochrymiuk, Novel wet combustion chamber concept CFD studies with triple water inlet, Energy 278 (2023) 127854.

[60] M. Mohamed, H. Soliman, G. Sims, Experimental investigation of two-phase flow splitting in an equal-sided impacting tee junction with inclined outlets, Exp. Thermal Fluid Sci. 35 (6) (2011) 1193–1201.

[61] P. Lu, et al., Analysis of pressure drop in T-junction and its effect on thermodynamic cycle efficiency, Appl. Energy 231 (2018) 468–480.

Appendix 5. Article [E]

Separation and Purification Technology 329 (2024) 125236

Contents lists available at ScienceDirect

Separation and Purification Technology

journal homepage: www.elsevier.com/locate/seppur

CO_2 capture using steam ejector condenser under electro hydrodynamic actuator with non-condensable gas and cyclone separator: A numerical study

Milad Amiri [a,*], Jaroslaw Mikielewicz [b], Dariusz Mikielewicz [a]

[a] Faculty of Mechanical Engineering and Ship Technology, Gdańsk University of Technology, ul. Gabriela Narutowicza 11/12, 80-233 Gdańsk, Poland
[b] Polish Academy of Science, Institute of Fluid-Flow Machinery, 80-231 Gdańsk, Poland

ARTICLE INFO

Editor: S. Yi

Keywords:
Steam ejector condenser
Direct-contact condensation
CFD
Gas-liquid separation
EHD

ABSTRACT

The concept for condensation of steam and CO_2 separation in a negative CO_2 emission gas power plant involves the utilization of a steam ejector condenser (SEC) for direct-contact condensation of vapor with inert gas (CO_2) on a spray of subcooled liquid, integrated with a separator to produce pure CO_2. Due to the increasing diffusion resistance and reduced convective heat transfer between the steam and subcooled water phases in the presence of non-condensable gas (CO_2), the study utilized an electrohydrodynamic (EHD) actuator to enhance heat transfer rate in the SEC. To optimize CO_2 purification, the effect of single, dual and quadruple inlets on separation efficiency was analysed. In the SEC, the Eulerian-Eulerian multiphase model is employed, treating water as the continuous phase and the compressible gas mixture (steam and CO_2) as the dispersed phase. The standard k-ε model is chosen to depict the turbulence in the ejector. The separator is transient, turbulent, and three-dimensional, using the control volume method. The RSM turbulent model and mixture model are utilized to simulate the turbulent two-phase flow in the gas–liquid separator. The findings indicated that when the mass flux of steam and voltage are increased, the condensation heat transfer coefficient also increases. For a mass flux of steam of 51 ($\frac{kg}{m^2.s}$), the condensation heat transfer coefficients were measured to be 0.98, 1.029, 1.08, and 1.134 ($\frac{MW}{m^2.K}$) at electrode voltages of 0, 20, 25, and 30 kV, respectively. In addition, a single-inlet cyclone attains a separation efficiency of 95.1 %, while incorporating two inlets improves the performance to 97.9 %. However, the most remarkable outcome is witnessed in cyclones with four inlets, where an impressive separation efficiency of 99.9 % is achieved.

1. Introduction

The emission of carbon dioxide (CO2) through the burning of fossil fuels in the power generation sector is a primary contributor to global climate change [1]. To mitigate CO2 emissions and ensure a reliable power supply, it is essential to implement efficient carbon capture technologies in power plants. In addition, capturing CO2 presents significant economic opportunities. Carbon capture technologies for power plants have gained worldwide attention, and multiple power plants can collaborate to collect CO2 [2], often with penalties for non-compliance. A novel approach to achieving electricity generation with negative CO2 emissions involves oxy-combustion in a wet combustion chamber, followed by the separation of water and CO2 using a steam ejector condenser (SEC), and the subsequent compression of the separated CO2. The negative CO2 emission power plant cycle comprises various components, with the steam ejector condenser and separator playing an indispensable role in obtaining pure CO2. Fig. 1 depicts the process flow diagram (PFD) of a gas power plant with negative CO2 emissions [3–6]. In Fig. 1b, the separation unit consists of the SEC and cyclone separator. The main function of the SEC is to condense water vapor from the exhaust gases while maintaining a compact system design with two inlets and one outlet. At the outlet of the SEC, the condensed water and CO2 are expected to enter the cyclone separator for the purpose of purifying the CO2.

The process of heat transfer in steam ejector condensers is of utmost importance as it greatly impacts the efficiency and performance of the system. Experimental and numerical results [7,8] indicate that the expansion of the steam plume and the heat transfer between phases are substantially hindered when non-condensable gas is present. Even a

* Corresponding author.
E-mail address: milad.amiri@pg.edu.pl (M. Amiri).

https://doi.org/10.1016/j.seppur.2023.125236
Received 14 July 2023; Received in revised form 31 August 2023; Accepted 27 September 2023
Available online 28 September 2023
1383-5866/

Nomenclature

Drag force coefficient C_D
Turbulent dispersion force coefficient C_{TD}
Specifies diffusion coefficient of ions (m^2/s) D_e
Stress diffusion term D_{ij}
Mean bubble diameter (m) d_β
Corona initiating electric field ($\frac{V}{m}$) E_0
Electric field strength vector (V/s) $\vec{E}$
Heat transfer coefficient on liquid side (w/m^2.k) h_w
Turbulent kinetic energy k
Electric current density (A/m^2) j
Steam condensation rates m_{sw}
Drag force $\mathbf{M}_{D\alpha}$
Turbulent dispersion force $\mathbf{M}_{TD\alpha}$
Static Pressure (Pa) P
Steam partial pressure (Pa) P_s
Shear production term P_{ij}
Total heat flux transfers from steam to phase interface (W) Q_s
Equivalent cylinder radius (m) r_{eff}
Volume fraction r
Source term S
Velocity vector (m/s) $\vec{u}$
Water saturation temperature (K) T_{sat}
Mass-averaged velocity (m/s) u_m
Drift velocity for secondary (m/s) $u_{dr,q}$
Corona onset voltage (V) V_0
Electric potential (V) V
Relative Reynolds number Re_r

Greek Symbols
Ion mobility (m^2/(V·s)) β
Density (kg/m^3) ρ
Mixture density (kg/m^3) ρ_m
charge density (C/m^3) ρ_c
Viscosity of the mixture $(kg.m^{-1}.s^{-1})$ μ_m
Pressure-strain term Π_{ij}
turbulent viscosity in the liquid phase $(kg.m^{-1}.s^{-1})$ $\mu_{t\alpha}$
Turbulent viscosity in the gas side $(kg.m^{-1}.s^{-1})$ $\mu_{t\beta}$
Turbulent dissipation rate ε
Dissipation term ε_{ij}
Dielectric permittivity (F/m) ε_s
Turbulent kinetic energy κ_α
gas volume fraction in the liquid phase γ_β

small fraction of non-condensable gas, as low as 1 % in mass, can lead to a reduction in the heat transfer coefficient by approximately 10–40 % [9]. Heat transfer in flows can be improved through three techniques: passive, active and a combination of passive and active methods. Passive methods can operate independently without requiring external inputs like mechanical actuation or electrical power [10]. On the other hand, active methods rely on external inputs to function. One type of active heat transfer enhancement technique is electrohydrodynamic (EHD) techniques, which involve the application of an electric field in a dielectric fluid medium. In recent years, the use of electrical fields in systems with dielectric mediums has emerged as a promising method for enhancing heat transfer. Electrohydrodynamic (EHD) techniques have been effectively applied in systems involving condensation and evaporation processes, especially in scenarios where significant energy is required for phase changes. Two-phase flow systems exhibit distinctive flow regimes determined by various factors, including volume fraction, phase velocities, and flow orientation. To accurately predict the transition between different two-phase flow patterns, several flow patterns have been developed. In the context of condensation, the heat transfer mechanisms are strongly influenced by whether the flow is gravity-driven (e.g., stratified, stratified wavy, and slug flows) or shear-driven (e.g., annular flows). This distinction is critical as it directly affects the heat transfer mechanism based on the phase that makes contact with the heat transfer surface [11]. The application of EHD in multi-phase flows presents greater complexity compared to single-phase flows. This complexity arises from the inherent intricacies of multi-phase flows, as well as the inclusion of force components in the EHD equation and the interactions between free charges and the liquid–vapor interface. Applications of electric field can introduce additional body forces to liquid–vapor phase flow systems [12]. These forces primarily stem from the distribution of the electrical field and the variations in the specific dielectric constant of the phases. As a result, they disturb the boundary layer near the surface and may cause redistributions of the two phases. The condensed liquid is subsequently collected in a separator, where centrifugal force is employed to separate the liquid from non-condensable gas (CO2).

Cyclones play a significant role in numerous industries such as mineral, chemical, environmental, and petroleum engineering, where they are employed for the separation of gases from solids or liquids [13,14]. Gas-liquid cyclones come in various types, with the Stairmand cyclone [15] being the most commonly utilized. This particular type of cyclone comprises a cylindrical section, a tangential inlet, a vortex finder, and a conical section. Cyclone separators can be categorized as either axial or tangential, depending on the direction of the inlet flow towards the cyclone. The tangential cyclone is designed with a tangential inlet flow, creating an outer vortex. The flow is then reversed at the end of the vortex and exits from the top in an axial direction. This unique configuration takes advantage of the density difference and two-phase interface, enabling the separation of mixtures through efficient centrifugal separation. Unlike energy-intensive methods such as permeable membranes, cyclone separators offer a practical and cost-effective solution for separation processes, minimizing the consumption of valuable energy resources. The liquid–gas flow within a cyclone is a complex phenomenon that has attracted significant attention. In the case of a cone cyclone, the primary mechanism for deaeration is the centrifugal force, which inevitably leads to some loss of flow pressure [16]. Cyclones come in various dimensions and types, resulting in different levels of pressure drops and centrifugal forces. Extensive research in the literature has investigated the pressure distribution and tangential velocity within cyclones, revealing significant changes in pressure and the profound effects of centrifugal forces [17]. Cyclones are devices that induce a swirling flow by introducing high-velocity fluids through one or more tangential inlets. This creates a vortex core within the device. The swirling flow enhances mixing through turbulence and vorticity effects, leading to the separation of higher-density particles or fluids from the base fluid. Specifically, this is referring to a cone cyclone, a type of cyclone separator that employs turbulence and physical instabilities to promote efficient mixing. This design consists of a cylinder with an outer cone, where the flow is tangentially injected into the cylinder. The liquid phase exits through the underflow outlet, while the gas phase exits through the overflow outlet. The effectiveness of a cyclone separator is determined by multiple factors, including its structural geometry and operational parameters [18]. Gao et al. [19] conducted a comparison between single and double inlet cyclones, focusing on the characteristics of the vortex lines. They observed that single inlet cyclones exhibited significant eccentricity, while double inlet cyclones showcased a more stable flow field. The presence of dual inlets in cyclones promotes continuous and smooth operation. However, specific quantitative data regarding the performance changes between the two configurations were not provided in their study. Dong et al. [20] conducted a computational fluid dynamic (CFD) analysis and highlighted that the double inlet cyclone exhibited a smaller vortex eccentricity, resulting in higher efficiency. However, this configuration also incurred a higher pressure drop. Examining the velocity distribution, Zhao et al. [21] investigated the flow field and performance of single, double, and quadruple inlet cyclones. They suggested that symmetrical inlets increased the tangential velocity and, subsequently, the separation efficiency, but it also led to an increased pressure drop. Vahedi [22] analyzed the flow fields of single, double, and quadruple inlet cyclones and concluded that the quadruple inlet cyclone achieved the highest tangential velocity, efficiency, and pressure drop. Le [23] also supported the finding that the quadruple inlet cyclone outperformed the single inlet cyclone in terms of efficiency and pressure drop.

In this paper, SEC and tangential-flow CO_2-water separator was designed to obtain the desired high-purity CO_2 flow for the Negative CO_2 emission gas Power Plant (nCO_2PP). To obtain a numerical model and optimize the performance of capturing CO2 section, firstly, effect of inlet mass flow rate of steam and back pressure on steam volume fraction

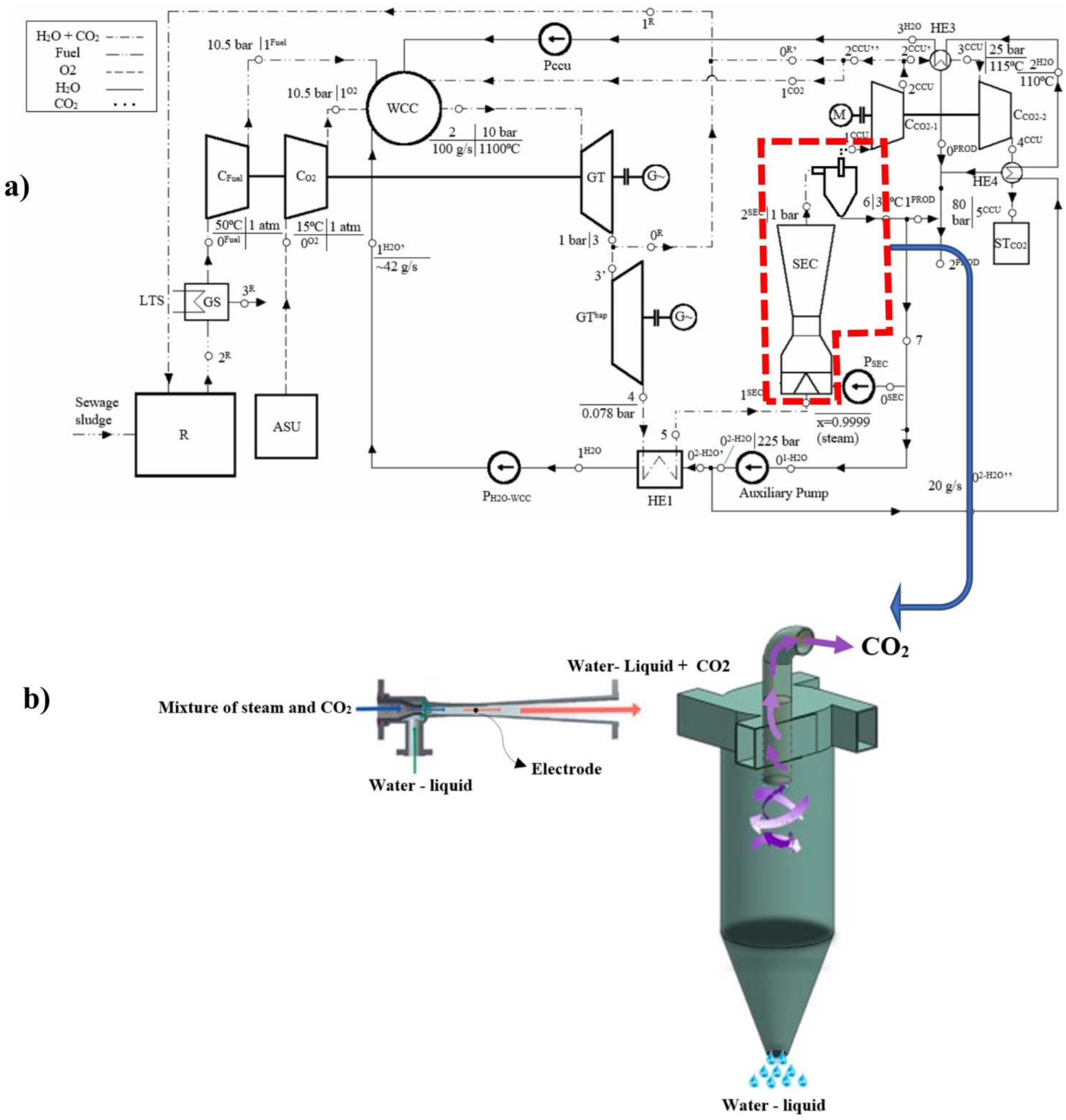

Fig. 1. (a) Negative CO_2 emission gas power plant process flow diagram (PFD), (b) Capturing CO_2 part consist of steam ejector condenser (SEC) under electro hydrodynamic actuator and cyclone separator [3,5].

could be defined. Then, effect of Non-Condensable Gas (CO2) on hydraulic- thermal parameters can be obtained using EHD in SEC, so that the numerical simulation on different value of steam inlet mass flux and voltage of electrode is conducted, and by applying 20 up to 30 (KV) and 40.8 ($\frac{kg}{m^2.s}$) up to 51 ($\frac{kg}{m^2.s}$) of mass flux of steam, the model is derived. After obtaining the model of SEC, the performance of separator affected by single, dual and quadruple inlets can be estimated.

2. Modeling

2.1. Steam ejector condenser (SEC)

In order to investigate the direct contact condensation (DCC) process of a steam jet in subcooled water within a two-phase ejector, a numerical study was conducted based on the design of the steam-water condensing ejector described below. The ejector consists of several components, including a central steam nozzle, a surrounding water nozzle, a mixing chamber, a throat, and a diffuser. Saturated steam at high pressure is ejected from the steam nozzle and comes into direct contact with subcooled water in the mixing chamber. During this interaction, condensation occurs. The resulting mixture then passes through the throat and diffuser section before exiting the outlet. The schematic diagram and dimensional parameters of the ejector are illustrated in Fig. 2.

2.2. Cyclone separator

The performance of a cyclone separator is influenced by various factors, and achieving optimal separation efficiency and minimal pressure loss requires careful consideration of component dimensions. Cyclone separators are commonly categorized into two types based on their structural characteristics: tangential and axial inlets. The tangential inlet type is widely used in industrial applications and is considered well-established, featuring a simple structure typically comprising a cylindrical and conical section. Fig. 3a illustrates the three-dimensional geometry of a tangential inlet cyclone separator. In this design, a CO2-water mixture enters the separator tangentially, generating rapid rotation within the annular space between the exhaust pipe and the cylinder. Under the influence of centrifugal force, water droplets in the mixture are propelled towards the wall and subsequently descend along it due to the combined effects of gravity and momentum. These water droplets are then discharged through the underflow outlet. Meanwhile, the purified CO2 rises upward through the central region and is expelled via the exhaust pipe. The dimensions of the three-dimensional tangential single inlet cyclone separator are indicated in Fig. 3b.

3. Governing equations

3.1. Steam ejector condenser (SEC)

In this study, the flow field exhibits non-uniform distribution of the gas and liquid phases, resulting in a significant imbalance between the two phases. To accurately capture this behavior, a Eulerian-Eulerian multiphase model is employed, treating the two phases separately. The continuous phase is represented by water, while the dispersed phase consists of a compressible gas mixture containing steam and non-condensable gas (CO2). In order to characterize the turbulent

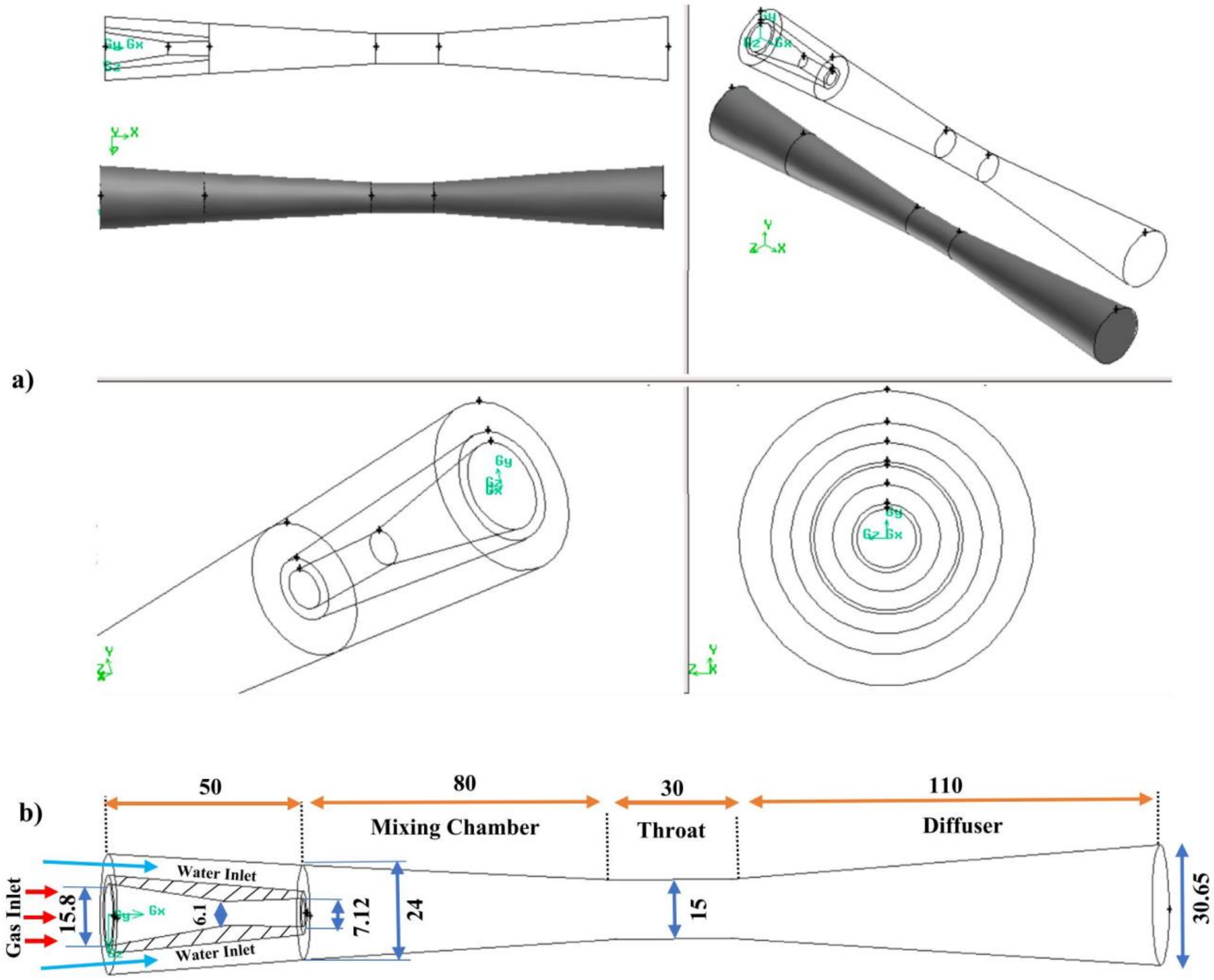

Fig. 2. Schematic and dimensions of steam–water injector [24] (in mm).

a)

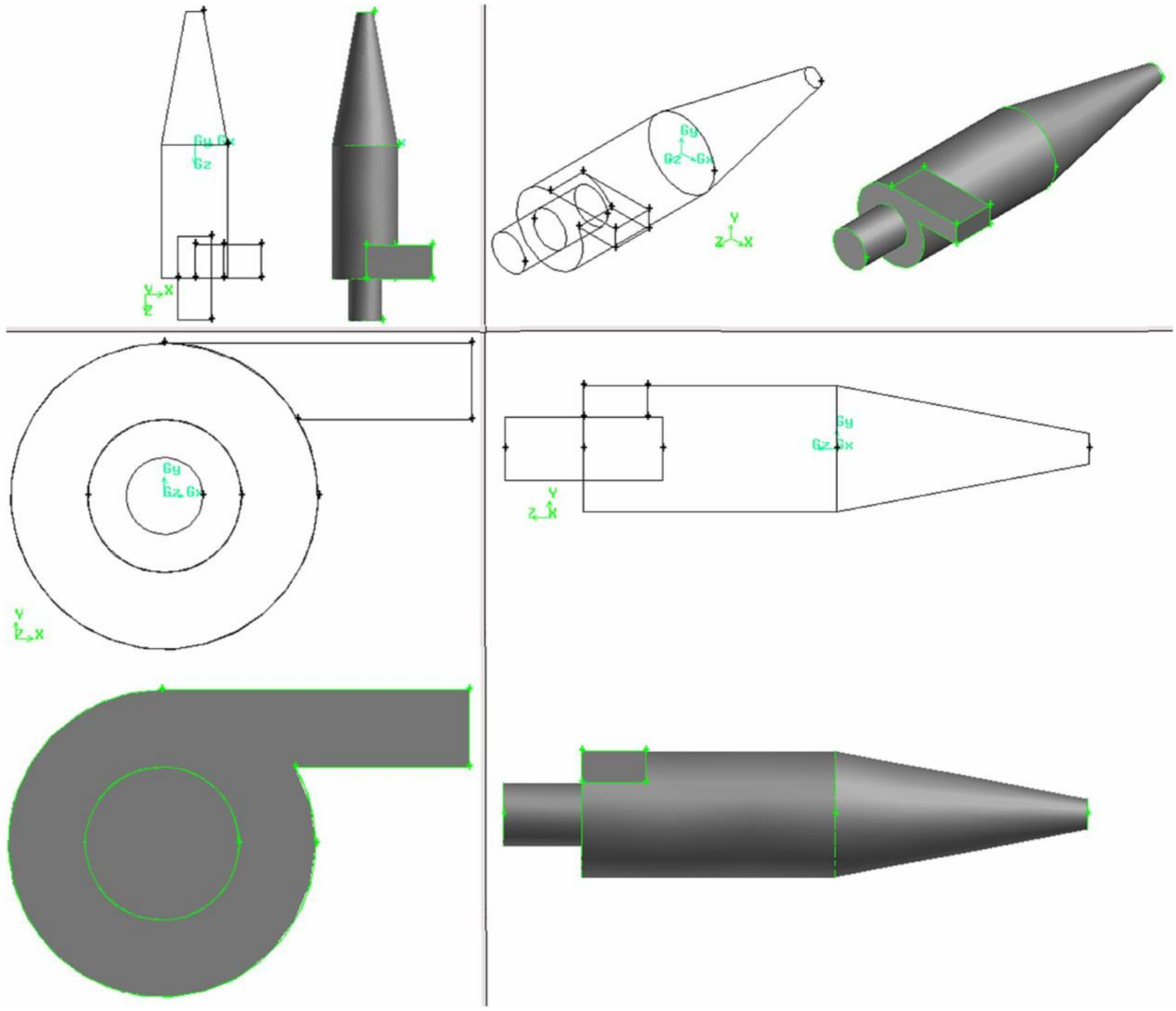

b)

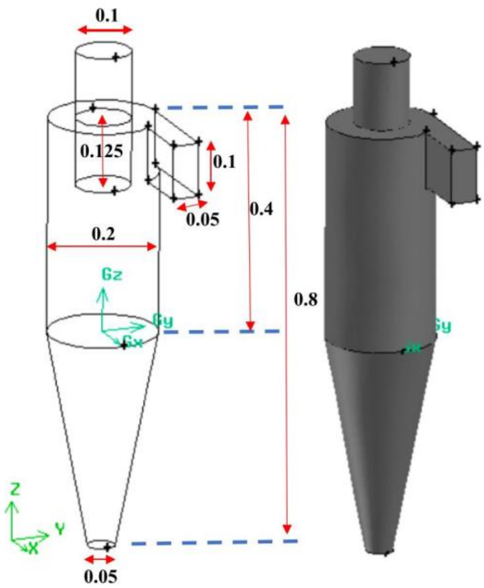

Fig. 3. (a) Geometry of the cyclone separator seen from different views and (b) its dimensions.

behavior within the ejector, the standard k -ε model is selected. The continuous phase, denoted as α, represents the liquid water, while the dispersed phase, denoted as β, represents the gas phase. The liquid phase is modeled using the k and ε equations associated with the standard k -ε model.

$$\frac{\partial}{\partial t}(r_\alpha \rho_\alpha k_\alpha) + \nabla(r_\alpha \rho_\alpha \boldsymbol{U}_\alpha k_\alpha) = \nabla\left(r_\alpha\left(\mu_\alpha + \frac{\mu_{t\alpha}}{\sigma_k}\right)\nabla k_\alpha\right) + r_\alpha(P_\alpha - \rho_\alpha \varepsilon_\alpha) \tag{1}$$

$$\frac{\partial}{\partial t}(r_\alpha \rho_\alpha \varepsilon_\alpha) + \nabla(r_\alpha \rho_\alpha \boldsymbol{U}_\alpha \varepsilon_\alpha) = \nabla\left(\mu_\alpha + \frac{\mu_{t\alpha}}{\sigma_\varepsilon}\right)\nabla \varepsilon_\alpha + r_\alpha \frac{\varepsilon_\alpha}{k_\alpha}(C_{\varepsilon 1} P_\alpha - C_{\varepsilon 2} \rho_\alpha \varepsilon_\alpha) \tag{2}$$

In the equations provided, ρ, r, k, $\boldsymbol{U}$ and ε represent the variables for density, volume fraction, turbulent kinetic energy, velocity vector, and turbulent dissipation rate, respectively. The turbulent viscosity for the liquid phase can be calculated using the following equation:

$$\mu_{t\alpha} = \frac{C_\mu \rho_\alpha k_\alpha^2}{\varepsilon_\alpha} \tag{3}$$

Here, $C_\mu, C_{\varepsilon 1}, C_{\varepsilon 2}, \sigma_k$ and σ_ε have values of 0.09, 1.44, 1.92, 1.0, and 1.3, respectively.

For the gas phase, which incorporates the turbulent kinematic viscosity of both the α and β phases, the following equation is utilized:

$$\sigma = \frac{\nu_{t\alpha}}{\nu_{t\beta}} \tag{4}$$

In this equation, σ represents a turbulent Prandtl number, which is set as 1 in the model. The turbulent viscosity for the gas phase can be obtained based on the turbulent viscosity of the liquid phase.

$$\mu_{t\beta} = \frac{\rho_\beta \mu_{t\alpha}}{\rho_\alpha} \tag{5}$$

3.1.1. Interfacial area density between steam and water

The heat transfer area between the two phases, which is crucial for calculating the steam condensation rate, is determined by the phase interface area per unit volume. In this study, the dispersed phase is modeled as clusters of standard sphere particles. The interfacial area density is computed by assuming the presence of tiny gas bubbles as spherical particles. The equation for calculating the interfacial area density is as follows:

$$A_{sw} = \frac{6\gamma_\beta}{d_\beta} \tag{6}$$

In this equation, d_β represents the mean diameter of the bubbles (or the characteristic length scale/interaction length) of the dispersed phase, while γ_β represents the volume fraction of gas in the liquid phase. This equation is widely utilized in numerical simulations of submerged steam jet condensation in subcooled water pools or pipes [25,26].

3.1.2. Interphase momentum transfer

In this model, the momentum transfers between the gas and liquid phases are accounted for through two forces: drag force ($\mathbf{M}_{D\alpha}$) and turbulent dispersion force ($\mathbf{M}_{TD\alpha}$). Drag force, $\mathbf{M}_{D\alpha}$, is determined as:

$$\mathbf{M}_{D\alpha} = -\mathbf{M}_{D\beta} = \frac{3}{4}\frac{C_D}{D_\beta} r_\beta \rho_\alpha |\mathbf{U}_\beta - \mathbf{U}_\alpha| (\mathbf{U}_\beta - \mathbf{U}_\alpha) \tag{7}$$

The drag force coefficient, denoted as C_D, can be incorporated into the Schiller-Naumann drag force model.

$$C_D = \max\left(\frac{24}{Re}\left(1 + 0.15Re^{0.687}\right), 0.44\right) \tag{8}$$

The turbulent dispersion force, $\mathbf{M}_{TD\alpha}$, is calculated using the Lopez-de-Bertodano model:

$$\mathbf{M}_{TD\alpha} = -\mathbf{M}_{TD\beta} = -C_{TD}\rho_\alpha \kappa_\alpha \nabla_{r_\alpha} \tag{9}$$

where κ_α represents the turbulent kinetic energy, and C_{TD} is the turbulent dispersion force coefficient, which is set to 0.3.

3.1.3. Interphase heat and mass transfer

In the presence of non-condensable gas in the steam jet condenser, the non-condensable component creates a gas layer near the phase interface. This gas layer enhances the diffusion resistance of steam to subcooled water and decrease the convective heat transfer between the two phases. To account for these effects, a two-resistance model that relies on the conduction-diffusion model [7] is implemented. In the gas side, the presence of non-condensable gas results in the formation of a layer that hinders direct contact between the steam and subcooled water. As a result, the interfacial area density is significantly lower compared to a pure steam jet. However, the heat transfer coefficient is typically large enough to consider zero resistance [27]. On the liquid side, the presence of subcooled water enhances steam condensation, while the non-condensable gas inhibits this effect. To simplify the numerical model, the subcooled water and non-condensable component are considered as a mixture when calculating the heat transfer coefficient on the liquid side. It is important to acknowledge that when calculating the characteristic number, the physical properties and velocity of the mixture differ from those of subcooled water. The transfer of total heat flux from steam to the phase interface can be explained as follows [9]:

$$\mathrm{Q_s} = \mathrm{m_{sw}H_s} \tag{10}$$

Where $\mathrm{m_{sw}}$ is the condensation rate of steam. The total heat flux from the phase interface to the subcooled water is composed of the enthalpy of water and the convective heat transfer between the interface and the water.

$$\mathrm{Q_w} = \mathrm{m_{sw}H_w} + \mathrm{h_w A_{sw}}(\mathrm{T_{sat}} - \mathrm{T_w}) \tag{11}$$

The heat transfer coefficient on the liquid side, h_w, is determined by the physical properties of the mixture and Nusselt number.

$$h_w = \frac{\lambda_{wa} Nu_{wa}}{d_g} \tag{12}$$

where $\mathrm{Nu_{wa}}$ is computed using the following equation [27]:

$$\mathrm{Nu_{wa}} = \begin{cases} 2 + 0.6\mathrm{Re_r^{0.5}Pr_{wa}^{0.33}} 0 \le \mathrm{Re_r} < 7760 < \mathrm{Pr_{wa}} < 250 \\ 2 + 0.27\mathrm{Re_r^{0.62}Pr_{wa}^{0.33}}\mathrm{Re_r} \ge 7760 < \mathrm{Pr_{wa}} < 250 \end{cases} \tag{13}$$

The relative Reynolds number, $\mathrm{Re_r}$, is utilized to capture the relative motion and shear effect between the liquid phase and gas phase. It is defined as follows [9]:

$$Re_r = \frac{\rho_{wa}|\mathbf{U}_g - \mathbf{U}_{wa}| d_g}{\mu_{wa}} \tag{14}$$

The calculation of the physical properties in the above equations is carried out using the following relationships [9]:

$$\lambda_{wa} = \frac{\alpha_w \lambda_w + \alpha_a \lambda_a}{\alpha_w + \alpha_a} \tag{15}$$

$$\mu_{wa} = \frac{\alpha_w \mu_w + \alpha_a \mu_a}{\alpha_w + \alpha_a} \tag{16}$$

$$Pr_{wa} = \frac{\alpha_w Pr_w + \alpha_a Pr_a}{\alpha_w + \alpha_a} \tag{17}$$

To account for the momentum transfer between water and CO2, the velocity of the mixture is determined using the mass-weighted average velocity of non-condensable gas and subcooled water [9].

$$\mathbf{U}_{wa} = \frac{\alpha_w \rho_w \mathbf{U}_w + \alpha_a \rho_a \mathbf{U}_a}{\alpha_w \rho_w + \alpha_a \rho_a} \quad (18)$$

By utilizing the equations mentioned earlier, it is observed that the thermal conductivity, dynamic viscosity and Prandtl number of the gas mixture decrease as the CO2 mass fraction increases. Consequently, both the resistance to gas diffusion and convection decrease with the increase of CO2 mass fraction, which is consistent with theoretical [7] and experimental [8] findings. Based on the two-resistance model, the phase interface is in a state of thermal equilibrium, meaning that Q_s is equal to Q_w at the phase interface. By combining Equations (10) and (11), it is possible to determine the rate of steam condensation per unit volume and time.

$$m_{sw} = \frac{h_w A_{sw}(T_{sat} - T_w)}{H_s - H_w} \quad (19)$$

where T_{sat} illustrates the saturation temperature of water under steam local partial pressure. The steam partial pressure can be calculated as follows:

$$P_s = P_{stat}\left(\frac{\alpha_s}{\alpha_s + \alpha_a}\right) \quad (20)$$

3.1.4. Modeling for electric field

The EHD enhancement method arises from the application of an electric field, which induces an electric force density (body force) acting on the molecules of a dielectric fluid. This electric force density is comprised of three terms [28].

$$\vec{F_e} = \rho_c \vec{E} - \frac{1}{2}\vec{E}^2 \nabla \varepsilon_s + \frac{1}{2}\nabla\left[\vec{E}^2 \rho\left(\frac{\partial \varepsilon_s}{\partial \rho}\right)\right] \quad (21)$$

Where ρ_c and $\vec{E}$ represent the charge density (C/m^3) and electric field strength vector (V/s), respectively. ε_s denotes the dielectric permittivity (F/m). The first term in the equation accounts for the influence of the electric field on free charges, specifically known as the electrophoresis or Coulomb force. The second and third terms in the equations represent the dielectrophoresis and electrostriction force densities, which correspond to the polarization forces induced by the electric field. However, in practice, these terms can be neglected due to the constant electric permittivity. As a result, the electrohydrodynamic force is primarily determined by the Coulomb force ($\rho_c \vec{E}$), which is included as a source term in the momentum equation. The governing equations for electrohydrodynamics are calculated using the following equations [29].

The Poisson's equation can be expressed as follows:

$$\nabla^2 V = -\frac{\rho_c}{\varepsilon_s} \quad (22)$$

V Represents the electric potential (V)

The electric field is formulated as:

$$\vec{E} = -\nabla V \quad (23)$$

The current continuity equation can be illustrated as follows:

$$\nabla . \vec{j} = 0 \quad (24)$$

Where j represents the electric current density (A/m^2) as expressed below:

$$\vec{j} = \rho(\rho_c \beta \vec{E} + \rho_c \vec{u} + D_e \nabla \rho_c) \quad (25)$$

The variables β and $\vec{u}$ represent the ion mobility (m^2/(V·s)) and velocity vector (m/s), respectively. D_e expresses the diffusion coefficient of ions (m^2/s). The three terms on the right side of Equation (25) correspond to the contributions drift, convection, and diffusion of electric charge, respectively. It is important to note that the diffusion of electric charges ($D_e \nabla \rho_c$) is highly negligible in micro-scale ionic flows and can be disregarded. In the case of gases, the charge convection term ($\rho_c \vec{u}$) in Equation (25) is approximately two orders of magnitude smaller than the drifting term of ions ($\rho_c \beta \vec{E}$). However, this assumption is not applicable to liquids due to their low ion mobility (in gases, the ion mobility is relatively high, and the ratio of $\frac{u}{\beta E}$ is typically on the order of 0.1 or even less than 0.1). In the case of liquids, the mentioned term ($\rho_c \vec{u}$) is considered since the fluid used in this study is water.

Based on these assumptions, the reformulated expression for the electric current density is as follows:

$$\nabla.(\rho_c \mathbf{u} - \rho_c \beta \nabla V) = 0 \quad (26)$$

Hence, equations (22) and (26) serve as the main equations governing the electrohydrodynamic effect. To analyze the electrical body force, these equations need to be solved simultaneously. FLUENT, a widely used commercial software for simulating heat transfer and fluid flow, lacks a default module for analyzing electrohydrodynamic phenomena. In this study, a simulation of the steam ejector condenser (SEC) in FLUENT has been developed using its UDF (User-Defined Function), UDM (User-Defined Memory), and UDS (User-Defined Scalar) features. The electric current density and Poisson's equations (Equations (22) and (26)) are defined through the UDS to calculate ρ_c and V. Subsequently, the UDM is implemented to obtain E from Equation (23). Lastly, the UDF is employed to solve the source terms (ρ_cE in the momentum equation and $\vec{J}.\vec{E}$ in the energy equation). Detailed instructions on adding equations and their respective source terms in FLUENT can be found in our previous study [28].

3.2. Cyclone separator

Computational fluid dynamics (CFD) has emerged as a cost-effective method for simulating fluid flow, complementing experimental and theoretical approaches in the field of fluid dynamics. Its extensive utilization in the study of turbulent flows has made it an invaluable tool in understanding fluid behavior. CFD simulations offer several advantages, including the optimization of performance, the capability to simulate conditions that are difficult to reproduce experimentally, the acquisition of comprehensive information, improved visualization of flow phenomena, cost savings, and reduced environmental impact [30]. Numerical modeling is a vital component of CFD simulations, enabling the generation of precise and detailed results. As a prominent leader in Computational Fluid Dynamics (CFD), Fluent offers advanced capabilities for simulating and analyzing fluid flow phenomena, including multiphase flow involving the simultaneous flow of different phases such as liquid and gas. Fluent provides two distinct approaches for multiphase flow simulation: The Euler-Lagrange approach and the Euler-Euler approach. The Euler-Lagrange method focuses on modeling a dispersed phase within a continuous fluid phase by tracking a large number of particles, bubbles, or droplets throughout the flow field using the Navier-Stokes equations. This approach facilitates the exchange of momentum, mass, and energy between the two phases. However, it is important to note that the Euler-Lagrange method assumes a low volume fraction of the dispersed phase, typically below 10–12 %, despite its higher mass loading. In contrast, the Euler-Euler approach treats both phases as interpenetrating continua, with each phase occupying a distinct volume without overlapping. This approach introduces the concept of volume fraction as a continuous function that varies in space and time, always summing to one. Within Fluent, three Euler-Euler multiphase models are available: Volume of Fluid (VOF), mixture, and Eulerian. The VOF model is well-suited for simulating stratified or free-surface flows, while the mixture and Eulerian models are more appropriate when the volume fractions of the dispersed phase exceed 10 %. For simpler problems, the mixture model is often preferred over the Eulerian model due to its reduced computational requirements and

Table 1
Boundary conditions for SEC and cyclone separator.

Cyclone		SEC	
Boundary	Types	Boundary	Values
Inlet	Velocity inlet	Steam inlet pressure (kPa)	140
Outlets	Pressure Outlet	Steam inlet temperature (K)	382
Wall	No Slip wall	Water inlet pressure (kPa)	96
		Water inlet temperature (K)	290
		Ambient pressure (kPa)	96

fewer solved equations [31]. In this study, the mixture model is utilized, also referred to as the algebraic slip model, which is a simplified version of the Euler-Euler approach. This model is specifically suitable for simulating flows containing a significant volume fraction of dispersed phases, such as bubbles, droplets, or particles (>10 %), where inter-particle collisions are prominent. The mixture model allows for different velocities of fluid phases and permits their interpenetration, facilitating the exchange of mass, momentum, and energy between the phases. Moreover, the mixture model has been successfully employed in CFD simulations of turbulent swirl two-phase flow within gas–liquid cyclone separators.

However, the continuous and dispersed fluid phases are computed using the following techniques:

The Reynolds-averaged Navier-Stokes equations, along with the continuity and momentum equations, are employed to solve for the continuous phase.

$$\frac{\partial \rho}{\partial t}+\frac{\partial(\rho u_i)}{\partial X_i}=0 \tag{27}$$

$$\frac{\partial(\rho u_i)}{\partial t}+\frac{\partial(\rho u_i u_j)}{\partial X_j}=\frac{\partial P}{\partial X_i}+\frac{\partial}{\partial X_i}\left(\mu\frac{\partial^2 u_i}{\partial X_j^2}+\frac{\partial^2 u_j}{\partial X_i^2}-\frac{2}{3}\delta_{ij}\frac{\partial u_k}{\partial X_k}+\frac{\partial}{\partial X_j}\right)(-\rho\overline{u_I u_J}) \tag{28}$$

$$(-\rho\overline{u_I u_J})=\mu_t\left(\frac{\partial^2 u_i}{\partial X_j^2}+\frac{\partial^2 u_j}{\partial X_i^2}\right)-\frac{2}{3}\left(\rho k+\mu_t\frac{\partial u_k}{\partial X_k}\right)\delta_{ij} \tag{29}$$

The equation governing the continuity of the mixture can be expressed as:

$$\frac{\partial(\rho_m)}{\partial t}+\frac{\partial(\rho_m u_m)}{\partial x_i}=0 \tag{30}$$

Mixture momentum:

$$\frac{\partial(\rho_m u_{mi})}{\partial t}+\frac{\partial(\rho_m u_{mi} u_{mj})}{\partial x_i}=\frac{\partial P}{\partial x_i}+\frac{\partial}{\partial x_j}\mu_m\left(\frac{\partial u_{mi}}{\partial x_j}+\frac{\partial u_{mj}}{\partial x_j}\right)+\rho g_i+\frac{\partial}{\partial x_i}\left(\sum_{q=1}^{n}\alpha_q\rho_q u_{dr,qi}u_{dr,qj}\right) \tag{31}$$

Where u_m represents the mass-averaged velocity, ρ_m denotes the density of the mixture, and μ_m corresponds to the viscosity of the mixture.

$$U_m=\frac{\sum_{q=1}^{n}\alpha_q\rho_q u_q}{\rho_m},\ \rho_m=\sum_{q=1}^{n}\alpha_q\rho_q,\ \mu_m=\sum_{q=1}^{n}\alpha_q\mu_q \tag{32}$$

Where $u_{dr,q}$ denotes the drift velocity for the secondary phase, which is calculated as: $u_{dr,q}=u_q-u_m$ (the difference between the velocity of the secondary phase (u_q) and the mass-averaged velocity of the mixture

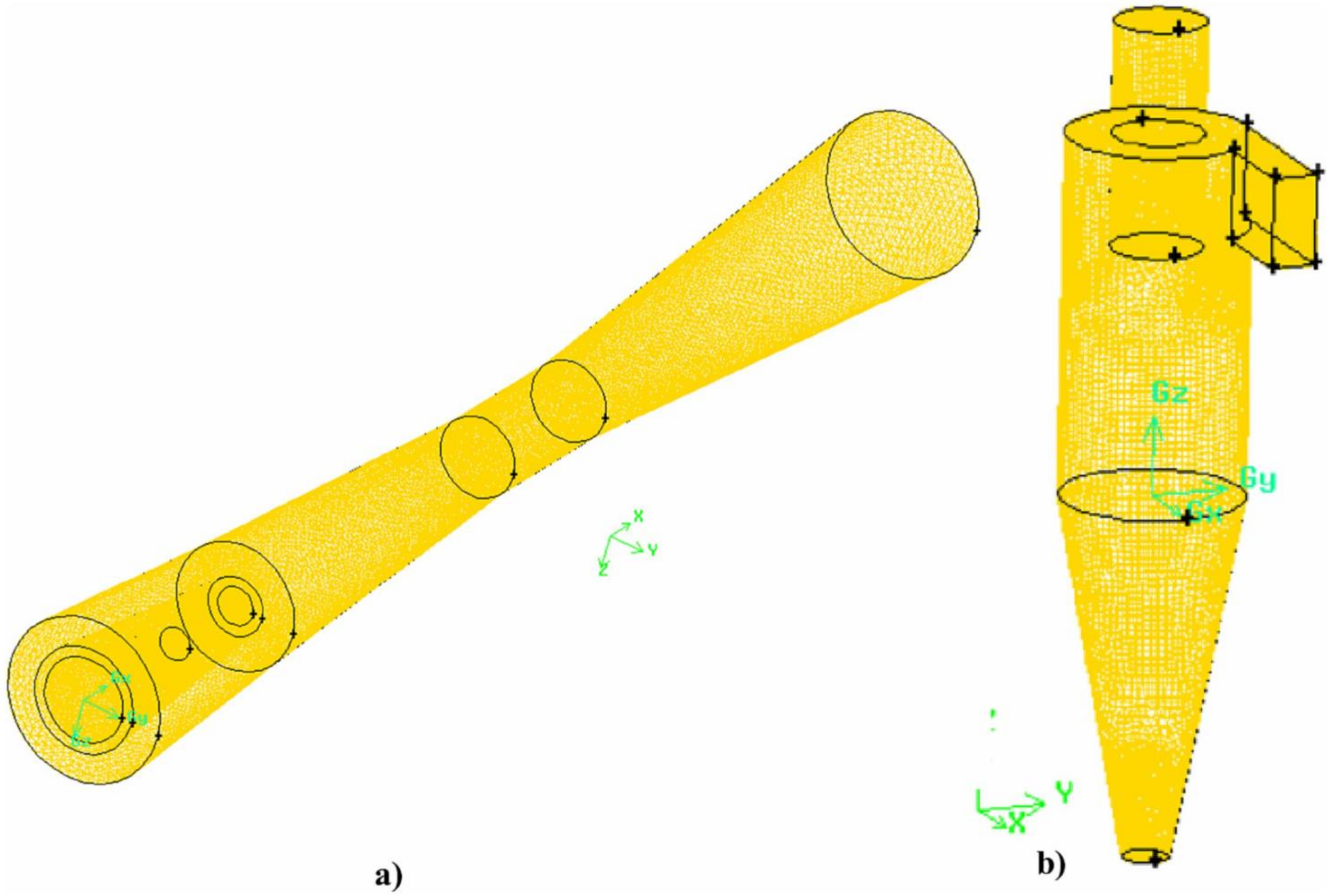

Fig. 4. Meshing of (a) Steam Ejector Condenser and (b) cyclone separator.

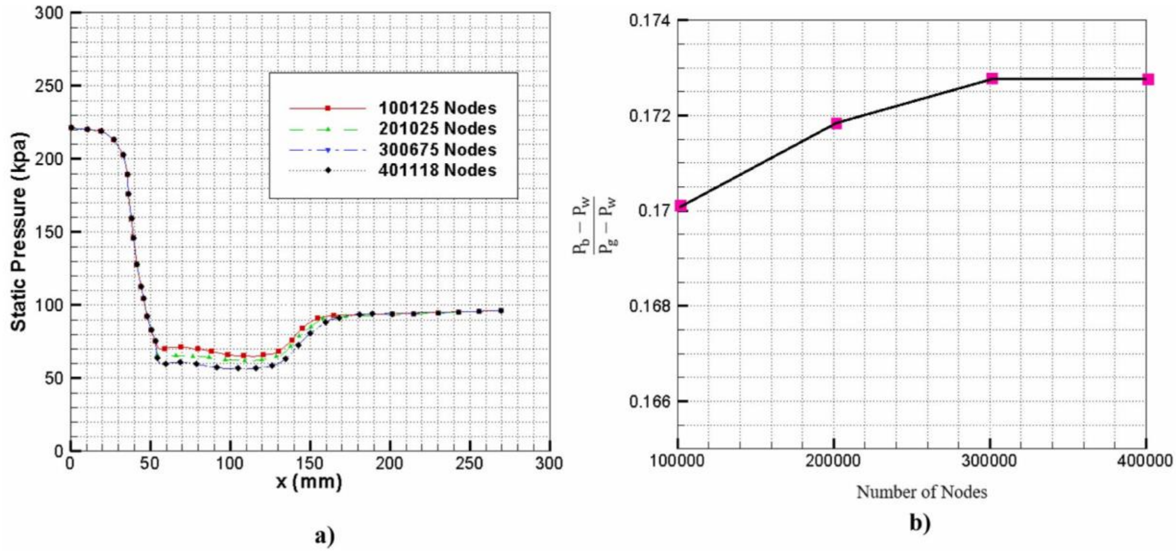

Fig. 5. Grid independency of SEC, (a) static pressure and (b) pressure ratio.

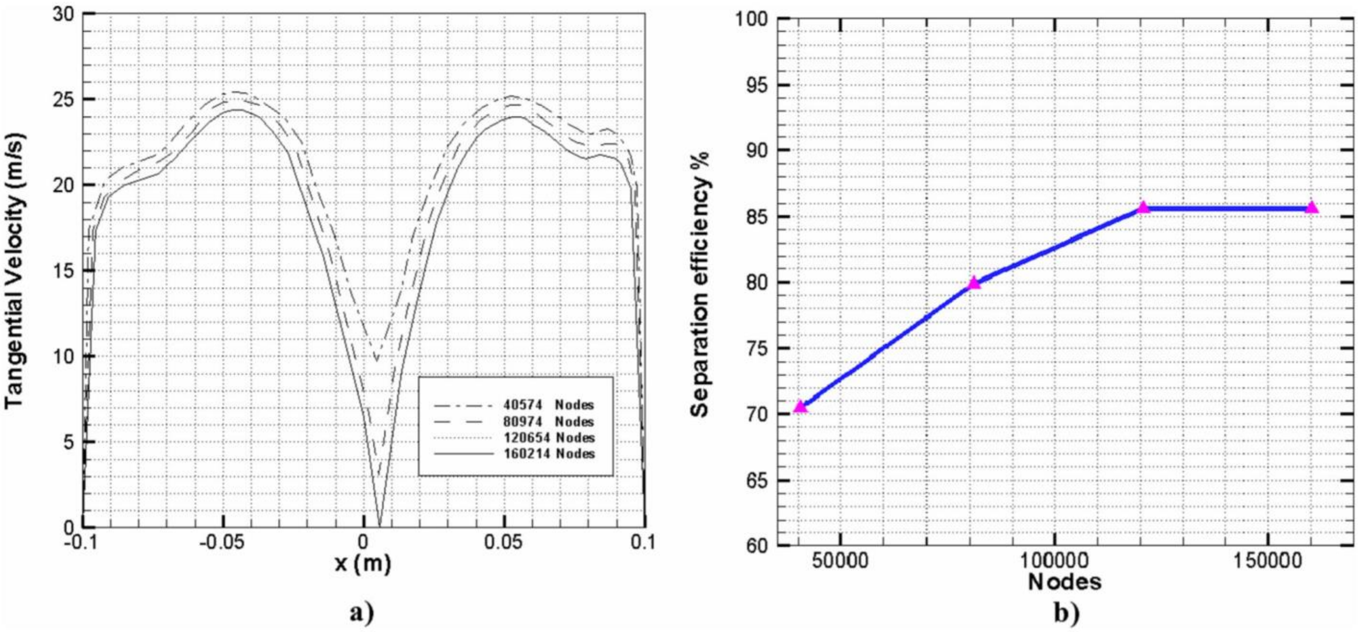

Fig. 6. Grid independency for (a) Tangential velocity and (b) separation efficiency of single inlet cyclone at 2.8 ($\frac{kg}{s}$) when volume fraction of water is 10%.

(u_m)).

Extensive research has been conducted by numerous scholars to investigate the separation performance of cyclone separators using various approaches, consist of experimental studies, numerical simulation and theoretical analysis. Currently, three primary methods are employed to study the flow field within cyclone separators numerically: The Reynolds Stress Model (RSM) [32], the RNG k-ε numerical model [33], and the Algebraic Stress Model (ASM) [34]. Among these, the k-ε model assumes isotropic turbulence, which limits its applicability to cyclone flow characterized by anisotropic turbulence. The ASM model exhibits shortcomings in predicting the recirculation zone and Rankine vortex in strongly swirling flow. On the other hand, the RSM model, which solves a transport equation for each component of Reynolds stress, is widely regarded as the most suitable model for cyclone flow [35]. It accounts for important factors such as streamline curvature, swirling, rotation, and rapid strain rate changes, allowing it to capture the anisotropic turbulence characteristics of cyclone separators. This makes the RSM model better suited for modeling complex swirling and rotational flows, enabling more accurate predictions of complex flow phenomena in cyclones, albeit at the cost of increased computational resources.

The transport equation for Reynolds Stress Model (RSM) can be expressed as follows.

$$\frac{\partial}{\partial t}\left(\rho\overline{u_i'u_j'}\right)+\frac{\partial}{\partial x_k}\left(\rho u_k\overline{u_i'u_j'}\right)=D_{ij}+P_{ij}+\Pi_{ij}+\varepsilon_{ij}+S \tag{33}$$

where the first two terms on the left side illustrate the local time derivative of stress and the convective transport term, respectively. The five terms on the right side can be described as follows:

$$\text{The stress diffusion term}: \; D_{ij} = -\frac{\partial}{\partial x_k}\left[\rho\overline{u_i'u_j'u_k'}+\overline{(P'u_j')}\delta_{ik}+\overline{(P'u_i')}\delta_{jk}-\mu\left(\frac{\partial}{\partial x_k}\overline{u_i'u_j'}\right)\right] \tag{34}$$

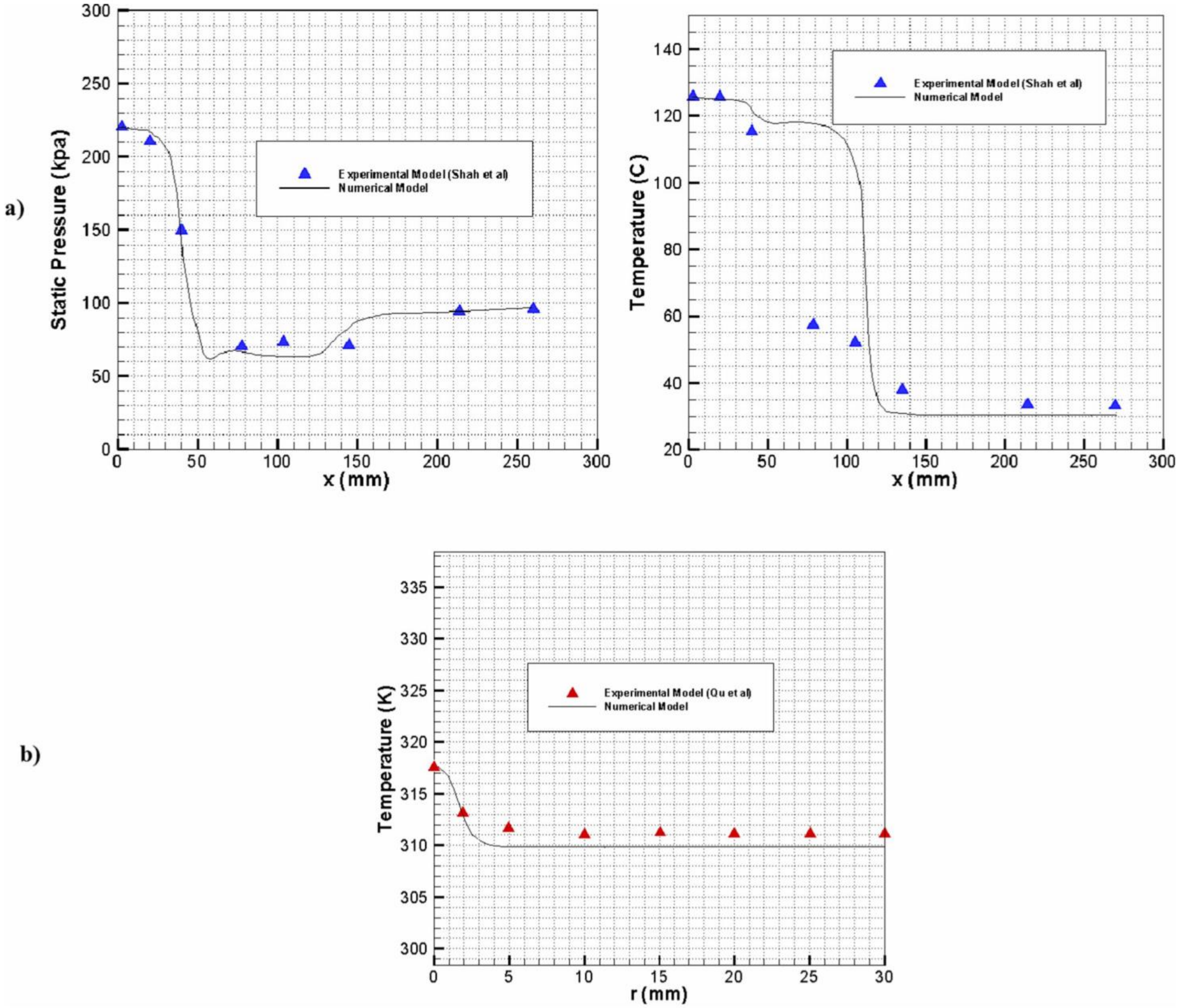

Fig. 7. Validation of SEC a) without non-condensable gas at mass flow rate of steam: 0.01 kg/s, temperature of steam: 398 K, mass flow rate of water: 0.49 kg/s, temperature of water:290 K, Pout = 96 kPa. b) With condensable gas at total mass flux: 235.5 ($\frac{kg}{m^2.s}$) and Steam mass fraction: 91.58 % at y = 18 mm.

$$\text{The shear production term}: \; P_{ij} = -\rho\left[\overline{u_i^{'}u_k^{'}}\frac{\partial u_j}{\partial x_k} + \overline{u_j^{'}u_k^{'}}\frac{\partial u_i}{\partial x_k}\right] \tag{35}$$

$$\text{The pressure} - \text{strain term}: \; \Pi_{ij} = p\overline{\left(\frac{\partial u_i^{'}}{\partial x_j} + \frac{\partial u_j^{'}}{\partial x_i}\right)} \tag{36}$$

$$\text{The dissipation term}: \; \varepsilon_{ij} = -2\mu\overline{\frac{\partial u_i^{'}}{\partial x_k}\frac{\partial u_j^{'}}{\partial x_k}} \tag{37}$$

$$\text{and the source term}: \; S \tag{38}$$

4. Numerical simulation and boundary conditions

4.1. Steam ejector condenser (SEC)

In this study, the steam-water ejector condenser with non-condensable gas (CO2) is numerically simulated using the FLUENT 2021 R1. The steam and water inlets are assigned a mass flow rate inlet boundary condition. Since most devices that generate steam do not have a superheater, the steam at the nozzle inlet is assumed to be in a saturated state under stagnation conditions. The ejector exit is treated as an opening boundary with a pressure equal to the back pressure. The wall of the ejector is assumed to have no-slip adiabatic conditions, and a scalable wall function is employed to simulate the flow in the boundary layer grids. CO2 is chosen as the non-condensable gas component. The Schiller-Naumann drag force model [36] and Lopez de Bertodano turbulent dispersion model [37] are used to account for the interphase momentum transfer, with the turbulent dispersion coefficient set to 0.3.

4.2. Cyclone separator

The multiphase mixture model in Fluent 2021 R1 was employed to accurately simulate the CO2-water flow in the cyclone separator. This model was chosen to account for the strong interaction between the CO2 and water phases in the swirling environment of the separator. The coupling between pressure and velocity was established using the SIMPLE (Semi-Implicit Method for Pressure Linked Equations) algorithm. To accurately estimate high-speed swirling flows and flows in curved domains, the PRESTO (PREssure STaggering Option) scheme was

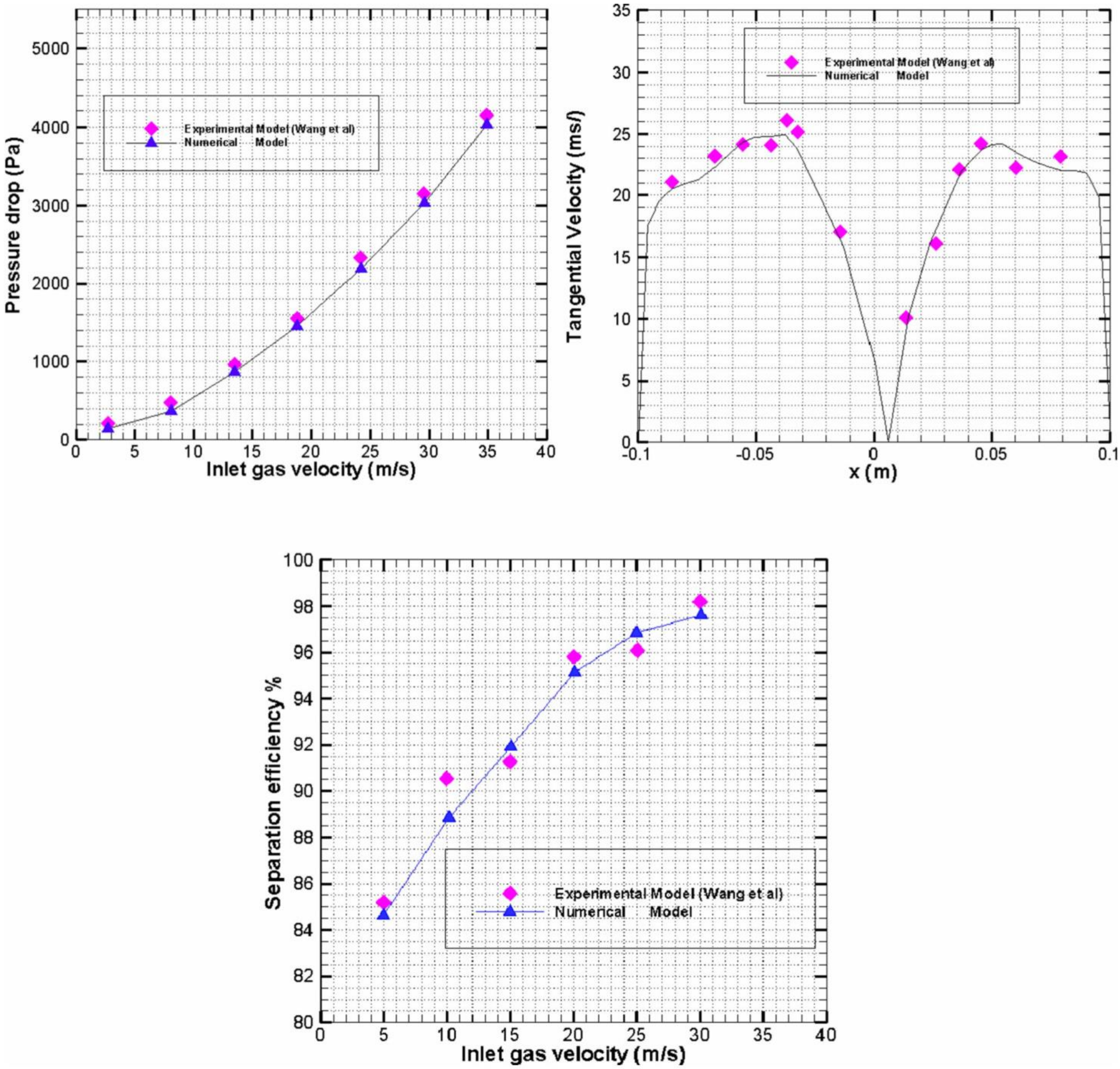

Fig. 8. Pressure drop, tangential velocity and separation efficiency comparison of experimental model (Wang et al) and current simulation.

implemented. Discretization of the volume fraction, kinetic energy and momentum equations was performed using the QUICK (Quadratic Upstream Interpolation for Convective Kinematics) method, which offers improved accuracy for rotational swirling flows compared to first- and second-order schemes. It is important to avoid using first-order discretization, as it can lead to higher errors and unreliable results [38]. The simulation employed a transient time-based approach, and during the iterative process, a convergence criterion was established with an accuracy level of 10^{-6}. To optimize the balance between simulation precision and computational costs, a time step size of 0.0001 s was selected. The boundary conditions for both the SEC and the cyclone separator are provided in Table 1.

5. Evaluation of numerical model

5.1. Grid independence

The geometry and mesh of the steam ejector condenser (SEC) and cyclone separator were created using Gambit 2.4.6, as depicted in Fig. 4. In order to ensure accuracy in the calculations, all edges of the model were meshed, followed by meshing the faces and volumes. Tet/Hybrid elements and the TGrid type were employed for meshing, which provided suitable cells for the computational fluid dynamics (CFD) simulations. A high-quality mesh was crucial to prevent errors resulting from numerical diffusion. Therefore, the mesh independence of the solutions for the SEC and cyclone separator was verified by conducting simulations with different grid configurations.

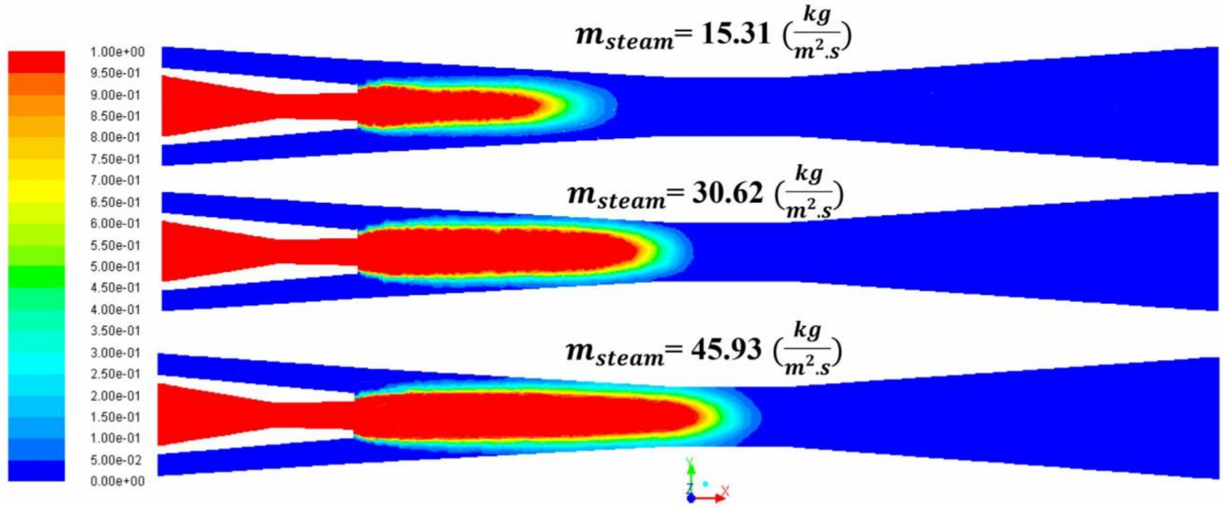

Fig. 9. Contours of steam volume fractions at different steam inlet mass flow rates.

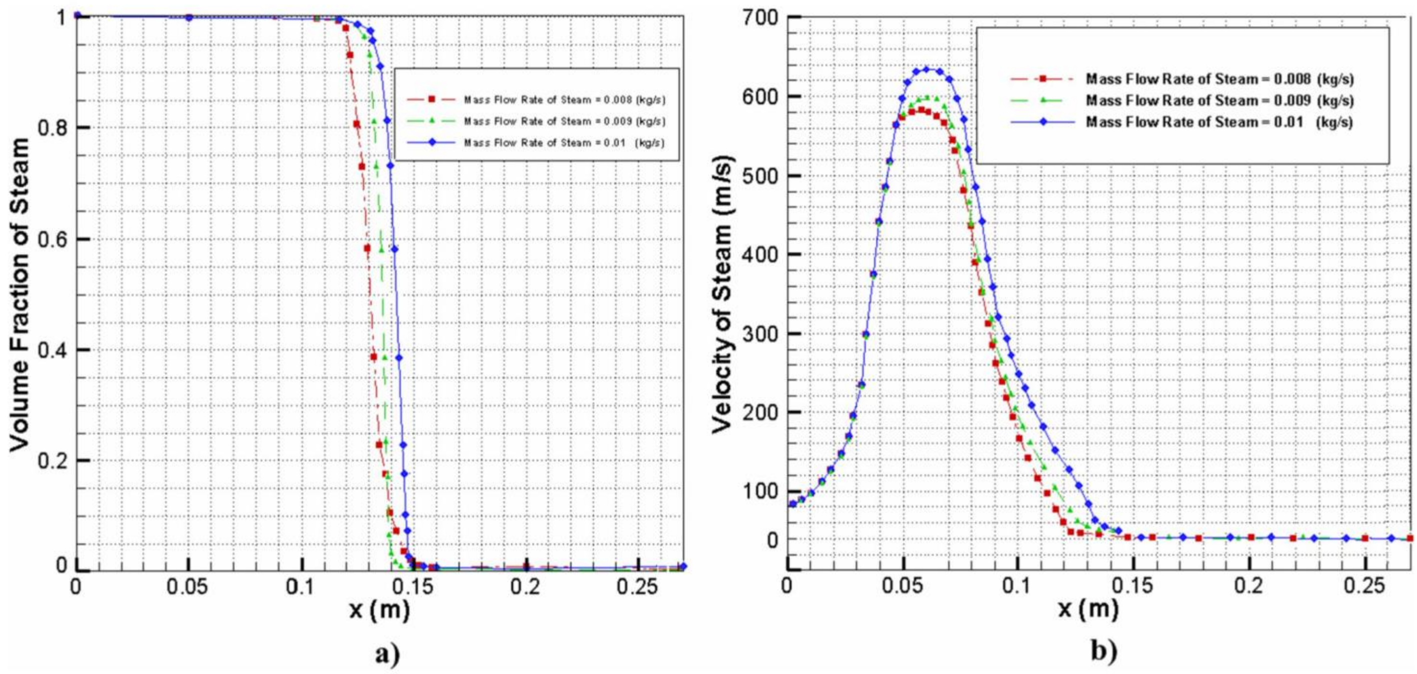

Fig. 10. A) steam volume fractions and b) steam velocities at different steam inlet mass flow rates ($\dot{m}_{steam}$) and..$T_{steam} = 398(K), \dot{m}_{water} = 490(\frac{g}{s}), T_{water} = 290(K)$, $P_{out} = 96(kpa)$

5.1.1. Steam ejector condenser

To evaluate the mesh independence and its impact on the results of the SEC, an analysis was performed on the static pressure distribution along the central line of the SEC and the pressure ratio at different nodes (see Fig. 5). The analysis revealed significant differences between the outcomes obtained from the 100,125 and 201,025 node configurations compared to those from the 300,675 and 401,118 node configurations. Furthermore, the results from the 300,675 and 401,118 node configurations exhibited a high level of agreement with each other. Therefore, considering computational efficiency and accuracy, the configuration with 300,675 nodes was selected as the optimal choice. This selection ensures enhanced computational efficiency without compromising the accuracy of the simulations.

5.1.2. Cyclone separator

To investigate the grid size independence in the cyclone separator, the tangential velocity and separation efficiency were analyzed using different node configurations, as depicted in Fig. 6. The results indicate that the outcomes obtained from the 40,574 and 80,974 node grids differ from the other configurations (120654 and 160214). Although the results from the 120,654 and 160,214 node grids are relatively similar, the 120,654 nodes were chosen to reduce computational expenses while maintaining accuracy.

5.2. Model validation

5.2.1. Steam ejector condenser

To validate the accuracy of the model, a comparison was made between the simulation results obtained with and without the presence of the non-condensable gas. Firstly, the numerical results without the non-condensable gas were compared with the experimental data from Shah [24], who conducted experimental studies on the transport phenomena of direct contact condensation (DCC). Shah's experiments involved different geometries, which were designed, fabricated, and assembled

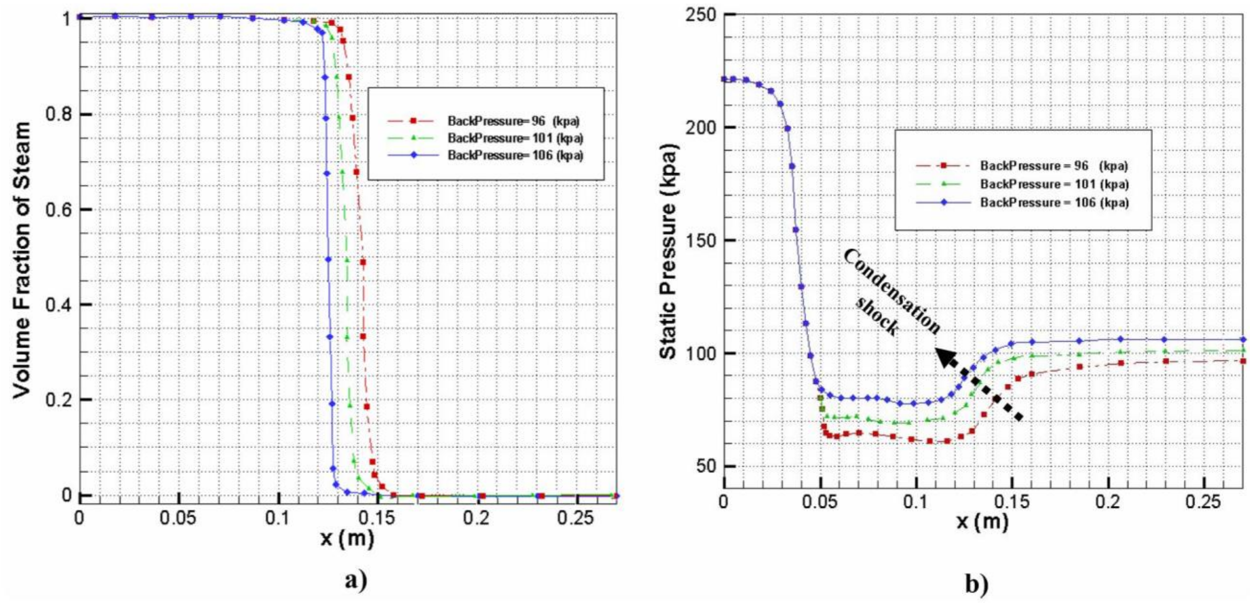

Fig. 11. A) volume fraction of steam and b) static pressure at different backpressures when.$\dot{m}_{steam} = 10(\frac{g}{s}), T_{steam} = 398(K), \dot{m}_{water} = 490(\frac{g}{s}), T_{water} = 290(K)$,

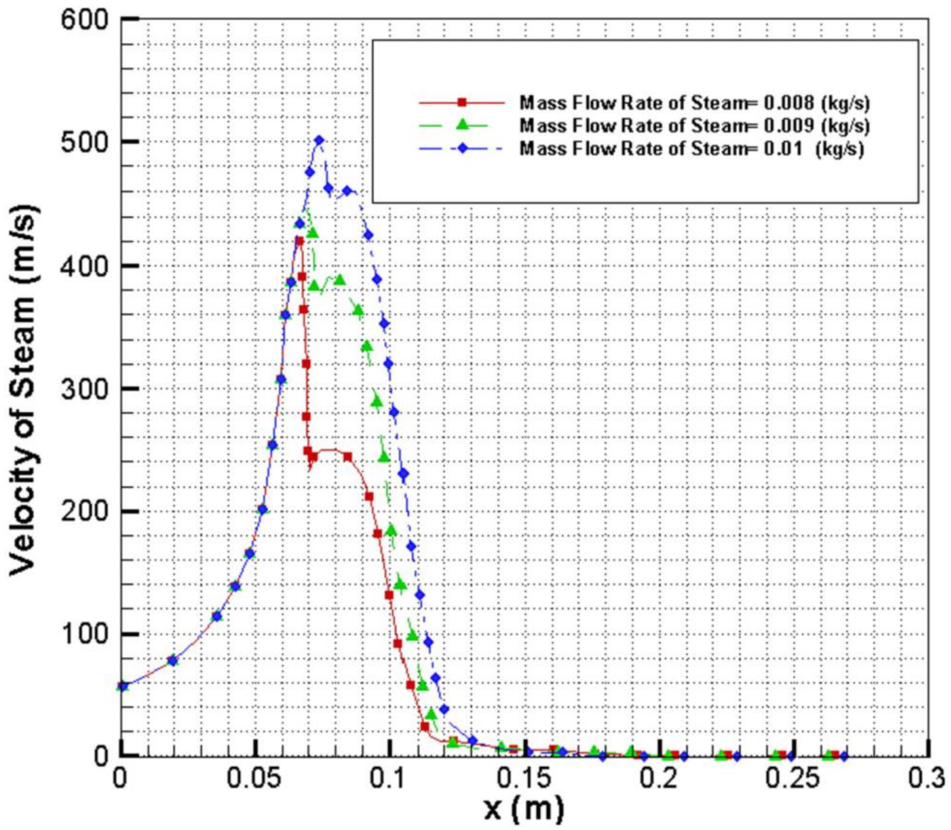

Fig. 12. Distributions of steam velocity along axis of SEC at different steam mass flow rate and 0.03 of CO_2 mass fraction.

ıto an experimental setup. The operating conditions for the experiıents included a mass flow rate of steam: 0.01 $\frac{kg}{s}$, temperature of steam: 98 K, mass flow rate of water: 0.49 $\frac{kg}{s}$, temperature of water:290 K and utlet pressure: 96 kPa. The comparison of axial static pressures and emperatures, as shown in Fig. 7a, demonstrates a satisfactory agreeıent between the numerical and experimental analyses.

Subsequently, a numerical simulation was performed to validate the eliability of the steam jet condensation model with non-condensable as using a submerged steam-non-condensable gas mixture jet in subcooled water [39]. Fig. 7b presents the experimental measurement of the axial steam temperature, which exhibits a close agreement with the distribution obtained from the numerical model. The successful comparison between the experimental and numerical results provides additional validation for the accuracy and reliability of the steam jet condensation model with non-condensable gas.

5.2.2. Cyclone separator

The predicted variations of pressure drop, tangential velocity, and separation efficiency were compared to the experimental results of

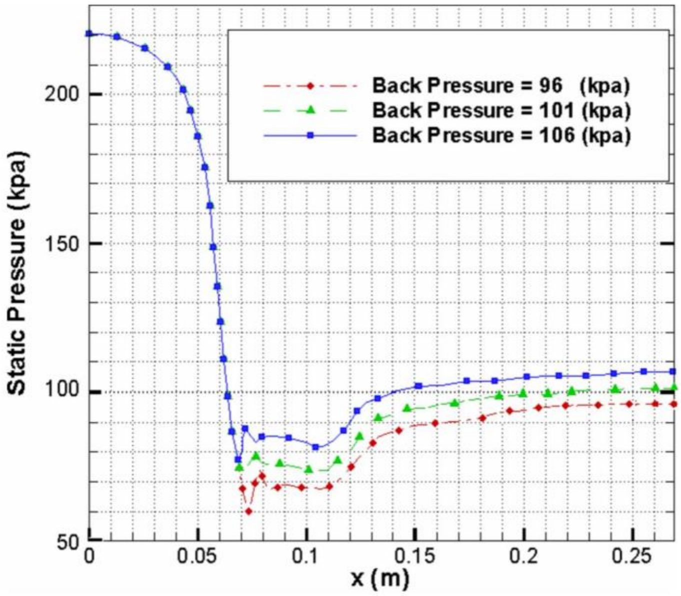

Fig. 13. Distributions of static pressure along axis of SEC at different back pressure and 0.03 of CO_2 mass fraction.

Wang et al. [40], as shown in Fig. 8. In their experimental setup, non-condensable gas was introduced into the cyclone inlet, and its flow rate was measured using a flowmeter. The velocities of both phases were set to 20 m/s. The outlet tube was open to the atmosphere, and the gas pressure at the top of the vortex finder was maintained at 1 atm. The volume fraction of the second phase was 10 %. Velocity and pressure measurements in the gas field were conducted using a five-hole probe equipped with pressure transducers. The amplified voltage signals from the pressure transducers were collected by a data acquisition system. The comparison between the experimental and numerical results, as depicted in Fig. 8, demonstrates a good agreement between the two, corroborating the accuracy of the numerical model based on the studies by Wang et al.

6. Results and discussion

6.1. Effect of inlet mass flow rate of steam on its volume fraction

In previous visualization research, the steam plume has been identified as a crucial element for understanding the heat, mass, and momentum transfer between steam and water. It exhibits diverse forms contingent upon the specific parameters of the inlet steam. When steam is injected into subcooled water, it generates a closed steam cavity, known as a steam plume, at the nozzle outlet. However, it is important to note that the behaviour of the steam plume is highly influenced by the mass flux of the steam at the inlet, particularly when it attains sonic or supersonic speeds. The steam plume continuously receives a supply of steam from the nozzle, which subsequently undergoes condensation as it interacts with the entrained water at the interface. The evaluation of the steam plume can be accomplished through a comprehensive analysis of the contours representing the steam volume fraction. Various parameters can be derived from these contours, with the maximum penetration length being of particular significance. This length predominantly reflects the variations in the volume of the steam plume. By closely examining the contours of the steam volume fraction and taking into account the maximum penetration length, valuable insights can be gained regarding the behaviour and characteristics of the steam plume under different inlet mass flow rates. In order to investigate the steam plume in different regions (mixing chamber and throat), contours of steam volume fractions at different steam inlet mass flow rates have been represented in Fig. 9.

As observed, the ellipsoidal shape of the steam plume is directly related to the inlet steam mass flow rate. For a steam inlet mass flow rate of 15.31 $(\frac{kg}{m^2.s})$, the maximum penetration occurs within the mixing chamber. However, as the steam inlet mass flow rate increases to 30.62 $(\frac{kg}{m^2.s})$ and 45.93 $(\frac{kg}{m^2.s})$ grams per second, the maximum penetration shifts to the throat of the SEC.

In our present investigation (Fig. 1.), the range of steam inlet mass flow rate for the SEC is 8–10 (g/s). Fig. 10a presents the detailed variation of axial steam volume fraction along the SEC. Initially, as the steam passes through the nozzle with isentropic expansion, there is some spontaneous condensation, although it can be considered as an approximate single-phase flow where the steam volume fraction remains nearly unchanged VFS (volume fraction of steam) = 1. As the high-velocity steam entrains and condenses onto the liquid water in the mixing chamber, the axial steam volume fraction continues to stay at VFS = 1 in the steam plume region. Subsequently, it experiences a sharp decrease at the two-phase mixing layer and eventually reaches VFS = 0 at the condensation terminus. Finally, the axial steam volume fraction at VFS = 0 indicates a single-phase liquid flow through the diffuser. Notably, the condensation terminus shifts downstream with an increase in the steam inlet mass flow rate. So, when the steam inlet mass flow rate is low, the condensation of steam occurs at a faster rate compared to higher steam inlet mass flow rates. However, as the steam inlet mass flow rate increases, the additional steam supplied exceeds the capacity of the water for condensation. To accommodate this increased steam volume, the steam plume expands its boundary, which enhances the condensation rate in the liquid phase. Consequently, with an increase in the steam inlet mass flow rate, the steam plume travels a longer distance.

Fig. 10b illustrates the centerline steam velocity along SEC at various steam inlet mass flow rates. For a steam inlet mass flow rate of 10 $(\frac{g}{s})$ the steam velocity at the nozzle outlet exceeds 600 m/s. This high velocity generates lower pressure, leading to a more powerful suction effect. As the steam inlet mass flow rate increases, the maximum steam velocity achieved at the nozzle outlet also rises.

6.2. The influence of backpressure on steam volume fraction and the position of condensation shock

The backpressure has a significant impact on the steam ejector condensation process and the volume fraction of steam along the central line of the steam ejector condenser (Fig. 11a). When the backpressure is increased, it creates a higher resistance for the condensing steam, resulting in a decrease in the condensation rate. This leads to a reduced volume fraction of steam along the central line of the condenser. On the other hand, when the backpressure is decreased, it reduces the resistance for steam condensation, resulting in an increased condensation rate and a higher volume fraction of steam along the central line. Therefore, controlling the backpressure is crucial for regulating the condensation efficiency and the distribution of steam volume within the steam ejector condenser.

The observation is evident in Fig. 11b when the backpressure is increased from 96 *kpa* to 106 *kpa*, it leads to a higher resistance for the condensing steam, causing the condensation shock to move upstream. This shift in the condensation shock position alters the distribution of static pressure within the condenser. Specifically, the static pressure increases in the region where condensation occurs due to the increased resistance. On the other hand, decreasing the backpressure reduces the resistance for steam condensation, resulting in a downstream shift of the condensation shock. Consequently, the distribution of static pressure within the condenser changes, with a decrease in the pressure at the condensation region.

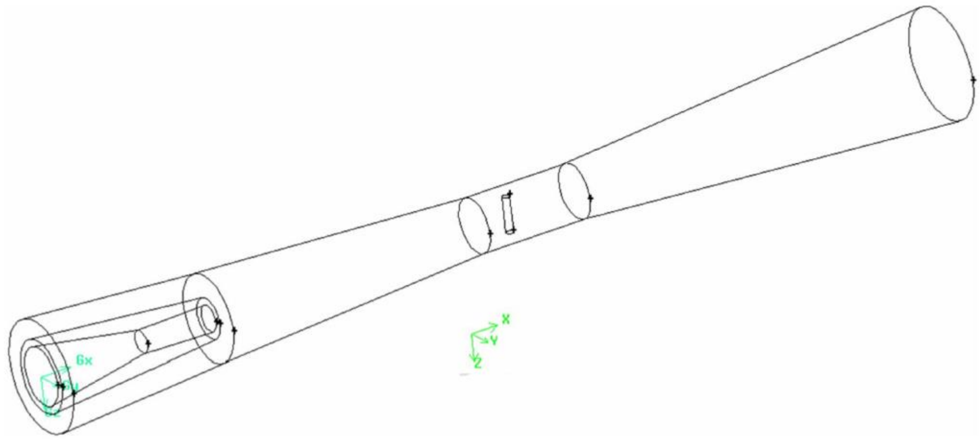

Fig. 14. Applied electrode in SEC.

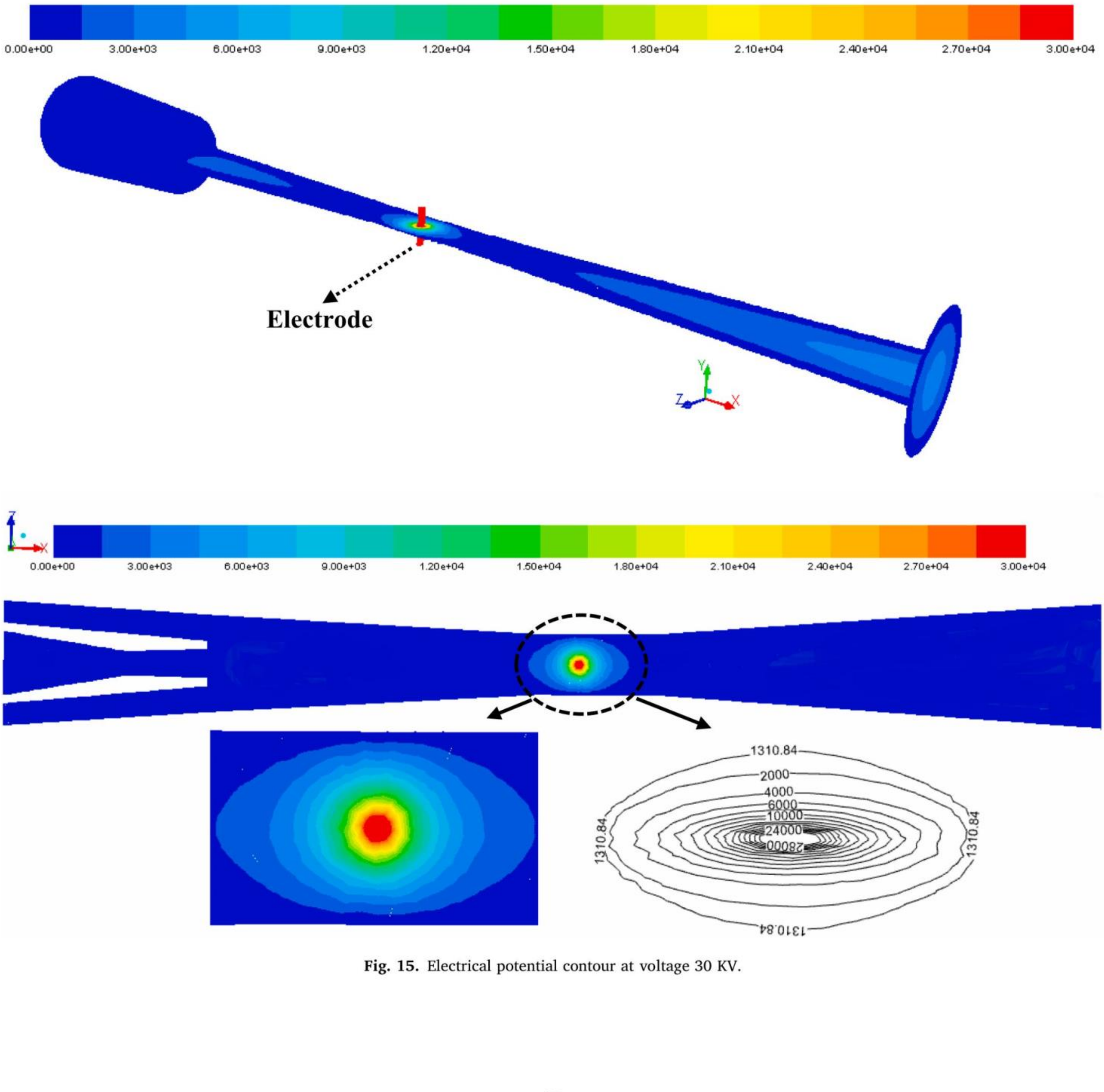

Fig. 15. Electrical potential contour at voltage 30 KV.

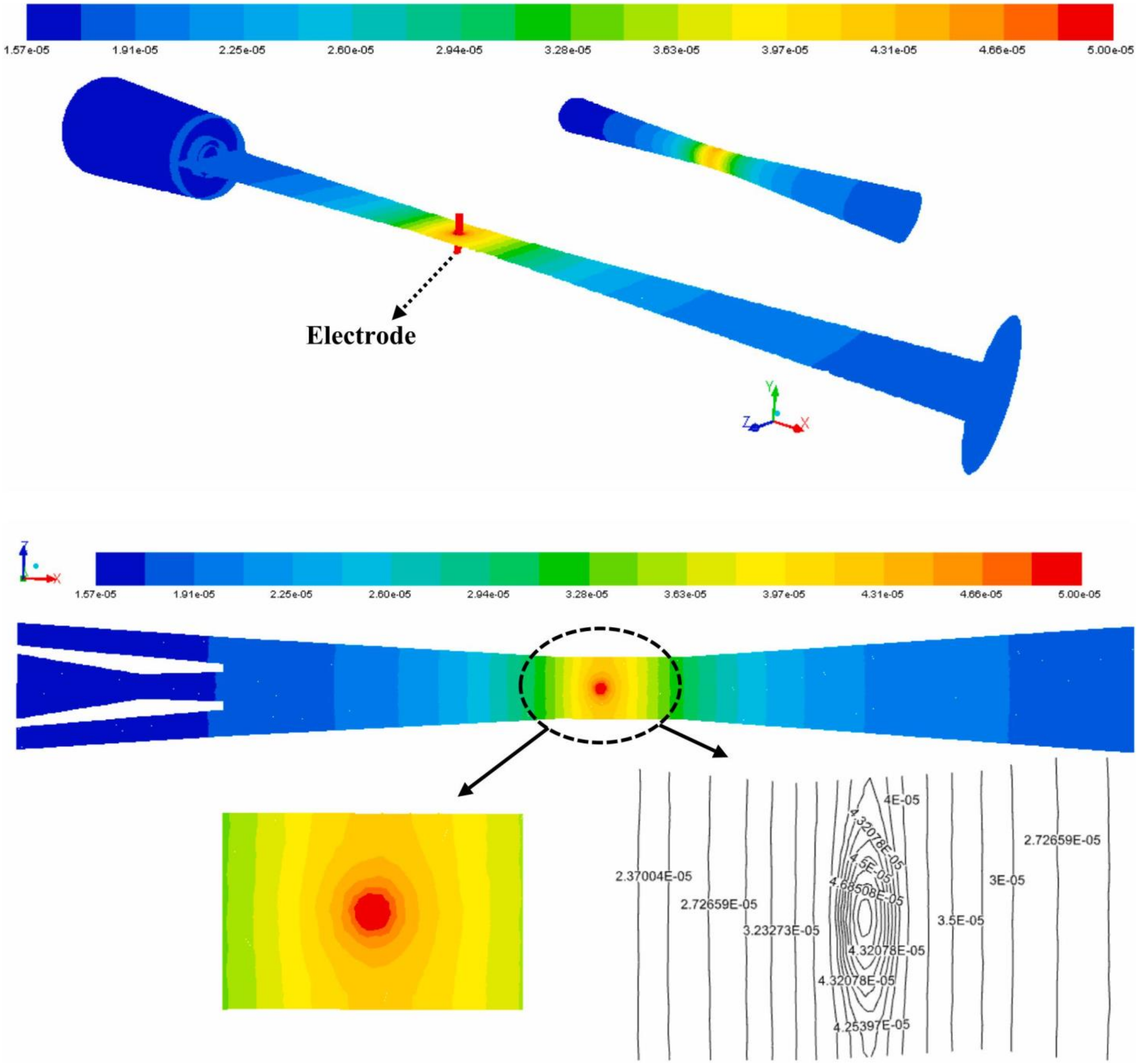

Fig. 16. Electric charge contour at voltage 30 KV.

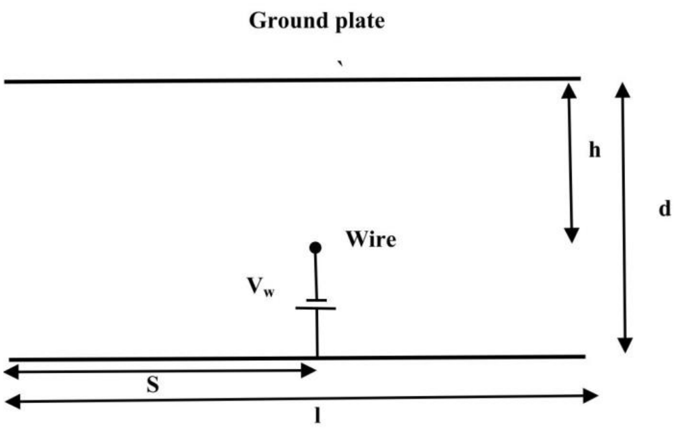

Fig. 17. Schematics of a single unit wire-plate [44].

6.3. Effect of Non-Condensable gas (CO_2) on hydraulic- thermal parameters

6.3.1. Hydraulic parameters

In general, a small amount of non-condensable gas is often mixed with the steam jet or subcooled water. When there is a minor leakage in pipeline systems or when non-condensable gas is dissolved in subcooled water, the presence of non-condensable gas is usually so minimal that it has little impact on the flow dynamics within the SEC equipment. However, in certain industrial situations, like the aforementioned PFD illustrated in Fig. 1, where a substantial quantity of non-condensable gas is produced, its influence on flow and heat transfer becomes significant and cannot be overlooked.

Evaluating the performance of a SEC requires assessing the distribution of hydraulic parameters within the ejector. Numerical simulation enables us to obtain comprehensive information about the flow fields. Figs. 12 and 13 illustrate the variations in steam velocity and static

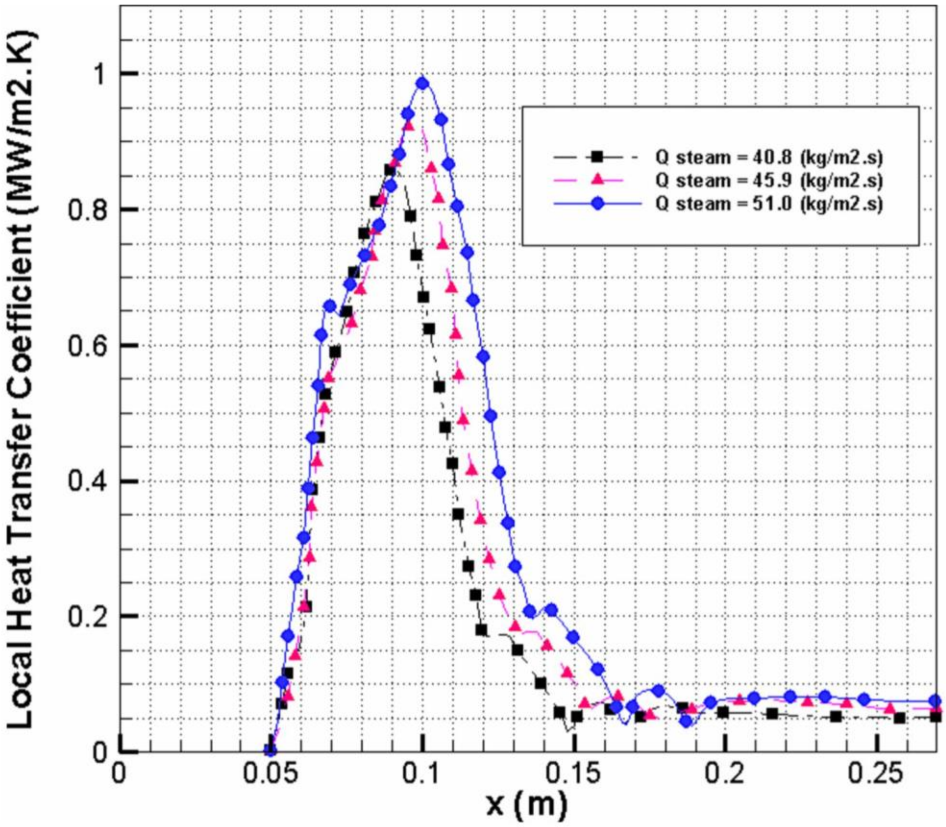

Fig. 18. Effect of steam inlet mass flux (Q) on local heat transfer coefficient at 0.03 of CO_2 mass fraction.

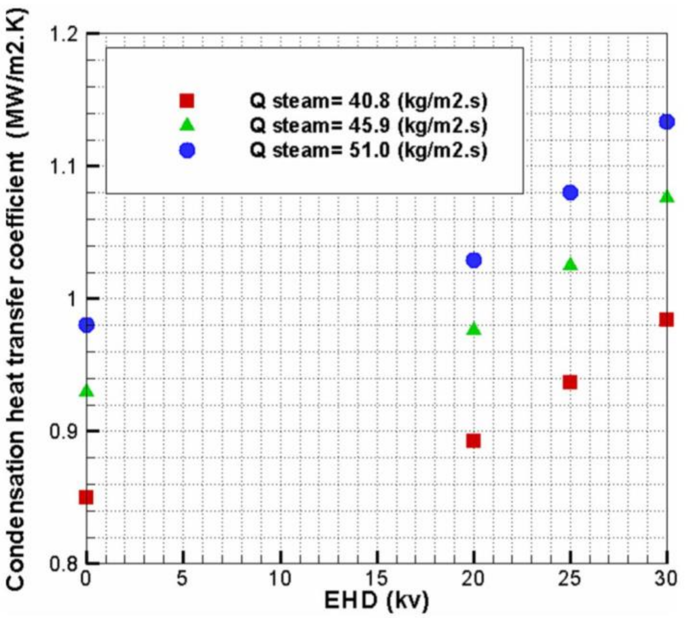

Fig. 19. Effect of EHD and steam inlet mass flux (Q) on condensation heat transfer coefficient at 0.03 of CO_2 mass fraction.

ressure at different steam inlet mass flow rates and back pressure. As ie steam mass flow rate increases, the steam velocity rises while the ressure drops. This implies that the expansion and compression waves i the mixing chamber intensify progressively with higher steam inlet iass flow rates. With the increase of back pressure (Fig. 13), the steam ressure and density in mixing chamber tends to become higher, which educes the intensity of the expansion and compression waves.

6.3.2. *Thermal parameters*

Experimental and numerical studies [7,8,39] have demonstrated the significant influence of non-condensable gas on the expansion of the steam plume and interphase heat transfer. Remarkably, even a small amount (1 %) of non-condensable gas can reduce the heat transfer coefficient by 10–40 %. Under specific conditions, an optimal quantity of non-condensable gas can stabilize the steam plume, leading to diminished pressure oscillations in both the condensation oscillation regime and stable condensation regime [41]. Conversely, an inappropriate gas content can exacerbate pressure oscillations [42]. When non-condensable gas is introduced into the steam-water condensing ejector, the presence of constricted channels complicates the alteration of the steam plume shape and pressure oscillation, consequently impacting the ejector's performance. The steam-water mixing layer exhibits high-speed flow and vigorous turbulence, promoting rapid steam condensation and effective momentum transfer between the two phases. However, the introduction of non-condensable component hampers the convection–diffusion effect between steam and water. Non-condensable gas forms a layer near the phase interface, impeding the diffusion of steam into subcooled water and reducing convective heat transfer between the phases.

Heat transfer enhancement in steam ejector condensers brings several benefits to improve their overall performance. By enhancing the heat transfer coefficient, condensers achieve greater heat transfer rates, leading to cost savings in terms of required heat transfer area. This enhancement also improves efficiency, reduces fouling, and lowers backpressure, resulting in lower operating costs and a reduced environmental impact. The enhancement of heat transfer in steam ejector condensers is achieved through the manipulation and reduction of the condensate film on the heat transfer surface. The application of electrohydrodynamic (EHD) techniques for heat transfer enhancement during condensation strongly relies on the pre-existing flow pattern. Specifically, in tube geometries, the EHD heat transfer enhancement is most pronounced when the flow pattern exhibits stratification or

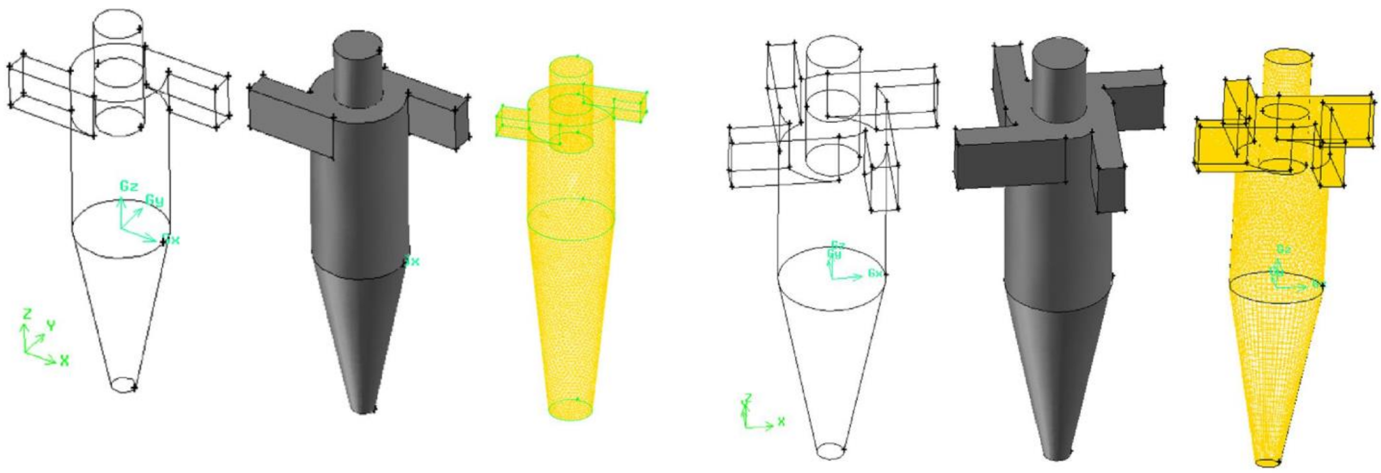

Fig. 20. Geometry and mesh of dual and quadruple inlets cyclones.

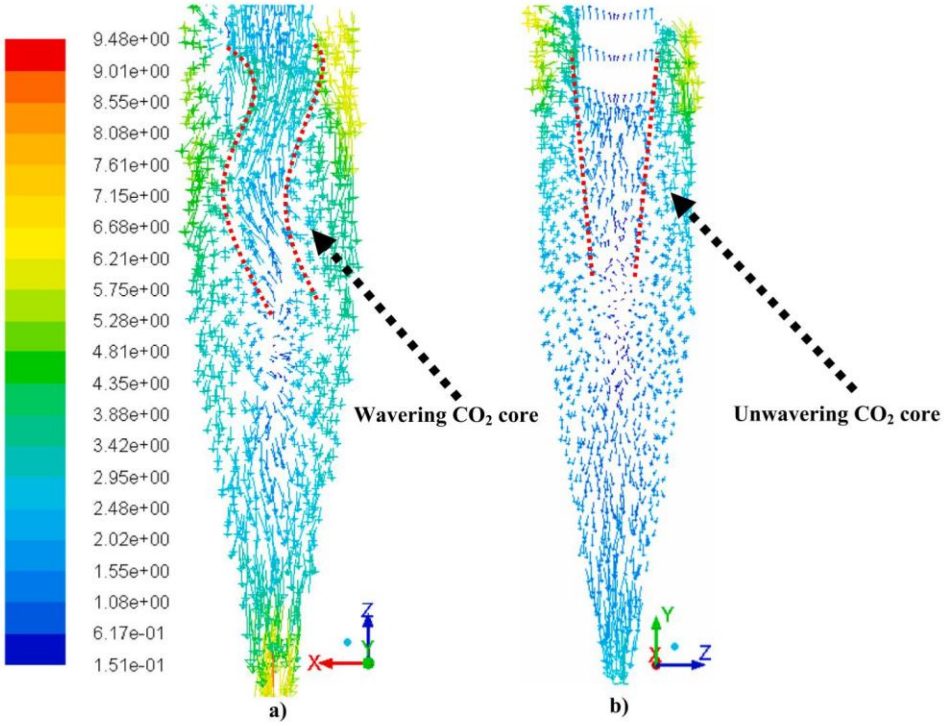

Fig. 21. Velocity vectors of mixture of CO_2 and water liquid, a) single inlet; b) quadruple inlets.

stratified-wavy characteristics, with gravity playing a dominant role in establishing this flow pattern [43]. In the stratified flow regime, characterized by lower vapor velocities, the condensate film becomes thicker, providing greater opportunities for EHD body forces to thin the film and enhance convection within the layer. The primary mechanisms responsible for heat transfer enhancement through EHD techniques involve the extraction of condensate from the heat transfer surface by liquid extraction and the dispersion of this liquid through electric body ›rces. Higher applied voltages lead to increased electric body forces, ffectively extracting more condensate from the surface, thereby nhancing heat transfer. Specifically, the liquid phase of the SEC, pos-essing a high dielectric permittivity, is drawn away from the inner urface of the tube toward the electrode surface. The findings indicate ıat a stronger electrical field yields improved performance of the heat ransfer system. The dominant electric body force density acting on the ondensate arises from the permittivity gradient, represented by the econd term in Eq. (21). This force attracts condensate, which has a igher permittivity than the surrounding vapor phase. Determining the most suitable electrode placement hinges on various considerations tied to the fluid dynamics and heat transfer intricacies within the system. Introducing the electrode into the mixing chamber has the potential to promote interaction among the incoming steam, CO_2, and water. However, the rapid and turbulent mixing in this zone might constrain the electrode's efficacy in boosting heat transfer, as the electrode's influence could be diffused amidst the turbulent flow dynamics. Alternatively, locating the electrode at the throat could offer a prospect for heightened heat transfer efficiency. Another possibility lies in siting the electrode within the diffuser segment, where the fluid expands and gradually decelerates, thereby affording an extended duration for heat exchange processes to unfold. It is noticeable that evaporation results from shock wave is neglected. Fig. 14 illustrates a graphical representation of the computational domain of electrode in SEC. The results of the electric potential and charge density are presented in Figs. 15 and 16. These figures demonstrate the presence of applied electric potentials on the surface of the discharge wire. Additionally, the charges are observed to be transported along the electric field, which is formed by

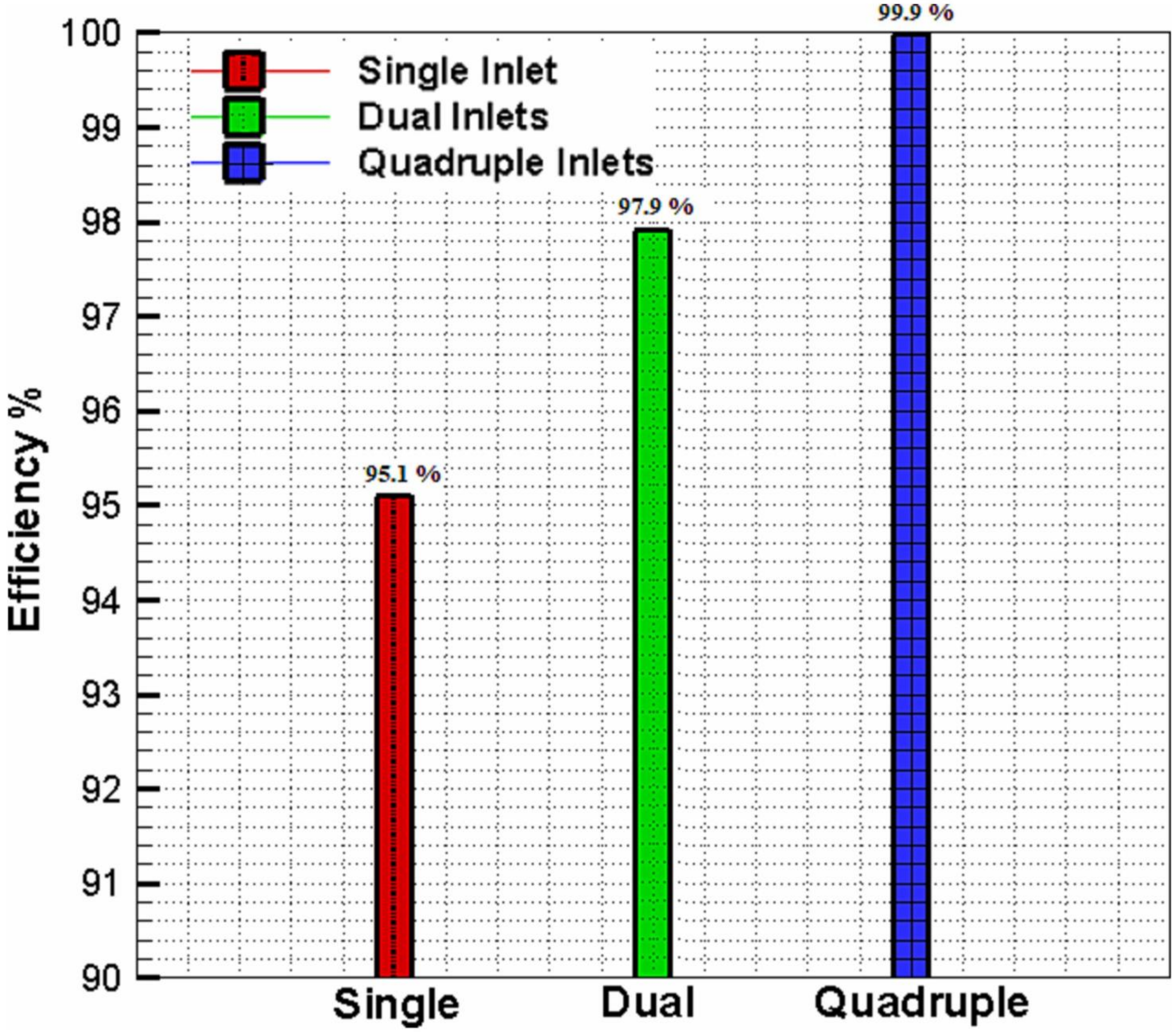

Fig. 22. Separation efficiency of single, dual and quadruple inlets cyclone at 0.03 of CO_2 mass fraction.

the divergence of the electric potential. Notably, the electrical potential and charge exhibit increased strength in the vicinity of the emitters.

It is crucial to recognize that the applied voltage can vary within a specific range, which is influenced by the geometry and conditions of the problem (Fig. 17). This range typically spans from the threshold voltage needed to initiate the electrohydrodynamic phenomenon to a voltage that causes the fluid to reach its breakdown limit. The determination of the threshold voltage for the onset of the electrohydrodynamic phenomenon can be achieved using the following relationship [44]:

$$_{eff} = \frac{4h}{\pi} for \frac{h}{s} \leq 2 \tag{39}$$

$$_0 = 3 \times 10^6 f \left\{ \frac{T_0 P}{T P_0} + 0.03 \sqrt{\frac{T_0 P}{P T_0 r_0}} \right\} \tag{40}$$

$$_0 = r_w E_0 \ln\left(\frac{r_{eff}}{r_w}\right) \tag{41}$$

Vhere $V_0(V), r_{eff}(m)$ and $E_0(\frac{V}{m})$ are the corona onset voltage, the equivlent cylinder radius and the corona initiating electric field, respectively. In addition, f (dimensionless), T_0(K) and P (atm) refer to roughness factor of the corona wire, temperature constant (293 K) and free-stream gas pressure, respectively. r_0 (m) and r_w (m) are radius of corona sheath and radius of corona wire, respectively. P_0 (atm) is pressure constant. So, corona initiating electric field (E_0) and corona onset voltage (V_0) are 7.0249 ($\frac{MV}{m}$) and 14.82 (KV), respectively.

Fig. 18 presents a comprehensive comparison, illustrating how the axial heat transfer coefficient varies along the axis of SEC at different steam inlet mass flux values. The heat transfer coefficient, represented as 'h', was computed using the methodology detailed in our previous study [28]. When high-speed steam is injected into the subcooled water flow, it imparts both momentum and heat to the water across the interface. As the steam mass flux rises, the relative velocity of the liquid phase at the steam-water interface also increases. This amplifies the turbulent intensity within the hot water layer near the interface. Consequently, the local heat transfer coefficient on the liquid side exhibits an augmentation with higher steam mass flux values.

Fig. 19 shows the variation of the condensation heat transfer coefficient with different electric fields in the SEC. As condensation occurs, the thickness of the liquid film gradually grows, causing an escalation in thermal resistance and subsequently reducing the heat transfer coefficient. Nevertheless, studies have demonstrated that the application of electrohydrodynamic (EHD) techniques and an increase in mass flux can effectively mitigate this phenomenon. Consequently, the heat transfer coefficient exhibits enhancement when both EHD techniques and mass flux are increased.

6.4. Cyclone separator

6.4.1. Effect of single, dual and quadruple inlets

The efficiency of particle separation in various industrial applications is a critical aspect directly impacted by the design and operation of cyclone separators. Among the factors influencing their performance, the inlet configuration plays a crucial role in determining how the fluid is introduced into the system. This section delves into an investigation of the effects of different inlet configurations, specifically single, dual and quadruple inlets, on the efficiency of cyclone separators. In the single inlet configuration, the fluid enters the system through a single entrance, while the dual and quadruple inlet configurations feature two and four entrances, respectively. The primary objective of this section is to thoroughly assess the impact of these inlet configurations on the effectiveness of particle separation. To achieve this goal, an analysis of the cyclone's internal flow structure has been conducted using state-of-the-art computational flow visualization techniques. The visualization of the dual and quadruple inlet cyclones' geometry and mesh can be observed in Fig. 20.

Fig. 21 illustrates the velocity vectors obtained from cyclones equipped with single and quadruple inlets. In the case of the single inlet cyclone, the intended purpose of the inlet chamber, designed to stabilize the flow upon entry, proved ineffective, resulting in irregular swirling motion within the cyclone. The velocity vectors in this configuration exhibit a fluctuating CO2 core accompanied by wavering velocity vectors directed towards the overflow outlet. On the other hand, the velocity vectors observed in the quadruple inlet cyclone demonstrate symmetrical patterns, with no wavering CO2 core along the cyclone's axis. The velocity distribution is highest near the cyclone walls and gradually diminishes towards the center. The turbulence present in the single inlet cyclone introduces an undulating nature to the flow, leading to inadequate separation between CO2 and water droplets and consequently diminishing the overall separation efficiency. The flow pattern within the cyclone, as well as the segregation and concentration of CO2 and water, are significantly influenced by the number of tangential inlets. This phenomenon was explored by Osei et al. [45], who highlighted the importance of the internal flow structure in determining the distribution of axial and tangential velocities within cyclones. The wavering nature of the flow in a single inlet cyclone detrimentally affects separation performance, as water droplets located near the boundary of reverse flow are carried upwards along with the CO2-rich fluid, ultimately exiting through the overflow outlet. In contrast, the unwavering flow structure observed in the quadruple inlet cyclone facilitates effective separation by enabling efficient segregation of CO2-rich and water-rich cores.

The separation efficiency achieved from the use of the single, dual and quadruple inlets cyclones indicated significant performance from the use of the quadruple inlet cyclone.

The separation efficiency was calculated, which was defined as follows:

$$= \left(\frac{\dot{m}_{liquidatinlet} - \dot{m}_{liquidatgasoutlet}}{\dot{m}_{liquidatinlet}}\right) \times 100 \qquad (42)$$

Where $\dot{m}$ is the mass flow rate.

The data in Fig. 22 reveals that increasing the number of inlets in cyclones improves the separation efficiency of water and CO2. A cyclone with a single inlet achieves 95.1 % separation efficiency, while two inlets enhance the performance to 97.9 %. However, the most remarkable result is seen in cyclones with four inlets, which achieve separation efficiency of 99.9 %.

7. Conclusion

In order to optimize the separation sections and ensure the production of high-purity CO2, a comprehensive numerical simulation was conducted. Integrating the SEC and cyclone separator offers a viable strategy for CO2 purification in Negative CO2 Emission Power Plants (nCO2PP). This integrated approach creates a dedicated separation section capable of achieving high-purity CO2 production. Implementing this combination presents a practical means to enhance the purification process within power plants focusing on enhancing steam condensation, effective backpressure management, optimizing heat transfer with EHD techniques and enhanced cyclone separation efficiency. Accomplished calculations validate that the novel presented model aligns well with experimental findings.

By conducting numerical analysis on the examined scenarios, the following results were obtained:

- Lower steam inlet mass flow rates expedite steam condensation, yielding efficient phase transition. However, higher mass flow rates surpass water's condensation capacity, leading to steam plume expansion. This results in intensified condensation in the liquid phase as the plume travels further. Implementing an inlet mass flow rate of around 10 g/s could enhance condensation efficiency. Additionally, controlling the steam inlet mass flow rate could potentially influence steam velocity at the nozzle outlet, facilitating adjustments in pressure and suction effects. These insights can guide operational decisions to achieve optimal steam condensation rates.
- Adjusting backpressure offers a mechanism to regulate condensation efficiency. Increased backpressure impedes steam condensation, leading to reduced volume fraction of steam. Conversely, lower backpressure minimizes resistance, increasing condensation rates and steam volume fraction. Precise backpressure management is paramount for adjusting condensation efficiency within the steam ejector condenser. Monitoring backpressure within a range, such as 96 to 106 kPa, allows optimization of static pressure distribution. Practical applications can involve real-time backpressure control systems to ensure effective condensation.
- When high-velocity steam is injected into a subcooled water flow, it imparts both momentum and heat to the water at the interface. As the steam mass flux increases, the relative velocity of the liquid phase at the steam-water interface also rises, intensifying the turbulence within the hot water layer nearby. This results in an augmentation of the local heat transfer coefficient on the liquid side, particularly with higher steam mass flux values. However, during condensation, the thickness of the liquid film gradually increases, which elevates thermal resistance and subsequently reduces the heat transfer coefficient. Nevertheless, research has demonstrated that the application of electrohydrodynamic (EHD) techniques and an increase in mass flux effectively mitigate this phenomenon. Consequently, both EHD techniques and mass flux contribute to enhancing the heat transfer coefficient.
- Augmenting the number of inlets in cyclones significantly improves separation efficiency for water and CO2. Cyclones with more inlets exhibit remarkable separation efficiencies; for instance, a cyclone with four inlets attains 99.9 % separation efficiency. In practical scenarios, adopting cyclones with multiple inlets could lead to improved separation performance, enhancing the overall system's effectiveness.

CRediT authorship contribution statement

Milad Amiri: Conceptualization, Methodology, Data curation, Formal analysis, Investigation, Project administration, Resources, Software, Validation, Visualization, Writing - original draft, Writing - review & editing. **Jaroslaw Mikielewicz:** Conceptualization, Investigation, Writing - review & editing. **Dariusz Mikielewicz:** Conceptualization, Supervision, Project administration, Funding acquisition, Investigation, Writing - review & editing.

Declaration of Competing Interest

The authors declare that they have no known competing financial interests or personal relationships that could have appeared to influence the work reported in this paper.

Data availability

Data will be made available on request.

Acknowledgements

The research leading to these results has received funding from the Norway Grants 2014–2021 via the National Center for Research and Development. Article has been prepared within the frame of the project: "Negative CO2 emission gas power plant" - NOR/POLNORCCS/NEGATIVE-CO2- PP/0009/2019–00 which is co-financed by programme "Applied research" under the Norwegian Financial Mechanisms 2014–2021 POLNOR CCS 2019 - Development of CO2 capture solutions integrated in power and industry processes. The authors would also like to express their gratitude to Pawel Ziolkowski and Kamil Stasiak.

References

[1] L. Guo, H. Jin, Y. Lu, Supercritical water gasification research and development in China, J. Supercrit. Fluids 96 (2015) 144–150.

[2] M. Spitoni, M. Pierantozzi, G. Comodi, F. Polonara, A. Arteconi, Theoretical evaluation and optimization of a cryogenic technology for carbon dioxide separation and methane liquefaction from biogas, J. Nat. Gas Sci. Eng. 62 (2019) 132–143.

[3] P. Ziółkowski, K. Stasiak, M. Amiri, D. Mikielewicz, Negative carbon dioxide gas power plant integrated with gasification of sewage sludge, Energy 262 (2023), 125496.

[4] P. Ziółkowski, et al., Mathematical modelling of gasification process of sewage sludge in reactor of negative CO2 emission power plant, Energy 244 (2022), 122601.

[5] P. Ziółkowski, et al., Thermodynamic analysis of negative CO_2 emission power plant using Aspen Plus, Aspen Hysys, and Ebsilon software, Energies 14 (19) (2021) 6304.

[6] D. Mikielewicz, M. Amiri, M. Klugmann, J. Mikielewicz, A novel concept of enhanced direct-contact condensation of vapour-inert gas mixture in a spray ejector condenser, Int. J. Heat Mass Transf. 216 (2023), 124576.

[7] K.-S. Liang, Experimental and analytical study of direct contact condensation of steam in water, Nucl. Eng. Des. 147 (3) (1994) 425–435.

[8] X. Yang, D. Chong, J. Liu, X. Zong, J. Yan, Experimental study on the direct contact condensation of the steam–air mixture in subcooled water flow in a rectangular channel, Int. J. Heat Mass Transf. 88 (2015) 424–432.

[9] Y. Zhou, et al., Numerical simulation on the direct contact condensation in a steam-water two-phase ejector with non-condensable gas, Int. J. Therm. Sci. 185 (2023), 108030.

[10] M.H. Mousa, N. Miljkovic, K. Nawaz, Review of heat transfer enhancement techniques for single phase flows, Renew. Sustain. Energy Rev. 137 (2021), 110566.

[11] M. K. Dobson and J. C. Chato, Condensation in smooth horizontal tubes, 1998.

[12] O.E. Ramadan, S. Soo, Electrohydrodynamic secondary flow, The Physics of Fluids 12 (9) (1969) 1943–1945.

[13] J. Yang, C. Liu, S. Li, B. Sun, J. Xiao, Y. Jin, A new pressure drop model of gas–liquid cyclone with innovative operation mode, Chem. Eng. Process. 95 (2015) 256–266.

[14] H. Safikhani, P. Mehrabian, Numerical study of flow field in new cyclone separators, Adv. Powder Technol. 27 (2) (2016) 379–387.

[15] W. Mazyan, A. Ahmadi, H. Ahmed, M. Hoorfar, Increasing efficiency of natural gas cyclones through addition of tangential chambers, J. Aerosol Sci 110 (2017) 36–42.

[16] L. Wiesegger, R. Knauss, G. Guntschnig, J. Brandner, R. Marr, Vapor–liquid phase separation in micro-/ministructured devices, Chem. Eng. Sci. 93 (2013) 32–46.

[17] X. Xu, Q. Yang, C. Wang, H. Wang, Impact of bubble coalescence on separation performance of a degassing hydrocyclone, Sep. Purif. Technol. 152 (2015) 80–86.

[18] C. Han, Y. Hu, W. Li, Q. Bie, Gas-solid separation performance and structure optimization in 3D printed guide vane cyclone separator, Adv. Powder Technol. 33 (11) (2022), 103815.

[19] Z. Gao, J. Wang, Z. Liu, Y. Wei, J. Wang, Y. Mao, Effects of different inlet structures on the flow field of cyclone separators, Powder Technol. 372 (2020) 519–531.

[20] S. Dong, Y. Jiang, R. Jin, K. Dong, B. Wang, Numerical study of vortex eccentricity in a gas cyclone, App. Math. Model. 80 (2020) 683–701.

[21] B. Zhao, H. Li, D. Wang, Q. Liu, Y. Su, Insight into performance and mechanism of energy loss for microscale vortex separator/reactor with symmetrical multi-inlets, Powder Technol. 395 (2022) 122–132.

[22] S.M. Vahedi, F. Parvaz, M. Kamali, H. Jafari Jebeli, "Numerical investigation of the impact of inlet channel numbers on the flow pattern, performance, and erosion of gas-particle cyclone, Iran J Oil Gas Sci. Technol. 7 (4) (2018) 59–78.

[23] D.K. Le, J.Y. Yoon, Numerical investigation on the performance and flow pattern of two novel innovative designs of four-inlet cyclone separator, Chemical Engineering and Processing-Process Intensification 150 (2020), 107867.

[24] A. Shah, "Thermal Hydraulic Analysis of Steam Jet Pump," Pakistan Institute of Engineering and Applied Sciences, Islamabad, Pakistan., 2012.

[25] Q. Xu, L. Liang, Y. She, X. Xie, L. Guo, Numerical investigation on thermal hydraulic characteristics of steam jet condensation in subcooled water flow in pipes, Int. J. Heat Mass Transf. 184 (2022), 122277.

[26] Q. Xu, C. Liu, Q. Liu, Y. Zhu, H. Zhou, L. Guo, Interfacial characteristics of steam jet condensation in subcooled water pipe flow–An experimental and numerical study, Chem. Eng. Sci. 251 (2022), 117457.

[27] X. Chen, M. Tian, X. Qu, Y. Zhang, Numerical investigation on the interfacial characteristics of steam jet condensation in subcooled water flow in a restricted channel, Int. J. Heat Mass Transf. 137 (2019) 908–921.

[28] M. Amiri, D. Mikielewicz, Three-dimensional numerical investigation of hybrid nanofluids in chain microchannel under electrohydrodynamic actuator, Numerical Heat Transfer, Part a: Applications 83 (10) (2023) 1146–1173.

[29] H. Moayedi, N. Amanifard, H.M. Deylami, Evaluation of using micropolar fluid approach for the EHD-enhanced forced convection through a rectangular channel using multiple electrode arrangements, Appl. Therm. Eng. 159 (2019), 113857.

[30] O.E. Olaleye, B. Van Ombele, A.A. Olusola, X. Li, CFD modeling analysis of a vertical gas liquid separator, J. Pet. Sci. Eng. (2022), 110733.

[31] M.H. Purnanto, S.J. Zarrouk, J.E. Cater, CFD modelling of two-phase flow inside geothermal steam-water separators, IPENZ Transactions 40 (2013) 1–10.

[32] E. Yohana, M. Tauviqirrahman, B. Yusuf, K.-H. Choi, V. Paramita, Effect of vortex limiter position and metal rod insertion on the flow field, heat rate, and performance of cyclone separator, Powder Technol. 377 (2021) 464–475.

[33] A. Surjosatyo, A. Respati, H. Dafiqurrohman, Analysis of the influence of vortexbinder dimension on cyclone separator performance in biomass gasification system, Procedia Eng. 170 (2017) 154–161.

[34] J.V.N. Nejad, S. Kheradmand, The effect of fluctuating boundary on flow field and performance parameters of cyclone separator, Powder Technol. 390 (2021) 401–416.

[35] A. Hoekstra, J. Derksen, H. Van Den Akker, An experimental and numerical study of turbulent swirling flow in gas cyclones, Chem. Eng. Sci. 54 (13–14) (1999) 2055–2065.

[36] L. Schiller, A drag coefficient correlation, Zeit. Ver. Deutsch. Ing. 77 (1933) 318–320.

[37] M.A.L. De Bertodano, Two fluid model for two-phase turbulent jets, Nucl. Eng. Des. 179 (1) (1998) 65–74.

[38] R. Utikar, N. Darmawan, M. Tade, Q. Li, G. Evans, M. Glenny, V. Pareek, Hydrodynamic simulation of cyclone separators, in: Computational fluid dynamics, InTech, 2010, pp. 241–266.

[39] X.-H. Qu, M.-C. Tian, Acoustic and visual study on condensation of steam–air mixture jet plume in subcooled water, Chem. Eng. Sci. 144 (2016) 216–223.

[40] B. Wang, D. Xu, K. Chu, A. Yu, Numerical study of gas–solid flow in a cyclone separator, App. Math. Model. 30 (11) (2006) 1326–1342.

[41] W. Li, Z. Meng, J. Wang, Z. Sun, Effect of non-condensable gas on pressure oscillation of submerged steam jet condensation in condensation oscillation regime, Int. J. Heat Mass Transf. 124 (2018) 141–149.

[42] X. Yang, N. Chen, Y. Zhou, J. Liu, J. Wei, Dynamics of chugging phenomenon induced by subsonic and supersonic steam–air jet condensation in water flow, Exp. Therm Fluid Sci. 136 (2022), 110672.

[43] A. Gidwani, M. Molki, M.M. Ohadi, EHD-enhanced condensation of alternative refrigerants in smooth and corrugated tubes, HVAC&R Research 8 (3) (2002) 219–237.

[44] J.H. Goo, J.W. Lee, Stochastic simulation of particle charging and collection characteristics for a wire-plate electrostatic precipitator of short length, J. Aerosol Sci 28 (5) (1997) 875–893.

[45] H. Osei, H. Al-Kayiem, A. Osman, Flow dynamics behaviour of a novel liquid–liquid hydrocyclone with varying upper cylindrical lengths and number of inlets, ARPN J. Eng. Appl. Sci. 11 (2016) 12159–12164.